

Exploring the Developing Preterm Brain with Diffusion Tensor Magnetic Resonance Imaging

Mustafa Anjari

A dissertation submitted for the degree of
Doctor of Philosophy

**Imperial College London
University of London**

December 2008

Robert Steiner MRI Unit
Imaging Sciences Department
MRC Clinical Sciences Centre

Department of Computing
Imperial College London

Abstract

The majority of preterm-born infants now survive beyond the perinatal period. However, this has been accompanied by increases in neurodevelopmental impairment not explained by the presence of focal lesions on conventional magnetic resonance imaging (MRI). Diffusion tensor imaging (DTI) is a quantitative MRI technique with the potential to assess micro-structural brain abnormalities. This project examines the developing preterm brain using computational analysis of DTI data.

Tract-based spatial statistics (TBSS) is a method for registering diffusion-derived fractional anisotropy (FA) data to allow objective investigation of cerebral white matter tracts. FA maps from term-born control infants and preterm infants at term age with no evidence of focal white matter abnormality on conventional MRI were used to assess the feasibility of using TBSS with neonatal DTI data, and then to investigate the effects of preterm birth on white matter microstructure at term. FA was found to be reduced in the preterm group in numerous white matter regions, with the most immature-born infants displaying more extensive regions of FA reduction.

The effects of various clinical variables on FA data processed using TBSS were assessed in another cohort of preterm infants imaged at term. This demonstrated for the first time that acute and chronic lung disease are independently associated with localised cerebral white matter abnormalities in the genu of the corpus callosum and the left inferior longitudinal fasciculus respectively.

Whilst using TBSS, only major white matter tracts can be studied. To enable analysis of whole brain DTI data, optimisation of a nonlinear registration algorithm based on basis-splines for retrospective unwarping of echo planar DTI data is presented.

This work provides new insights into the microstructural neuro-imaging correlates of preterm birth, and suggests a method that may allow subsequent voxelwise analysis of diffusion data from more regions of the developing brain than can currently be studied.

The work presented in this thesis was conducted by the author at the Robert Steiner MRI Unit, MRC Clinical Sciences Centre, Hammersmith Hospital and the Department of Computing, Imperial College London between July 2005 and June 2008.

This work has not been submitted for the purpose of obtaining any other degree.

Mustafa Anjari

Acknowledgements

I would like to begin by thanking my supervisors, Serena Counsell, David Edwards and Daniel Rueckert. They have been a constant source of encouragement and I will always be grateful for their guidance and continuous generosity with their time, expertise and friendship.

Many thanks are also due to all the other past and present members of the Imaging Sciences Department at Hammersmith Hospital and the Visual Information Processing Group at South Kensington. In particular, I would like to acknowledge Paul Aljibar, Joanna Allsop, Alvaro Bertelsen, Kanwal Bhatia, Jeroen Dudink, Gianlorenzo Fagiolo, Ioannis Gousias, Jo Hajnal, Alex Hammers, Tayyib Hayat, my lab mates Shuzhou Jiang and Shaihan Malik, David Larkman, Mary Rutherford, Dominic Spill and Latha Srinivasan. They have filled the past three years with stimulating discussions and have made the lab an inviting and fun place to work. Marta Varela and Rita Nunes have spent many evenings reading through sections of my thesis, and for that, coupled with everything else they have provided during the last two years, deserve my special thanks.

Professor Junia Melo gave me the first opportunity to visit a research laboratory and discover what life as a scientist entailed. Her kindness and mentorship were key in encouraging me to undertake the PhD.

Finally, my family have been a constant source of support, patience and love, especially during the last few months. Thank you for helping me to get through them.

Contents

Abstract	2
Acknowledgements	5
Contents	6
List of Figures	13
List of Tables	17
List of Abbreviations	19
List of Publications	22
Papers	22
Abstracts	23
Chapter 1: Introduction	24
1.1 Motivation	24
1.2 Aim	25
1.3 Hypothesis	26
1.4 Thesis outline	26
1.4.1 Chapter 2	26
1.4.2 Chapter 3	27
1.4.3 Chapter 4	28
1.4.4 Chapter 5	28
1.4.5 Chapter 6	29
1.4.6 Chapter 7	29
Chapter 2: Background - Magnetic Resonance Imaging, Diffusion MRI and Image Registration	30
2.1 Magnetic resonance imaging	30
2.2 Nuclear magnetic resonance	31

2.2.1	Relaxation	33
2.2.2	Signal reception	35
2.3	Magnetic resonance imaging	35
2.3.1	Image formation	35
2.3.2	Image contrast	41
2.4	Echo-planar imaging	43
2.5	Diffusion MRI	44
2.5.1	Diffusion	44
2.5.2	Diffusion weighted imaging	46
2.5.3	Diffusion tensor imaging	51
2.5.3.1	Limitations of the diffusion tensor model	57
2.6	Echo-planar diffusion weighted imaging	58
2.6.1	Problems with echo planar imaging	59
2.6.1.1	Geometric distortion artefacts associated with inhomogeneities in the B0 field	59
2.6.1.2	Blurring	61
2.6.1.3	Nyquist ghosting	61
2.6.1.4	Fat artefact	61
2.6.1.5	Eddy current effects in diffusion tensor EPI	62
2.6.1.6	Additional challenges	66
2.6.2	Correction of errors in echo planar imaging data	66
2.6.2.1	Correction for distortions arising from B0 inhomogeneity effects	67
2.6.2.2	Correction for distortions arising from residual eddy current effects	68
2.6.2.3	Correction strategies for motion-related artefacts	71
2.7	Image registration	71
2.7.1	Introduction	71
2.7.2	Transformation models	74
2.7.2.1	Rigid transformations	75
2.7.2.2	Affine transformations	76
2.7.2.3	Nonlinear transformations	78
2.7.3	Similarity measures	80

2.7.3.1	Voxel-based metrics	80
2.7.3.1.1	Sum of squared difference (SSD)	80
2.7.3.1.2	Cross-correlation	81
2.7.3.2	Entropy-based metrics	81
2.7.3.2.1	Mutual information (MI)	82
2.7.3.2.2	Normalised mutual information (NMI)	82
2.7.3.3	Histogram-based density estimation	83
2.7.4	Interpolation	83
2.7.5	Regularisation	84
2.7.6	Optimisation	84
2.7.7	Applications of image registration	85
2.7.7.1	Image registration for EPI distortion correction	85
2.7.7.2	Image registration for population-based analysis of MRI data	86
2.7.7.2.1	Spatial normalisation	86
2.7.7.2.2	Target selection	86
2.7.7.3	Registering EPI data to an anatomical image	87
2.7.8	Image registration software	88
2.7.8.1	FMRIB's Linear Image Registration Tool (FLIRT)	88
2.7.8.2	Automated Image Registration's alignlinear and align_warp	90
2.7.8.2.1	Alignlinear	90
2.7.8.2.2	Align_warp	93
2.7.8.3	Tract-based Spatial Statistics (TBSS)	94
2.7.8.4	Registration models based on free-form deformations	101
2.7.8.4.1	B-splines	102
Chapter 3: The Developing Brain and Preterm Birth		104
3.1	Brain development	104
3.1.1	Microscopic development of the brain	104
3.1.2	Oligodendrocyte development	107
3.1.3	Myelination	107
3.2	Preterm birth	109
3.2.1	Incidence of preterm birth	109

3.2.2	Some clinical variables associated with preterm birth	109
3.2.2.1	Preterm premature rupture of membranes	109
3.2.2.2	Acute lung disease	110
3.2.2.3	Chronic lung disease	111
3.2.2.4	Retinopathy of prematurity	111
3.2.3	Brain injury in the preterm infant	112
3.2.3.1	Germinal layer haemorrhage	113
3.2.3.2	Periventricular haemorrhagic infarction	114
3.2.3.3	Periventricular leukomalacia	115
3.2.4	Neurodevelopmental outcomes associated with preterm birth	118
3.2.4.1	Motor outcomes	118
3.2.4.2	Sensory outcomes	118
3.2.4.3	Cognitive and behavioural outcomes	119
3.3	MRI of the developing brain	120
3.3.1	MRI and myelination	121
3.3.1.1	MRI appearances of myelination	121
3.3.2	Diffusion weighted imaging and diffusion tensor imaging of the developing brain	123
3.3.2.1	White matter changes	123
3.3.2.3	Grey matter changes	124
3.3.3	MRI of diffuse white matter injury	124
3.3.4	Quantitative MR studies of brain development and pathology in preterm infants	125
3.4	Conclusions	127
3.5	Aims	128
Chapter 4: The Effect of Preterm Birth on Fractional Anisotropy at Term		130
4.1	Introduction	130
4.2	Aim	131
4.3	Materials and methods	131

4.3.1	Subjects	131
4.3.1.1	Preterm infants	131
4.3.1.2	Extremely preterm infants	132
4.3.1.3	Term control infants	132
4.3.2	Magnetic resonance imaging	133
4.3.2.1	Diffusion tensor imaging	133
4.3.3	Image processing and analysis	134
4.3.4	Statistical considerations	135
4.4	Results	136
4.4.1	Voxelwise thresholding	136
4.4.2	TBSS-defined region of interest-based analysis	140
4.5	Discussion	147
4.6	Summary	150
4.7	Further questions	150
Chapter 5: Fractional Anisotropy Changes Associated with Lung Disease Amongst Preterm-Born Infants		151
5.1	Introduction	151
5.2	Aim	152
5.3	Materials and methods	153
5.3.1	Subjects	153
5.3.2	Magnetic resonance imaging	156
5.3.2.1	Diffusion Tensor Imaging	156
5.3.3	Data analysis	156
5.4	Results	158
5.4.1	Confounding variables	158
5.4.1.1	Increasing prematurity	158
5.4.1.2	Age at imaging	158
5.4.2	Study variables	158
5.4.2.1	Acute lung disease	158
5.4.2.2	Chronic lung disease	159

5.4.3	Exploratory variables	159
5.4.3.1	Gender	159
5.4.3.2	Evidence of serious infection	160
5.4.3.3	Prolonged rupture of membranes	160
5.5	Discussion	168
5.6	Summary	172
Chapter 6: Optimisation of a B-Spline Based Registration Algorithm for Retrospective Correction of Geometric Distortions in Neonatal DTI		
Data		173
6.1	Introduction	173
6.2	Aim	174
6.3	Materials and methods	174
6.3.1	Subjects	174
6.3.2	Magnetic resonance imaging	175
6.3.2.1	Diffusion tensor imaging	175
6.3.3	Image registration	175
6.3.3.1	Image similarity measure	176
6.3.3.2	Transformation models	176
6.3.3.2.1	Affine registration model	176
6.3.3.2.2	Nonlinear registration model	176
6.3.3.2.3	Affine and nonlinear registration parameters	177
6.3.3.3	Optimal transformation	177
6.3.3.4	Comparison with other registration algorithms	178
6.3.3.4.1	FLIRT	178
6.3.3.4.2	Align_warp	179
6.3.4	Validation of geometric and motion correction distortion algorithm	180
6.3.4.1	Fiducial localisation error	181
6.4	Results	190
6.4.1	Optimised B-spline based registration of EPI data to high resolution anatomical data	190

6.4.2	Consistency of landmark positioning (fiducial localisation error)	199
6.4.3	Visual comparison of optimised B-spline registration algorithm, FLIRT and align_warp	202
6.4.4	Landmark-based comparison of optimised B-spline registration algorithm, FLIRT and align_warp	207
6.4.4.1	Overall comparison of registration performance (fiducial registration error)	207
6.4.4.2	Registration performance across subjects (fiducial registration error)	209
6.4.4.3	Registration performance across landmarks (fiducial registration error)	212
6.4.4.4	Statistical comparison of registration performance	215
6.5	Discussion	218
6.6	Limitations	220
6.7	Suggestions for further work	222
6.7.1	Deweight the cost function	222
6.7.2	Individually tailoring the coregistration parameters	222
6.7.3	Coregistering tensor-derived scalar maps	223
6.7.4	Normalisation to a study-specific average space	224
6.8	Conclusion	224
Chapter 7: Summary and Final Remarks		226
7.1	Summary	226
7.2	Conclusion and final remarks	228
Appendices		230
Appendix A: The reproducibility of landmark positioning at each landmark		230
Appendix B: The effect of different registration methodologies for achieving correspondence in different brain regions		234
Reference List		242

List of Figures

Figure 2.1: Classical interpretation of nuclear magnetic resonance	31
Figure 2.2: Magnetisation vectors and frames of reference	32
Figure 2.3: Longitudinal and transverse relaxation following a 90° RF pulse for grey and white matter	34
Figure 2.4: Frequency encoding	36
Figure 2.5: Use of a field gradient for selective excitation of a slice	38
Figure 2.6: Pulse sequence diagram for a gradient echo image	39
Figure 2.7: The relationship between image space and k-space	40
Figure 2.8: Spin-echo formation	41
Figure 2.9: Proton density-weighted, T1-weighted and T2-weighted images	42
Figure 2.10: Echo-planar imaging sequence	43
Figure 2.11: Concentration distribution at different times for free, isotropic diffusion	45
Figure 2.12: Pulse diagram for the Stejskal-Tanner PGSE sequence	47
Figure 2.13: Diffusion weighted images	50
Figure 2.14: Diffusion ellipsoids	54
Figure 2.15: Sample fifteen direction diffusion gradient scheme	56
Figure 2.16: Scalar maps that can be derived from DTI data	57
Figure 2.17: Signal loss and pile up resulting from inhomogeneities in the B_0 field	60
Figure 2.18: Nyquist ghosting and fat artefacts in echo-planar images	62
Figure 2.19: The effect of eddy currents on gradient waveforms	63
Figure 2.20: Distortion resulting from eddy currents	65
Figure 2.21: Image registration algorithm	73
Figure 2.22: Affine transformations	77
Figure 2.23: Schematic diagram of the affine registration algorithm employed by AIR	91
Figure 2.24: Creating the mean FA skeleton	96
Figure 2.25: Identifying the local tract centre	98

Figure 2.26: Projecting the mean FA skeleton onto each subject's aligned FA map	99
Figure 2.27: An example of a mean FA skeleton 'distance map'	100
Figure 3.1: The development of the human cerebral cortex	105
Figure 3.2: Myelination in the central nervous system	108
Figure 3.3: Preterm brain development assessed with MRI	120
Figure 3.4: Diffuse excessive high signal intensity	125
Figure 4.1: The effect of preterm birth on FA at term equivalent age	137
Figure 4.2: The effect of preterm birth on λ_1 at term equivalent age	138
Figure 4.3: The effect of preterm birth on λ_2 at term equivalent age	139
Figure 4.4: The effect of preterm birth on λ_3 at term equivalent age	140
Figure 4.5: A box plot of FA values in regions of difference between term-born control infants and preterm infants imaged at term	143
Figure 4.6: A box plot of FA values in regions of difference between term-born control infants and preterm infants born ≤ 28 weeks GA imaged at term	146
Figure 5.1: The effect of increasing prematurity at birth on cerebral white matter at term equivalent age	160
Figure 5.2: The effect of acute lung disease on FA at term-equivalent age	161
Figure 5.3: The effect of acute lung disease on FA in the genu of the corpus callosum at term-equivalent age	162
Figure 5.4: The effect of chronic lung disease on FA at term-equivalent age	163
Figure 5.5: The effect of chronic lung disease on FA in the left inferior longitudinal fasciculus at term-equivalent age	164
Figure 6.1: Landmark 1	182
Figure 6.2: Landmark 2	182
Figure 6.3: Landmark 3	183
Figure 6.4: Landmark 4	183
Figure 6.5: Landmark 5	184
Figure 6.6: Landmark 6	184
Figure 6.7: Landmark 7	185
Figure 6.8: Landmark 8	185
Figure 6.9: Landmark 9	186

Figure 7.10: Landmark 10	186
Figure 6.11: Landmark 11	187
Figure 6.12: Landmark 12	187
Figure 6.13: Landmark 13	188
Figure 6.14: Landmark 14	188
Figure 6.15: Landmark 15	189
Figure 6.16: An overview of some of the B-spline based registration models used	192
Figure 6.17: Distortions in EPI data in two different slices	193
Figure 6.18: Slice-by-slice registration	194
Figure 6.19: A hierarchical distortion correction registration algorithm using free-form deformations based on B-splines	196
Figure 6.20: Reproducibility of landmark positioning at each landmark	199
Figure 6.21: A histogram showing the distance between the mean landmark position and the individually placed landmarks for all fifteen landmarks placed on each subject's T2-weighted image	201
Figure 6.22: A histogram showing the distance between the mean landmark position and the individually placed landmarks for all fifteen landmarks placed on each subject's $b = 0$ s/mm ² image	201
Figure 6.23: T2-weighted and $b = 0$ s/mm ² image correspondence before and after registration (sagittal slice)	203
Figure 6.24: T2-weighted and $b = 0$ s/mm ² image correspondence before and after registration (axial slice)	205
Figure 6.25: T2-weighted and $b = 0$ s/mm ² image correspondence before and after registration (coronal slice)	206
Figure 6.26: Histograms of the difference between corresponding landmarks on the $b = 0$ s/mm ² and T2-weighted images prior to and following registration with the different models used	208
Figure 6.27: Registration performance across subjects	211
Figure 6.28: Registration performance across landmarks	214
Figure 6.29: Box and whisker diagrams for final corresponding landmark distances using the different registration models	217

Figure A.1: Reproducibility of landmark positioning at Landmarks 1-6	231
Figure A.2: Reproducibility of landmark positioning at Landmarks 7-12	232
Figure A.3: Reproducibility of landmark positioning at Landmarks 13-15	233

List of Tables

Table 2.1: Tissue contrast in MRI with respect to TR and TE	42
Table 3.1: The Papile classification of IVH/PHI in the premature neonate	115
Table 3.2: Age-associated changes in myelin appearance on MRI	122
Table 4.1: Mean for FA, λ_1 , λ_2 and λ_3 in term-born control infants and preterm infants imaged at term	142
Table 4.2: Mean for FA, λ_1 , λ_2 and λ_3 in term-born control infants and preterm infants born ≤ 28 weeks GA imaged at term	144
Table 5.1: A correlation table of the association between each of the confounding variables, study variables and exploratory variables in the study population	155
Table 5.2: FA multivariate linear model summary in the genu of the corpus callosum	166
Table 5.3: FA multivariate linear model summary in the left inferior longitudinal fasciculus	167
Table 6.1: FLIRT registration parameters	179
Table 6.2: Alignlinear and align_warp registration parameters	180
Table 6.3: The parameters required for registration using a FFD model based on B-splines	197
Table 6.4: Optimised B-spline registration parameters	198
Table 6.5: Mean differences between corresponding landmarks in the T2-weighted and $b = 0$ s/mm ² image on a subject-by-subject basis	210
Table 6.6: Mean differences between corresponding landmarks in the T2-weighted and $b = 0$ s/mm ² image on a landmark-by-landmark basis	213
Table 6.7: Significance matrix for all landmarks in all subjects	216
Table B.1: Landmark 1	234
Table B.2: Landmark 2	235
Table B.3: Landmark 3	235
Table B.4: Landmark 4	236

Table B.5: Landmark 5	236
Table B.6: Landmark 6	237
Table B.7: Landmark 7	237
Table B.8: Landmark 8	238
Table B.9: Landmark 9	238
Table B.10: Landmark 10	239
Table B.11: Landmark 11	239
Table B.12: Landmark 12	240
Table B.13: Landmark 13	240
Table B.14: Landmark 14	241
Table B.15: Landmark 15	241

List of Abbreviations

2D	Two-Dimensional
3D	Three-Dimensional
ADC	Apparent Diffusion Coefficient
AIR	Automated Image Registration
BET	Brain Extraction Toolkit
BW	BandWidth
CC	Corpus Callosum
CLD	Chronic Lung Disease
CP	Cerebral Palsy
CSF	Cerebro-Spinal Fluid
CSO	Centrum SemiOvale
DTI	Diffusion Tensor Imaging
DWI	Diffusion-Weighted Imaging
EPI	Echo Planar Imaging
FA	Fractional Anisotropy
FDT	FMRIB Diffusion Toolkit
FFD	Free-Form Deformation
FMRIB	Functional Magnetic Resonance Imaging of the Brain
FOV	Field of View
FSE	Fast Spin Echo
FSL	FMRIB Software Library
GA	Gestational Age
GABA	Gamma AminoButyric Acid
GLH	Germinal Layer Haemorrhage
HPI	Haemorrhagic Parenchymal Infarction
IQ	Intelligence Quotient

IVH	IntraVentricular Haemorrhage
IZ	Intermediate Zone
MI	Mutual Information
MPRAGE	Magnetization Prepared Rapid Acquisition Gradient Echo
MR	Magnetic Resonance
MRI	Magnetic Resonance Imaging
MZ	Marginal Zone
N-CAM	Neuronal Cell Adhesion Molecule
NMI	Normalised Mutual Information
NMR	Nuclear Magnetic Resonance
NSA	Number of Signal Averages
PD	Proton Density
PE	Phase-Encode
PGSE	Pulsed Gradient Spin Echo
PHI	Periventricular Haemorrhagic Infarction
PLIC	Posterior Limb of the Internal Capsule
PMA	PostMenstrual Age
PRIDE	Philips Research Integrated Development Environment
PROM	Prolonged Rupture of Membranes
PVL	Periventricular Leukomalacia
RA	Relative Anisotropy
RF	Radio-Frequency
RMS	Root Mean Square
ROI	Region of Interest
SEM	Standard Error of the Mean
SENSE	SENSitivity Encoding
SG	Subpial Granular layer
SP	SubPlate
SPSS	Statistical Package for the Social Sciences
SSD	Sum of Squared Differences
SVZ	SubVentricular Zone

T	Tesla
TBSS	Tract-Based Spatial Statistics
TE	Echo Time
TR	Repetition Time
VBM	Voxel-Based Morphometry
VZ	Ventricular Zone
WM	White Matter

List of Publications

Papers

Anjari M, Counsell SJ, Srinivasan L, Allsop JM, Hajnal JV, Rutherford MA, Edwards AD. (2008). *The effects of lung disease on cerebral white matter development in preterm infants*. Pediatrics (in press).

Counsell SJ, Edwards AD, Chew ATM, **Anjari M**, Dyet LE, Srinivasan L, Boardman JP, Allsop JM, Hajnal JV, Rutherford MA, Cowan, FM. (2008). *Specific relations between neurodevelopmental abilities and local cerebral microstructural change in children born preterm*. Brain. 131(Pt 12): 3201-8

Porter EJ, Counsell S, Allsop J, **Anjari M**, Rutherford M, Edwards AD, Azzopardi D. (2008). *Diffusion tensor imaging analysed with tract based spatial statistics identifies extensive areas of white matter damage in infants with hypoxic ischaemic encephalopathy*. Pediatrics (in press).

Jiang S, Xue H, Counsell S, **Anjari M**, Allsop J, Rutherford M, Rueckert D, Hajnal JV (2008). *DTI of the Brain in Moving Subjects: Application to in-utero fetal and ex-utero brain studies*. Submitted.

Anjari M, Srinivasan L, Allsop JM, Hajnal JV, Rutherford MA, Edwards AD, Counsell SJ. (2007). *Diffusion tensor imaging with tract-based spatial statistics reveals local white matter abnormalities in preterm infants*. NeuroImage. 15;35(3):1021-7.

Jiang S, Xue H, Counsell S, **Anjari M**, Allsop J, Rutherford M, Rueckert D, Hajnal JV. (2007). *In-utero three dimension high resolution fetal brain diffusion tensor imaging*. Medical Image Computing and Computer Assisted Intervention. 10(Pt 1):18-26.

Abstracts

Dudink J, **Anjari M**, Cowan FM, Rutherford MA, Edwards AD, Counsell SJ. (2008). *Thalamo-cortical connectivity in preterm infants with unilateral periventricular haemorrhagic infarction assessed using probabilistic tractography*. Book of Abstracts, 45th Annual Meeting of the European Society of Paediatric Radiology.

Anjari M, Srinivasan L, Allsop JM, Hajnal JV, Rutherford MA, Edwards AD, Counsell SJ. (2007). *The effect of increasing prematurity on cerebral white matter studied using tract-based spatial statistics*. Book of Abstracts, 48th Annual Meeting of the European Society for Paediatric Research. Abstract #4325.6.

Porter EJ, Counsell S, **Anjari M**, Edwards AD, Rutherford MA, Cowan F, Allsop JM, Fitzpatrick J, Durighel G, Azzopardi D. (2007). *Cerebral white matter damage after hypoxic ischaemic encephalopathy analysed by tract based spatial statistics of magnetic resonance diffusion images*. Acta Paediatrica. 96:9.

Chapter 1

Introduction

1.1 Motivation

The incidence of preterm birth throughout the developed world is increasing, and advances in perinatal care now mean that the majority of these infants will survive (Moser et al., 2007). These improvements have been most pronounced amongst infants born extremely preterm, but have been accompanied by increasing awareness of subsequent neurodevelopmental deficits amongst this group, which may continue beyond childhood and adolescence and into adulthood.

Following preterm delivery, the architecture of the developing brain is often assessed using cranial ultrasound. This is useful for detecting a range of lesions including intraventricular and parenchymal haemorrhage, post-haemorrhagic ventricular dilatation and cystic periventricular leukomalacia. However, there have been concerns that ultrasound is unable to detect some of the more widespread subtle abnormalities of cerebral white matter that are seen on conventional magnetic resonance imaging (MRI) amongst infants born preterm (Maalouf et al., 2001; Childs et al., 2001; Miller et al., 2003; Debillon et al., 2003), which have been shown to predict adverse neurological outcome (Dyett et al., 2006). The non-invasive, non-ionising nature of MRI makes it an ideal tool for investigating the developing preterm brain. The advent of magnetic resonance methods such as diffusion weighted imaging (DWI) (Le Bihan et al., 1986) and diffusion tensor imaging (DTI) (Basser et al., 1994) that can measure the diffusion of water molecules within the brain and can therefore be used to probe tissue microstructure

has allowed the detection of even more subtle neurological abnormalities that cannot be seen with conventional MRI. Infants born preterm have been shown to have increased diffusivity of water at term-equivalent age compared to term-born control infants (Huppi et al., 1998; Counsell et al., 2006), which has been shown to correlate to adverse neurological outcome at two years of age (Krishnan et al., 2007).

Diffusion-derived MRI data has traditionally been analysed using region of interest (ROI) techniques, whereby regions are manually placed on the images and the diffusion parameters noted. There are, however, a number of limitations in performing ROI analyses of data, particularly when performing group-wise comparisons of data from multiple subjects. ROIs are subjective and involve massive data-reduction which impedes the power of any group-wise analysis. Equally there are problems with how well the ROI represents the tissue of interest, with questions about partial-volume effects and accuracy of placement. This has led to the search for objective and observer-independent methods for investigating diffusion data, which pose their own challenges but are now becoming more and more widely used.

1.2 Aim

The aim of this work was to investigate the developing preterm brain using objective group-wise analysis of diffusion tensor imaging data and to relate neuroanatomical features to clinical variables using robust statistical methods. Two different approaches were attempted: first to study white matter changes using the technique of Tract Based Spatial Statistics, and second to develop an improved registration technique for whole-brain diffusion studies.

1.3 Hypothesis

In the absence of focal lesions on conventional MRI, objective group-wise analysis of diffusion tensor imaging data will reveal differences in brain microstructure between preterm infants imaged at term corrected age and term-born control infants which are related to clinical variables.

1.4 Thesis outline

In order to address the aims of the thesis, the following chapters are included:

1.4.1 Chapter 2: Background - Magnetic Resonance Imaging, Diffusion MRI and Image Registration

First, the physical principles underlying nuclear magnetic resonance (NMR) and magnetic resonance imaging are outlined. The principal intrinsic sources of tissue contrast in MRI are first introduced (proton density, the longitudinal relaxation constant (T1), the transverse relaxation constant (T2), and the time constant of the free-induction decay due to the loss of phase coherence (T2*)). Then the main extrinsic sources of contrast are addressed, including the repetition time between successive pulses (TR) and the time between the application of a pulse and the peak of the echo signal (TE). Spatial encoding of the NMR signal is discussed, along with the reconstruction required to transform the received electromagnetic signal into a magnetic resonance image. Echo planar imaging (EPI) is amongst the most popular fast imaging techniques used in MRI, and the basic underlying principles of this method are outlined.

The concept of molecular diffusion is presented, and how the diffusion of water can be used as the main contrast agent in MRI using the Stejskal-Tanner Pulsed Gradient Spin

Echo sequence. Diffusion weighted imaging is then introduced, as is diffusion tensor imaging (DTI), which can provide rotationally invariant metrics of diffusion.

EPI is the most widely used sequence for performing diffusion MRI, but poses a series of challenges that must be considered when collecting and analysing echo planar DTI data. The most important of these are reviewed and strategies for minimising and correcting for distortions in the data are described.

Image registration, the process of aligning different images in order to achieve anatomical or functional correspondence, is introduced. The requirements for voxel-based image registration algorithms are discussed, as well as the transformation models, interpolation methods, similarity metrics and optimisation methods commonly employed for registration of magnetic resonance images. The application of registration techniques for the correction of distortions arising from acquiring diffusion data is then discussed, as are the requirements for using registration methods to perform population-based analyses of MRI data. Finally, some commonly used affine and nonlinear registration tools included in MRI data analysis packages are briefly described, including the free-form deformation based on B-splines that was optimised to register neonatal DTI data to anatomical images in this work.

1.4.2 Chapter 3: Background - The Developing Brain and Preterm Birth

The microscopic development of the brain from the first phase of cellular proliferation to the commencement of (and processes involved in) myelination of the brain are discussed. Next the incidence of, and various adverse neurological outcomes associated with, preterm birth are reviewed. The correlation between various focal and diffuse forms of brain injury and neurodevelopmental outcome is then considered. Finally, the contribution of conventional and diffusion MRI in elucidating the various stages of brain development and brain injury associated with preterm birth is presented.

1.4.3 Chapter 4: The Effect of Preterm Birth on Fractional Anisotropy at Term

Diffusion-derived scalar maps from preterm infants at term-equivalent age and term-born control infants are compared. This is performed using a widely available software-package for aligning fractional anisotropy (FA) data to allow for subsequent group-wise comparison. Despite the fact that neonates have smaller brains than adults and higher brain water content, this chapter shows that this technique, tract-based spatial statistics (TBSS) can be used with neonatal DTI data. In the absence of focal abnormalities on conventional magnetic resonance image, this work demonstrates for the first time that this objective, observer-independent method reveals local abnormalities in the cerebral white matter of preterm infants at term. Investigating the eigenvalues of the diffusion tensor revealed that this was due to elevated diffusivity perpendicular to the major white matter pathways, consistent with an oligodendrocyte and/or axonal abnormality.

1.4.4 Chapter 5: Fractional Anisotropy Changes Associated with Lung Disease Amongst Preterm-Born Infants

A different cohort of preterm infants born at a range of gestational ages was also processed with TBSS to assess the effects of acute and chronic lung disease, gender and premature rupture of membranes (PROM) on FA at term-equivalent age. Having regressed out the effects of prematurity at birth and age at scan (both of which were highly linearly correlated with FA) using a general linear model, it was found that acute lung disease was associated with a highly localised region of reduced FA in the genu of the corpus callosum, whilst chronic lung disease status correlated with an FA decrease in the left inferior longitudinal fasciculus, a major white matter association fibre. Comparisons between gender and between positive and negative PROM status did not reveal any differences in FA. Highly localised associations between lung disease and white matter microstructural measures have not previously been documented, and it is interesting to speculate the clinical significance of these findings. It is currently unclear

whether these results are unique to this cohort or are can be generalised, but may help to predict potential adverse outcome and may act as a biomarker for different forms of neonatal intervention.

1.4.5 Chapter 6: Optimisation of a B-Spline Based Registration Algorithm for Retrospective Correction of Geometric Distortions in Neonatal DTI Data

The method used in the previous chapters restricts group-wise analysis of diffusion data to major white matter pathways. In order to extend this analysis to the whole of the brain, the data need to be correctly standardised prior to voxelwise analysis. Unfortunately, as diffusion data are most often acquired with an EPI readout, ensuring correct image alignment is challenging. In this chapter, a partial optimisation of an image registration algorithm using a free-form deformation model based on B-splines is presented that improves the correspondence between anatomical MRI data and diffusion data acquired with EPI. This is validated by comparing the distance between corresponding landmarks on the two images before and after registration, and compared to two other widely-used image registration algorithms. The potential and the limitations of this work are discussed, before some suggestions for future work are presented.

1.4.6 Chapter 7: Summary and Final Remarks

Provides an overall summary of the results presented in this thesis. Finally, the challenges that lie ahead in enhancing our understanding of the effects of preterm birth and associated clinical variables on white matter microstructure using automated analysis of whole brain DTI data are considered.

Chapter 2

Background - Magnetic Resonance Imaging, Diffusion MRI and Image Registration

2.1 Magnetic resonance imaging

Magnetic Resonance Imaging (MRI) is a non-invasive, non-ionising imaging technique based on the principles of Nuclear Magnetic Resonance (NMR) (Bloch, 1946; Purcell et al., 1946). An image is generated by placing an object in a strong external magnetic field, applying energy to the system at given frequency and measuring the way in which the energy is released. MRI offers exquisite soft tissue contrast and three-dimensional anatomical images can be obtained that allow multi-planar reformatting if required. These advantages resulted in MRI becoming an important clinical and research tool in medical imaging, particularly of the brain. The following sections present a brief overview of MRI and the nuclear magnetic resonance phenomenon relevant to the understanding of subsequent chapters. A more complete description can be found in a number of different sources including Haacke (Haacke et al., 1999) and Nishimura (Nishimura, 1996), from which many of the figures in this chapter have been adapted.

2.2 Nuclear magnetic resonance

Nuclei with a non-zero spin number (i.e. with an odd number of protons and/or neutrons), such as ^1H , the most commonly used nucleus in MRI, possess an intrinsic spin angular momentum. In classical terms, they can be seen as a rotating charged sphere, possessing an intrinsic magnetic moment (Figure 2.1a). The vector sum of all the magnetic moments in a sample is its net magnetization. In the absence of an external magnetic field, the magnetic moments of the individual nuclei are randomly oriented and so the net magnetisation is zero (Figure 2.1b).

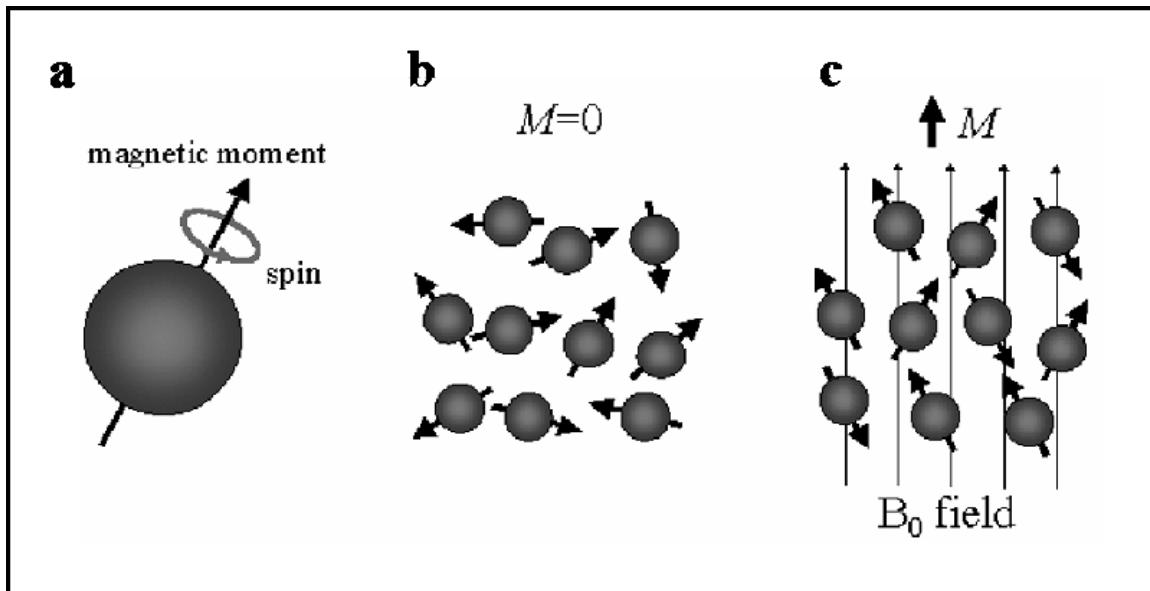


Figure 2.1: Classical interpretation of nuclear magnetic resonance (NMR)

A nuclear spin can be thought of as an infinitesimally small charged sphere spinning about its axis (a). An ensemble of such spins are randomly orientated in space (b). When a static magnetic field, B_0 , is applied the spins tend to align in the direction of the field, resulting in a net magnetization M (c).

However, when placed in a static magnetic field (B_0 e_z), the magnetic moments of the nuclei will, in a classical perspective, align themselves with the B_0 field (Figure 2.1c). Some will be parallel to the field and others, fewer, anti-parallel, thus creating a net

magnetization vector parallel to B_0 . The proportion of nuclei in each state can be changed by providing energy to the system, through the application of an external electromagnetic field at the resonant frequency. This is the same frequency at which, when disturbed from its equilibrium position, the net magnetization will precess around the direction of the field B_0 . It can be shown that this frequency (called the Larmor frequency, ω_0) is given by:

$$\omega_0 = \gamma B_0 \quad [2.1]$$

where γ is the gyromagnetic ratio, a constant typical of every nucleus. For a proton in a water molecule, $\omega_0 = 128$ MHz at a field strength of 3 Tesla, and is therefore in the radio-frequency (RF) spectrum. For this reason, the externally applied magnetic field rotating at the Larmor frequency that is used to perturb spins precessing around the static magnetic field is often called the RF (B_1) field.

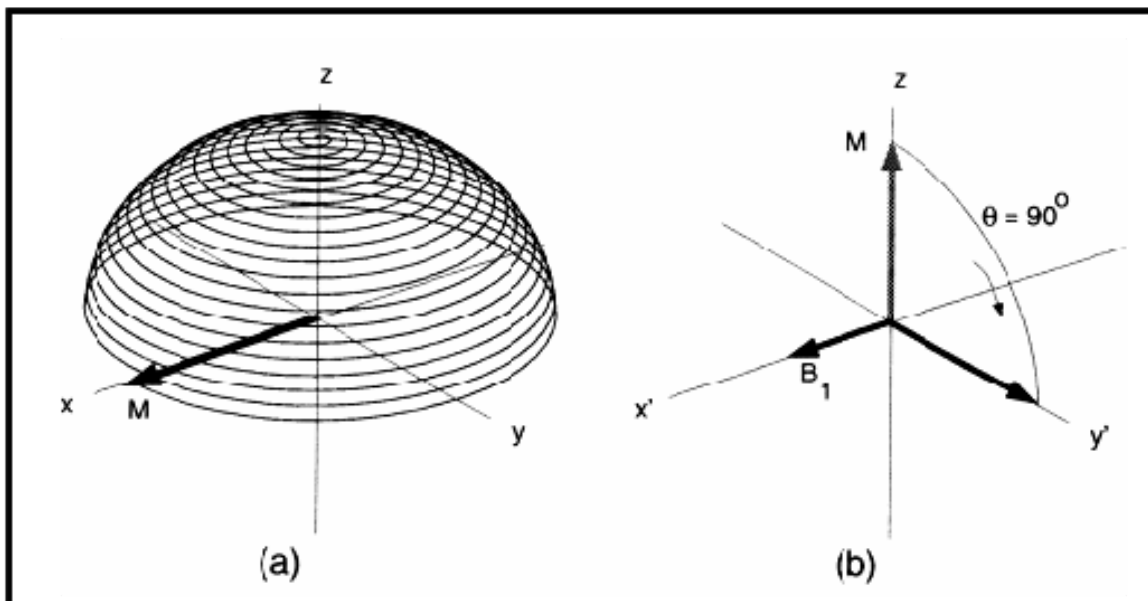


Figure 2.2: Magnetisation vectors and frames of reference

The application of the field B_1 induces rotation of the magnetisation towards the transverse plane. In the laboratory frame of reference the magnetisation vector follows a spiral trajectory (a). In the rotating frame of reference it is simply tipped onto the transverse plane (b).

If an external transverse magnetic field (B_1) in resonance with the system (i.e. rotating at the Larmor frequency) is applied to the system, the effective magnetic field will change so that the magnetic moment will start precessing around a different direction (defined by the vector sum of both B_0 and B_1 – Figure 2.2a). To more easily visualise this motion, a new frame of reference is introduced which rotates with angular frequency ω_0 around e_z . In the rotating frame, the motion of the net magnetization is simply a rotation from the direction of B_0 towards the plane transverse to it (Figure 2.2b). By the end of the application of the B_1 field, the angle the magnetization describes with relation to B_0 is called the flip angle. A flip angle of 90° will therefore correspond to a rotation to the xy plane. The excitation B_1 fields are applied during short periods and due to their frequencies are called RF pulses.

2.2.1 Relaxation

After the application of the RF pulse, the magnetisation gradually returns to its equilibrium state, in a process called relaxation. The time-varying signal generated is called free induction decay (FID), and represents the basic signal recorded in an NMR experiment.

The longitudinal component of magnetisation (i.e. the component parallel to the B_0 field) returns to its original value, while the transverse component decays away. These processes are characterised by the relaxation time constants T_1 and T_2 respectively. Longitudinal (T_1) relaxation is accomplished through energy exchange with the surrounding lattice and is therefore also called spin-lattice relaxation. Transverse (T_2) relaxation (spin-spin relaxation) is dominated by the interaction between neighbouring spins and is therefore also called spin-spin relaxation. It can be shown (Bloch, 1946) that both relaxation processes are well modelled by exponential curves (Figure 2.3). Consider an example where a 90° RF pulse has been applied. T_1 is the time taken for the magnetization in the longitudinal plane (M_z) to return to approximately 63% of its value prior to the application of the RF pulse (M_{0z}), and T_2 the time taken for the

magnetization in the transverse plane (M_T) to fall to 37% of its original (maximum) value (M_{0T}) after the pulse.

$$M_z = M_{0z} (1 - \exp(-t/T_1)) \quad [2.2]$$

$$M_T = M_{0T} \exp(-t/T_2) \quad [2.3]$$

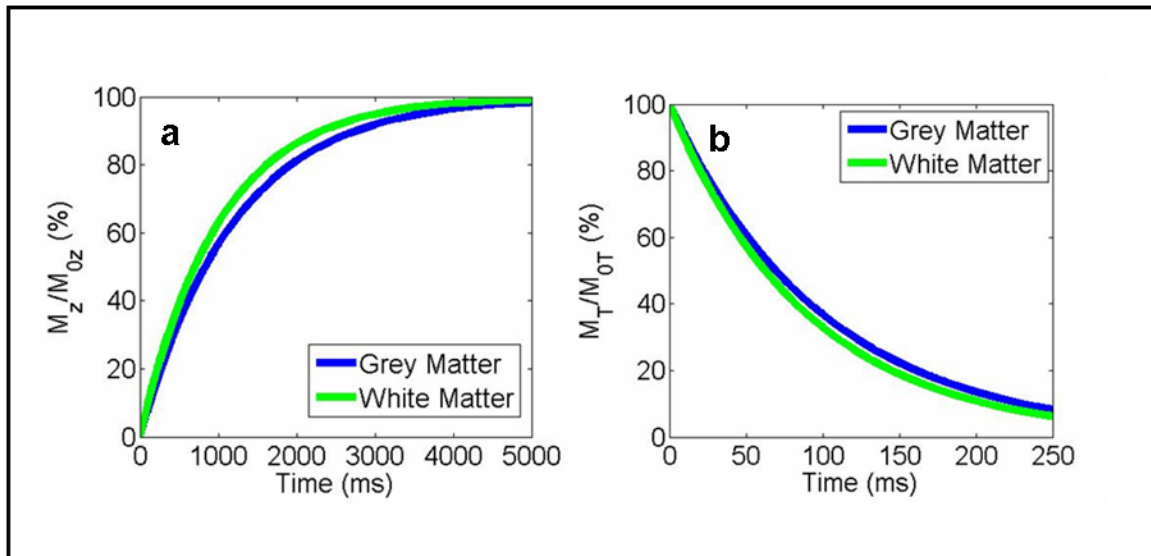


Figure 2.3: Longitudinal and transverse relaxation following a 90° RF pulse for grey and white matter

The longitudinal magnetization, M_z , recovers towards equilibrium as described in Equation 2.2 with a tissue dependent recovery constant T_1 (a). The transverse magnetization decays towards zero with a tissue dependent decay constant T_2 as described in Equation 2.3 (b).

In the presence of a static external magnetic field, the transverse magnetization decays faster than through the interactions with other spins only. This transverse relaxation constant is dubbed T_2^* and is dependent on scanner characteristics such as the inhomogeneity of the B_0 field. T_2^* is always less than T_2 .

2.2.2 Signal reception

By placing coils of wire with their axis perpendicular to B_0 , the variation of the direction of the transverse component of the magnetization can be detected according to Faraday's law of electromagnetic induction:

$$\varepsilon = -\frac{d\Phi}{dt} \quad [2.4]$$

where ε is the electromotive force and Φ is the flux of the magnetic field.

2.3 Magnetic resonance imaging

The first image obtained using NMR techniques was reported by Lauterbur (Lauterbur, 1973). The processes that underlie image formation in NMR are briefly outlined below. A more complete treatment of this subject can be found in Nishimura (Nishimura, 1996). For biological tissues, it is possible to generate images with good anatomical contrast based on differences in the T_1 , T_2 and proton densities of the different tissues.

2.3.1 Image formation

In order to be able to obtain an image from the NMR signal, it is necessary to be able to distinguish the contribution from each point in the object in the observed signal. This is usually accomplished through the application of spatially varying magnetic fields, usually called magnetic field gradients (G). The magnetic (B) field seen by every nucleus is now the sum of the main magnetic field (B_0) and the gradient fields:

$$B = B_0 + G.r \quad [2.5]$$

and the Larmor frequency of the spins is now also a function of position

$$\omega_0 = \gamma B_0 = \gamma(B_0 + G_x r) \quad [2.6]$$

If a field gradient is applied along the x axis, all spins that lie at a particular value of x will precess at the same frequency $\omega(x)$. The signal picked up in the receive coils will contain contributions from all the frequencies in the sample. After the removal of the Larmor frequency (ω_0) from the signal (demodulation), a mathematical operation called Fourier transform can be used to retrieve the number of spins spinning at a given frequency (i.e. lying at each plane on the x axis). This forms the basis of a spatial encoding technique called frequency encoding (Figure 2.4).

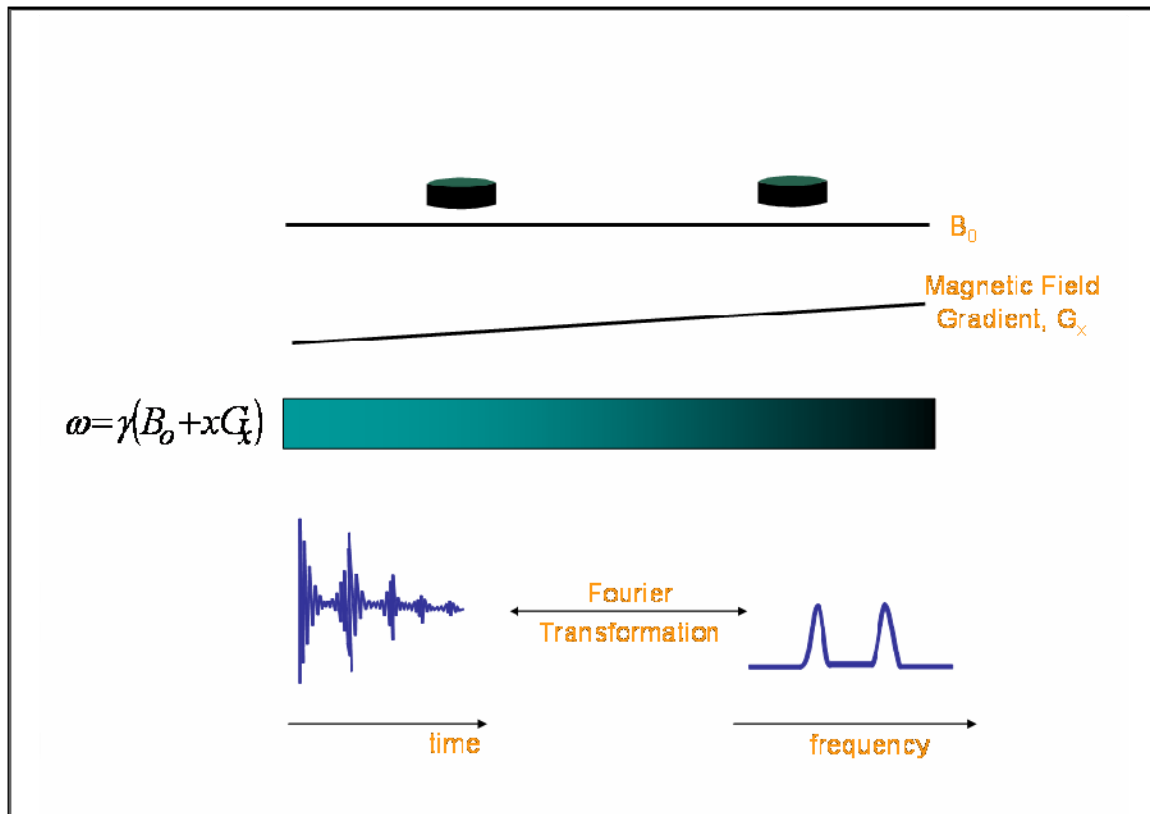


Figure 2.4: Frequency encoding

In the presence of a spatially varying gradient field along the x axis (G_x), two points along this field will precess at slightly different frequencies. Fourier transformation of the two different resonance frequencies allows the determination of their relative position along G_x .

The use of gradient fields also allows the location of spins to be determined based on the phase (ϕ) of the rotation they are undergoing. If a gradient G_y field is applied in the y direction from time 0 to time t, the frequency of the spins will vary along this direction (see Equation 2.6) and they will therefore have accrued a different rotation phase (ϕ) depending on their position along the y axis. Mathematically:

$$\phi(t) = \int_0^t \omega d\tau = \gamma \int_0^t B d\tau = \omega_0 t + \gamma y \int_0^t G(y) d\tau \quad [2.7]$$

The differences in phase acquired after the application of a gradient can also be used to spatially encode the signal, in a process called phase encoding. In two-dimensional imaging, frequency encoding is used along one direction (conventionally named x) and phase encoding along the other (y). Slice selection is usually used along the z direction. Three-dimensional volumetric images can be generated by also applying phase encoding along a 3rd (z) direction to encode the spins in 3 dimensions.

Selective excitation of a single slice (slice select) is achieved by applying a linear field gradient perpendicularly to the plane of the desired slice at the same time as a narrow band RF pulse. In this way, only the spins with resonance frequencies centred around the transmitting frequency and within the bandwidth (range of frequencies) of the RF pulse will be excited, as illustrated in Figure 2.5. If a gradient is applied along the z axis, the excited spins will be located within a transverse slice, perpendicular to this axis. By sequentially selecting slices centred at different z values, a 3D image can be built up. The thickness of this slice, Δz , will be related to the strength of the gradient G_z and the bandwidth (BW) of the pulse by:

$$\Delta z = \frac{BW}{\gamma G_z} \quad [2.8]$$

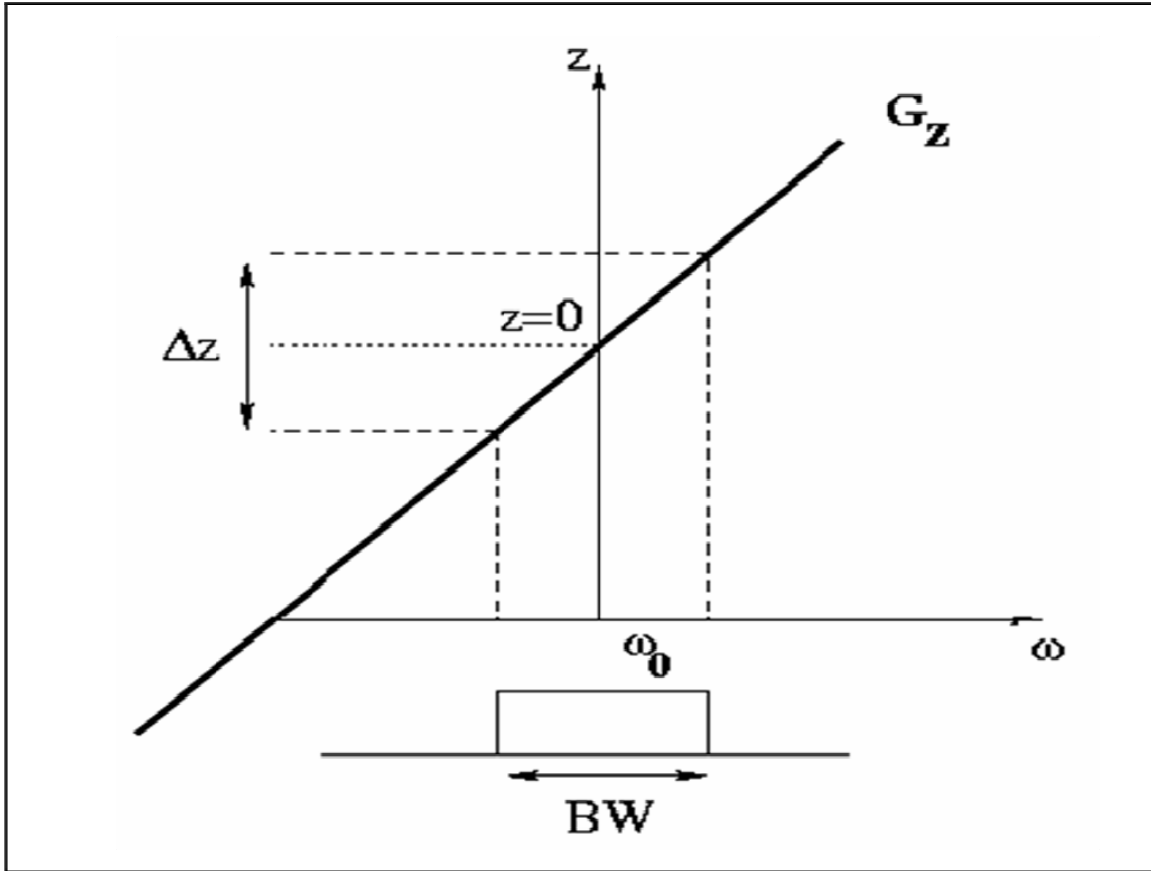


Figure 2.5: Use of a field gradient for selective excitation of a slice

By applying a field gradient G_z , the resonance frequency ω varies linearly with z . The application of an excitation pulse with a rectangular frequency profile will excite only the spins at locations z which match the range of frequencies in the bandwidth (BW).

As explained above, the localization of the magnetic resonance signal is encoded in the frequency and phase of the received signal. However, in order to be able to relate the frequency and phase of the signal to their localization, it is necessary that gradient fields be applied in a given order. The timings of the application of gradient and RF pulses are usually displayed in a diagram called the pulse sequence (Figure 2.6).

The phase acquired by the spins in the sample at a given time is a function of the gradients played out up to that moment in time. When analysing a pulse sequence, it is useful to consider the time integral of the gradient fields applied along each direction.

These define (apart from constants) the coordinates of the reciprocal Fourier-space also known as k-space (Figure 2.6).

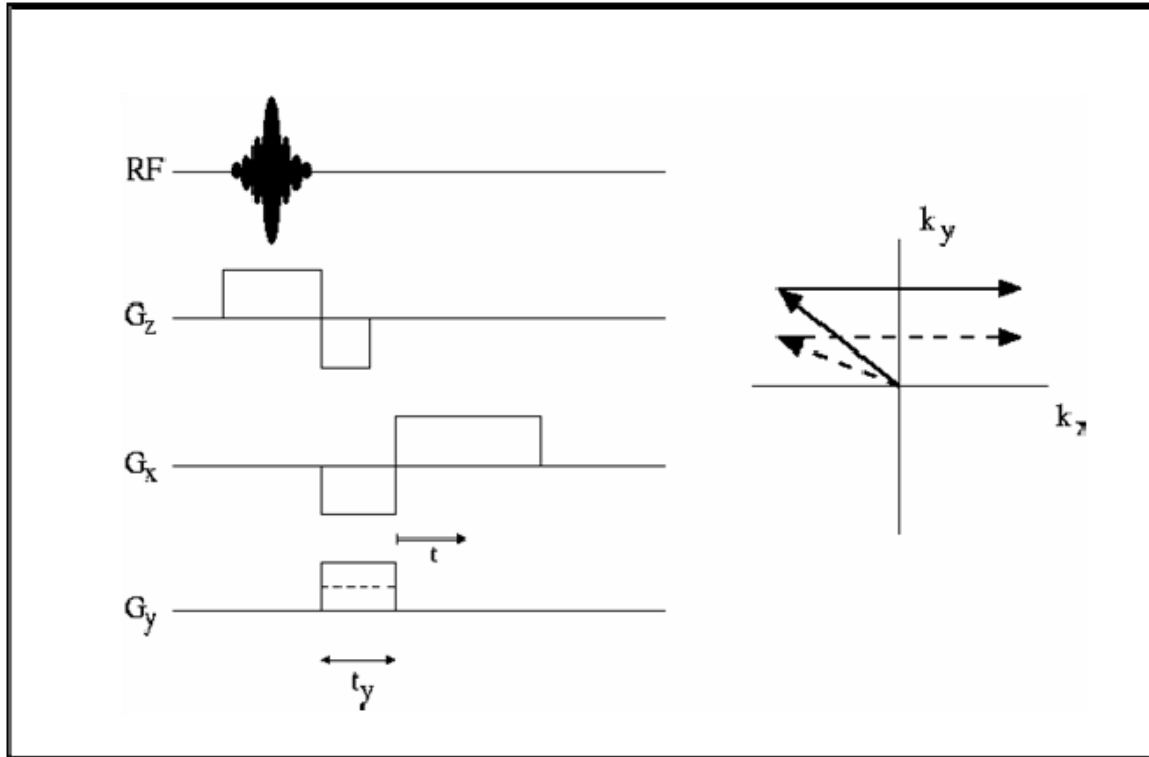


Figure 2.6: Pulse sequence diagram for a gradient echo image and corresponding trajectory in k-space

To select a single slice in the sample, a slice select gradient, G_z , is applied at the same time as an excitation RF pulse. According to Equation 2.7, G_z causes the spins to accumulate a phase according to their position along the z direction. This is not desired and so, to refocus the spins, a negative G_z gradient with half of the area is subsequently played out.

Afterwards, the signal is read out in the receiver coils at the same time that the readout gradient, G_x , is played out along the x direction. To ensure that the signal will be in phase half-way through the application of this gradient, a dephaser gradient, G_x' , with half the

area of the readout gradient is previously applied. In k -space, this corresponds to the acquisition of a k_x line, as seen in Figure 2.6.

To spatially encode along another direction, this experiment is repeated placing a phase-encode gradient, G_y , between the slice select and the readout gradients. This corresponds to moving to a different point position in k_y by an amount proportional to the phase-encode gradient's area. This means that during the readout a different k_x will be acquired. By repeating the experiment with different G_y amplitudes, all of k -space can be populated and then be converted into an image following the application of a 2D Fourier transform (Figure 2.7).

The interval between sampled points in k -space determines the image's dimensions (field of view, FOV) and that, together with the number of k -space points acquired in each direction, determines the image's resolution.

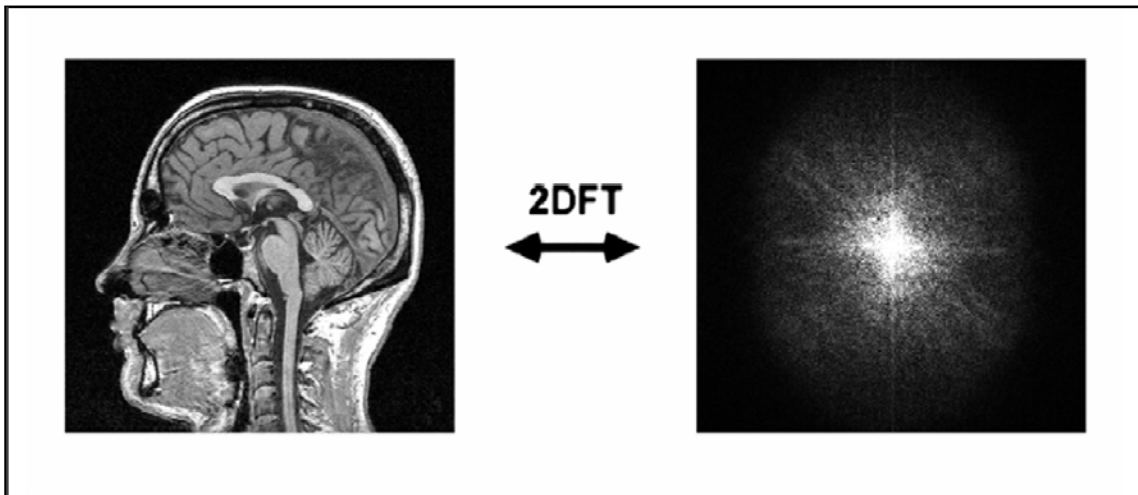


Figure 2.7: The relationship between image space and k -space

An image of a human head and its k -space representation. The image on the left was reconstructed from the acquired signal k -space (right) by application of a two-dimensional Fourier transform.

2.3.2 Image contrast

As explained previously, after the excitation the transverse component of the signal relaxes with a time constant T_2^* . The time between the excitation and the readout is called the echo time, TE , and its choice contributes to the contrast in the image. The repetition time, TR , the time between excitation pulses, determines the amount of longitudinal recovery the signal from each tissue experiences and can also be manipulated to generate the desired contrast.

To refocus the dephasing caused by stationary fields and therefore allow the spins to dephase with a T_2 rather than a T_2^* time constant during the time TE , a 180° excitation pulse can be introduced at time $TE/2$. This is called a spin echo pulse sequence (Figure 2.8).

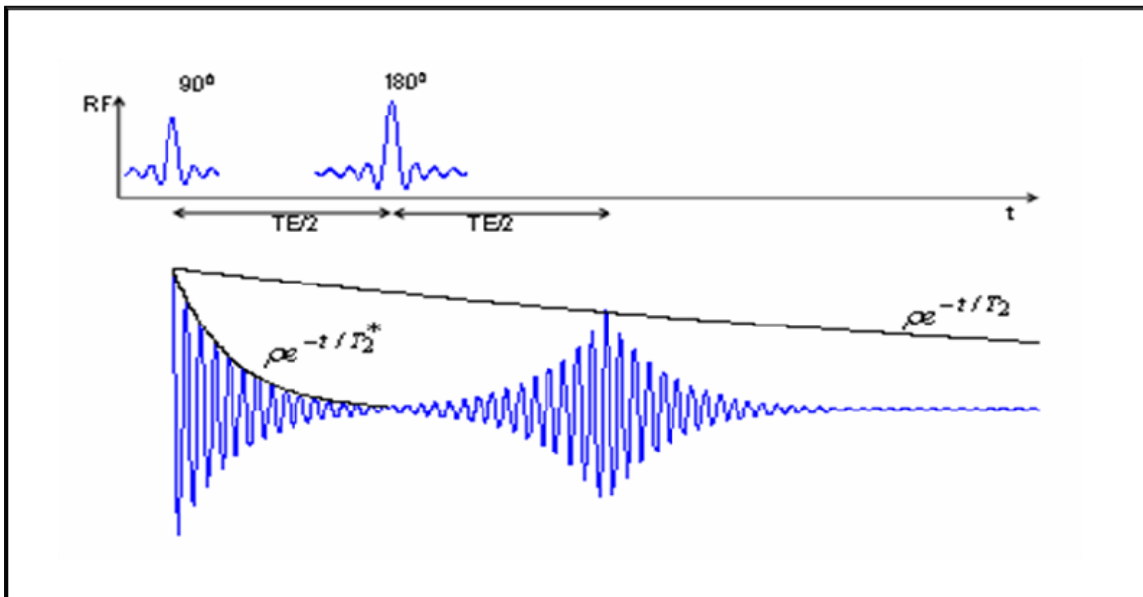


Figure 2.8: Spin-echo formation

The contrast in an image is a function of the tissues' T_1 , T_2 (or T_2^*) and proton densities (PD). By suitably manipulating TE and TR , one of these mechanisms can become the

main source of the contrast and it is said that the generated images are T1-, T2-, T2*- or PD-weighted. Table 2.1 shows a simplification of how the choice of TE and TR affects the weighting of the generated images, and Figure 2.9 shows examples of images with PD, T1- and T2-weightings.

	Short TE	Long TE
Long TR	PD-weighted	T2-weighted
Short TR	T1-weighted	

Table 2.1: Tissue contrast in MRI with respect to TR and TE

Key: TR, repetition time; TE, echo time; PD, proton density.

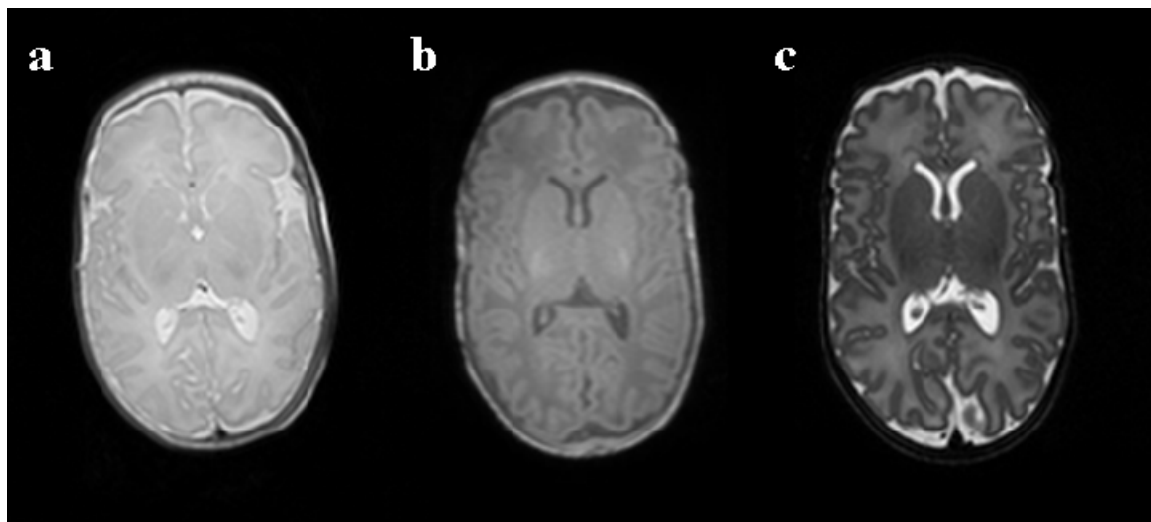


Figure 2.9: Proton density-weighted (a), T1-weighted (b) and T2-weighted (c) images from a neonate scanned on a 3 Tesla MR system

Compared to adult images, the relative contrast between grey matter and white matter in T1- and T2-weighted neonatal brain images is reversed.

2.4 Echo-planar imaging

MR images acquired as described above usually take a few minutes to acquire, given that only one k_y line is acquired every TR. Fast imaging techniques acquire a greater portion of k-space following every excitation. Echo planar imaging (EPI) (Mansfield, 1977) is one of the most popular fast imaging techniques.

In single shot EPI, all k-space lines are acquired following a single excitation (Figure 2.10). After an initial displacement to the bottom of k-space, resulting from the initial negative G_y lobe illustrated in Figure 2.10b, the scan “blips” upwards in the k_y direction after traversing and reading out each k_x line. The k-space trajectory of a single-shot echo-planar sequence that completes the scan of k-space in a single readout is demonstrated in Figure 2.10a. This is one of the fastest types of MR scans and therefore places significant demands on the gradient and receiver hardware.

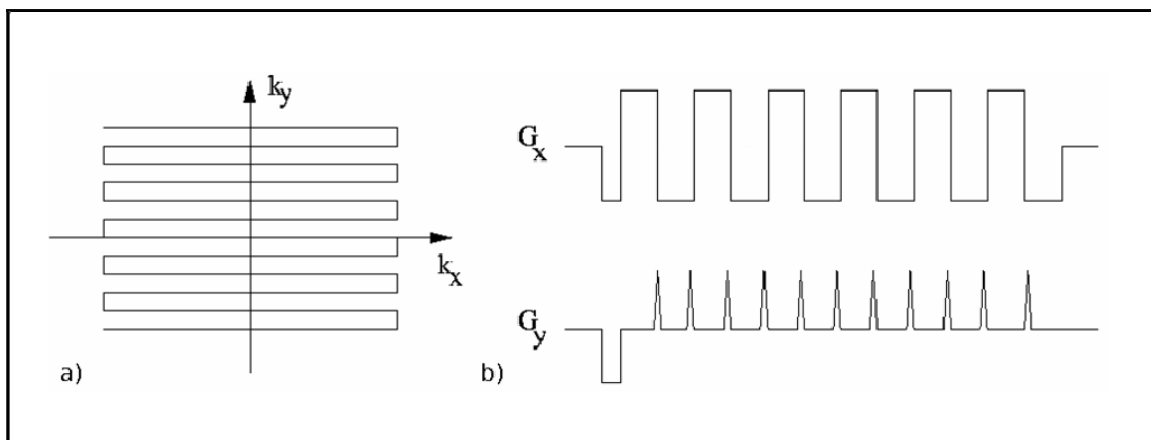


Figure 2.10: Echo-planar imaging sequence
k-space trajectory (a); Gradient waveforms during signal acquisition (b).

2.5 Diffusion MRI

2.5.1 Diffusion

In the 19th century, while observing particles of pollen in a water solution, Robert Brown noticed that the pollen grains were moving. This phenomenon, known as molecular diffusion or Brownian motion, is due to the random translational motion of water molecules, resulting from the thermal energy they carry. Diffusion weighted MRI utilises this phenomenon in order to probe the microstructure of tissues. A detailed description of the concepts involved in diffusion MRI can be found in Mori (Mori, 2007).

In a homogeneous medium, there is no preferred orientation for molecular motion and diffusion is said to be isotropic. However, molecules diffusing within an anisotropic medium will tend to move more easily along certain directions in comparison to others. In the vicinity of white matter fibres in the brain, the presence of both the cellular membrane and of the surrounding myelin sheaths hinders the motion of water molecules perpendicular to the axis of the axons. Diffusion will hence occur preferably along the direction of the fibres rather than radially to this. By performing measurements of diffusion along different directions it is therefore possible to obtain information regarding the orientation of white matter fibres in the brain. The fact that this is done non-invasively helps to explain the success of diffusion weighted imaging and its rapidly expanding use as a neuro-imaging research tool.

The diffusion process can be described statistically. If $P(\mathbf{r}_0; \mathbf{r}, t)$ is the probability that a molecule initially at position \mathbf{r}_0 arrives at another position \mathbf{r} after time t , then in an ideal homogenous fluid without boundaries, P is a Gaussian function such that;

$$P(\mathbf{r}_0; \mathbf{r}, t) = \frac{e^{-(\mathbf{r}-\mathbf{r}_0)^2 / 4Dt}}{(4\pi Dt)^{\frac{3}{2}}} \quad [2.9]$$

where D is the diffusion coefficient and t is time. D is a measure of the movement of molecules within their environment and is measured in units of mm^2/s .

Figure 2.11 shows the distributions obtained for three different diffusion times in a case where all molecules are initially at the same position. From this figure it is demonstrated that the molecules, all initially placed in the origin, will progressively disperse and that the overall concentration in space will tend to become more homogeneous.

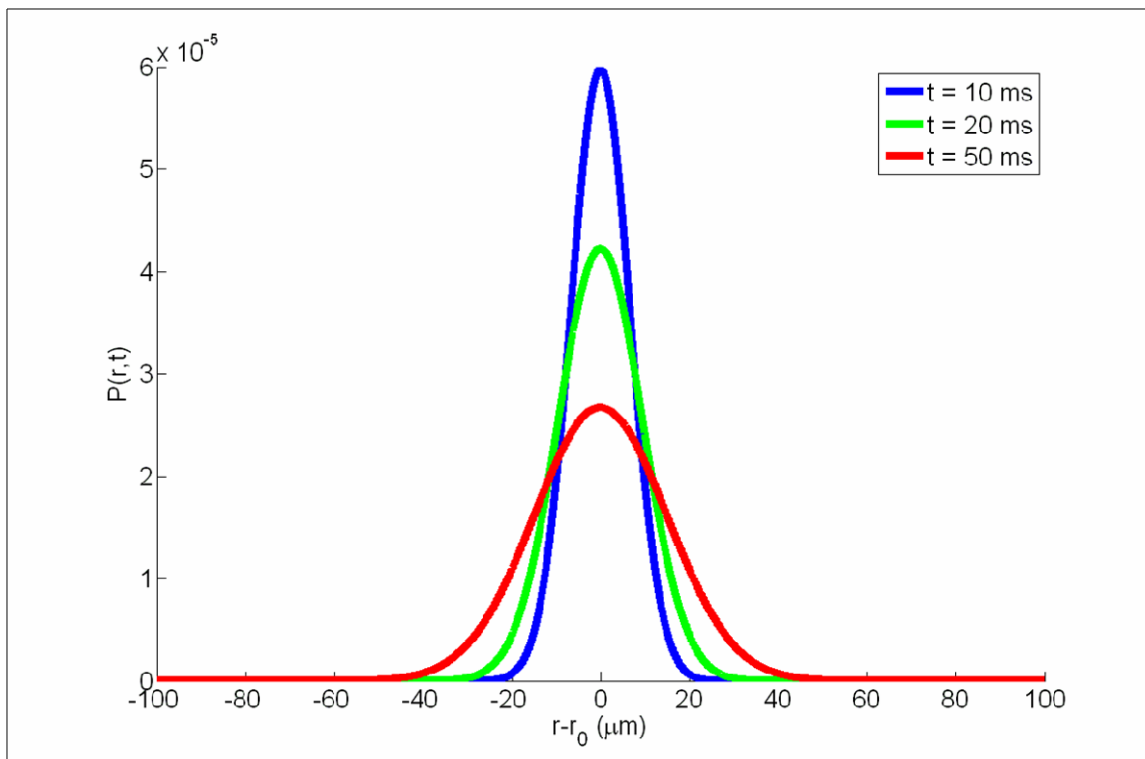


Figure 2.11: Concentration distribution at different times for free, isotropic diffusion in the case when all the molecules are initially located at position r_0

From Equation 2.9, it is possible to derive the Einstein relation for free three dimensional isotropic motion:

$$l = \sqrt{6Dt} \quad [2.10]$$

where l = root mean square distance travelled by a molecule in time t (Einstein, 1926).

The above equation relates the root mean square displacement (RMS) with the diffusion coefficient D and the diffusion time t . In the case of water, the diffusion coefficient at room temperature is $2.3 \times 10^{-3} \text{ mm}^2/\text{s}$. The RMS displacement for a diffusion time of 1 second is therefore in the order of $100 \text{ }\mu\text{m}$.

Einstein also showed that the self diffusion coefficient depends on factors such as the size of the molecules, intermolecular interactions (viscosity) and temperature. According to the Stokes-Einstein equation, for spherical particles of radius r , the diffusion coefficient increases with temperature (T), due to the increased thermal energy of molecules, and decreases with viscosity (η) as the resistance to motion becomes greater:

$$D = \frac{k_B T}{6\pi\eta r} \quad [2.11]$$

where k_B is the Boltzmann constant ($\sim 1.38 \times 10^{-23} \text{ J K}^{-1}$), which at the particle level relates energy and temperature.

2.5.2 Diffusion weighted imaging

The equations shown above rely on the assumption of free diffusion. This assumption is, however, no longer valid for diffusion within brain tissue as the presence of barriers reduces the overall mobility of water. For this reason the diffusion coefficient measured by MRI is not simply a measurement of intrinsic diffusion and is therefore commonly known as apparent diffusion coefficient (ADC). The value measured for the ADC will be a function of the diffusion time. For a very short diffusion time, the ADC will be close to the self-diffusion coefficient, as the molecules are not given enough time to interact with the barriers. However, as time increases the effect of the barriers becomes apparent, resulting in a lower ADC. As the diffusion time increases and enough time is given for the molecules to probe their environment, the ADC eventually reaches a steady value.

A widely used technique to measure diffusion using MRI is the Stejskal-Tanner pulsed field gradient diffusion weighted spin echo (PGSE) sequence, shown in simplified form in Figure 2.12. During the first diffusion gradient, spins accumulate a phase shift which depends on their position. A 180° pulse is applied to invert the spins. A second diffusion gradient is applied which is equal in amplitude to the first. Stationary spins do not lose signal as the phase shifts are equal, but due to the 180° pulse they have the opposite sign and cancel each other out. However, moving spins are not completely refocused, resulting in a loss of signal.

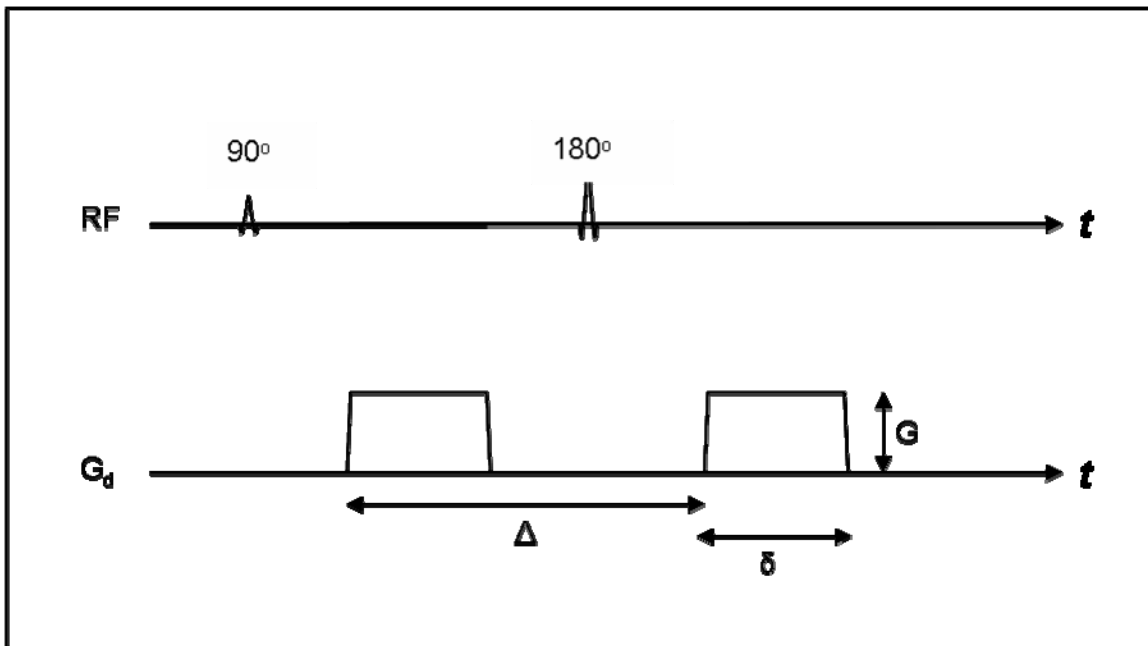


Figure 2.12: Pulse diagram for the PGSE sequence suggested by Stejskal and Tanner (Stejskal and Tanner, 1965)

The diffusion gradients are shown in the axis G_d and their relative timings labelled. G = amplitude of diffusion gradients, δ = duration of the pulsed gradient; Δ = time interval between the leading edges of the two pulsed gradients.

In the presence of a spatially varying magnetic field, random motion of protons in diffusing water molecules results in dephasing of the magnetic resonance signal, producing a reduction in its amplitude. Since spatially varying magnetic fields are used

for slice selection and spatial encoding in all MR images, diffusion of water molecules results in a reduction in signal intensity in all images, although the effect is normally quite small. In order to obtain a reliable measure of diffusion, large magnetic field gradients are deliberately applied, making it the dominant image contrast mechanism.

The apparent diffusion coefficient, D , can be calculated from Equation 2.12:

$$S = S_0 e^{-bD} \quad [2.12]$$

where S = signal in the diffusion weighted image, and S_0 = signal in the reference image (i.e. the image with no diffusion weighting). b , the strength of the magnetic diffusion gradient, is given by Equation 2.13:

$$b = \gamma^2 G^2 \delta^2 (\Delta - \delta/3) \quad [2.13]$$

where γ = gyromagnetic ratio for protons, G = amplitude of the pulsed gradient, δ = duration of the pulsed gradient; Δ = time interval between the leading edges of the two pulsed gradients (Le Bihan et al., 1986).

During typical diffusion times of 50-100 ms, water molecules in brain tissue move over distances of around 1-15 μm , bouncing, crossing and interacting with many tissue components, such as cell membranes, fibres and macromolecules. These processes impede motion so that, in tissue, the distance travelled by a water molecule due to diffusion is less than that in free water (at the same temperature). Hence, the diffusion of water molecules in vivo provides information regarding structural features and tissue organisation.

In a homogenous medium diffusion of water molecules is equal in all directions; that is to say, diffusion is isotropic. However, diffusion in tissue is not necessarily the same in all directions and so the measured apparent diffusion coefficient depends on the direction of diffusion sensitisation with which the rate of diffusion is measured. For this reason, data is acquired in a number of different directions of diffusion sensitisation.

Figure 2.13 shows four diffusion weighted images acquired with diffusion gradients applied in different directions. If the gradients are applied parallel to the local white matter tract direction, then water molecules diffusing along this direction will be incompletely refocused following the second gradient. This will lead to signal attenuation, as can be seen in (a), where the direction of the applied diffusion gradient is left-right and the genu of the corpus callosum appears dark. If diffusion is highly restricted in this direction then signal attenuation is minimal, as shown by the high signal intensity along the optic radiations. In (b) the diffusion gradient has been applied in the anterior-posterior direction, and the genu of the corpus callosum now appears bright whilst the anterior limb of the internal capsule, the external capsule and the optic radiations look dark. Grey matter has approximately the same intensity in all of the images ((a), (b), (c) and (d)), since diffusion here is isotropic at the resolution probed by diffusion weighted imaging (DWI). Diffusion is also isotropic within the ventricles, but these appear much darker than grey matter as there is very little restriction to diffusion, and so there is significant signal attenuation regardless of the direction of the applied diffusion gradient.

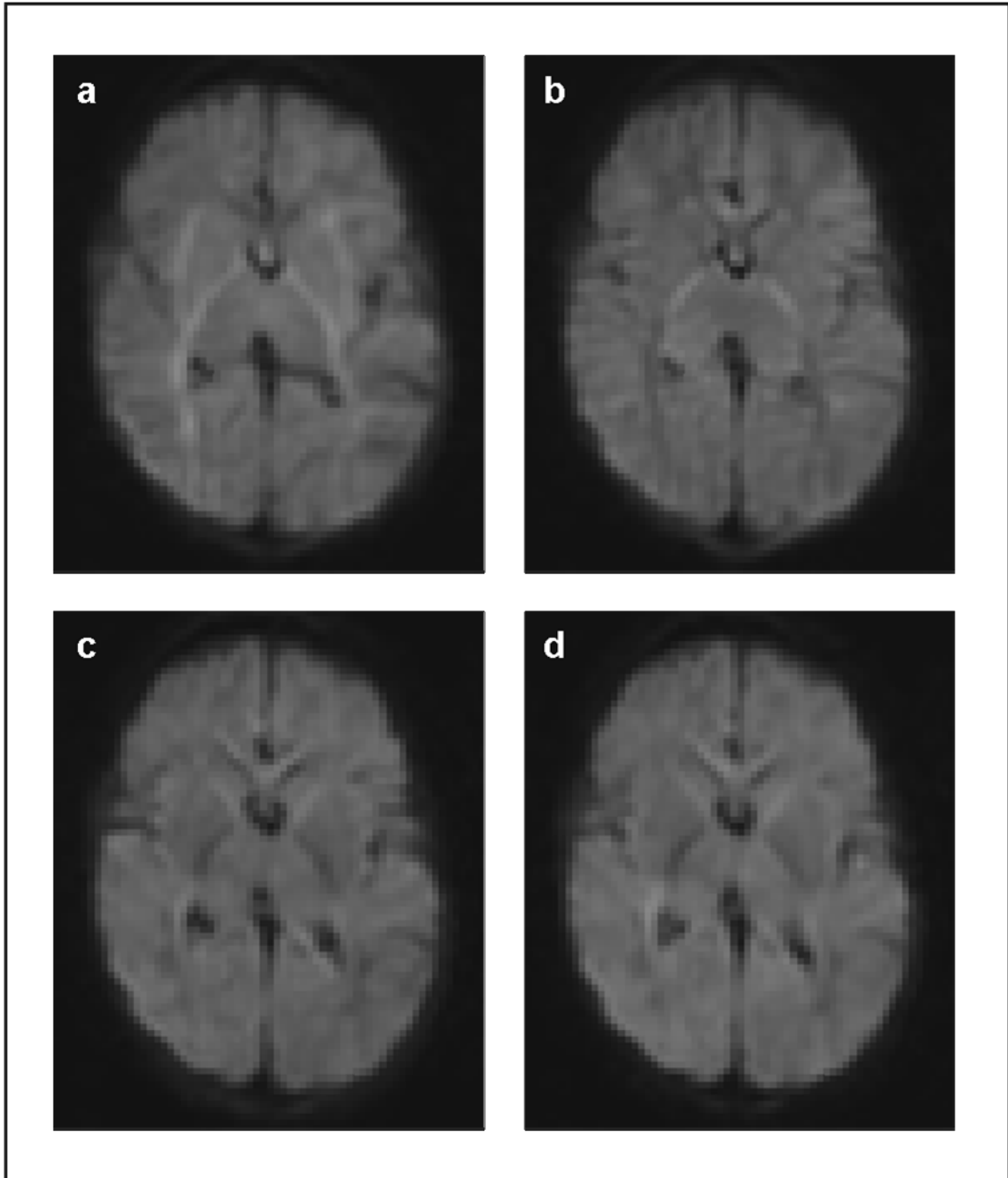


Figure 2.13: Diffusion weighted images

Example diffusion weighted images at the level of the thalamus of a preterm infant born at 30 weeks gestation and imaged at term-equivalent age. In each case the b -value is the same (750 s/mm^2), but the diffusion gradients are applied in different directions.

As the measured ADC frequently depends on the direction of the applied diffusion gradient (Figure 2.13), one method to obtain a mean measure of diffusion consists in

acquiring DWIs in 3 directions of diffusion sensitisation (x, y and z) and calculate a mean ADC value using Equation 2.14:

$$ADC = \frac{ADC_x + ADC_y + ADC_z}{3} \quad [2.14]$$

2.5.3 Diffusion tensor imaging

As already mentioned, in the most general case diffusion may not necessarily be the same along every direction. In that situation, instead of using a scalar coefficient diffusion can be described using a tensor. The probability that a particle initially at position r_0 will be at position r after a time t will now be given by:

$$P(r, t) = \frac{1}{\sqrt{|D|(4\pi t)^3}} \exp\left[\frac{-(r - r_0)^t D^{-1}(r - r_0)}{4t}\right] \quad [2.15]$$

As in the previous case, this equation applies to free diffusion. If motion is hindered, the shape of the diffusion ellipsoid may no longer be Gaussian. In order to take this into account, and similarly to before, diffusion tensor imaging (DTI) is often used to estimate an effective diffusion tensor, D_{eff} , in each voxel.

DTI provides a measurement of diffusion in tissues, which is independent of the direction of the applied diffusion gradients and the choice of laboratory frame of reference. A minimum of seven measurements are required to fully characterise the diffusion tensor, six linearly independent measurements obtained using diffusion sensitizing gradients and one obtained without any diffusion weighting. D is given by Equation 2.16:

$$\ln\left(\frac{S(b)}{S(b=0)}\right) = -\sum_{i=1}^3 \sum_{j=1}^3 b_{ij} D_{ij} = -(b_{xx}D_{xx} + 2b_{xy}D_{xy} + 2b_{xz}D_{xz} + b_{yy}D_{yy} + 2b_{yz}D_{yz} + b_{zz}D_{zz}) \quad [2.16]$$

where b_{ij} is the component of the i th row and j th column of a 3×3 symmetric b matrix, b ; D_{ij} is the corresponding component of the 3×3 symmetric matrix of the effective diffusion tensor, D . $S(b)$ is the signal intensity for a gradient sequence with b matrix, b ; $S(b = 0)$ is the signal intensity for a gradient sequence in which b is zero (Basser et al., 1994).

Since the eigenvalues of this tensor represent the diffusivities along the main axes, the tensor has to be positive definite. The tensor must also be symmetrical. Both of these conditions ensure that the principal eigenvectors (also called of principal diffusion directions) are orthogonal to each other and may therefore be used to form a local orthogonal coordinate system. The relationship between the tensor, its eigenvectors ε_i and eigenvalues λ_i may be written in the following way:

$$D = (\varepsilon_1 | \varepsilon_2 | \varepsilon_3) \begin{pmatrix} \lambda_1 & 0 & 0 \\ 0 & \lambda_2 & 0 \\ 0 & 0 & \lambda_3 \end{pmatrix} (\varepsilon_1 | \varepsilon_2 | \varepsilon_3)^T \quad [2.17]$$

This D tensor describes an ellipsoid, whose surface represents the root mean square diffusive displacement. As the tensor is symmetrical ($D_{ij} = D_{ji}$), instead of nine elements, only six are independent (Basser et al., 1994). It has nine elements and is symmetric, which means that $D_{ij} = D_{ji}$, so only six of the values are independent:

$$D = \begin{pmatrix} D_{xx} & D_{xy} & D_{xz} \\ D_{yz} & D_{yy} & D_{yz} \\ D_{zx} & D_{zy} & D_{zz} \end{pmatrix} \quad [2.18]$$

D_{xx} , D_{xy} , D_{xz} , D_{yy} , D_{yz} , D_{zz} are the independent elements. A frame of reference, called the “principal frame” can be defined so that the axes are coincident with the principal axes of the diffusion ellipsoid and the off-diagonal elements of the diffusion coefficient disappear. In this rotated system, the diffusion tensor is diagonal. The directions of the principal axes are specified by the eigenvectors of the diffusion tensor. When D is expressed in the principal frame, the diagonal matrix elements are the principal diffusivities of the rotated coordinate system: $\lambda_{x'}$, $\lambda_{y'}$ and $\lambda_{z'}$, the eigenvalues of the

diffusion tensor. The six scalars that represent the diffusion tensor can be expressed in terms of the three eigenvalues, $\lambda_{x'}$, $\lambda_{y'}$ and $\lambda_{z'}$, which are rotationally invariant, i.e. the eigenvalues are properties of the diffusion ellipsoid rather than of a particular coordinate system, such as that defined by the gradient system in the MRI scanner. The principal direction of diffusion is given by the eigenvector that corresponds to the largest eigenvalue (Basser, 1995).

In order to visualise the tensor, the surfaces of iso-probability are normally considered. For an isotropic tensor where all three diffusivities have the same value λ , this surface will correspond to a sphere, whereas an ellipsoid will be obtained for the anisotropic case (Figure 2.14).

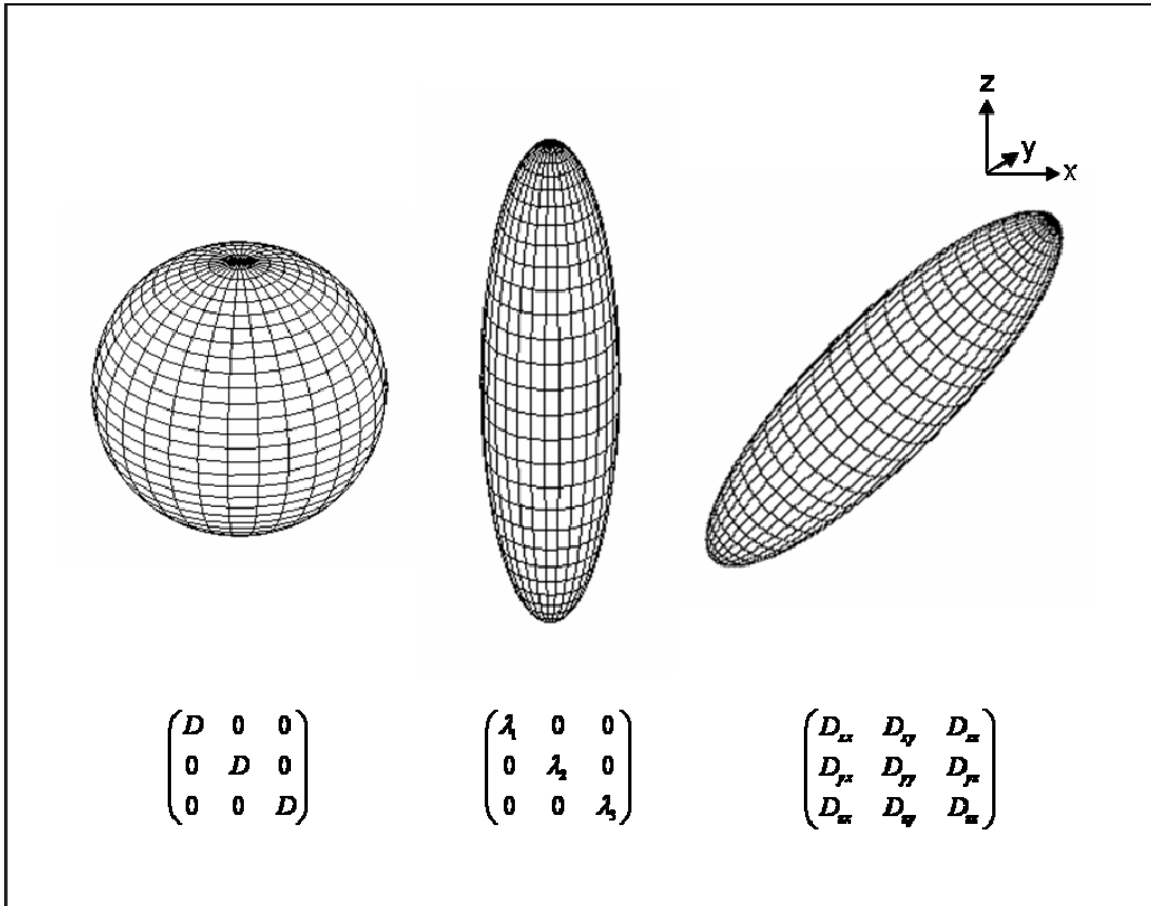


Figure 2.14: Diffusion ellipsoids

The tensors used to describe diffusion can be represented as ellipsoids, with the three main axes describing an orthogonal coordinate system. The directions of the main axes represent the eigenvectors and their lengths represent the eigenvalues of the tensor. The longest main axis of the diffusion ellipsoid represents the value and direction of the principal diffusion direction, whereas the shortest axis denotes the value and direction of minimum diffusion. If the tissue is isotropic at the scale probed by DTI, diffusion is the same in all directions and the ellipsoid will be spherical (a). The tensor is diagonal with all diffusivities equal to the scalar diffusion coefficient D ; In an anisotropic medium, diffusion along one direction may be preferred over others. In this case the surface of isoprobability is an ellipsoid. If the laboratory frame coincides with the principal directions of the ellipsoid, the tensor will be diagonal with diffusivities λ_1 , λ_2 and λ_3 along each of the three axes (b); In general the principal axis of the ellipsoid will not coincide with the laboratory frame and all elements will be necessary to characterise the tensor (c).

Although the assumption of Gaussianity is not always valid throughout the brain, from the tensor it is possible to extract useful parameters to summarise diffusion properties. The advantage of using invariant scalar parameters instead of reporting the full tensor is

that those do not depend on the frame used. A measurement of the average diffusivity in space may be obtained by using the trace of the tensor:

$$\text{Trace}(D) = \lambda_1 + \lambda_2 + \lambda_3 \quad [2.19]$$

Several indices can also be used to express the tensor's level of anisotropy, the degree to which diffusion along one direction is preferred over others. On maps generated by these parameters, white matter tracts, which exhibit a high anisotropy index, appear bright. Grey matter and cerebrospinal fluid, on the other hand, are represented by dark shades according to their low or absent anisotropy. The most commonly used index is the fractional anisotropy (FA), which measures the fraction of the effective diffusion tensor that can be ascribed to anisotropic diffusion:

$$FA = \sqrt{\frac{3}{2}} \sqrt{\frac{(\lambda_1 - \langle \lambda \rangle)^2 + (\lambda_2 - \langle \lambda \rangle)^2 + (\lambda_3 - \langle \lambda \rangle)^2}{\lambda_1^2 + \lambda_2^2 + \lambda_3^2}} \quad [2.20]$$

where $\langle \lambda \rangle$ is the mean diffusivity = $(\lambda_1 + \lambda_2 + \lambda_3)/3$.

A value of 0 corresponds to a perfectly isotropic tensor while an FA of 1 corresponds to the limit of infinite anisotropy.

In addition to calculating mean diffusivity and diffusion anisotropy, DTI can be used to investigate the nature of diffusion parallel (axial diffusion, λ_{\parallel}) and perpendicular (radial diffusion, $(\lambda_2 + \lambda_3)/2$) to white matter tracts. Analysing DTI data in this way helps to gain an understanding of the causes behind changes in anisotropy.

As mentioned, theoretically it is possible to determine the tensor by acquiring one non-diffusion weighted image plus six diffusion weighted images, provided that the diffusion gradients have been chosen to lie in non-collinear directions. In practice, as the images are noisy, a higher number of images tends to be acquired. For this reason, data sets with 15, 32 or even more directions are commonly acquired, especially if the final goal is to perform fibre tracking. Figure 2.15 shows the fifteen direction diffusion gradient scheme

used to acquire DTI data in this work. This scheme samples diffusion fairly isotropically in space. In general, the diffusion tensor is then estimated by fitting the DWIs using linear least squares fitting. This is a mathematical procedure for finding the best fitting line to a given set of points by minimising the sum of the squares of the residuals of the points from the line, and is often used to find an approximate solution to an over-determined system of linear equations.

Figure 2.16 shows some of the scalar maps that can be derived from DTI data.

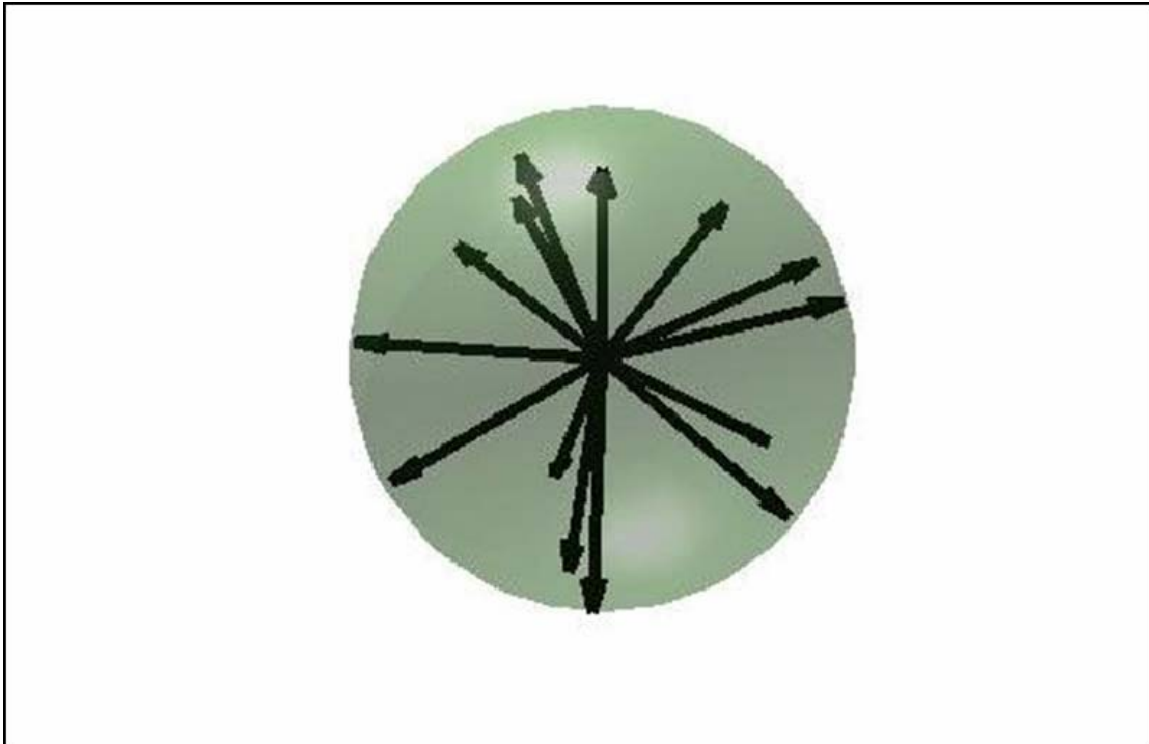


Figure 2.15: Sample 15 direction diffusion gradient scheme

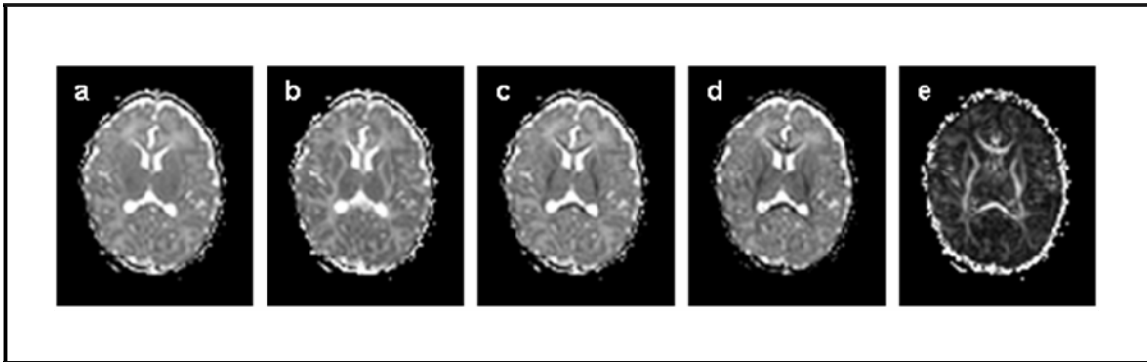


Figure 2.16: Scalar maps that can be derived from DTI data

A number of different scalar maps can be derived from DTI data. Amongst the most widely used of these indices of diffusion are (a) ADC; (b) λ_1 , the eigenvalue corresponding to the magnitude of diffusion along the major axis of diffusion; (c) λ_2 , the eigenvalue corresponding to the magnitude of diffusion along the intermediate axis of diffusion; (d) λ_3 , the eigenvalue corresponding to the magnitude of diffusion along the minor axis of diffusion; (e) FA, the magnitude of the effective diffusion tensor that can be attributed to anisotropic diffusion.

2.5.3.1 *Limitations of the diffusion tensor model*

There are two major assumptions in the DTI model that do not necessarily hold within the brain:

1. that diffusion is Gaussian (that is, the diffusion characteristics of water molecules can be represented by a Gaussian distribution); and
2. that it is sufficient to characterise diffusion within each voxel using a single diffusion tensor.

However, it has been shown that the fact that diffusion within the brain is restricted and divided into different compartments means that it is not Gaussian (Assaf and Cohen 2000; Beaulieu 2002; Assaf and Basser 2005; Alexander et al., 2002; Jensen et al. 2005; Assaf and Pasternak, 2008), though this is only manifest when using very high b values (>2500 s/mm²) (Assaf and Cohen 2000; Beaulieu 2002; Cohen and Assaf 2002; Assaf and Pasternak, 2008). The second assumption, however, is less valid; a single diffusion tensor is often inappropriate to represent the many thousands of different water compartments (including extracellular water as well as water within neurons and glial

cells) in a typical imaging voxel in the brain. The measured diffusion tensor is an average of these compartments, and if a voxel contains contributions from different brain tissue classes or two or more non-parallel fibre pathways then the DTI model will be inadequate (Papadakis et al. 2002; Tuch et al. 2002; Jansons and Alexander 2003; Assaf and Pasternak, 2008).

There have been numerous approaches proposed to overcome these problems. Multiple tensor models, such as those suggested by Tuchs (Tuch et al. 2002), Jansons (Jansons and Alexander 2003) and Pasternak (Pasternak et al. 2004, 2006) overcome the partial volume effect, but still assume Gaussian diffusion (Assaf and Pasternak, 2008). This assumption is not required with diffusion spectrum imaging and q-space imaging methods, but these are very time consuming and computationally demanding, and are not currently appropriate for clinical imaging.

2.6 Echo-planar diffusion weighted imaging

In order to make DWIs sensitive to the microscopic motion of water molecules, they inevitably become sensitised to any other type of motion. Traditional spin echo methods of acquiring DWIs are relatively lengthy, taking several minutes to acquire data in one direction of sensitisation. During this time, motion such as blood flow, tissue pulsation related motion or macroscopic motion of the head can result in inconsistencies between different data segments, leading to artefacts in the images. This is clearly a great disadvantage when imaging uncooperative neonates. As explained in Section 2.4, EPI (Mansfield, 1977) is able to provide images after only a single radiofrequency (RF) excitation and thereby enables imaging in a fraction of the time of conventional MRI. Diffusion weighted images are usually obtained using EPI techniques, and multiple images of the whole brain, sensitive to different diffusion directions can be acquired within a few minutes. Therefore, this technique is highly suited to obtaining diffusion weighted MRI in neonates.

2.6.1 Problems with echo planar imaging

However, data acquired with an EPI readout many contain a number of significant artefacts. These can be seen in Figure 2.17 and Figure 2.18 and include:

- Distortions associated with inhomogeneities in the B0 field;
- Image blurring;
- Nyquist ghosting;
- Fat artefacts;
- Eddy current effects.

These artefacts, which are common to all EPI data, are described in the following section.

2.6.1.1 Geometric distortion artefacts associated with inhomogeneities in the B0 field

The long readout times required by EPI make it extremely sensitive to inhomogeneities in the static magnetic (B0) field. The low bandwidth of EPI in the phase-encoding direction causes a much less manageable artefact in shape distortion in this direction.

Even in the presence of a perfect magnet, field variations will exist due to differences in the magnetic properties of distinct types of tissue within the sample. The magnetic behaviour of a substance can be represented through its magnetic susceptibility. While the magnetisation created within a paramagnetic substance (with a positive magnetic susceptibility) will reinforce the magnetic field applied, opposition to the magnetic field occurs for a diamagnetic substance, one with a negative magnetic susceptibility. The most significant differences in susceptibility observed in the head are located at air-tissue boundaries. As air is slightly paramagnetic, while brain tissue is mildly diamagnetic, field variations may be observed close to these boundaries. Given that the field variations induced are proportional to the magnetic field applied, the inhomogeneities are especially pronounced at higher field strengths such as 3 Tesla. Indeed, the MR frequency may differ from point-to-point in regions of air-bone-tissue interfaces by more than 125 Hz at

this field strength. This results in inaccuracies in the spatial localisation of the magnetic resonance signal, and can lead to areas of signal void and corresponding regions of signal pile up in the images, particularly near the sinuses.

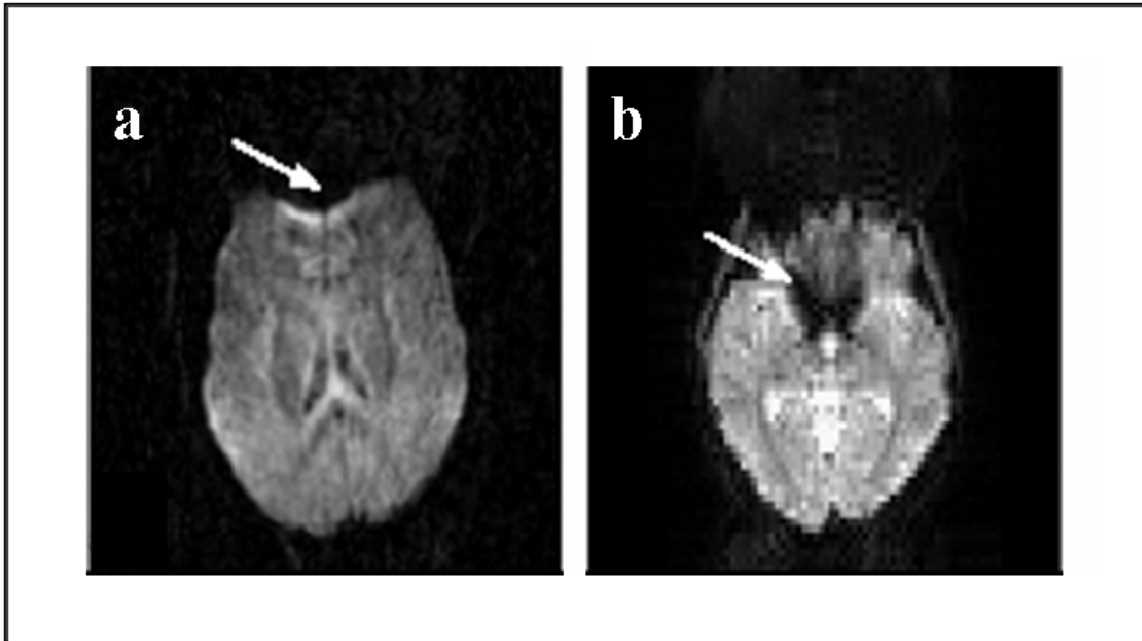


Figure 2.17: Signal loss and pile up resulting from inhomogeneities in the B₀ field
Transverse EPI image acquired from an adult at the level of the frontal sinuses (a) and the optic radiations (b) show the effects of tissue magnetic susceptibility differences on the spatial localisation of signal. There is a signal void (white arrow) immediately posterior to the frontal sinuses, and the signal has instead been localised to a region posterior to its true location, resulting in signal pile-up in this area.

2.6.1.2 *Blurring*

Because of the long acquisition times, different k-space points will have experienced different amounts of transverse decay. This leads to image blurring, particularly along the phase-encoding direction.

2.6.1.3 *Nyquist ghosting*

A replica of the image is generated, shifted from the main image by half a field of view in the phase encode direction (Figure 2.18a). This is caused by a mismatch in the sampling pattern or in the gradients applied when acquiring k_x lines in different directions (from left to right or from right to left).

2.6.1.4 *Fat artefact*

Due to their different electronic environments, protons in fat molecules have a slightly different resonance frequency from those in water. Signal from fat is therefore misplaced in MR images. In echo planar images, due to the short acquisition bandwidth along the phase encode direction, if not suppressed the fat that surrounds the skull can be misplaced by tens of voxels along the phase encode direction (Figure 2.18b).

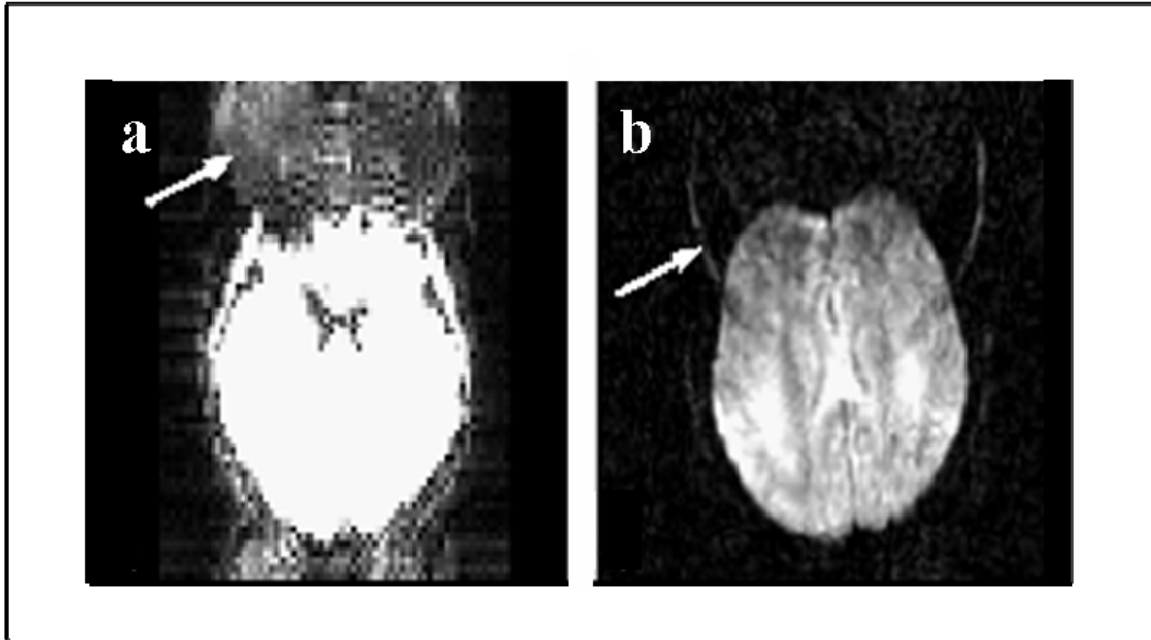


Figure 2.18: Nyquist ghosting and fat artefacts in echo-planar images

Nyquist ghosting results in a replica of the acquired image shifted by half a field of view along the phase encode direction (a). Fat artefacts arise because protons in fat and water have different resonance frequencies when placed in an external magnetic field, leading to incorrect signal localisation (b). These can be improved by suppressing the signal from fat by applying an additional ‘presaturation’ pulse prior to each slice selection pulse.

2.6.1.5 Eddy current effects in diffusion tensor EPI

As diffusion tensor calculations are performed on a voxel-by-voxel basis, it is essential that all the diffusion weighted images are correctly aligned to the image with no diffusion weighting applied. The generation of eddy current fields upon the application of the diffusion gradients complicates this task. As the fields persist during the readout window of an EPI acquisition, different geometric distortions will be induced in the images, depending on the direction along which diffusion is being measured. If the effect of these fields is not taken into account, the spatial resolution of the images computed from this set of data will be degraded, and inaccurate estimates of the diffusion parameters obtained around tissue boundaries will result.

Eddy currents arise as a consequence of the rapid and powerful pulsing of the gradient coils. The eddy current fields are induced in the presence of conducting structures and oppose changes in the main magnetic field in accordance with Faraday's law of electromagnetic induction.

The fields generated by the diffusion gradients are particularly significant as, in order to obtain diffusion contrast in the minimum echo time possible (to minimise blurring effects), the diffusion gradients tend to be as strong and short as possible. In the presence of eddy currents, the shape of the gradients effectively applied will differ from that prescribed, with the ramping up and down occurring in a smoother way (Figure 2.19).

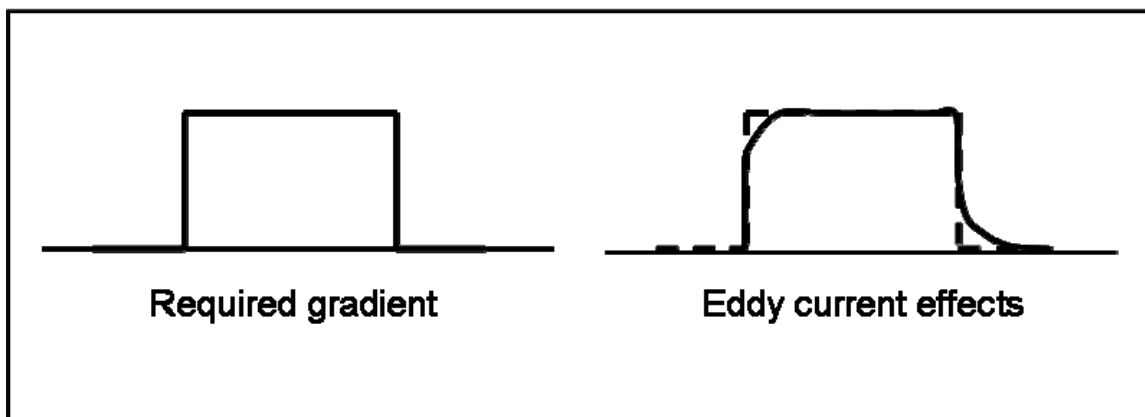


Figure 2.19: The effect of eddy currents on gradient waveforms

In the presence of eddy current fields the shape of the gradients is distorted. An ideal rectangular-shaped gradient is shown on the left. On the right is shown how the eddy currents distort the ideal shape (hatched line), producing smoother transitions (solid line).

Depending on the intensity and duration of the diffusion gradients, the eddy current fields may still be considerable during the readout window. The effect of these residual fields on diffusion weighted EPI images was first described by Jezzard and Balaban (Jezzard and Balaban, 1995).

The amplitude of the eddy currents will depend on the magnitude, duration and separation of the diffusion gradients. The direction of the eddy current may not coincide

with that of the gradient which has produced it, as cross-terms may be present. A gradient applied along, for example, the x axis may also produce a y-component in addition to the expected x term.

The phase accrued by the spins determines which voxel they are mapped onto in the image. If extra undesirable gradient fields are present, additional phase accumulation will occur. This will lead to an incorrect assignment of the position of the affected spins and ultimately to geometrical distortions of the images. The nature of the effect of the eddy current fields on EPI images will depend on their orientation relative to the imaging gradients. The distortions occur primarily along the phase encode (PE) direction due to its low bandwidth.

An eddy current along the readout direction will shift each line of k-space by a different amount depending on its coordinate k_y along the phase encode direction. These differential shifts will result in shearing of the image as shown in Figure 2.20.

If the eddy current field is oriented along the phase encode direction, the size of the phase encode blips will either increase (causing the object to be magnified as the field of view is reduced) or decrease (causing shrinkage of the object). This effect is represented in Figure 2.20.

One of the effects of an eddy current field in z is to cause signal loss. The additional field makes the resonance frequency of the spins vary along the slice direction, leading to signal dephasing. Eddy currents along the slice direction also result in a global translation of the image along the phase encode direction due to the extra phase accumulated. The amount of translation depends on the distance from iso-centre as the strength of the static field is made to vary along the z direction.

Therefore, in summary, depending on the nature of the eddy currents, their effect on the image is:

- shearing in the image plane;

- scaling in the PE direction;
- signal loss and translation along the PE direction;
- translation along the PE direction.

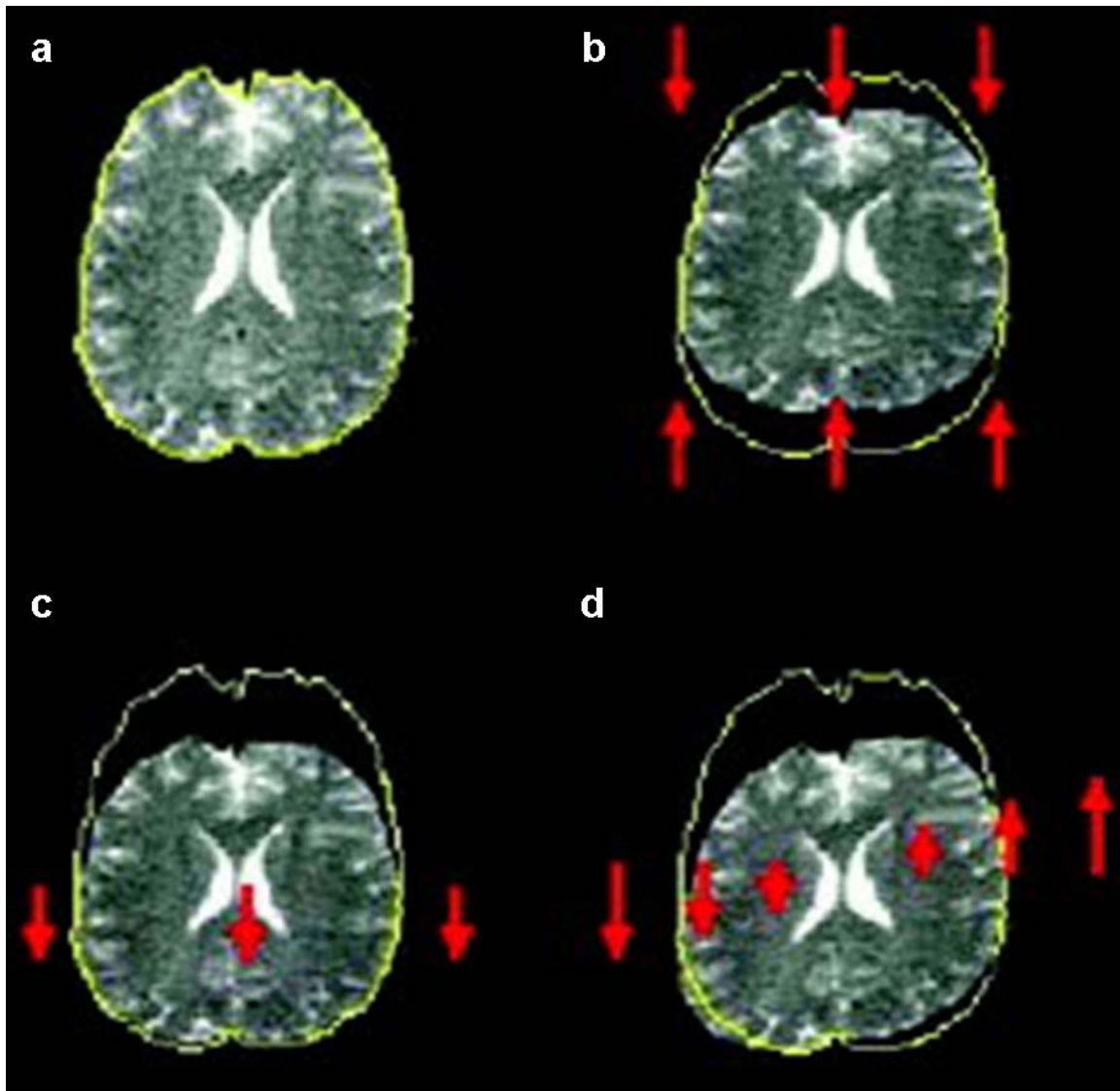


Figure 2.20: Distortion resulting from eddy currents, from Le Bihan (Le Bihan et al., 2006)

(a) Undistorted image; (b) contraction; (c) shift; (d) shear.

2.6.1.6 Additional challenges

The rapid switching of gradients required by echo-planar diffusion tensor imaging places significant challenges on the MRI hardware, and can lead to artefacts such as spikes and other forms of experimental noise distorting the data. Single-shot EPI minimizes head motion artefacts, but artefacts associated with respiratory motion and cardiac pulsatility may still be problematic.

Finally, despite their numerous advantages, single-shot EPI techniques are limited in the resolution that they can provide and provide poorer tissue contrast compared to anatomical imaging. This can be a limitation when studying the neonatal brain with its inherently smaller size than the adult brain.

2.6.2 Correction of errors in echo planar imaging data

As already mentioned, the diffusion tensor calculation relies on the assumption that a given voxel corresponds to the same anatomical location in the $b = 0$ s/mm² image and all the diffusion weighted images in a DTI dataset. Eddy currents lead to image misalignment between measurements corresponding to different diffusion gradient directions. For this reason, the calculated anisotropy values may have large errors or the direction of the highest diffusion supposed to correspond to fibre direction may be incorrect (Netsch and van Muiswinkel, 2004). The distortion is overwhelmingly in the phase-encoding direction due to the long time between the acquisitions of two adjacent samples in this direction, and in the neonatal brain, the brainstem and cerebellum are particularly affected by distortion from local magnetic field inhomogeneities.

2.6.2.1 Correction for distortions arising from B₀ inhomogeneity effects

Numerous strategies have been proposed to correct for the spatial displacements and intensity modulations arising from field inhomogeneities in the main magnetic field. Acquiring two rather than one set of echo planar images with opposite phase-encoding directions make regions that appear compressed due to signal pile-up in one image easily distinguishable in another, as displacements in the phase-encode direction in the images will have identical magnitude but opposite polarity. This allows the reconstruction of an image with significantly reduced distortions (Andersson et al., 2003; Jones et al., 1999).

Measuring the B₀ field across the field of view (also known as acquiring a field map) and using this to unwarped the EPI data was first proposed by Jezzard and Balaban (Jezzard and Balaban, 1995), and has been shown by Hutton (Hutton et al., 2002), to improve correspondence with an undistorted anatomical MR image acquired during the same scanning session. Generally, these methods involve acquiring two images with different echo times using a gradient echo or spin echo sequence. The measured difference in phase at a particular voxel in the images is proportional to the difference in echo time as well as the local inhomogeneity in the B₀ field. The derived B₀ field values are used to approximate the signal loss and geometric distortion and to then compensate for these artefacts. These unwarping strategies have since been incorporated into diffusion data analysis packages (<http://www.fil.ion.ucl.ac.uk/spm/toolbox/fieldmap>; <http://www.fmrib.ox.ac.uk/fsl/fugue/index.html>).

Standard shimming refers to the process of applying additional small correction gradients on top of the main magnetic field to make the field more uniform. Scanners often have first order shim coils that are on all the time and can remove linearly varying gradients in the main magnetic field. However, since the resolution in the through-slice direction is usually coarser than in-plane resolution, intravoxel dephasing is most common in this direction. As a result, applying z-shimming, whereby an extra gradient along the z-axis is

applied for a short period after excitation to compensate for this intravoxel dephasing has also been suggested (Frahm et al., 1988; Gu et al., 2002; Glover, 1999; Song, 2001).

2.6.2.2 *Correction for distortions arising from residual eddy current effects*

Several approaches have been suggested in the literature to either correct for or minimise eddy current effects. The effect of eddy currents can be corrected either by acquiring extra data to estimate these fields (Calamante et al., 1999) or by estimating them retrospectively from the images themselves (Andersson and Skare, 2002). Modifications to the standard single spin-echo sequence have also been suggested to minimise the eddy currents at source (Alexander et al., 1997; Reese et al., 2003), as well as achieving a more rectangular gradient waveform by re-adjusting the gradient pre-emphasis unit (Papadakis et al., 2000; Schmithorst and Dardzinski, 2002).

If the eddy currents are approximately constant during the EPI acquisition, their effects in both k-space and image domain are linear. Each eddy current component can be estimated by acquiring a series of profiles along the corresponding direction (Jezzard et al., 1998). Once the eddy current components are estimated for each slice and diffusion orientation, the actual data can be corrected accordingly. Using this method, it is also possible to correct for time varying eddy currents, which can be done by comparing the estimates obtained using different pairs of echoes. If the eddy currents were constant in time, the same value should be obtained in all cases, except for noise. By fitting a polynomial to the estimates obtained from consecutive pairs of echoes, the time dependence can also be taken into account (Jezzard et al., 1998). However, the main disadvantage of the method is that it requires an increase in acquisition time; when using a single-shot sequence the scanning time is increased by a factor of three.

An alternative approach consists of estimating the amount of distortion generated from the images themselves. Haselgrove and Moore (Haselgrove and Moore, 1996) first

proposed using image registration, described in Section 2.7, to correct for distortions induced by eddy currents, whereby each diffusion weighted image is individually mapped to an undistorted spin echo T2-weighted image acquired during the same scan. The authors used iterative cross-correlation (Section 2.7.3.1.2) as their image similarity measure, but a difficulty with this approach is that the contrast of the images changes as the amount of diffusion-weighting increases, and the cerebrospinal fluid, in particular, appears bright on the T2-weighted images, but becomes increasingly darker as the b-value is increased. Cross-correlation does not perform well when the contrast of the images being aligned differs significantly, and Bastin (Bastin, 1999) found that this method is unsuitable for images acquired with a b-value of more than 300 s/mm^2 . One possibility to estimate the amount of translation and scaling induced in the images is therefore to use a method to compare an image with moderate diffusion-weighting with the reference T2-weighted image (on a phase-encode column-by-column basis) and then extrapolate these parameters to higher b value images. This procedure is very computationally demanding, though, and the subject may move between acquisitions and therefore this method is not frequently used to correct for distortions produced by eddy current effects.

Horsfield (Horsfield, 1999) suggested estimating the eddy current fields by acquiring images with diffusion-weighting along each of the three axes of the laboratory frame of reference. Superposition can then be used to estimate the corrections required for any given diffusion direction and slice orientation. As above, however, this method requires a lot of computation, with a reported processing time for a six-direction diffusion dataset of approximately one day (Horsfield, 1999).

A faster post-processing method, which has the advantage of simultaneously correcting for both motion and image distortions was suggested by Andersson and Skare (Andersson and Skare, 2002). When fitting the data with the tensor model, increased residuals should be obtained in the presence of both motion and eddy current distortions. The authors therefore proposed to determine the set of parameters that minimises the sum of the squares over all voxels of the errors between the estimated and measured signal

intensities. The set of transformations considered include both rigid body motion and shear, scaling and translation along the phase encode direction. To account for the spatial variability of the eddy current induced distortions, these are allowed to vary from slice to slice in a smooth way. This approach is, however, incomplete in that the reference (non-diffusion weighted) volumes are not used. To correct for any discrepancies between these volumes and the diffusion weighted ones the authors suggest using a multi-modality registration method.

More recently, Rohde (Rohde et al., 2004) has suggested a method to align the diffusion weighted images to a T2-weighted image that simultaneously corrects for subject motion and eddy current effects. In this approach, the diffusion data is transformed using a combination of translations, rotations, scales and shears in a way that that maximises the similarity (the authors used mutual information (Section 2.7.3.2.1) as their similarity metric) between each individual diffusion weighted volume and the reference volume.

All the post-processing methods described above assume that eddy current fields lead to geometric distortions which can be corrected for using translations, rotations, scales and shears (affine transformations). This would be true if the eddy current fields remained constant throughout the entire acquisition window, however temporally varying eddy currents are also present, both short-lived (which produce image blurring that cannot be corrected for by image registration strategies), and longer-lived. Shen and colleagues (Shen et al., 2004) have shown that although most of the distortions can be corrected for using affine transformations, some residual errors do persist, and proposed combining data from pairs of images with diffusion sensitising gradients reversed to correct for higher-order distortions. In the absence of this additional data, however, there is much active work in developing retrospective correction models for DWI/DTI data that include nonlinear transformation models and so can address some of these spatially varying eddy current effects (Kybic et al., 2000; Studholme et al., 2000; Netsch and van Muiswinkel, 2004).

2.6.2.3 *Correction strategies for motion-related artefacts*

As a by-product of diffusion sensitisation, diffusion weighted images are sensitive to any kind of motion. Diffusion data acquired with EPI is largely insensitive to bulk head motion, however, since each individual diffusion weighted image can be acquired as rapidly as 150 ms. However, some authors have suggested that incorporating cardiac gating may improve the diffusion tensor estimation (Pierpaoli et al., 2003; Skare and Andersson, 2001), but this is not normally employed and has an associated time penalty, which can be only partially reduced by acquiring different image slices at different phases of the cardiac cycle (Nunes et al., 2005).

2.7 Image registration

2.7.1 Introduction

Medical image registration is the process of determining a mapping between the coordinates in a source image and a reference (or target) image in order to achieve biological, anatomical or functional correspondence (Crum et al., 2004; Hajnal et al., 2001) and so can aid clinical interpretation and/or analysis. In the context of neuro-imaging, registration allows different brain images from either the same subject (intra-subject registration) or different subjects (inter-subject registration) to be combined into a common frame of reference. Commonly used applications of image registration methodologies include longitudinally tracking changes related to brain maturation and ageing, characterising size and shape variations amongst different subjects or study populations, and fusing data from different imaging modalities in which corresponding structures may have different intensities (inter-modality registration).

Image registration algorithms can generally be divided into two main groups:

1. voxel-based, which aim to estimate and improve the geometrical correspondence between two images based on the intensity values in each image, and
2. feature-based, whereby the same features are extracted in each image and the registration is driven by attempting to bring these into spatial correspondence.

In a broad study of various inter-modality brain image registration approaches, it was reported that voxel-based methods are on the whole more reliable and accurate for rigid registration than feature-based algorithms (West et al., 1997), and are now much more widely-used amongst the neuro-imaging community. The following descriptions will therefore focus on this first group of image registration algorithms.

In order to determine a mapping between a reference (or target) image and a source image that maximises the similarity between the images, the model of a typical voxel-based registration algorithm requires the following components:

1. A transformation (or deformation) model that deforms the source image to target space.
2. A regularisation method that constrains any transformation to be smooth and therefore not to break topology.
3. An interpolation method to estimate image intensities in locations that do not coincide with any of the source image's voxel locations.
4. A similarity measure to calculate the similarity of the images when the transformation is applied.
5. An optimisation method to select the transformation that gives the best similarity.

Figure 2.21 gives an overview of the steps involved in an image registration algorithm. Maximising the correspondence between the images entails finding the best transformation under the model used, represented by the set of transformation parameters that provide optimal similarity between the images.

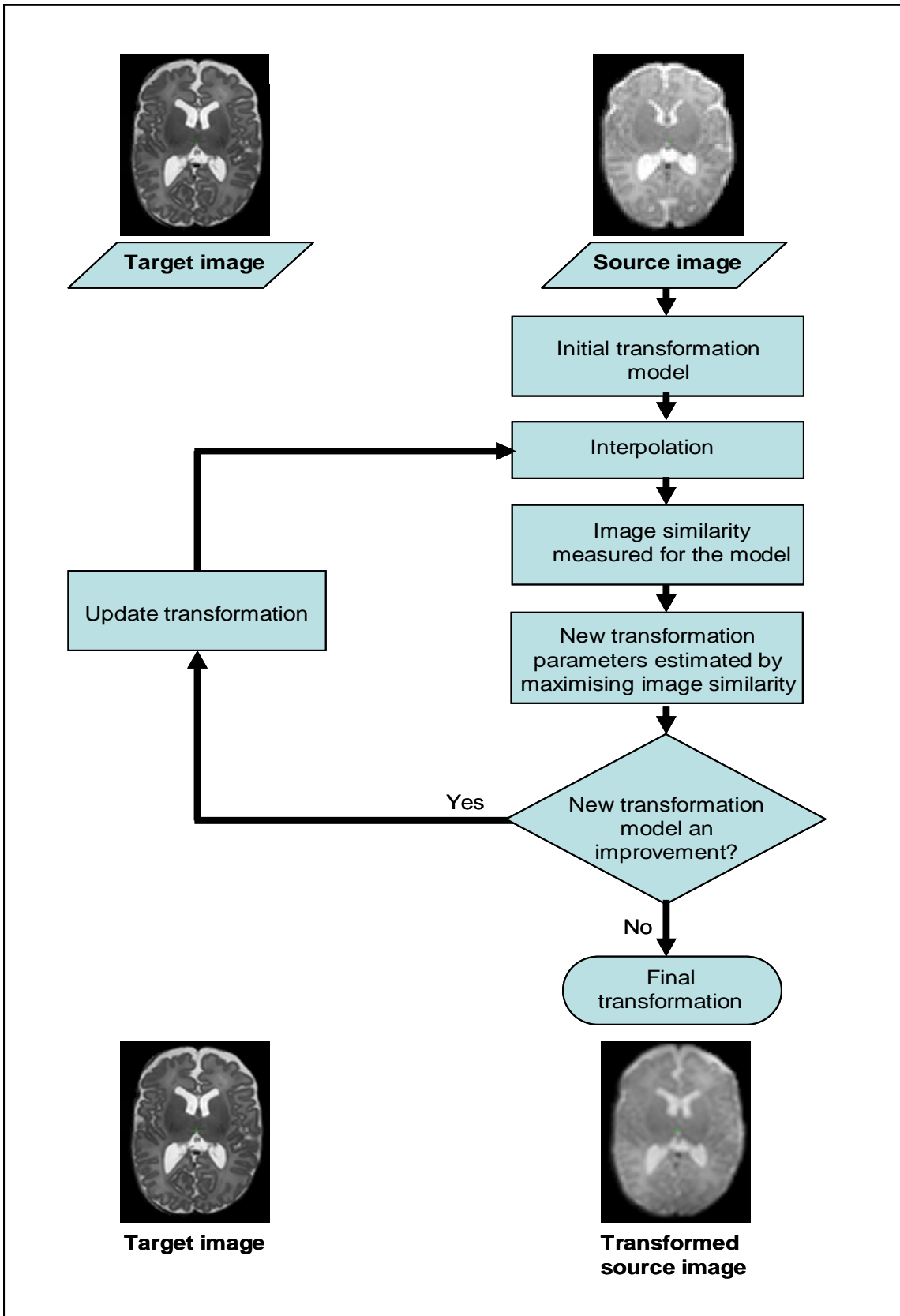


Figure 2.21: Image registration algorithm

An image registration algorithm first requires the source data to be transformed into reference (target) space using a transformation model. Since the location in a source image which is mapped to the corresponding location in the target image may not coincide with any of the source image's voxel locations, the intensity at this location then needs to be estimated using an interpolation method. A similarity measure evaluates the correspondence between the source and target images under the transformation, before new parameters are estimated by maximising the similarity.

The following section briefly reviews rigid, affine and nonlinear transformation models, before describing in more detail the voxel-based registration model used in this work. A more comprehensive discussion of image registration methodologies can be found in Hajnal (Hajnal et al., 2001).

2.7.2 Transformation models

The alignment of a pair of images requires finding the transformation that correlates the position of features in one image to the position of features in the other image. Modelling the transformation with respect to a fixed frame of reference, the transformation that maps a position x in one image to position x' in another image is given by:

$$T : x \mapsto x' = T(x) \quad [2.21]$$

In general, transformation models can be divided into broad categories based on their geometric properties. Rigid transformations preserve distances between points. These are a subset of affine transformations, which map straight lines to straight lines but also allow for scales and shears, and so angles and distances may not be preserved. The term global is frequently used to describe rigid or affine transformations, since all the voxels in the source image undergo the same transformation. Nonlinear transformations, however, allow for more localised deformations, which can be useful if the images to be registered vary in anatomy or in local levels of distortion.

The application required for image registration affects the choice of the type of transformation model used. If the data to be registered are brain images from the same neonatal subject imaged at the same timepoint but with different modalities, then in the absence of image acquisition artefacts a rigid transformation is appropriate. This is due to the constraints placed upon brain movement by the skull, which can be considered to be rigid. However, the difference between two brain images of the same child acquired at different timepoints would be better represented by an affine transformation, as there would be changes in brain size over time. In this second case, however, or if one or both of the images to be registered contain local deformations in the image, there may be local differences after the application of a global transformation, which may require an additional nonlinear step to attain improved correspondence.

2.7.2.1 *Rigid transformations*

Rigid transformations preserve distances and angles, and therefore allow for rotations and translations. In three dimensions this gives six degrees of freedom (i.e. six free parameters): translations in the x, y and z directions and rotations about the same three axes. A rigid transformation is given by a rotation R followed by a translation t and maps a point $x = (x, y, z)$ to a point $x' = (x', y', z')$ and can be written as:

$$x \mapsto Rx + t \tag{2.22}$$

where

$$R = \{r_{ij}\}, i, j \in \{1, 2, 3\}$$

is the matrix describing the rotational component of the transformation and

$$t = (t_x, t_y, t_z)$$

is the vector describing the translational component.

Using homogeneous coordinates, the transformation T can therefore be described by the following matrix:

$$T_{rigid}(x) = \begin{pmatrix} x' \\ y' \\ z' \\ 1 \end{pmatrix} = \begin{pmatrix} r_{11} & r_{12} & r_{13} & t_x \\ r_{21} & r_{22} & r_{23} & t_y \\ r_{31} & r_{32} & r_{33} & t_z \\ 0 & 0 & 0 & 1 \end{pmatrix} \begin{pmatrix} x \\ y \\ z \\ 1 \end{pmatrix} \quad [2.23]$$

For translation only, the matrix simplifies to:

$$T_{rigid_translation}(x) = \begin{pmatrix} x' \\ y' \\ z' \\ 1 \end{pmatrix} = \begin{pmatrix} 1 & 0 & 0 & t_x \\ 0 & 1 & 0 & t_y \\ 0 & 0 & 1 & t_z \\ 0 & 0 & 0 & 1 \end{pmatrix} \begin{pmatrix} x \\ y \\ z \\ 1 \end{pmatrix} \quad [2.24]$$

For a rotation α about the x-axis, the transformation is given by:

$$T_{rigid_rotation}(x) = \begin{pmatrix} x' \\ y' \\ z' \\ 1 \end{pmatrix} = \begin{pmatrix} 1 & 0 & 0 & 0 \\ 0 & \cos \alpha & \sin \alpha & 0 \\ 0 & -\sin \alpha & \cos \alpha & 0 \\ 0 & 0 & 0 & 1 \end{pmatrix} \begin{pmatrix} x \\ y \\ z \\ 1 \end{pmatrix} \quad [2.25]$$

2.7.2.2 *Affine transformations*

Rigid-body transformations are a subset of a more general group of transformations which include also scaling and shear parameters in the transformation matrix. As a result, parallel lines are still maintained, but the angles between lines can change.

$$x \mapsto Ax + t \quad [2.26]$$

where

$$A = \{a_{ij}\}, i, j \in \{1, 2, 3\}$$

is the matrix describing the rotational, shear and scale components of the transformation and

$$t = (t_x, t_y, t_z)$$

is the vector describing the translational component. Affine transformations in two-dimensions can be represented by the following matrix:

$$T_{\text{affine}}(x) = \begin{pmatrix} x' \\ y' \\ z' \\ 1 \end{pmatrix} = \begin{pmatrix} a_{11} & a_{12} & a_{13} & t_x \\ a_{21} & a_{22} & a_{23} & t_y \\ a_{31} & a_{32} & a_{33} & t_z \\ 0 & 0 & 0 & 1 \end{pmatrix} \begin{pmatrix} x \\ y \\ z \\ 1 \end{pmatrix} \quad [2.27]$$

Figure 2.22 demonstrates the types of transformation that can be obtained from rigid-body and affine deformation models.

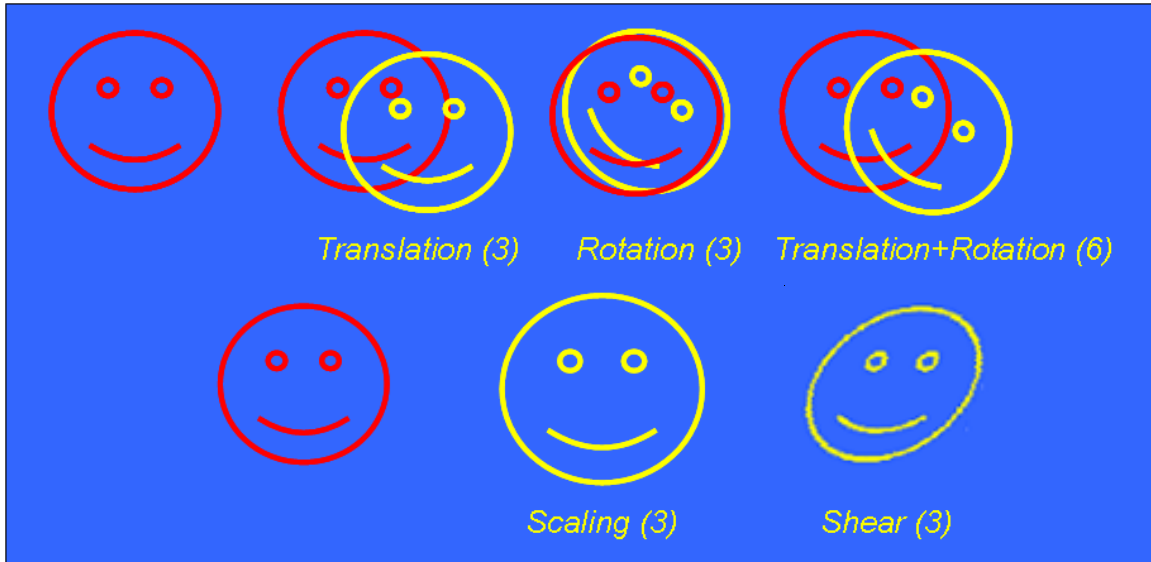


Figure 2.22: Affine transformations (from Crum et al., 2004)

Rigid transformations (top row) allow translations and rotations to map the coordinates of the source image (in yellow) to the coordinates of the target (reference) image (in red). Translations can be applied from, and rotations can be applied about, each of the coordinate axes. As a result, in three-dimensions a rigid transformation allows six degrees of freedom (DOF). If there are differences in size or in the angles between lines in the two images, however, then the images can be brought into increased correspondence by allowing scaling or shearing of the source image (bottom row). Scales

can be applied along each of the coordinate axes and shears along each of the image planes, so affine transformations can be described by twelve independent parameters. Although these transformations can be used to correct for global differences in shape and/or size, they cannot be used to achieve correspondence between pairs of images that contain localised differences, such as when aligning images from different subjects or images distorted by artefacts arising from data acquired with an EPI readout.

2.7.2.3 *Nonlinear transformations*

The transformation matrix described by an affine transformation can be used to take into account global differences in size, shape and orientation between a pair of images. In order to provide a dense correspondence between images where the transformation needs to vary from one part of the image to another, the transformation needs to be characterised by more than just the parameters used to define a rigid or affine transformation. In other words, the effect of the transformation needs to vary locally across the image.

Nonlinear transformations can be represented as smooth displacement fields. These require a smooth assignment of vectors to each location in an image. One of the most widely used methods of achieving this is to use spline-based registration techniques, described in Section 2.7.8.4.1. These generally require a set of corresponding control points or landmarks to be identified in the images. The landmarks can be manually placed in the source and target images to represent corresponding locations, can be automatically selected using feature-recognition algorithms or be equally spaced throughout the image on a regular lattice aligned with the coordinate system of the images. The location of the control points in the target image is then mapped to the corresponding point in the source image, and between these control points splines are used to interpolate deformation vectors at the control points.

Popular alternatives to spline-based registration techniques include elastic models (Bajcsy et al., 1989) and viscous fluid models (Christensen et al., 1994; Christensen et al., 1996; Bro-Nielsen et al., 1996). The former consider a source image to be a linear, elastic solid and register this to a target by finding an equilibrium between an external image

matching force and an internal force that constrains the registration. However, the assumption of linear elasticity may be invalid for large deformations so that grossly different images cannot usually be adequately registered (discussed in Crum, 2004). The viscous fluid model proposed by Christensen (1994) allows larger and more localized deformations, but may also increase the potential propensity for inaccurate registration due to the expansion of one region instead of the shifting or distorting of another (Crum, 2004).

Finite element registration models subdivide an image into a number of different cells, and label each of these depending on the type of tissue present within that element. An image of the head, for example, may be split into numerous elements containing predominantly bone, cerebrospinal fluid or nervous tissue, which are usually labelled as rigid, fluid or elastic respectively. Each cell within the source image is then deformed in relation to its label in order to achieve maximal voxel similarity or landmark correspondence with the target image (see Miga et al. (1999) and Ferrant et al. (2000) for examples of applications of finite element brain registration models).

2.7.3 Similarity measures

As described above, the aim of image registration is to match a source image to a target, or reference, image. In order to do this, some measure of similarity between the images under a transformation T is required. Presented here is a brief overview of some commonly used voxel-based and entropy-based image similarity metrics. A more comprehensive review can be found in Hajnal (Hajnal et al., 2001).

2.7.3.1 *Voxel-based metrics*

Voxel-based metrics of similarity quantify a measure of the difference between voxel intensities at corresponding locations in two images. Given a target I_1 , a source I_2 and a transformation T , the overall similarity of these images is given by the sum of the differences at each corresponding voxel location x over the image domain Ω .

2.7.3.1.1 *Sum of squared difference (SSD)*

The sum of squared distances between a source and a target image is given by:

$$SSD = \sum_{x \in \Omega} (I_1(x) - I_2(T(x)))^2 \quad [2.28]$$

where $I_2(T(x)) = I_2(x')$ is the intensity of voxel x in the source image under the transformation T .

The SSD similarity metric assumes that a pair of images will be identical when registered, except for the presence of noise in the data. As a result, it is only used when performing intra-modality registration, when each tissue class will have identical intensity ranges in both images. SSD can be strongly affected by a few voxels in an image pair that have large intensity differences, and can drive a registration algorithm using this measure as a similarity metric to a suboptimal result.

2.7.3.1.2 *Cross-correlation*

The cross-correlation similarity metric is given by:

$$CC = \frac{\sum_{x \in \Omega} (I_1(x) - I_1(\bar{x}))(I_2(x) - I_2(\bar{x}))}{\sqrt{\sum_{x \in \Omega} (I_1(x) - I_1(\bar{x}))^2} \sqrt{\sum_{x \in \Omega} (I_2(x) - I_2(\bar{x}))^2}} \quad [2.29]$$

where $I_1(\bar{x})$ and $I_2(\bar{x})$ represent the mean image intensities in the target and source images respectively.

Cross-correlation assumes a linear relationship between corresponding intensities in an image pair. Unlike SSD, their dynamic ranges might differ but an intensity scaling and shift can be used to map intensities at corresponding locations, with any residuals again being due to noise.

2.7.3.2 *Entropy-based metrics*

The variability of intensities in different MRI modalities means that corresponding structures in different images need not have the same voxel intensities. If the intensity pairs are viewed as entries in the joint probability density function of the image pair, however, entropy-based similarity metrics, which use information from the whole image, can be used (for a review of entropy-based registration, see Pluim et al., 2003).

It is possible to provide estimates of the probability $p(I_1)$ of the occurrence of a particular intensity I_1 in the target image, the probability $p(I_2)$ of intensity I_2 occurring in the source and the probability $p(I_1, I_2)$ of their occurrence at corresponding voxel locations. The marginal (or Shannon) entropies, which represent the information content of an image, are defined to be:

$$H(I_1) = -\sum_{i_1 \in I_1} p(i_1) \log p(i_1) \quad [2.30]$$

$$H(I_2) = - \sum_{i_2 \in I_2} p(I_2) \log p(I_2) \quad [2.31]$$

The joint entropy, $H(I_1, I_2)$, given by:

$$S_{JE}(I_1, I_2) = H(I_1, I_2) = - \sum_{i_1 \in I_1, i_2 \in I_2} p(I_1, I_2) \log p(I_1, I_2) \quad [2.32]$$

where $p(I_1, I_2)$ represents the joint probability density function of the images I_1 and I_2 . As the images get better aligned, their joint entropy often decreases, indicating less disorder in the overlap. However, if for example the images are transformed in such a way that only background (and not anatomical structure) is aligned, this will still result in a good joint entropy.

2.7.3.2.1 Mutual information (MI)

An extension of the joint entropy metric of similarity is mutual information, which incorporates the individual entropies of the images. A registration using MI as a similarity metric, which needs to be maximised, then seeks a trade off between maximising the marginal entropies of the images while reducing their joint entropy.

$$MI = H(I_1) + H(I_2) - H(I_1, I_2) \quad [2.33]$$

2.7.3.2.2 Normalised mutual information (NMI)

MI can be used as a similarity metric to register images in which there is not a linear relationship between corresponding intensities. However, like joint entropy, MI is not overlap invariant: a reduction in overlap leads to an increase in mutual information but also causes an increase in misalignment. As a result, NMI has been proposed (Studholme, 1999), which instead represents the ratio of the sum of the marginal entropies of the source and target images to the joint entropy and has been shown to be overlap invariant:

$$NMI(I_1, I_2) = \frac{H(I_1) + H(I_2)}{H(I_1, I_2)} \quad [2.34]$$

2.7.3.3 *Histogram-based density estimation*

In order to use entropy-based metrics to measure similarity, an estimation of the probability density functions of image intensities in the target and source image is required. Kernel density estimations can be used to achieve this (Thevenaz and Unser, 2000), but the most common approach is to construct a joint 2D histogram of the image intensities of the source and target images. This requires binning, the partitioning of a range of intensities in the target and source images into distinct intervals (bins) of fixed width. The joint probability that a voxel lies within a particular range of intensities is then given by the number of samples in the corresponding bin divided by the total number of samples in the histogram. The marginal probabilities can be similarity calculated, and the entropies calculated as above.

2.7.4 Interpolation

The voxel- and entropy-based similarity metrics described above are based on the correspondences in intensities between the target voxel locations and the transformed source voxel intensities. However, the source locations are not likely to coincide with the locations of the voxel centres in the source image. As a result, the source intensities need to be interpolated from the sampled source values before evaluating the similarity metric.

Nearest neighbour, whereby the intensity at a point $I_2(x)$ is given by the intensity of the voxel centred nearest to that point, is the simplest interpolator, but more sophisticated interpolation schemes such as tri-linear interpolation (Thevenaz et al., 2000), B-spline interpolation (Unser, 1999) and sinc interpolation (Hajnal et al., 1994) are also used (for a survey, see Lehmann et al., 1999), with the choice dependent on the trade-off between cost of interpolation and the quality produced.

2.7.5 Regularisation

The many additional degrees of freedom allowed by nonlinear registration methods over affine models may mean that a structure in the source image is warped to match a different structure in the target image. This is not because they anatomically correspond, but because they have related image intensities. As a result, an additional term is frequently incorporated into the registration optimisation that regularises (or constrains) a transformation to be smooth. If $C_{\text{similarity}}$ represents the similarity metric and C_{reg} represents a measure of the plausibility or regularity of the transformation, then the overall objective cost function C is given by:

$$C = -C_{\text{similarity}} + \lambda C_{\text{reg}} \quad [2.35]$$

where λ is a constant representing the relative contributions of the similarity and regularisation terms during the optimisation. A value of λ that is too low may still lead to implausible warps in the deformation field and a value too high may prevent the algorithm from sufficiently aligning the images, so the value of λ needs to be carefully chosen and is often empirically determined for the class of images to be registered. The registration problem then becomes one of minimising the cost function under the similarity metric and regularisation tool used.

2.7.6 Optimisation

In order to determine the transformation that maximises the similarity between a pair of images, a method of optimisation is needed. In general, the most appropriate methods for this are iterative strategies that improve image correspondence at each iteration until a maximum is found.

One of the most widely used of these iterative optimisation strategies is the gradient descent method. With this approach, the transformation parameters are individually perturbed by a chosen step size and the similarity metric is re-evaluated for each perturbation. The parameter giving the biggest increase in similarity is then selected and the transformation is updated by modifying this parameter, with the process repeated until no further increase in similarity is achieved.

2.7.7 Applications of image registration

2.7.7.1 *Image registration for EPI distortion correction*

Before DTI data acquired with an EPI readout can be analysed, the individual diffusion weighted images need to be registered to the $b = 0$ s/mm² image and the data fitted to the tensor model. Many current distortion-correction registration methods use registration algorithms limited to affine transformations (Mistry and Hsu, 2006; Jenkinson and Smith, 2001), the implicit assumption being that the data simply need to be rotated and translated, scaled and sheared with respect to one another to achieve correspondence. However, the distortions produced in echo planar DTI data are more complex, and a recent study found that nonlinear registration of DWIs to a $b = 0$ s/mm² image using the algorithm incorporated in the Automated Image Registration software package (Woods et al., 1998a) produces fewer distortions than affine registration alone (Kim et al., 2006). This resulted in decreased tensor fitting error and increased mean FA in the regions studied (Kim et al., 2006). There is much ongoing work in developing retrospective correction models incorporating nonlinear transformations (Kybic et al., 2000; Studholme et al., 2000; Netsch and van Muiswinkel, 2004).

2.7.7.2 *Image registration for population-based analysis of MRI data*

2.7.7.2.1 *Spatial normalisation*

In order to perform automated group-wise analysis of MRI data, it is necessary to spatially normalise different subjects' images. That is to say, every subject's data is reoriented into a particular reference frame, so that corresponding anatomy across subjects is represented at the same voxel location. This then allows voxelwise cross-subject statistics to be performed, in order to compare data across subjects and/or between different population groups. This is the general approach employed by most voxel-based analysis tools proposed for analysing MRI data, such as the widely used voxel-based morphometry (VBM) technique as employed in the Statistical Parametric Mapping (SPM) package (Ashburner and Friston, 2000; Good et al., 2001).

In order to use these approaches, however, it is important that

- a. An appropriate target (or reference) space is chosen; and
- b. An appropriate image registration algorithm is used.

2.7.7.2.2 *Target selection*

A number of different stereotaxic spaces with accompanying brain atlases have been proposed as targets for reporting MRI data. The Montreal Neurological Institute (MNI) 152 template, the average of 152 adult brains registered to a standard space using affine transformations (Evans et al., 1992) is amongst the most widely used and has been adopted as the standard template by the International Consortium for Brain Mapping (<http://loni.ucla.edu/ICBM>). Single subject targets have also been suggested, including the 'Talairach brain', a dissected and photographed brain with approximately labelled Brodmann areas (Talairach and Tournoux, 1988), and the 'Colin27' brain, generated from the averaging of high-resolution MRI data from a single adult subject scanned 27 times (Holmes et al., 1998). If the study population have different brains to the chosen

target, however, such as the presence of enlarged ventricles or reduced grey matter volumes in Alzheimer's disease, it can be difficult to achieve appropriate normalisation. In that case, data from different subjects may not be in alignment and the dangers of analysing imperfectly registered MRI data with voxel-based techniques to make neuroanatomical inferences has been well documented (Bookstein, 2001).

An alternative approach to spatial normalisation is to use a study-specific template as the registration target space. If carefully selected, this has the advantage of being more similar to the data being analysed, so images require less warping to be transformed into this space. One method for determining which image should be chosen as the target is to register each subject in the dataset to every other, and then to use as the final target the "most typical" subject of the group, defined as the image which minimises the amount of warping required for all other subjects to align to it (e.g. in Smith et al., 2006).

There remains, however, the problem that the chosen target image may not be truly representative of the population, especially if there a lot of anatomical variation between the subjects. This may be the case when analysing neonatal MRI data and the performance of a registration algorithm may be diminished if the images to be aligned are very dissimilar. As a result, registering the images to a new coordinate system at the average of a population has been proposed (Guimond et al., 2000; Studholme et al., 2003; Bhatia et al., 2004).

2.7.7.3 *Registering EPI data to an anatomical image*

Registration of DTI data acquired with an EPI readout to a common image template is difficult. As well as overcoming differences in anatomy, differences in distortion also have to be addressed. Spatial normalisation can be improved, however, by first coregistering the data to a high-resolution anatomical (i.e. T1- or T2-weighted) image. This allows for unwarping of some of the distortions, and makes subsequent alignment with the template image more robust. As a result, a two-step registration of EPI data to a template image prior to automated group-wise analysis is usually implemented: each

point x in EPI space is mapped to a corresponding point x' in the same subject's anatomical space with a transformation T , which is in turn mapped to a point in target space with transformation T' :

$$x \mapsto T(x) = x' \mapsto T'(x') = x'' \quad [2.36]$$

2.7.8 Image registration software

There are a number of brain image registration tools incorporated into image processing software packages that are freely available for download. Amongst the most widely used of these is the linear image registration software included in the Functional MRI of the Brain (FMRIB) Software Library (FSL), developed by collaborators at Oxford University (Jenkinson and Smith, 2001; Jenkinson et al., 2002). Usage of registration algorithms incorporating nonlinear transformations is also gaining prominence. The ‘align_warp’ tool developed by Woods and colleagues at the University of California at Los Angeles and incorporated in the Automated Image Registration version 5 (AIR 5.0) software suite (Woods et al., 1998a; Woods et al., 1998b) is a popular choice. Tract-based spatial statistics, a tool for processing diffusion tensor imaging data incorporates Rueckert's B-spline based nonlinear registration tool (Rueckert et al., 1999). The following section presents a brief overview of these methods and the image registration algorithms that they use to achieve spatial correspondence between pairs of images.

2.7.8.1 *FMRIB's Linear Image Registration Tool (FLIRT)*

FLIRT is a voxel-based linear image registration tool that uses a “hybrid global-local optimisation technique” in conjunction with an apodised cost function in order to register a floating source image to a fixed reference image. The latest version of the software, release 5.4.2, is included as part of FSL 4.0. A full description of the algorithm used can be found in Jenkinson (Jenkinson and Smith, 2001; Jenkinson et al., 2002). The software allows the selection of cost functions appropriate for intra-modal (least squares and

normalised correlation) and inter-modal (mutual information and normalised mutual information) registration, and a choice of interpolation (nearest neighbour, trilinear, sinc and B-spline) required to calculate the cost function at corresponding points in the source and target image. The cost function is apodised (or modified) by deweighting contributions to the cost function calculation from locations at or near to the edge of overlapping regions between the source and target image. This helps to smooth local discontinuities in the cost function as the transformation parameters are smoothly varied, which arise because the degree of overlap changes as the source image is transformed, and can result in the in the optimisation method being stuck in a local minimum.

In order to aid the efficiency of the search strategy, the global-local optimisation method uses prior knowledge about the physical dimensions of the data (including the voxel size and field of view) as well as the user inputted initial degree of correspondence between the images to be registered. As in Section 2.7.8.4, a coarse-to-fine approach is then used at four different scales: 8 mm, 4 mm, 2 mm and 1 mm. The source and target image are initially blurred with a Gaussian kernel of full width half maximum (FWHM) 7mm and then resampled at each scale.

Though the algorithm can allow full twelve degree of freedom affine transformations, at the 8 mm and 4 mm scales the search is limited to the x , y and z rotation parameters followed by a full local optimisation of x , y and z translation parameters and global scale (i.e. seven DOFs). A coarse search over the rotation parameters is initially employed, followed by a full local optimisation of translation and global scale for each rotation tried using a set of N one-dimensional golden searches (Press et al., 2002). After a finer search over the rotation parameters with one cost function evaluated at each rotation, the full local optimisation of rotations, translations and scale at that resolution level for each local minimum of the cost function detected at the previous stage is carried out.

In order to further reduce the possibility of converging to a local (rather than a global) minimum of the cost function at the second (i.e. the 4 mm scale) search stage, the best three transformation parameters from the first (8 mm scale) search stage are all

optimised. In addition, some perturbations of these initial candidate transformations are also performed, and these are locally optimised. The single best minimum cost solution from the optimisation results is then selected, and it is only this transformation that is optimised at the third (2 mm scale) search stage. At this stage, and at the final (1 mm scale) search stage, the registration solution is optimised for full twelve DOF affine transformations.

2.7.8.2 *Automated Image Registration's alignlinear and align_warp*

Align_warp is a registration tool that uses a nonlinear model to estimate the transformation parameters between a source and a target image. It can use the parameters from alignlinear, an affine transformation tool as the starting estimate for a nonlinear registration, and is included as part of the fifth version of the AIR software package (<http://bishopw.loni.ucla.edu/AIR5/>). Outlines of both the affine and nonlinear transformation models used are given below. Full descriptions can be found in Woods (Woods et al., 1998a; Woods et al., 1998b).

2.7.8.2.1 *Alignlinear*

Figure 2.23 is a schematic diagram of the affine registration algorithm used in alignlinear. As is the approach employed by FLIRT, the algorithm uses a hierarchical registration approach, with the data first sampled at low density before the cost function is computed at progressively larger sampling densities. In other words, the cost function is initially computed using image intensity data from only a few voxels in the images, until finally all the voxels are used to determine the cost function.

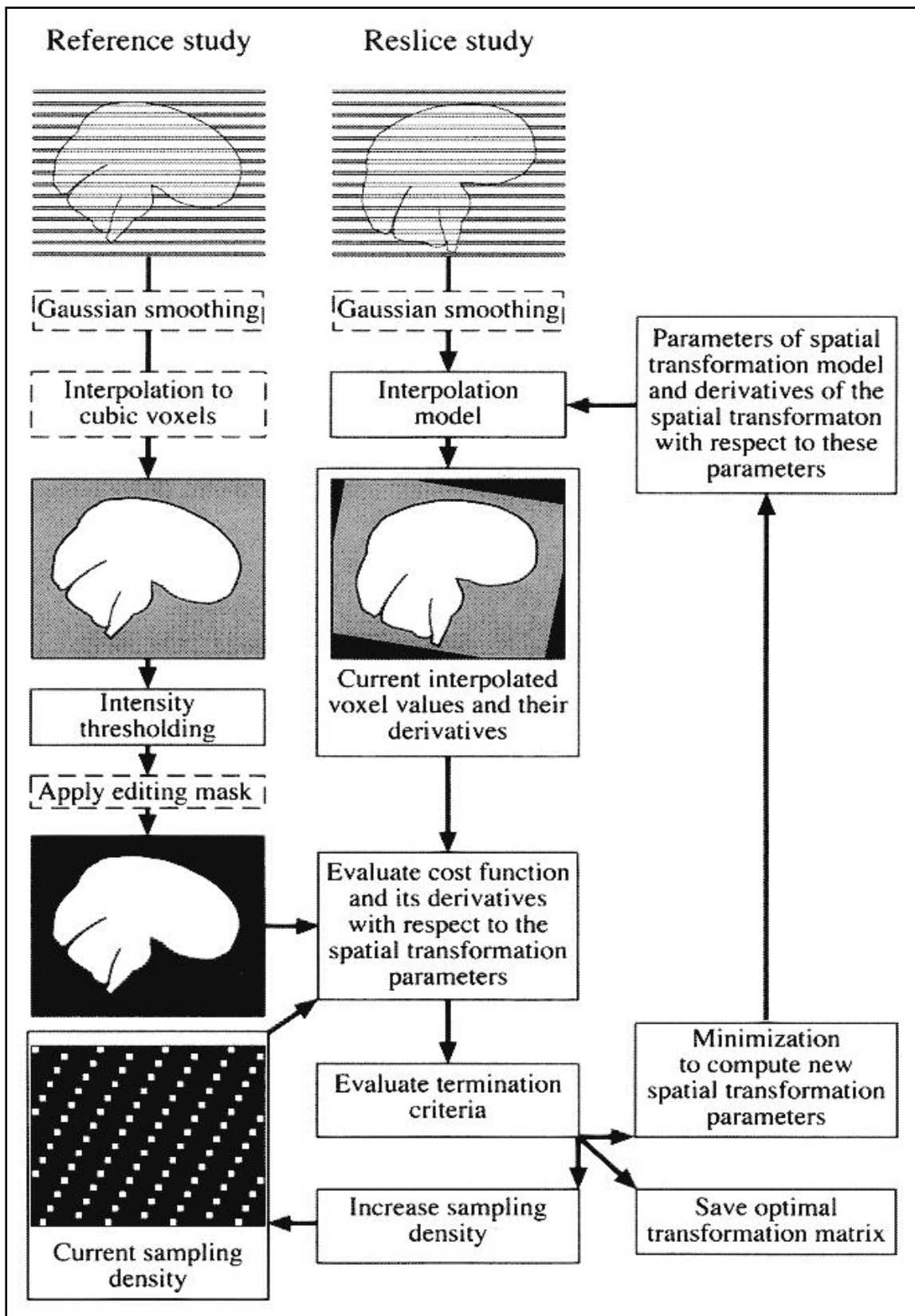


Figure 2.23: Schematic diagram of the affine registration algorithm employed by AIR's alignlinear, from Woods (Woods et al., 1998a)

The algorithm aims to match the reslice image (i.e. the source image) to the reference study (i.e. the reference, or target image). Following optional smoothing of the images with a Gaussian kernel (all boxes bordered by hatched lines represent optional procedures), the source image is resampled to match the target image, with the resampling based on the current parameters of the spatial transformation used. As described in Section 2.7.4, this requires an interpolation model, and by default a trilinear interpolator is used. A cost function is evaluated for this transformation and interpolation model, using either the standard deviation of the ratio of the resampled source and target images (Woods et al., 1992), least squares (Hajnal et al., 1995) or least squares difference (Alpert et al., 1996) as the similarity metrics. This is initially computed for only a limited voxel sampling in order to improve computational efficiency. The derivatives of the cost function with respect to the spatial transformation are calculated, and used to compute new parameters. In this way, the cost function is minimised in an iterative manner, with two different termination criteria tested every iteration to evaluate whether to continue iterating. These termination criteria are:

1. if the predicted change in the cost function associated with moving the current position in parameter space to the predicted minimum is positive, or
2. if the number of iterations at a given sampling density reaches the maximum limit, or if successive iterations are performed without improvement in the calculated cost function at this sampling density.

The parameters at this sampling density that resulted in the lowest actual value of the cost function is then saved and used as the initial parameter estimate at the next sampling density until the optimal transformation parameters are found at the highest sampling density. By default, the initial cost function is computed for every 81st voxel, with the sampling increased at subsequent levels to achieve a final sampling of every voxel.

In order to speed up the registration process and avoid the matching of non-brain structures driving the registration parameter optimisation, a mask can be applied to the target image, with regions outside the mask excluded from the evaluation of the cost function. However, masking the target images in this way can lead to a tendency to align the edges of the mask, which may significantly affect the cost function optimisation.

To partially eliminate this bias in the linear registration of a source image to a masked target image, the final transformation parameters are computed from averaging the final linear transformation parameters of the source \rightarrow target registration and the inverse of the target \rightarrow source registration.

Unlike FLIRT, AIR allows all model parameters to be adjusted from the first iteration. That is to say, if a full twelve DOF affine registration is being performed, then at the lower spatial sampling densities as well as rotations and translations, scale and shear parameters are also varied and are used to help minimise the evaluated cost function.

2.7.8.2.2 *Align_warp*

The `align_warp` tool can use the output from an initial affine registration of a source and target image as the initial transformation parameter estimates for a subsequent nonlinear registration of the images. In this way, global differences in orientations or scale between the images can be accounted for prior to matching local anatomy between the images using a voxel-based registration algorithm.

The nonlinear model initially computes the coordinates of a voxel in the source image as a second order polynomial of its corresponding location in the target image, with a total of thirty spatial transformation parameters (i.e. thirty degrees of freedom) (Woods et al., 1998b), with the choice of cost functions and interpolation models the same as for the affine registration tool. Successively higher order registration models with higher order polynomials can then be sequentially initialised with the optimal transformation parameters at the previous order polynomial. In the latest version of the software, twelfth order nonlinear models with 1365 degrees of freedom can be used.

Nonlinear transformations cannot be analytically inverted and therefore the method used in `align_warp` for removing biases associated with defining one image as the target image and the other as the reference image cannot be used. Instead, the nonlinear algorithm also includes voxels outside the mask in the target image that are included in the corresponding voxel of the interpolated source image. The termination criteria for the iterative cost function optimisation is similar to that for the affine registration algorithm, but with different default values, with sparse sampling used to calculate the cost function at higher nonlinear models to allow reasonable computational times (Woods et al., 1998b). As in the multi-level free-form deformation model based on B-splines used in

this work, linear transformations are analytically combined with nonlinear transformations prior to applying them to finally transform a source image into target space so that the source data is not interpolated more than once.

2.7.8.3 Tract-based Spatial Statistics (TBSS)

As mentioned in Section 2.7.7.3, registering DTI data to an anatomical image prior to spatial normalisation can help reduce inaccuracies in registration when aligning diffusion data from different subjects into a common reference frame. An alternative approach to analysing diffusion-derived FA data from multiple subjects has recently been proposed that avoids the challenges of registering DTI data to anatomical data as an intermediate step, and instead registers all the FA data directly into a common reference frame (Smith et al., 2006). In TBSS, this is performed using the B-spline based registration method introduced in Section 2.7.8.4.1 and implemented by Rueckert in the Image Registration Toolkit (ITK) software package ((Rueckert et al., 1999); <http://wwwhomes.doc.ic.ac.uk/~dr/software>).

If no target image space is defined, initially each subject's FA map is registered to every other subjects FA map using an affine (registration parameters: 3 resolution levels, 64 bins, 20 iterations, 4 steps, 5 mm step length, similarity measure = cross correlation, 20 mm initial control point spacing) followed by a nonlinear (registration parameters: 1 resolution level, 64 bins, 20 iterations, 4 steps, 5 mm step length, similarity measure = cross correlation, 20 mm control point spacing) registration algorithm (wwwhomes.doc.ic.ac.uk/~dr/software). For all of the registrations to a particular infant's diffusion space, the average (median) amount of nonlinear warping required to transform the other datasets into that target space is then calculated. The 'most typical' subject is then defined as the one requiring the least amount of warping to align all the other images to it. All subjects' FA data is then aligned to this common space (Smith et al., 2006). In TBSS v1.0, all the data is then affine-transformed into $1 \times 1 \times 1 \text{ mm}^3$ MNI152 space by default, though the program code can be modified to resample the data to produce 1 mm^3 isotropic voxels whilst remaining in the space of the 'most typical' subject. This is useful

if the study population (as in this work) is very different from MNI152 (adult) space. In that case, all subsequent processing is carried out using this space and resolution.

The transformed FA images are then averaged to create a mean FA image (Figure 2.24a; Smith et al., 2006). This is used in turn to generate a thresholded image that only represents the centres of the major white matter pathways of the group, the so called mean FA skeleton (Figure 2.24a). This initially requires an estimation of the direction perpendicular to the local white matter tract surface at all voxels in the image (Figure 2.24b-d), followed by non-maximum suppression in this direction (Smith, 2006). That is to say, along all voxels in the direction perpendicular to the local white matter tract a search is made, with the voxel with the highest FA value identified as the centre of the tract.

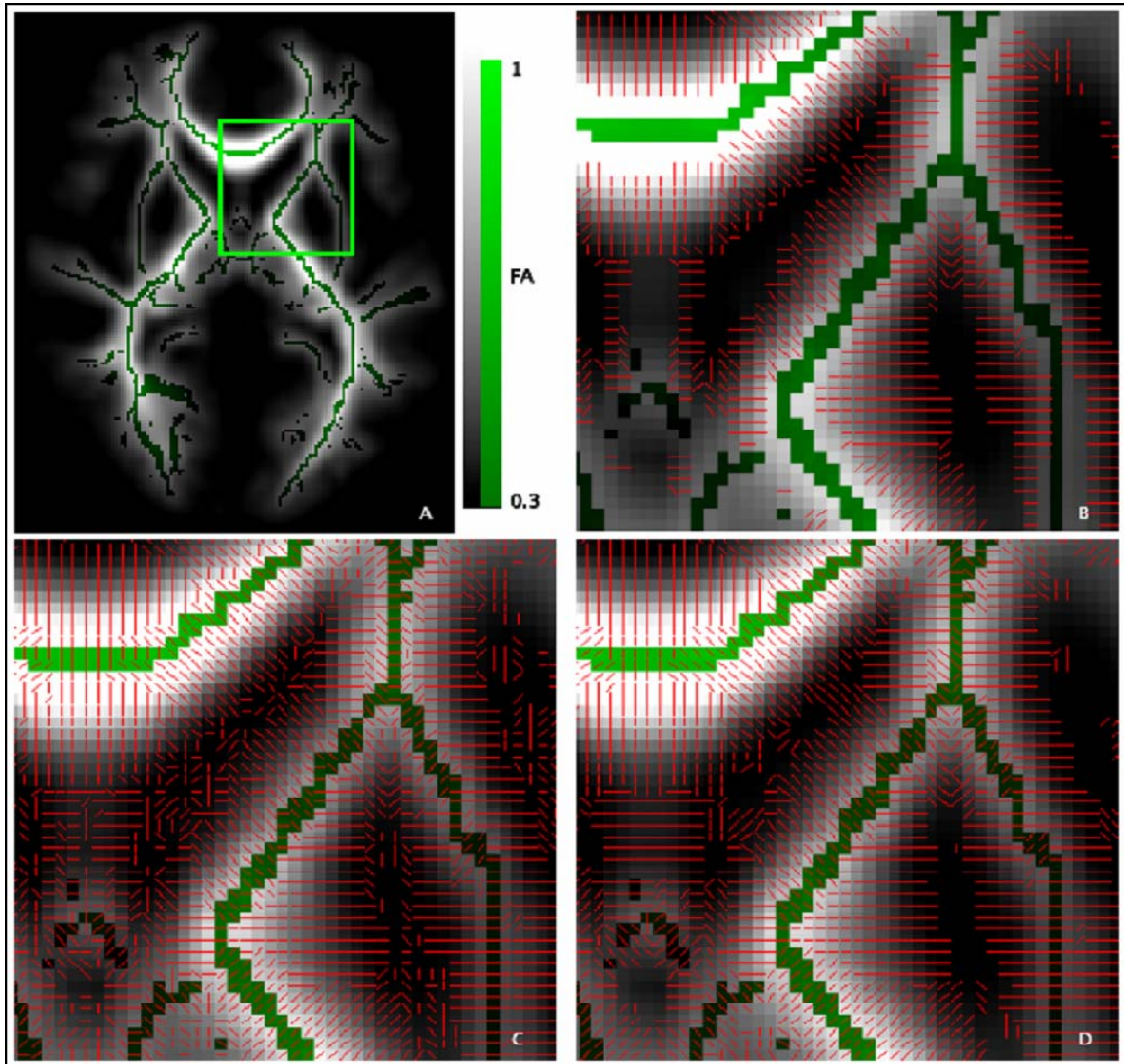


Figure 2.24: Creating the mean FA skeleton (from Smith et al., 2006)

The original mean FA image (in greyscale) with the overlying final mean FA skeleton (in green) and the region of interest used in the remaining images; (b) The first stage of skeletonisation is achieved by using the local centre of gravity of FA values to estimate the local surface direction perpendicular to the white matter tract (shown in red); (c) Remaining perpendiculars to the local tract direction are then found by calculating the second derivative of the mean FA image; (d) The perpendicular direction vector image is finally smoothed by taking the mode of the directions in the local $3 \times 3 \times 3$ neighbourhood of voxels.

Finding the orientation of the local tract surface is achieved based on the assumption that if a voxel of interest lies away from the centre of a tract, then FA will be greater in neighbouring voxels on one side of the voxel than the other. The direction in which FA is highest then points towards the nearest tract centre. This is quantified by finding the centre of gravity of FA values of the local 3 x 3 x 3 voxel neighbourhood. The vector from the centre of the current voxel to the local centre of gravity should then point towards the tract centre (Figure 2.25).

If the local centre of gravity of FA values is close to the centre of the current voxel, however, then the direction perpendicular to the local white matter tract surface is estimated by finding the direction of maximum FA change in the local 3 x 3 x 3 voxel neighbourhood. The mean FA value of each pair of voxels at opposite ends of the neighbourhood is subtracted from the FA value of the centre voxel, and the direction resulting in the maximum difference is assumed to be perpendicular to the local tract (Figure 2.25).

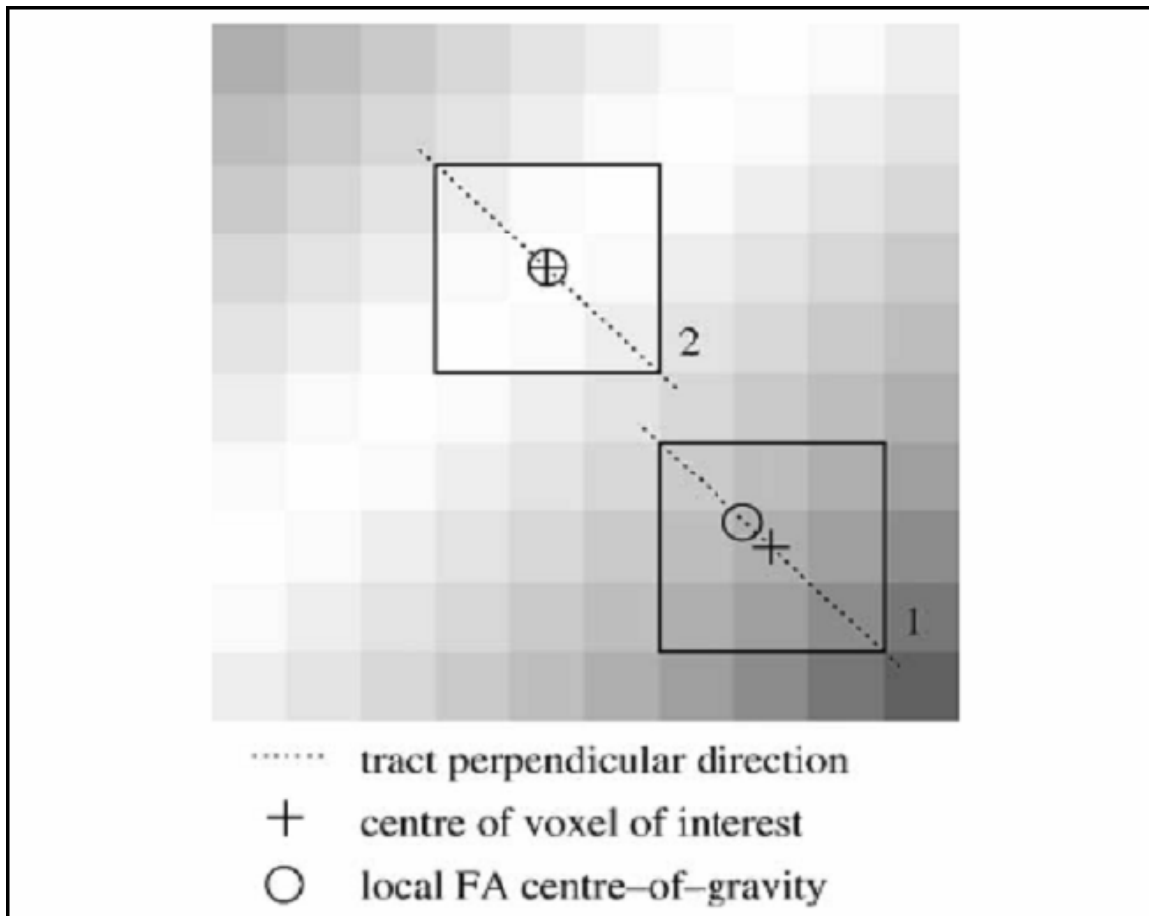


Figure 2.25: Identifying the local tract centre (from Smith et al., 2006)

(1) Example of a voxel where the local centre of gravity points in the local tract perpendicular direction; (2) a voxel lying directly on the local tract centre.

The robustness of the estimated local direction perpendicular to the white matter tract is improved by replacing every direction estimate with the most common direction of the local 3 x 3 x 3 set of estimated directions (Figure 2.23d).

The mean FA skeleton is then generated by finding the centre of each tract (Figure 2.24a). At each voxel, the FA value is compared with the two nearest voxels in the local direction perpendicular to the white matter tract; if the FA value is larger than that of both the neighbouring voxels then it forms part of the skeleton. Thresholding can then be applied to restrict analysis to the major white matter pathways of the brain.

The intensities at each voxel of the skeleton for each subject in the dataset are then determined by projecting the skeleton onto each subject's aligned FA data (Figure 2.26). Rather than assuming that every voxel in the skeleton projects directly onto the centre of a white matter tract for every subject, however, at each voxel the method then searches perpendicular to the local tract direction in a manner similar to that used to generate the skeleton to determine whether FA is higher at a nearby voxel. If so, then that voxel is assumed to correspond to the true centre of the white matter pathway in that region, and the skeleton is filled with the FA value at that voxel rather than the voxel in the image that that part of the skeleton was first projected onto (Figure 2.26). This is constrained by forcing the search to stay nearer to the starting section of the skeleton than to any other section of the skeleton (Figure 2.27), and by limiting the maximum search distance by applying a Gaussian weighting function with a 20 mm full-width half maximum to the search.

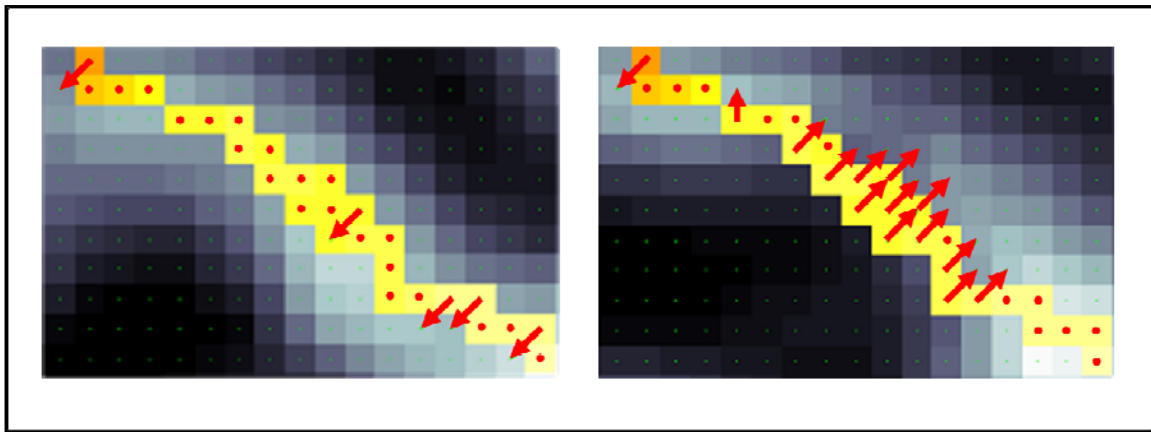


Figure 2.26: Projecting the mean FA skeleton onto each subject's aligned FA map (adapted from Smith et al., 2006)

A region of interest showing the projection of the mean FA skeleton (yellow) onto two different subjects' aligned FA maps (greyscale). On the left, the FA map was well aligned, and at most voxels the mean FA skeleton was already directly projected onto the appropriate voxel at the centre of the white matter tract (red dots). On the right, the FA map was less well aligned, but the subsequent perpendicular search strategy ensured voxels from the true tract centre were found (red arrows).

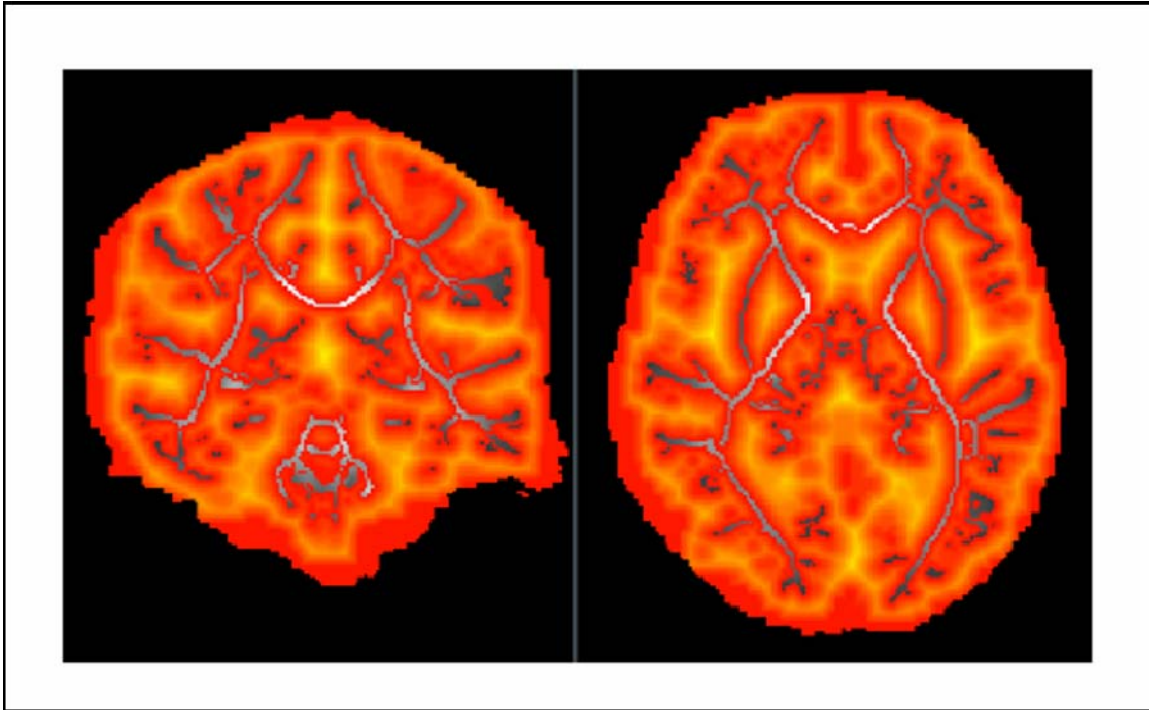


Figure 2.27: An example of a mean FA skeleton “distance map” (from Smith et al., 2006)

The mean FA skeleton is projected onto each subject’s aligned FA map. Residual misalignment from each voxel in the skeleton is then corrected for by searching in the perpendicular tract direction to find the true tract centre and assigning its intensity value to the skeleton voxel. This is constrained by the skeleton “distance map”. The red–yellow overlay encodes, for each brain voxel, how far the nearest skeleton voxel is. This is used during the projection of individual FA maps onto the skeleton in order to ensure that values are only taken onto the nearest part of the skeleton. The underlying mean FA skeleton (in greyscale) can be seen where the distance is zero.

This additional search step helps to minimise interpretation errors arising from the fact that automated voxel-based methods for analysing DTI data always raise the possibility that reported differences in intensity between groups may be due to misalignment between the images. This is particularly important when comparing data from preterm infants at term-equivalent age and term-born control infants. Gross differences in anatomy (preterm infants often have a more elongated brain shape in the anterior-posterior axis and larger ventricles than their term-born peers) may lead to misregistration, particularly when only affine or low degree of freedom nonlinear transformations are used. The additional perpendicular search strategy has been shown to

improve the Gaussianity of the cross-subject distribution of FA values at each voxel (Smith et al., 2006). This would be expected if the method does actually take FA values from the centre of the same point of the same tract in all subjects. Voxelwise cross-subject statistics can then be performed on the data to assess differences between or amongst groups of subjects.

2.7.8.4 *Registration models based on free-form deformations*

The technique of using regularly-spaced control points, so-called pseudo-landmarks, within an image lattice to be matched between a source and a target image is the approach used within the free-form deformation (FFD) model for nonlinear transformations (Rueckert et al., 1999). FFD models work by manipulating this underlying mesh of control points to produce a smooth transformation that deforms the source image into the space of the target image. This is achieved by using a locally-controlled blending function that smoothly estimates the control point transformation vectors.

Most of these models use a multi-level approach to determine the final transformation. Initially, the deformation field is estimated by using fairly few, widely separated control points, which allows for optimisation of the more global aspects of the nonlinear warp. Once this has been achieved, additional control points are added by subdividing the initial control point lattice and hence increasing the density of control points. The parameters for this lattice are subsequently optimised, allowing for the capture of the nonlinear differences between the images at a more local scale, and in turn can form the starting estimates for another optimisation step with an even finer control point spacing. This can diminish the risk of a registration algorithm converging towards a local rather than global optimum, particularly if the images are initially blurred to reduce high-frequency detail, and so such a coarse-to-fine multilevel approach is widely used (Rueckert et al., 1999; Schnabel et al., 2001; Shen and Davatzikos, 2002; Boardman et al., 2006).

2.7.8.4.1 B-splines

The term spline originally referred to a pliable strip of wood or metal that was bent into a desired shape for drawing curves on paper. This concept has since been used in computer graphics to refer to a smooth curve that runs through a series of given points (for a review, see Unser, 1999). There are many different splines that can be used to smooth or interpolate data to be registered using FFD models, amongst the most popular of which are B-splines. Unlike thin-plate splines (Bookstein, 1989) or elastic-body splines (Davis et al., 1997) B-splines are locally controlled. That is to say, displacing a control point $\Phi_{i,j,k}$ only affects the transformation in the local neighbourhood of that particular control point and not the global mesh of control points, making B-spline-based methods highly computationally efficient.

The FFD can then be written as the three-dimensional tensor product of one-dimensional cubic B-splines (Lee et al., 1996; Lee et al., 1997). If the domain of an image volume is denoted by

$$\Omega = \{(x, y, z) | 0 \leq x \leq X, 0 \leq y \leq Y, 0 \leq z \leq Z\} \quad [2.37]$$

and Φ represents a mesh of $n_x \times n_y \times n_z$ control points $\Phi_{i,j,k}$ with uniform spacing δ , then a point $x = (x, y, z)$ is transformed to its new location $x' = (x', y', z')$ by

$$T(x) = x' = x + \sum_{l=0}^3 \sum_{m=0}^3 \sum_{n=0}^3 B_l(u) B_m(v) B_n(w) \phi_{i+l, b+j, c+k} \quad [2.38]$$

where

$$i = \lfloor x/n_x \rfloor - 1, j = \lfloor y/n_y \rfloor - 1, k = \lfloor z/n_z \rfloor - 1, u = x/n_x - \lfloor x/n_x \rfloor, v = y/n_y - \lfloor y/n_y \rfloor, w = z/n_z - \lfloor z/n_z \rfloor$$

and where B_l represents the l th basis function of the B-spline:

$$\begin{aligned} B_0(u) &= (1-u)^3 / 6 \\ B_1(u) &= (3u^3 - 6u^2 + 4) / 6 \\ B_2(u) &= (-3u^3 + 3u^2 + 3u + 1) / 6 \\ B_3(u) &= u^3 / 6 \end{aligned}$$

Smooth interpolation methods are used to calculate image intensities between control points. However, during the registration process an unconstrained deformation may allow for folding and tearing of the deformation field, and hence break topology. As described in Section 2.7.5, it is therefore important to regularise B-spline-based registration models to prevent matching of unrelated structures by constraining the transformation to be smooth.

Chapter 3

The Developing Brain and Preterm Birth

3.1 Brain development

The brain is the most complex organ in the body and is involved in the coordination and regulation of all other organ systems. The following section reviews the microscopic development of the brain from the first phase of cellular proliferation.

3.1.1 Microscopic development of the brain

The first of the two main phases of cellular proliferation in the developing brain occurs from around 8 to 16 weeks GA and is associated with neuronal proliferation and the generation of radial (Bergman) glia. Glial cell proliferation characterises the second phase and occurs from around 20 weeks gestational age (GA). These cells are initially produced in the ventricular zone (germinal matrix), which initially contains "progenitor" cells, which divide to produce the postmitotic neurons and glia. Subsequent gliogenesis and neurogenesis is thought to take place in the subventricular zone (Volpe, 2001), a paired brain structure adjacent to the lateral walls of the lateral ventricles. Neural progenitor proliferation in these two germinal zones is reported to be regulated by the principal inhibitory (gamma aminobutyric acid, GABA) and excitatory (glutamate) neurotransmitters (Haydar et al., 2000).

The long processes of radial glial cells form a scaffold between the ventricular zone to the pial surface, along which newly generated neurons migrate towards the margins of the cerebral hemispheres to form the cortex. The earliest formed cells accumulate at the outer margin of the cerebral hemispheres to form the preplate. The preplate is then divided into the marginal zone, at the pial surface, and the subplate. More newly formed neurons then migrate to form the cortical plate, between the marginal zone and the subplate. The inner layer of the cortex is formed before the outer layers and migrating cells pass through earlier formed layers to the margin of the cortical plate to eventually form six histologically distinct layers parallel to the cortical surface.

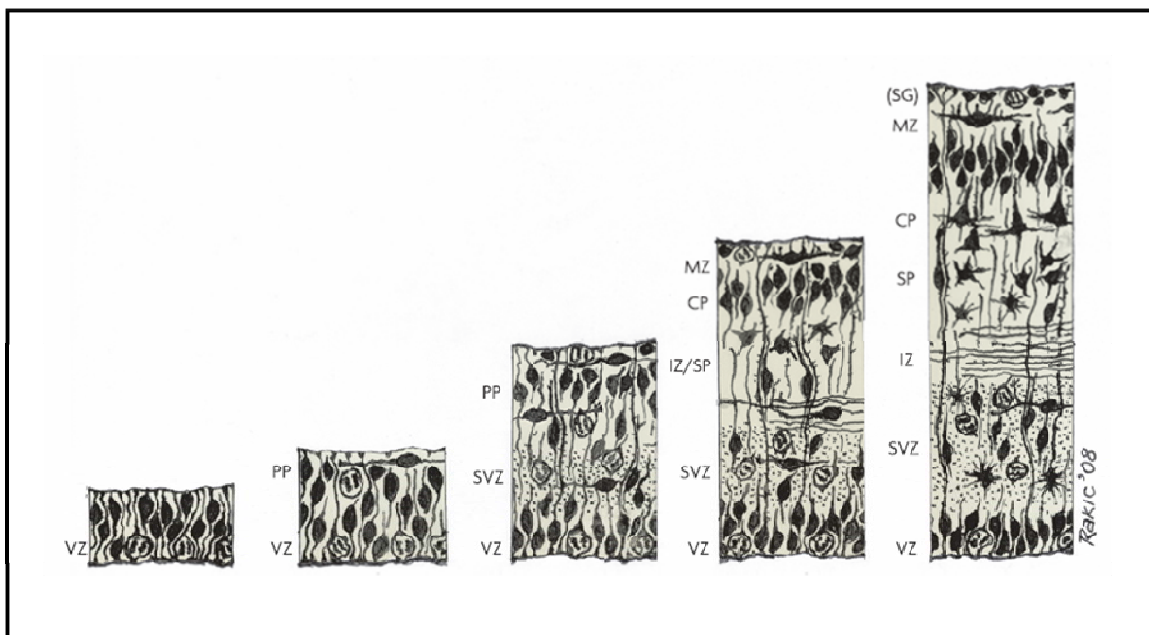


Figure 3.1: The development of the human cerebral cortex

A schematic drawing of different stages of the development of the cortex, adapted from Bystron (Bystron et al., 2008). The figure shows the embryonic cellular zones that arise during corticogenesis.

Key: CP, cortical plate; IZ, intermediate zone; MZ, marginal zone; SG, subpial granular layer (part of the marginal zone); SP, subplate; SVZ, subventricular zone; VZ, ventricular zone.

The subplate zone is a temporary layer of the cerebral wall that in humans develops at around 13 postovulatory weeks and gradually disappears after 32-34 postovulatory weeks. Neurons that form this layer travel to the marginal zone before true cortical neurons migrate to the cortical plate and are critical to cortical organization. At first they form part of the preplate zone, prior to its splitting into the subplate and marginal zones. Subplate neurons rapidly differentiate and develop a dendritic tree with spines expressing receptors for various chemical mediators, enabling them to form reciprocal connections to the thalamus and cerebrocortical sites. In this way, subplate neurones form a functional synaptic link for 'waiting' thalamo-cortical and cortico-cortical afferents, whose neuronal targets have not yet arrived at the cortical plate (reviewed in Kostovic and Jovanov-Milosevic, 2008).

The outgrowth of axons is at first mediated by the glycoproteins neural cell adhesion molecule (N-CAM) and neuronal-cadherin situated on the cell surface (Takeichi, 1988). Laminin, an extracellular matrix protein, interacts with integrins on the axonal surface to stimulate axonal extension and guide axons through the developing brain to target sites (reviewed in McKerracher et al., 1996).

Inhibitors to axonal growth found on some axonal surfaces cause axons to group together to form bundles. These in turn develop into projection fibres (transmitting impulses between the cortex and locations elsewhere in the brain), association fibres (connecting cortical regions of the same hemisphere) and commissural fibres (linking corresponding regions of the two hemispheres) (Clarke et al., 1989), many of which are subsequently pruned. Astroglial cells and macrophages are first detected between 25 and 44 weeks gestation, prior to the full myelination of these structures (Carpenter and Sutin, 1983) and may be involved in the axonal fibre tract remodelling through apoptosis and pruning (Caviness Jr, 1989).

3.1.2 Oligodendrocyte development

Oligodendrocytes are a class of glial cell whose main function in the brain is the myelination of axonal processes, which is crucial in the efficient propagation of electrical signals along the axon. They are the predominant glial cell type in the white matter of the central nervous system, and indeed their synthesis of myelin is the reason why white matter appears that colour to the naked eye.

The cells arise from the oligodendrocyte precursor (or progenitor) cells generated in the proliferative ventricular and subventricular zones during the last months of gestation and the early postnatal period (Back et al., 2002; Niehaus et al., 1999). As these cells migrate away from these germinal zones and into the white matter, they first differentiate into pre-oligodendrocytes, then post-mitotic immature oligodendrocytes and finally into mature oligodendrocytes capable of myelination.

3.1.3 Myelination

Myelination begins around the start of the second trimester of pregnancy and continues into adulthood (Gilles et al., 1983). The process begins with the proliferation of a population of glial cells which differentiate into oligodendrocytes and align along neuronal axonal projections. The plasma membranes of these oligodendrocytes become the myelin membrane (Bunge, 1968), made up of a phospholipid bilayer containing large proteins including proteolipid protein, oligodendrocyte specific protein, myelin-oligodendrocyte basic protein and myelin basic protein (Arroyo and Scherer, 2000). A flat, membranous process containing a network of microtubules and microfilaments extends outwards from the oligodendrocyte cell body and wraps around neighbouring axons in a spiral fashion. Myelin is initially laid down on the fibre closest to the oligodendrocyte cell body, but each oligodendrocyte is capable of myelinating tens of axons (Figure 3.2).

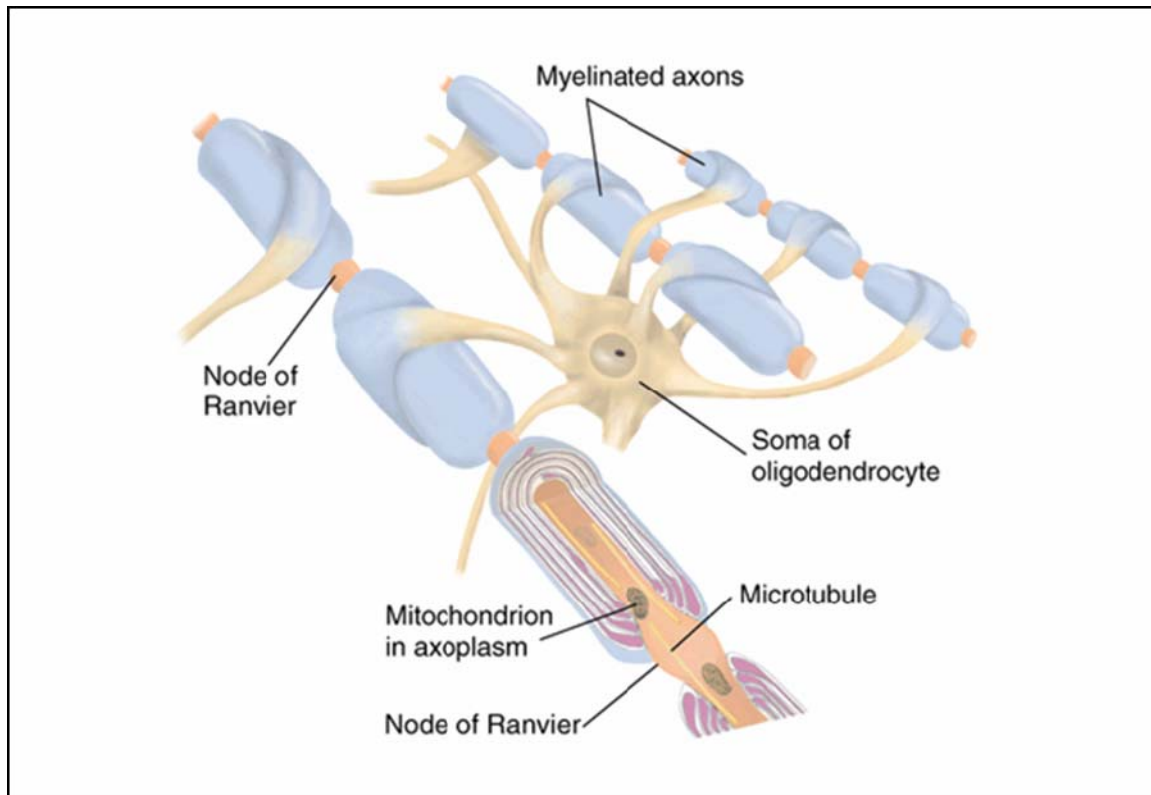


Figure 3.2: Myelination in the central nervous system (from <http://homepage.psy.utexas.edu/HomePage/class/Psy308/salinas/Cells/oligo.gif>)

A single oligodendrocyte may myelinate many axons in the central nervous system. Loss of a small number of oligodendrocytes may therefore have pronounced neurological effects due to axonal conduction deficits.

Histological studies have shown that myelination occurs in an ordered, systematic fashion. In the brain, sensory nerve root fibres myelinate before motor nerve root fibres. The first fibres to myelinate in the brain are the central fibres of the vestibular and cochlear systems of the brain stem, which are concerned with hearing, and myelination generally proceeds in a caudal-to-cranial and a posterior-to-anterior pattern (Reimer et al., 1999).

3.2 Preterm birth

3.2.1 Incidence of preterm birth

The World Health Organization defines preterm birth as birth prior to 37 completed weeks of gestation (Morrison and Rennie, 1997) and its incidence in England and Wales is rising. In 2005 preterm births made up 7.1% of all live births, up from 5.6% in 2000 (Office of National Statistics, 2005). This mirrors a trend throughout the Western world, although there is considerable variability between countries and in the USA, for example, 12.7% of births are preterm (Hamilton et al., 2006). The reasons for this are unclear, although some have argued that an increase in multiple births associated with in vitro fertilisation therapy is in part responsible (Blondel and Kaminski, 2002). Improvements in neonatal care, particularly in the use of antenatal steroids and postnatal surfactant to aid respiratory function and development, have had a dramatic impact on survival. Although outcomes vary widely across different neonatal intensive care units, around 90% of these preterm infants will survive, including over half of infants born at 26 weeks GA and a quarter born at 24 weeks GA (Levene, 2004).

3.2.2 Some clinical variables associated with preterm birth

There are numerous clinical factors, antenatal insults and events that can precipitate preterm birth (for a review, see Goldenberg et al., 2008). Here some of the most relevant causes and consequences of prematurity are reviewed.

3.2.2.1 *Preterm premature rupture of membranes*

A significant risk factor for preterm births is preterm premature rupture of membranes (preterm PROM), defined as spontaneous rupture of the amniotic sac that takes place before 37 weeks of gestation. This occurs in 3% of pregnancies and accounts for around

one third of all preterm births (Mercer, 2003). PROM is an important cause of morbidity and mortality, particularly when associated with only brief delay between membrane rupture and delivery, infection in the perinatal period or compression of the umbilical cord (Mercer, 2003).

The pathology of PROM is multifactorial, with infection and/or inflammation of the chorion and amnion thought to be important, especially if preterm rupture occurs early in gestation (Bendon et al., 1999). Skinner (Skinner et al., 1981) showed reduced collagen content in human amniotic membranes in females with PROM, and increases in amniotic fluid matrix metalloproteases with decreases in tissue inhibitors of matrix metalloproteases have been reported in this group (Vadillo-Ortega et al., 2002). Prior preterm delivery, previous cervical colonisation, uterine distension, vaginal bleeding, sexually transmitted infections and cigarette smoking have all been reported to be associated with preterm PROM (reviewed in Mercer, 2003). This is possibly due to stretching or degradation of the membranes, local inflammation or raised susceptibility to bacterial colonisation of the uterus. Although the evidence is not conclusive, it is thought by many that most cases of PROM without obvious cause are due to infection.

3.2.2.2 *Acute lung disease*

The majority of morbidity and mortality amongst infants born preterm arise as a result of respiratory complications. Following birth, the foetal route of gas exchange via the placenta is cut off, and the lungs must assume this role. However, these organs are amongst the last to mature during the prenatal stage, and infants born preterm usually have underdeveloped lungs. Acute lung disease (also called infant respiratory distress syndrome) requiring mechanical ventilation and surfactant therapy is common in this population, with an incidence of about 50% amongst those born at less than 30 weeks gestational age (Ramanathan, 2008).

At a histological level, lung abnormalities include reduced functional surface area, insufficient alveolarisation and fibrin deposition in the air spaces (Sinha et al., 2008). The

principal physiological abnormality is reduced surfactant production, leading to increased alveolar surface tension and collapse, atelectasis and decreased lung compliance. This is now treated with considerable success by antenatal steroid therapy and postnatal surfactant administration.

However the mainstay of respiratory therapy has been mechanical ventilation. Ventilation has been shown to reduce morbidity and mortality amongst infants born preterm (Birenbaum et al., 1983) but causes biotrauma to the lung tissue. This can cause long-term pulmonary insufficiency, and 30-40% of these infants develop chronic lung disease. Abnormal respiratory function and the iatrogenic consequences of treatment can lead to periods when O₂ and CO₂ levels are above or below the normal range. This may precipitate retinopathy of prematurity (Kim et al., 2004) and interfere with normal growth and development (Sinha et al., 2008).

3.2.2.3 *Chronic lung disease*

Chronic lung disease, usually defined as supplemental oxygen requirement at 36 weeks gestational age, frequently arises when the immature developing lungs of preterm-born infants are subjected to repetitive injury. This is thought to result from hypo- or hyper-inflation of the developing alveoli, leading to local inflammation and disruption of normal development. This can result in permanent reductions in alveolarisation and at least transient accumulation of fluid in the lung. Frequently, this injury arises from, or is exacerbated by, mechanical ventilation.

3.2.2.4 *Retinopathy of prematurity*

The vasculature of the retina, the light-sensitive layer at the back of the eye, is not fully developed until 36 weeks post-conception, and birth before this can result in retinopathy of prematurity (ROP). Believed to be caused by disordered vascular growth in the

postnatal period, ROP may result in retinal scarring and, in more serious cases, retinal detachment and blindness (Zin, 2001).

Incidence varies strongly with the degree of prematurity. Hussain (Hussain et al., 1999) reported that 21.3% of a group of preterm infants born at 22-36 weeks gestation had ROP of any stage, but that none of the cohort delivered after 32 weeks did. Septicaemia, acidosis, vitamin E deficiency and intraventricular haemorrhage have all been implicated in the pathogenesis of ROP (reviewed in Gilbert, 1997), but the most important additional risk factor seems to be altered oxygenation levels (Mccolm and Fleck, 2001). It is though that mechanical ventilation and/or supplementary oxygenation leads to retinal hyperoxia, which in turn causes vasoconstriction and a downregulation in vascular endothelial growth factor, resulting in obstruction of vessel growth. The period of proliferation that follows produces vessels that are at a highly increased risk of rupture. More recently, fluctuating levels of oxygenation have also been reported to raise the incidence of ROP amongst infants with a birth-weight ≤ 1500 g (York et al., 2004). Though the mechanism by which this occurs remains incompletely defined, these findings have lead to moves to try and stabilize the delivery of oxygen to preterm infants.

3.2.3 Brain injury in the preterm infant

Antenatal factors coupled with the suboptimal environment to which preterm infants are exposed after birth can affect the development of the central nervous system, and render the developing preterm brain very susceptible to injury. There may be periods of hypo/hyperoxia, hypo/hypercarbia, acidosis, hypo/hyperglycaemia, arterial hypo/hypertension, impaired cerebral venous drainage, infection and inflammation, sub-optimal nutrition, endocrine disturbance and increased noise, and preterm infants have a high risk of acquiring brain injury in the perinatal period. This may include germinal layer haemorrhage (GLH) and intraventricular haemorrhage (IVH), as well as the white

matter abnormalities of parenchymal haemorrhagic infarction and focal or diffuse periventricular leukomalacia, all of which are briefly described in the next section.

3.2.3.1 *Germinal layer haemorrhage*

The germinal matrix, the site of production of neurons and glial cells within the brain, is not fully involuted until 36 weeks gestational age. Until this time, the arterial supply to this structure, from the anterior cerebral artery, the middle cerebral artery and from the internal carotid artery are vulnerable to rupture (Takashima and Tanaka, 1978). The resultant haemorrhage may occur at any site along the immature ventricle wall, but is generally seen on ultrasound examination at the heads of the caudate nuclei. Haemorrhage is thought to initially occur into the sub-ependymal tissue, separating the ependymal layer from the neuropil; this is termed germinal layer haemorrhage (GLH). When bleeding penetrates the ependymal surface and blood enters into the ventricles it is termed intraventricular haemorrhage (IVH). GLH and IVH are the most common forms of intracranial neonatal haemorrhage, with the incidence of GLH/IVH increasing with decreasing birth weight (Volpe, 1989; Volpe, 1998). The pathogenesis of GLH/IVH is multifactorial and still unclear, but is thought to include decreases and increases in cerebral blood flow, and increases in cerebral venous pressure (Hambleton and Wigglesworth, 1976; Ment et al., 1981; Levene et al., 1982; Ment et al., 1984; Calvert et al., 1988; Bada et al., 1990).

Ventricular dilatation is frequently observed secondary to IVH, though the mechanism of injury has not been fully elucidated. Many researchers have proposed that the flow and reabsorption of cerebrospinal fluid (CSF) is blocked by blood clots that obstruct the arachnoid villi (Fawer and Levene, 1982), and it has been shown that the CSF of preterm infants contains low levels of plasminogen, a mediator of clot lysis (Whitelaw et al., 1995). Blood is also known to irritate the ependymal lining of the ventricular system causing this layer to be shed and replaced by glial tissue. This glial proliferation may itself lead to mechanical obstruction of CSF flow and cause hydrocephalus (Larroche,

1972; Fukumizu et al., 1995; Fukumizu et al., 1996), which can itself lead to periventricular white matter damage due to pressure effects. However experimental proof of these hypotheses remains elusive.

The neurological outcomes associated with GLH and IVH are variable, depending principally on haemorrhage severity, its effects on CSF drainage, and the extent and site of any parenchymal infarction (Papile et al., 1983; Resch et al., 1996; Levy et al., 1997). Haemorrhages that are confined to the germinal matrix and without the involvement of the adjacent parenchyma have good prognosis (de Vries et al., 1998). However, it is hypothesised that GLH may damage oligodendrocyte progenitors and disrupt their migration, potentially resulting in impaired myelination of axonal fibres. Furthermore, GLH may result in damage to astrocytic precursors bound for the upper layers of the cerebral cortex, and thereby lead to impaired cortical neuronal development (Evrard et al., 1992). Studies in animal models have suggested that the presence of free iron from blood in the CSF may lead to white matter damage due to increased levels of free radical formation (Batton and Nardis, 1987). As developing oligodendrocytes are particularly vulnerable to injury from free radical attack (Back et al., 1998), it is possible that haemorrhage in the CSF may play a role in white matter damage (Volpe, 2001).

3.2.3.2 *Periventricular haemorrhagic infarction*

Typically occurring in the deep white matter adjacent to the lateral ventricles, periventricular haemorrhagic infarctions (PHIs) are ischaemic parenchymal injuries with associated haemorrhage (Volpe, 1989; Barkovich, 2000). PHI develops in about 10-15% of cases of IVH, with between 80% and 90% of these developing within the first four days of postnatal life (de Vries et al., 2001). An incidence of 1% amongst infants born ≤ 2500 g has been reported, with the injury proposed to be the result of a failure of drainage of the medullary veins into the terminal vein due to a blood clot (Takashima et al., 1986; Gould et al., 1987). It is currently thought that the raised venous pressure and blood stasis that ensues causes white matter infarction. Dependent on the site and extent

of the lesion, the long-term neurological sequelae are often severe (Bassan et al., 2006; Bassan et al., 2007), with damage to the motor fibres potentially resulting in hemiplegia (Takashima et al., 1986). Survival is rare if the lesions are bilateral.

The spectrum of IVH/PHI in the preterm-born neonate has been divided into four grades (Table 3.1), dependent on severity (Papile et al., 1978).

Grade	Description
I	Germinal matrix haemorrhage without (or with minimal) IVH.
II	Bleeds extending from the subependymal germinal zone into the ventricles, but without any associated ventriculomegaly.
III	IVH with ventriculomegaly, either due to parenchymal injury or communicating hydrocephalus.
IV	White matter infarction secondary to raised venous pressure and blood stasis (PHI).

Table 3.1: The Papile classification of IVH/PHI in the premature neonate (adapted from Barkovich, 2000)

These have important prognostic value with respect to short- and long-term neurological outcomes, and are now widely used. In a follow-up study of a large cohort of infants that had ultrasound-defined IVH/PHI, 67% of infants with haemorrhage of grades I and II survived, compared to only a quarter of those infants with grade III/IV haemorrhages (van de Bor et al., 1993). Other studies have found that infants with grades I and II haemorrhage have a less than 10% incidence of neurological sequelae at six years of age (Whitaker et al., 1996), but those with IVH associated with dilated ventricles have an incidence five times greater.

3.2.3.3 *Periventricular leukomalacia*

Predominantly affecting preterm infants between 23 to 32 weeks gestation, a period where oligodendrocyte precursors are particularly vulnerable to damage from hypoxia-ischaemia (Volpe, 1998), free radical mediated injury (Back et al., 1998; Fern and Moller, 2000; Back et al., 2001) and materno-foetal infection (Dammann and Leviton, 1999), periventricular leukomalacia (PVL) has been classically defined as focal necrotic lesions in the developing cerebral white matter that subsequently progress to the formation of cysts (Banker and Larroche, 1962; Volpe, 2003). First described in 1962, this 'cystic' form of PVL usually illustrated bilateral lesions that were found within the frontal and parietal-occipital periventricular white matter, adjacent to the anterior and posterior horns of the lateral ventricles (DeReuck et al., 1972; Shuman and Selednik, 1980; Leviton and Gilles, 1984; Back et al., 2007). The clinical outcome of this may be cerebral palsy, with the more extensive the abnormalities observed on ultrasound, the greater the risk of severe motor (and cognitive) deficits (Holling and Leviton, 1999).

Recent studies, however, suggest that the incidence of cystic PVL amongst infants born preterm or with a low birth weight is rapidly diminishing. Adjusting for gestational age, Hamrick (Hamrick et al., 2004) found that amongst preterm infants born with a birth weight ≤ 1500 g, the ultrasound-defined incidence of cystic PVL declined 6.1 fold between 1992-2002, to 0.2% of all births between 2000-2002. However, there has been a corresponding increase in cases of a more diffuse form of white matter change reported amongst these infants, which has been described as non-cystic PVL or diffuse white matter injury (Maalouf et al., 1999; Counsell et al., 2003a; Inder et al., 2003). Maalouf (Maalouf et al., 1999) reported that the MR neuroimaging correlate of this change, diffuse excessive high signal intensity on conventional T2-weighted imaging, is present in 75% of all preterm infants imaged at term, which has characteristics compatible with widespread axonal and/or oligodendrocyte abnormality on diffusion weighted imaging (Counsell et al., 2006).

Several potential mechanisms have been proposed for the pathogenesis of PVL during this period of glial proliferation, differentiation and myelination (Goldman, 1992). PVL occurs in areas that were thought to represent arterial border zones between main areas of

arterial supply (Perlman, 1998), and the anatomy of the vascular supply to the white matter may be an important factor. Blood flow to the cerebral white matter is low at this stage of development (Borch et al., 1998) and blood vessel density in the white matter is lower between 28 and 36 weeks than in earlier or later periods of development (Miyawaki et al., 1998). Prolonged hypoperfusion potentially exposes these areas to severe ischaemia and there is evidence of prolonged loss of cerebrovascular autoregulation following asphyxia, which may exacerbate the fact that autoregulatory control mechanisms within the cerebral vasculature may be immature. This may leave the preterm brain vulnerable to fluctuations in blood pressure and blood flow (Volpe, 2001).

When neurons or their processes are damaged by hypoxic-ischaemic injury, the excitatory neurotransmitter glutamate is released in large quantities and additional factors may lead to the presence of excitotoxic free-radicals such as reactive oxygen and nitrogen species (Back et al., 1998; Laszkiewicz et al., 1999). With their increased metabolic demand, cells that are actively differentiating may be more sensitive to this profound change in the internal milieu. Pre-myelinating oligodendrocytes, which are present in the periventricular white matter in the third trimester are known to have glutamate receptors and may thus be damaged by toxic amounts in a similar way to neurons (Kinney and Back, 1998; McDonald et al., 1998).

Traditionally, PVL was thought to only result from ischaemic causes. However, infection, which has independently been reported as a risk factor for preterm birth (reviewed in Goldenberg et al., 2000) can cause elevation of pro-inflammatory cytokines that may also mediate white matter damage (Dammann and Leviton, 1999). Chorioamnionitis has been associated with damage to the developing white matter and is associated with increased risk of cystic PVL lesions (Wu, 2002).

3.2.4 Neurodevelopmental outcomes associated with preterm birth

Despite difficulties in teasing out which of the antecedents to, or associations with, preterm birth render the developing brain vulnerable to injury, it has been shown that neurological morbidity is more severe with prolonged premature exposure to the extrauterine environment (Marlow et al., 2005) and more severe in boys than in girls (Wood et al., 2005). The section reviews some of the motor, cognitive and behavioural outcomes associated with preterm birth.

3.2.4.1 *Motor outcomes*

Motor difficulties following preterm delivery have been widely reported in the literature. Amongst preterm infants born weighing less than 1000g, between 4-12% have been reported to develop cerebral palsy (CP) (reviewed in Behrman and Stith Butler, 2006). The relationship between preterm birth and CP has been shown to be inversely related to gestational age (Drummond and Colver, 2002), with male infants at particular risk of adverse motor outcome (Wood et al., 2005).

Chronic lung disease and postnatal corticosteroid delivery are more common amongst extremely preterm-born infants, and have also been independently shown to increase the risk of CP (Skidmore et al., 1990; Shinwell et al., 2000).

3.2.4.2 *Sensory outcomes*

Compared to a group of age- and gender-matched controls, extremely preterm-born infants are at an increased risk of sensorineural hearing loss and visual impairment/blindness at school age (Marlow et al., 2005).

3.2.4.3 *Cognitive and behavioural outcomes*

There have been many studies reporting a reduction in general intelligence quotient (IQ) and its verbal and performance subscales amongst preterm-born infants compared to matched term-born control subjects (Botting et al., 1998; Saigal et al., 1991; Bhutta et al., 2002; Anderson and Doyle, 2003). Small population sizes, different ages at assessment and different assessment criteria have made such studies difficult to compare, and the effects of recent clinical practice on cognitive outcome has been difficult to fully evaluate. In a meta-analysis of the data from fifteen studies containing 1556 preterm infants and 1720 term-control infants, however, preterm-birth was associated with an eleven-point reduction in cognitive score (95% confidence interval 9.5-12.5), with the reduction directly proportional to birth-weight and GA (Bhutta et al., 2002). In a more recent study of all infants born in the UK and Ireland at less than 25 weeks of completed gestation, IQ scores at school age were found to be 24 (95% confidence interval 20-27) points lower than matched controls (Marlow et al., 2005). Scores were positively correlated with GA, and were found to be lower amongst boys than girls. As many as 52% of these children will require some form of special needs or educational support because of learning difficulties (Rivkin, 2000). Impairments often continue into adolescence, with a high prevalence of behavioural problems documented, including psychiatric and attention deficit disorders (Szatmari et al., 1990; Botting et al., 1997; Indredavik et al., 2005; Nosarti et al., 2005).

These problems were initially thought to be due to damage to the corpus callosum resulting in an inadequate transfer of information between the cerebral hemispheres. However, the broad spectrum of reported problems related to preterm birth suggests that a diffuse injury or one that affects a central processing structure is more likely. The neuro-imaging correlates for these developmental impairments remain incompletely defined.

3.3 MRI of the developing brain

The inherent sensitivity of MRI to changes in water content and the biochemical environment make it an ideal modality to investigate the developing brain, allowing the differentiation of the cortex, white matter and central grey matter structures (Battin et al., 1998). As can be seen on conventional MRI, the sulci and gyri of the cortex develop at different rates in different regions of the brain (Figure 3.3). Prior to term, the folding of the central sulcus is the most advanced at any given age, followed by the main sulci in medial occipital lobe, the parietal lobe, the frontal and the posterior temporal lobes in that order. The anterior temporal region is the least well developed. By term the cortex has extensive folding with the formation of tertiary sulci.

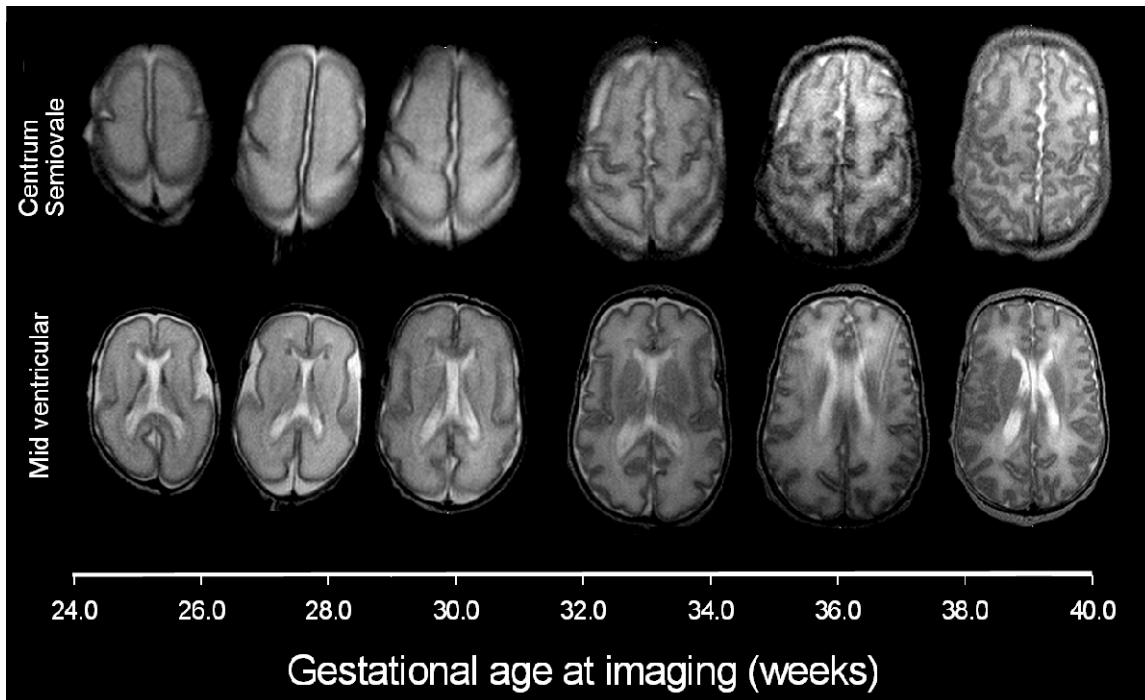


Figure 3.3: Preterm brain development assessed with MRI (adapted from Counsell et al., 2003b)

These transverse T2-weighted images were taken of a preterm infant born at 23 weeks gestation and scanned serially between 25 weeks and 39 weeks gestational age. They show the normal development of sulcation and gyration during this time at the level of the centrum semiovale (top row) and the mid-ventricular level (bottom row).

3.3.1 MRI and myelination

Unmyelinated cerebral white matter is demonstrated as high signal intensity on T2-weighted imaging and low signal on T1-weighted imaging. This is due to the fact that the developing brain has higher water content and so both T1 and T2 are longer than in the more mature brain. As white matter structures myelinate their appearance on MRI changes, due to an increase in the lipid content and a relative decrease in water content. Myelinated white matter is seen as regions of high signal intensity on T1-weighted imaging and low signal intensity on T2-weighted imaging (Barkovich, 2000). The hypointense appearance of myelin on T2-weighted images corresponds to the time of tightening of myelin around the axon and the saturation of polyunsaturated fatty acids within the myelin membrane (Barkovich et al., 1988; Husted et al., 1993). The reduction in signal intensity on T2-weighted imaging is probably due to a reduction in the number of aqueous protons due to the development of the hydrophobic inner phospholipid layer (Barkovich et al., 1988).

3.3.1.1 MRI appearances of myelination

Myelin has been demonstrated by in vivo MRI in numerous white matter tracts and grey matter nuclei in the preterm brain, corresponding to those sites that demonstrate myelination on histology at this age. However, brain maturational changes corresponding to myelination are detected at different rates and different times on conventional T1 and T2-weighted images, the reasons for which remain ill-defined. Table 3.2 shows the ages at which changes of myelination first appear on conventional imaging (data from Barkovich et al., 1988; Barkovich, 2000; Counsell et al., 2002).

Anatomical region	T1-weighted images	T2-weighted images
Superior cerebellar peduncle	28 gest wks	27 gest wks
Median longitudinal fasciculus	25 gest wks	29 gest wks
Medial lemnisci	27 gest wks	30 gest wks
Lateral lemnisci	26 gest wks	27 gest wks
Middle cerebellar peduncle	Birth	Birth to 2 mos
Cerebral white matter	Birth to 4 mos	3-5 mos
Posterior limb internal capsule		
Anterior portion	First month	4-7 mos
Posterior portion	36 gest wks	40 gest wks
Anterior limb internal capsule	2-3 mos	7-11 mos
Genu corpus callosum	4-6 mos	5-8 mos
Splenium corpus callosum	3-4 mos	4-6 mos
Occipital white matter		
Central	3-5 mos	9-14 mos
Subcortical	4-7 mos	11-15 mos
Frontal white matter		
Central	3-6 mos	11-16 mos
Subcortical	7-11 mos	14-18 mos
Centrum semiovale	2-4 mos	7-11 mos

Table 3.2: Age-associated changes in myelin appearance on MRI (from Barkovich, 2005)

Key: gest wks, gestational weeks; mos, months

3.3.2 Diffusion weighted imaging and diffusion tensor imaging of the developing brain

3.3.2.1 *White matter changes*

ADC values and diffusion anisotropy measures in the developing brain change with age. Cerebral white matter ADC values decrease with increasing maturity, with those of preterm infants being higher than term infants, which are in turn elevated compared to those of adults (Toft et al., 1996; Huppi et al., 1998; Neil et al., 1998; Morriss et al., 1999; Tanner et al., 2000; Mukherjee et al., 2001; Mukherjee et al., 2002; Schneider et al., 2004). In addition, ADC values are higher in white matter than grey matter in neonates, and these values converge with increasing maturity (Neil et al., 1998; Tanner et al., 2000). Anisotropic measures of diffusion increase in the white matter with increasing gestational age (Huppi et al., 1998; Neil et al., 1998; Mukherjee et al., 2001; Mukherjee et al., 2002; Schneider et al., 2004) and it has been shown that changes in anisotropy with development are predominantly due increasing restriction of diffusion perpendicular to the local white matter tract direction (Suzuki et al., 2003; Partridge et al., 2004).

The level of anisotropy in the cerebral white matter is affected by both microscopic factors (the degree of myelination) and macroscopic factors (the density and coherency of fibre tracts). However, anisotropic diffusion is observed in the corpus callosum, posterior limb of the internal capsule and optic radiations in the preterm brain before myelination has occurred in these structures (Toft et al., 1996; Tanner et al., 2000). In the rat brain, DWI reveals anisotropic diffusion in white matter before myelin is evident either histologically or on conventional MRI (Wimberger et al., 1995), thought to be due to premyelination processes including an increase in axon diameter (Hildebrand and Waxman, 1984), axonal membrane changes (Fields and Waxman, 1988) and early oligodendroglial wrapping around axons (Remahl and Hildebrand, 1990). This is associated with an increase in the concentration of microtubule-associated proteins, which may restrict water motion perpendicular to axons (Watson, 1991).

These findings suggest that there is an increase in white matter anisotropy immediately preceding the beginning of myelination. More gradual increases over many months or years follow as myelin matures. Quantitative anisotropy measurements may therefore provide a marker for white matter development and be sensitive to forms of white matter injury associated with preterm birth that disrupt myelination (Neil et al., 1998).

3.3.2.3 *Grey matter changes*

As well as being used to investigate white matter development, diffusion MRI has also been used to study developmental changes in cortical grey matter. At the resolution offered by MRI, anisotropy has been shown to decrease from 26 to 32 weeks GA until diffusion is almost isotropic, as it is in adult grey matter (McKinstry et al., 2002). Prior to 32 weeks GA, cortical cytoarchitecture is dominated by radial glia and apical dendrites, which are perpendicular to the cortical layers, resulting in non-zero anisotropy. Once the basal dendrites and thalamocortical afferent fibres reach the cortex, however, the resulting multi directional arrangement of fibres leads to an overall reduction of anisotropy.

3.3.3 MRI of diffuse white matter injury

Numerous studies have documented the value of MRI in discriminating focal perinatal brain injury following preterm birth (for reviews, see Counsell et al., 2003b; O'Shea et al., 2005; Boardman et al., 2007). More recently, conventional MRI has demonstrated diffuse white matter abnormality in the majority of preterm infants at term equivalent age that is significantly more common than focal injury. In one study, around 75% of preterm infants at term were found to have areas of diffuse excessive high signal intensity (DEHSI) within the white matter on T2-weighted MRI (Figure 3.4), with a correspondingly low signal on T1-weighted imaging (Maalouf et al., 1999). It has been suggested that DEHSI may be the neuro-imaging correlate of diffuse PVL or telencephalic leukoencephalopathy (Volpe, 2003), and a diffusion weighted imaging

study has shown that apparent diffusion coefficient values are significantly higher amongst infants with DEHSI than infants with normal appearing white matter, and are similar to those with overt white matter pathology (Counsell et al., 2003a).

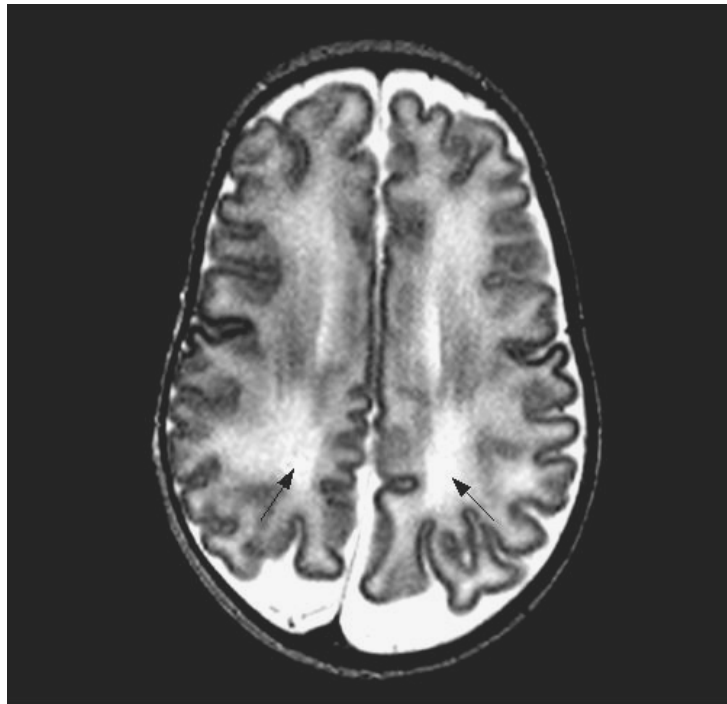


Figure 3.4: Diffuse excessive high signal intensity (DEHSI)

DEHSI can be seen in this transverse T2-weighted image at the level of the centrum semiovale in the posterior white matter (arrows).

3.3.4 Quantitative MR studies of brain development and pathology in preterm infants

Quantitative MR techniques can be used in addition to qualitative evaluation of MRI data to investigate development and pathology in the preterm brain. These techniques produce objective and reproducible measurements of brain growth and include measures of cortical folding, brain volumes, T1 and T2 relaxation measures and brain water diffusion parameters.

Computerised methods of measuring the cortex have shown a logarithmic increase in brain volume, cortical surface area and the complexity of cortical folding from 24 weeks GA until term (Ajayi-Obe et al., 2000). However, the normal scaling relation between cortical surface area and cerebral brain volume during the perinatal period is disrupted amongst infants born preterm, which is related to the degree of prematurity at birth and is more pronounced amongst males than females (Kapellou et al., 2006). The level of disruption to the scaling relation correlates with neurological outcome at two years, suggesting that this measure may be used as a neuro-imaging substrate for impairment following preterm birth.

Tissue segmentation methods have been used to quantify regional reductions in brain tissue volume that predict poor neurodevelopment. Preterm infants at term equivalent age have reduced parieto-occipital, sensorimotor and inferior occipital cortices and increased lateral ventricle volumes, and white matter volumes in the sensorimotor and midtemporal regions in these infants correlated with early neurodevelopmental assessment scores (Peterson et al., 2003). Using deformation based morphometry, a technique that identifies macroscopic anatomical differences between subjects by aligning their data and analysing the parameters describing the estimated nonlinear transformations, Boardman demonstrated reductions in thalamic and lenticular volumes that were correlated with the degree of prematurity at birth (Boardman et al., 2006).

Three dimensional volumetric MRI has revealed reduced cortical grey matter volume in preterm infants at term equivalent age that had cystic PVL on previous ultrasound or MRI scans. This suggests that cystic PVL has an impact on cerebral cortical development that may explain the cognitive deficits associated with this condition (Inder et al., 1999). MRI studies have also shown that the thalami (Lin et al., 2001), corpus callosum, pons and cerebellum (Argyropoulou et al., 2003) are smaller in infants with these lesions compared to controls.

Structural differences in the brains of survivors of preterm birth persist into adolescence. Hippocampal volume reductions (Abernethy et al., 2002; Nosarti et al., 2002), increased lateral ventricle volumes (Stewart et al., 1999; Nosarti et al., 2002), reduced cerebellar volume (Allin et al., 2001), diminished volume of the caudate nucleus (Abernethy et al., 2002) and thinning of the corpus callosum (Cooke and Abernethy, 1999; Stewart et al., 1999) have been identified. However, reduced global brain growth in the neonatal period is not inevitable after premature birth, and in the absence of chronic disease or factors continuing beyond the perinatal period early brain growth is preserved in the majority of preterm-born infants (Boardman et al., 2007).

Elevated ADC values (Counsell et al., 2003a) and diminished RA values in white matter (Huppi et al., 2001) have been reported to be associated with abnormal white matter at term equivalent age. Compared to those with normal-appearing white matter, preterm infants with evidence of white matter injury have been reported to fail to demonstrate the normal maturational decrease in ADC near-term age (Miller et al., 2002), and it has recently been shown that elevated mean ADC values at the level of the centrum semiovale in preterm infants imaged at term are associated with reduced developmental quotient scores at two years corrected age (Krishnan et al., 2007).

3.4 Conclusions

In conclusion, there is increasing evidence that brain development following preterm birth may be altered, and in particular that preterm birth may be associated with subtle differences of cerebral white matter. This is thought to be the neuropathological substrate for the subsequent neurocognitive impairment that such infants are known to be at increased risk from.

The value of conventional MRI in discriminating focal perinatal brain injury following preterm birth is clear, and diffusion-weighted and diffusion-tensor MRI may allow the additional detection of abnormalities not seen on T1- and T2-weighted images. However, the observer-independent analysis of diffusion-derived MRI data has been hampered by the lack of a robust algorithm for aligning such images to enable automated analysis on a voxel-by-voxel basis. The use of such a tool would also aid the investigation of the association between certain clinical variables or events and measures of diffusion in different parts of the brain. Ultimately, this might be used to predict which preterm infants may be particularly susceptible to brain injury in the perinatal period, and therefore may be at increased risk of subsequent functional deficit. If found to be valid and robust, this approach may also allow assessment of the success of therapeutic interventions in altering brain microstructure.

3.5 Aims

The aims of this work were to:

1. Determine if TBSS, a newly proposed method for aligning diffusion-derived fractional anisotropy maps to allow subsequent groupwise comparisons of DTI data could be implemented in the preterm population;
2. Test the hypothesis that preterm infants have microstructural differences in cerebral white matter compared to term born control infants in the absence of focal abnormalities such as cystic periventricular leukomalacia or haemorrhagic parenchymal infarction on conventional MR imaging;
3. Investigate the association between both acute respiratory distress at birth and chronic lung disease and cerebral white matter in preterm infants imaged at term, and

4. Develop a method which will allow non-subjective cross-subject comparisons of whole brain DTI data, without the need to perform the data reduction processes entailed in both TBSS and ROI approaches.

Chapter 4

The Effect of Preterm Birth on Fractional Anisotropy at Term

4.1 Introduction

As described in Section 3.3.3, there is evidence that early brain development following preterm birth may be associated with subtle abnormalities of cerebral white matter compared to matched term-control subjects, which can appear as diffuse increased high signal on T2-weighted images or increases in the apparent diffusion coefficient on diffusion weighted imaging in the absence of focal lesions on conventional MRI (Counsell et al., 2003a).

Regions of interest (ROIs) can be drawn directly onto unregistered diffusion tensor images to measure diffusion parameters in different areas of the brain and have revealed differences in white matter microstructure between preterm infants at term and matched term-born control subjects. However, the complex global spatiotemporal changes occurring in the developing neonatal brain cannot be fully captured by such analyses. Tract based spatial statistics (TBSS), outlined in Section 2.7.8.3, is an automated observer independent approach for aligning diffusion-derived fractional anisotropy data, which is considered to provide a measure of white matter integrity, in order to objectively

assess group-wise microstructural differences in the major white matter pathways of the brain (Smith et al., 2006).

4.2 Aim

The aim of this study was to determine if TBSS could be implemented in the preterm population, and to test the hypothesis that preterm infants have microstructural differences in cerebral white matter compared to term born control infants in the absence of focal abnormalities such as cystic periventricular leukomalacia (cPVL) or haemorrhagic parenchymal infarction (HPI) on conventional MR imaging.

4.3 Materials and methods

The MRI data used in this study were acquired by other researchers as part of a number of ongoing studies at Hammersmith Hospital. Ethical permission was granted by the Hammersmith Hospital Research Ethics Committee (2003/6564 and 04/Q0406/125). Written, informed parental consent was obtained for each subject.

4.3.1 Subjects

4.3.1.1 *Preterm infants*

DTI data was acquired from 26 preterm infants (11 female, 15 male) imaged at term equivalent age. The median (range) gestational age of the infants at birth was $28^{+6.5}$ (25^{+4} – 32^{+4}) weeks, and the median birth weight was 1084 (654 - 1848) grams. The median

post-menstrual age at the time of imaging was 41^{+2} ($38^{+1} - 45^{+2}$) weeks. The median weight and head circumference at the time of imaging were 3200 (1980 - 5500) grams and 36.0 (31.5 - 39.6) centimetres respectively.

4.3.1.2 *Extremely preterm infants*

In the subgroup of 11 preterm infants (4 female, 7 male) who were born at 28 weeks gestation or less, the median (range) gestational age of the infants at birth was 26^{+5} ($25^{+5} - 28^{+0}$) weeks, and the median birth weight was 920 (714 - 1200) grams. The median post-menstrual age at the time of imaging was 41^{+0} ($38^{+1} - 44^{+0}$) weeks. The median weight and head circumference at the time of imaging were 3060 (2000 - 3685) grams and 35.5 (31.5 - 38.7) centimetres respectively.

4.3.1.3 *Term control infants*

DTI was also obtained on 6 healthy, term-born control infants (2 female, 4 male). The median (range) gestational age of the infants at birth was 39^{+5} ($39^{+0} - 40^{+5}$) weeks, and the median birth weight was 3300 (3106 - 4000) grams. The median post-menstrual age at the time of imaging was 41^{+5} ($41^{+0} - 46^{+0}$) weeks. The median weight and head circumference at the time of imaging were 3500 (3300 - 4510) grams and 36 (34.0 - 37.8) centimetres respectively.

There were no significant differences in age at scanning ($p = 0.24$) or in gender ($p = 0.53$) between the preterm-born group and the term-born controls. There were no significant differences in age at scanning ($p = 0.14$) or in gender ($p = 0.47$) between the subset of preterm infants born ≤ 28 weeks gestational age and term-born control infants.

4.3.2 Magnetic resonance imaging

MRI was performed on a Philips Achieva 3 Tesla system (Philips Medical Systems; Best, the Netherlands) with a maximum gradient strength of 80 mT/m and a slew rate of 200 mT/m/ms. A six-channel phased array head coil was used and each subject's head was immobilised using a pillow filled with polystyrene beads, from which the air had been removed. Ear protection was used for each infant, comprising both earplugs individually moulded from a silicone-based putty (President Putty; Coltene/Whaledent, Mahwah, New Jersey, USA) placed in the external ear and commercially available neonatal earmuffs (Natus MiniMuffs; Natus Medical Inc, San Carlos, California, USA).

The preterm infants were scanned following sedation with oral chloral hydrate (25-50 mg/kg). Term-born controls were imaged during natural sleep following feeding and were not sedated. All examinations were supervised by a paediatrician experienced in MRI procedures, and pulse oximetry and electrocardiograph monitoring were performed on all infants throughout the MRI examination.

4.3.2.1 *Diffusion tensor imaging*

A volume shim was performed prior to obtaining the DTI data in order to minimise distortions from magnetic field inhomogeneities due to air-bone-tissue interfaces. Following a reference image obtained with a minimal b value (~ 0 s/mm²), whole-brain single shot echo planar DTI data was acquired in the transverse plane in 15 non-collinear directions using the following parameters: TR 8000 ms, TE 79 ms, slice thickness 2 mm, field of view 224 mm, matrix 128 x 128 (voxel size = 1.75 x 1.75 x 2 mm³), b value = 750 s/mm². Depending on head size, between 36 and 49 slices were obtained to ensure full brain coverage. The data were acquired with a sensitivity encoding (SENSE) factor of 2 and the scanning time for this sequence was approximately 5 minutes.

4.3.3 Image processing and analysis

Data was transferred off-line and the diffusion weighted images were registered to the $b = 0$ image by affine transformations using the Philips Research Integrated Development Environment (PRIDE) Diffusion Registration tool (Release 0.4). Scanner data was then converted into analyze file format using Johns Hopkins University's DTI Studio (version 2.1) software (Jiang et al., 2006).

Images were brain-extracted using BET (Smith, 2002), part of the FSL package (Smith et al., 2004) on a Linux operating system. Fractional anisotropy, λ_1 , λ_2 and λ_3 maps were generated using FDT (Behrens et al., 2003).

Voxelwise statistical analysis was carried out using TBSS v1.0 (introduced in section 2.7.8.3) implemented in FSL (Smith et al., 2006). First of all, each subject's FA data was registered to every other subject's FA data using an affine (3 resolution levels, 64 bins, 20 iterations, 4 steps, 5 mm step length, similarity measure = cross correlation, initial control point spacing $20 \times 20 \times 20 \text{ mm}^3$) followed by a nonlinear (1 resolution level, 64 bins, 20 iterations, 4 steps, 5 mm step length, similarity measure = cross correlation, control point spacing $20 \times 20 \times 20 \text{ mm}^3$) registration algorithm (wwwhomes.doc.ic.ac.uk/~dr/software) based on Basis-splines (B-splines). For all of the registrations to a particular infant's diffusion space, the average (median) amount of nonlinear warping required to transform the other datasets into that target space was calculated. The 'most typical' subject was then defined as the one requiring the least amount of warping to align all the other images to it. All subjects' FA data was then aligned to this common space and resampled to produce $1 \times 1 \times 1 \text{ mm}^3$ voxels to generate a mean FA image with isotropic voxel dimensions. This was then thinned using non-maximal suppression perpendicular to the local tract orientation to generate a mean FA skeleton representing the centres of all tracts common to the group. The skeleton was thresholded to $\text{FA} \geq 0.20$ to include the major white matter pathways but exclude peripheral tracts where there was significant inter-subject variability and/or partial volume effects with grey matter. Each subject's aligned FA data was then projected onto

this skeleton to generate a four-dimensional image (the three-dimensional FA skeleton data for each subject in the cohort) and the resulting data was fed into voxelwise cross-subject statistical analysis. TBSS pre-processing was also applied to the λ_1 , λ_2 and λ_3 maps.

4.3.4 Statistical considerations

The permutation-based non-parametric inference approach incorporated in FSL's Randomise tool (Nichols and Holmes, 2002) was used to analyse the data. This allowed for inference of the statistic maps given that for each voxel in the dataset, the cross-subject null distribution of FA values was not necessarily Gaussian. Voxel t-values were tested against the null distribution (generated by 5000 random permutations of subject ordering with respect to the model) of maximum values of each of the test statistics. This allowed for control of family-wise errors whilst searching over the whole skeleton for regions of significant FA differences between the preterm and the term-born groups.

ROI-based analysis was performed in areas of the brain where uncorrected voxelwise cross-subject statistics revealed significantly different FA values between the preterm-born group and term-born control infants. The mask for each ROI was generated on each subject's FA map that had been aligned and projected onto the mean FA skeleton, allowing inclusion in the analysis of only those voxels from tract centres. The same ROIs were also positioned on the aligned λ_1 , λ_2 and λ_3 maps. Regional differences between term controls and preterm infants, and between term controls and the subgroup of preterm infants who were born ≤ 28 weeks GA, were tested for significance using a Student's t-test or Mann-Whitney U test as appropriate, with a Bonferroni correction for multiple comparisons. FA values in the left and right posterior portions of the posterior limbs of the internal capsule were significantly different and so these regions were analysed separately.

4.4 Results

4.4.1 Voxelwise thresholding

Regions within the centrum semiovale, frontal white matter and the genu of the corpus callosum were found to have a significantly lower FA in preterm infants imaged at term equivalent age compared to term-born controls (cluster-based thresholding fully corrected for multiple comparisons, cluster-size = 3, $p < 0.05$) (Figure 4.1a-d). Those infants born at less than or equal to 28 weeks gestational age ($n = 11$) displayed additional reductions in FA in the posterior aspect of the posterior limb of the internal capsule, the external capsule and the isthmus and middle portion of the body of the corpus callosum, and had larger regions of reduced anisotropy within the centrum semiovale, frontal white matter and genu of the corpus callosum (Figure 4.1e-h).

In order to explore this reduction in FA, the three eigenvalues of the diffusion tensor were analysed. Regions which exhibited decreased FA showed elevated intermediate (λ_2) and/or minor (λ_3) eigenvalues in both preterm groups (cluster-based thresholding (cluster-size = 3, $p < 0.05$) (Figure 4.3 and 4.4). The preterm groups also displayed an increase in the principal eigenvalue (λ_1) in the regions of the frontal white matter and genu of the corpus callosum (Figure 4.2). A small number of isolated voxels showed higher FA and/or decreased λ_1 , λ_2 or λ_3 in the preterm infants (seen in red on Figure 4.1 and blue in Figures 4.2-4.4). However, these did not correspond to any well-defined brain region.

Re-grouping the preterm infants for analysis by sex revealed no gender-related differences in FA, λ_1 , λ_2 or λ_3 in any brain regions.

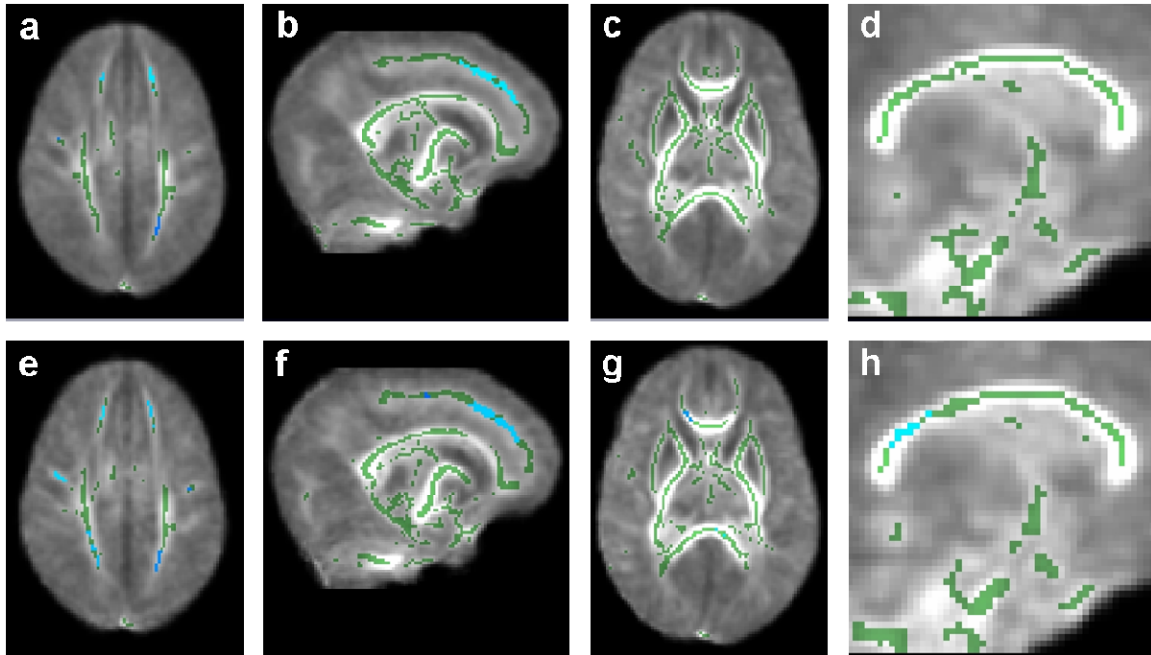


Figure 4.1: The effect of preterm birth on FA at term equivalent age

Mean FA skeleton overlaid on the mean FA map. Regions of the mean FA skeleton in green represent areas where there were no significant differences in FA values in the preterm infants imaged at term compared to the term-born controls. Areas in blue are regions where the FA was significantly lower in the preterm group (a-d), and can be observed in the centrum semiovale (a), frontal white matter (b) and genu of the corpus callosum (c). Those infants born ≤ 28 weeks gestational age (e-h) had greater regions of reduced anisotropy within the centrum semiovale (e), frontal white matter (f) and genu of the corpus callosum (g). Voxelwise cross-subject statistics uncorrected for multiple comparisons ($t > 3$, $p < 0.05$) displayed additional reductions in FA in the posterior aspect of the posterior limb of the internal capsule and the external capsule. These areas of FA difference were used for subsequent ROI-based analyses of TBSS-processed FA data (Table 4.1 and 4.2).

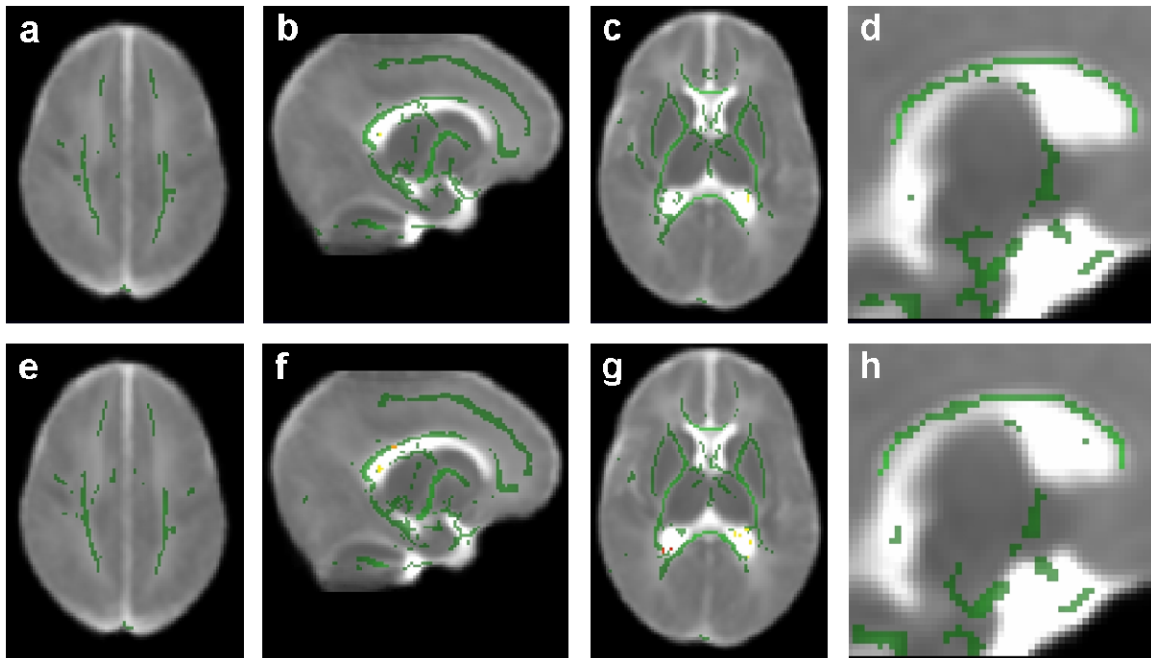


Figure 4.2: The effect of preterm birth on λ_1 at term equivalent age

Mean FA skeleton overlaid on the mean λ_1 map. Regions in green represent areas where there was no significant difference in λ_1 values in the preterm infants imaged at term (a-d) and in the subset of infants born ≤ 28 weeks gestational age (e-h) compared to the term-born controls. Areas in red are regions where the λ_1 was significantly higher in the preterm group following cluster-based multiple comparison correction (cluster-size = 3, $p < 0.05$).

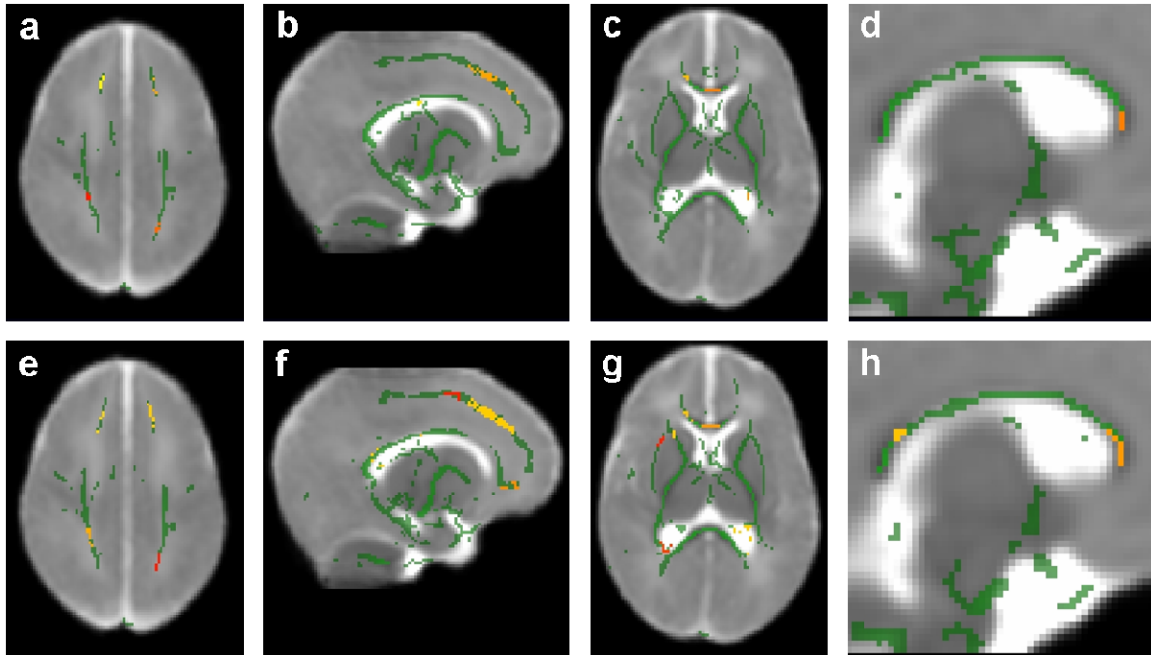


Figure 4.3: The effect of preterm birth on λ_2 at term equivalent age

Mean FA skeleton overlaid on the mean λ_2 map. Regions in green represent areas where there was no significant difference in λ_2 values in the preterm infants imaged at term (a-d) and in the subset of infants born ≤ 28 weeks gestational age (e-h) compared to the term-born controls. Areas in red/orange represent regions where the λ_2 was significantly higher in the preterm group (cluster-size = 3, $p < 0.05$), and can be observed in the centrum semiovale (a), frontal white matter (b) and genu of the corpus callosum (c). Those infants born ≤ 28 weeks gestational age (e-h) had greater regions of increased λ_2 within the centrum semiovale (e), frontal white matter (f) and genu of the corpus callosum (h, i), and displayed additional increases in λ_2 in the posterior aspect of the posterior limb of the internal capsule (g), external capsule (g) and the isthmus of the corpus callosum (h).

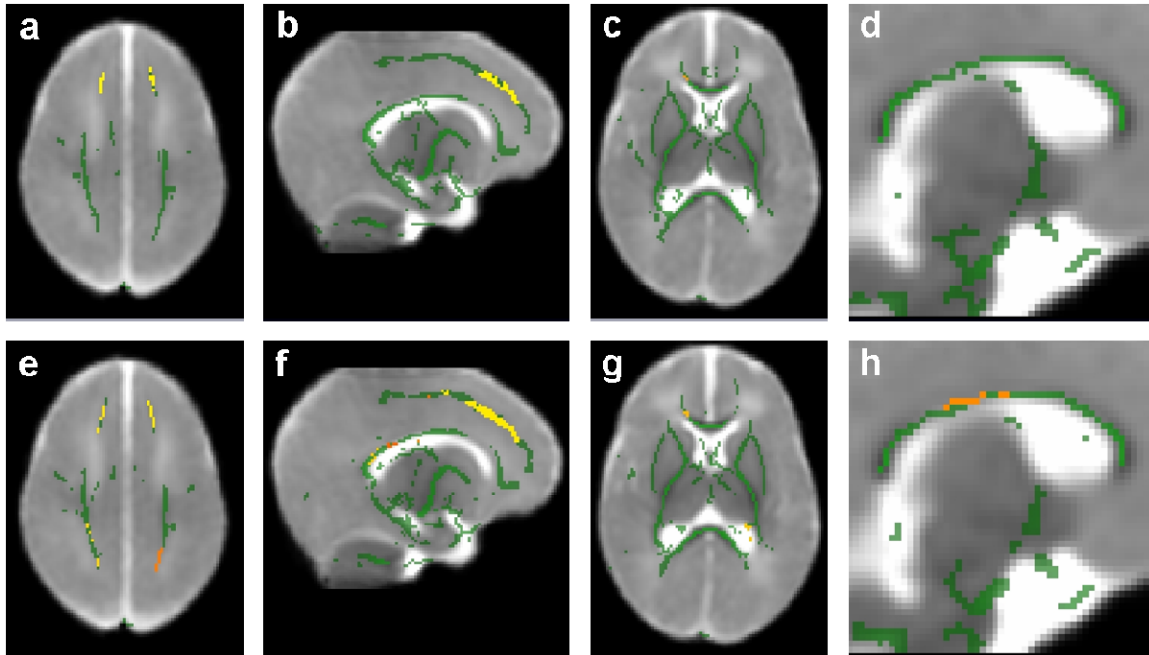


Figure 4.4: The effect of preterm birth on λ_3 at term equivalent age

Mean FA skeleton overlaid on the mean λ_3 map. Regions in green represent areas where there was no significant difference in λ_3 values in the preterm infants imaged at term (a-d) and in the subset of infants born ≤ 28 weeks gestational age (e-h) compared to the term-born controls. Areas in red/orange/yellow represent regions where the λ_3 was significantly higher in the preterm group (cluster-size = 3, $p < 0.05$), and can be observed in the centrum semiovale (a), frontal white matter (b), and genu of the corpus callosum (c). Infants born ≤ 28 weeks gestational age (e-h) had greater regions of increased λ_3 within the centrum semiovale (e), frontal white matter (f) and genu of the corpus callosum (g, h), and displayed additional increases in λ_3 in the posterior aspect of the posterior limb of the internal capsule (g), external capsule (g) and the middle body and isthmus of the corpus callosum (h).

4.4.2 TBSS-defined region of interest-based analysis

Having used TBSS to objectively survey the whole FA skeleton and detect regions of anisotropy differences between the infant groups, FA, λ_1 , λ_2 , and λ_3 values were then assessed in these areas, using t-tests or Mann Whitney U as appropriate, corrected for multiple comparisons using a post-hoc Bonferroni test.

ROI analysis revealed significantly reduced FA and elevated λ_2 and λ_3 but no difference in λ_1 in the centrum semiovale, frontal white matter and genu of the corpus callosum in

the preterm-born group compared to term-born control infants (Table 4.1, Figure 4.5). Infants born at ≤ 28 weeks had additional reductions in FA and elevations in λ_2 and λ_3 in the posterior aspect of the posterior limb of the internal capsule, the external capsule and the isthmus and middle portion of the body of the corpus callosum (Table 4.2, Figure 4.6).

		<i>Term-born control infants (n = 6)</i>	<i>Preterm infants at term (n = 26)</i>	<i>p</i>
CSO	FA	0.29 ± 0.03	0.22 ± 0.03	<0.001
	λ1	1.68 ± 0.08	1.76 ± 0.11	0.060
	λ2	1.26 ± 0.08	1.42 ± 0.11	<0.001
	λ3	0.94 ± 0.08	1.14 ± 0.12	<0.001
Frontal WM	FA	0.28 ± 0.02	0.22 ± 0.03	<0.001
	λ1	1.63 ± 0.08	1.70 ± 0.08	0.404
	λ2	1.27 ± 0.07	1.43 ± 0.08	0.004
	λ3	0.90 ± 0.04	1.10 ± 0.10	<0.001
Genu CC	FA	0.68 ± 0.06	0.56 ± 0.06	<0.001
	λ1	2.20 ± 0.13	2.59 ± 0.39	0.300
	λ2	0.79 ± 0.21	1.38 ± 0.39	0.003
	λ3	0.46 ± 0.13	0.69 ± 0.19	0.006

Table 4.1: Mean (\pm standard deviation) for FA, $\lambda 1$ ($\times 10^{-3} \text{ mm}^2 \text{ s}^{-1}$), $\lambda 2$ ($\times 10^{-3} \text{ mm}^2 \text{ s}^{-1}$) and $\lambda 3$ ($\times 10^{-3} \text{ mm}^2 \text{ s}^{-1}$) in term-born control infants and preterm infants imaged at term

Key: CSO = centrum semiovale, WM = white matter, CC = corpus callosum.

ROIs were defined in areas of the brain where voxelwise statistical analysis revealed significant reductions in FA at term in preterm infants compared to gender-matched term-born controls. The ROIs were drawn in the space of the most typical infant in the group and projected onto all subjects' aligned diffusion data. In all regions the observed reduction in FA amongst the preterm-born group can be explained by elevations in $\lambda 2$ and $\lambda 3$ (i.e. by elevations in diffusivity perpendicular to the white matter tracts).

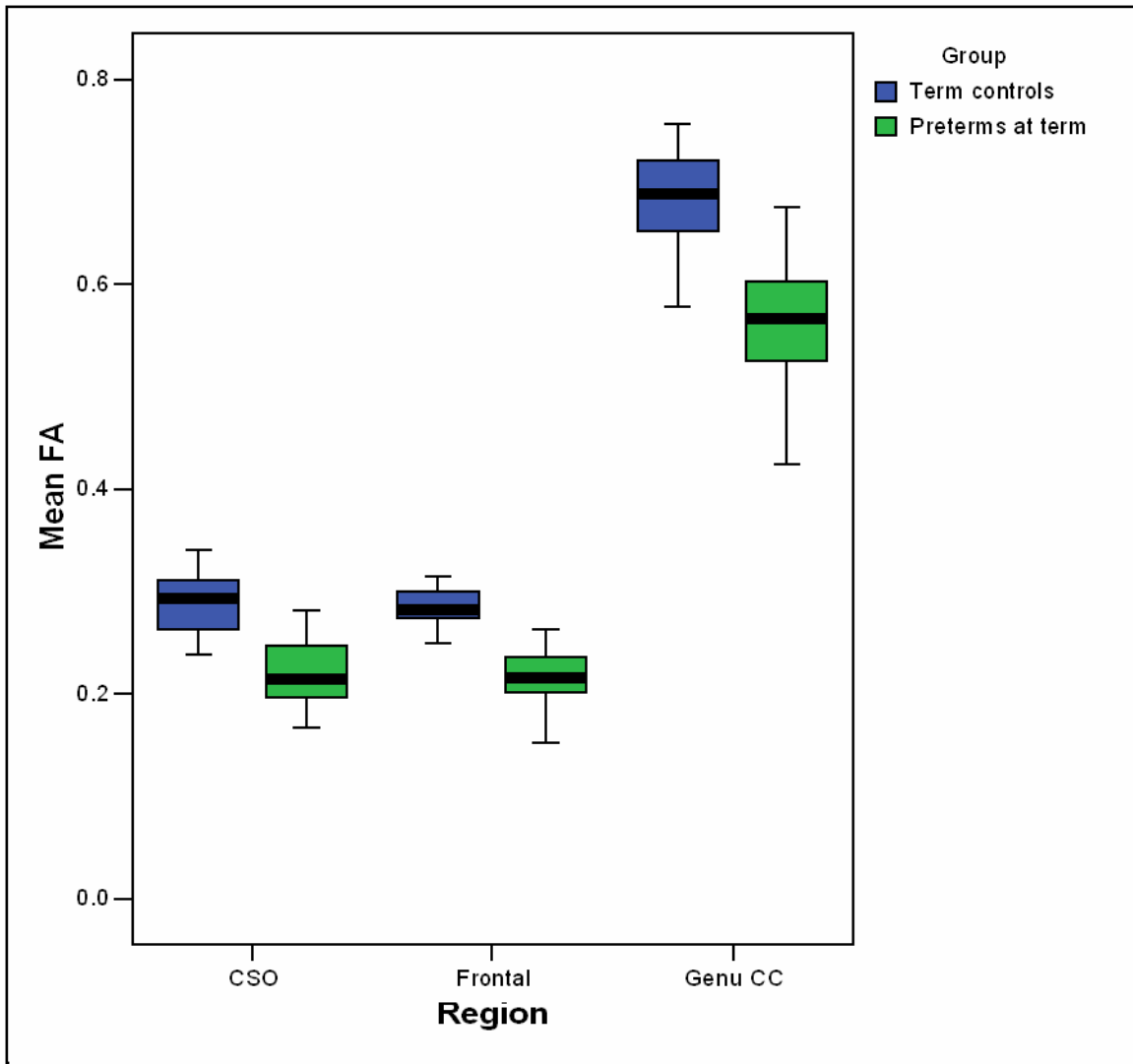


Figure 4.5: A box plot of FA values in regions of difference between term-born control infants and preterm infants imaged at term

ROIs were defined in areas of the brain where voxelwise statistical analysis revealed significant reductions in FA at term in preterm infants compared to gender-matched term-born controls. The ROIs were drawn in the space of the most typical infant in the group and projected onto all subjects' aligned diffusion data. The bold lines represent the median value of the mean FA across subject in the regions studied, the boxes the inter-quartile range of mean FA values and the whiskers the absolute range.

Key: CSO = centrum semiovale, Frontal = frontal white matter, CC = corpus callosum.

		<i>Term-born control infants (n = 6)</i>	<i>Preterm infants at term (n = 11)</i>	p
CSO	FA	0.29 ± 0.03	0.21 ± 0.03	<0.001
	λ1	1.69 ± 0.08	1.78 ± 0.09	0.048
	λ2	1.26 ± 0.08	1.45 ± 0.10	<0.001
	λ3	0.93 ± 0.08	1.17 ± 0.11	<0.001
Frontal WM	FA	0.28 ± 0.02	0.21 ± 0.02	<0.001
	λ1	1.62 ± 0.08	1.68 ± 0.05	0.424
	λ2	1.26 ± 0.06	1.43 ± 0.06	<0.001
Genu CC	FA	0.68 ± 0.05	0.54 ± 0.05	<0.001
	λ1	2.16 ± 0.11	2.51 ± 0.19	0.008
	λ2	0.73 ± 0.13	1.29 ± 0.22	<0.001
	λ3	0.47 ± 0.09	0.75 ± 0.12	0.008
External Capsule	FA	0.30 ± 0.03	0.24 ± 0.02	<0.001
	λ1	1.52 ± 0.08	1.53 ± 0.06	>0.99
	λ2	1.18 ± 0.07	1.27 ± 0.07	0.008
	λ3	0.81 ± 0.07	0.94 ± 0.08	<0.001
Left Posterior PLIC	FA	0.45 ± 0.04	0.38 ± 0.03	0.008
	λ1	1.68 ± 0.04	1.68 ± 0.10	>0.99
	λ2	0.91 ± 0.07	1.04 ± 0.09	0.040
	λ3	0.68 ± 0.06	0.78 ± 0.06	0.024
Right Posterior PLIC	FA	0.52 ± 0.04	0.44 ± 0.05	0.040
	λ1	1.79 ± 0.04	1.75 ± 0.08	>0.99
	λ2	0.81 ± 0.08	0.97 ± 0.08	0.008
	λ3	0.64 ± 0.06	0.73 ± 0.06	0.080
Middle Body CC	FA	0.50 ± 0.06	0.40 ± 0.04	<0.001
	λ1	2.14 ± 0.28	2.65 ± 0.86	>0.99
	λ2	1.06 ± 0.12	1.60 ± 0.63	0.016
	λ3	0.82 ± 0.12	1.17 ± 0.22	0.024
Isthmus CC	FA	0.53 ± 0.04	0.43 ± 0.05	<0.001
	λ1	2.01 ± 0.15	2.37 ± 0.42	0.488
	λ2	0.90 ± 0.10	1.34 ± 0.29	0.016
	λ3	0.70 ± 0.10	1.05 ± 0.25	0.040

Table 4.2: Mean (± standard deviation) for FA, λ1 ($\times 10^{-3} \text{ mm}^2 \text{ s}^{-1}$), λ2 ($\times 10^{-3} \text{ mm}^2 \text{ s}^{-1}$) and λ3 ($\times 10^{-3} \text{ mm}^2 \text{ s}^{-1}$) in term-born control infants and preterm infants born ≤ 28 weeks GA imaged at term

Key: CSO = centrum semiovale, WM = white matter, CC = corpus callosum, PLIC = posterior limb of the internal capsule.

ROIs were defined in areas of the brain where voxelwise statistical analysis uncorrected for multiple comparisons revealed significant reductions in FA at term in extremely preterm infants compared to gender-matched term-born controls. In most regions the observed reduction in FA amongst the preterm-born group can be explained by elevations in λ_2 and λ_3 .

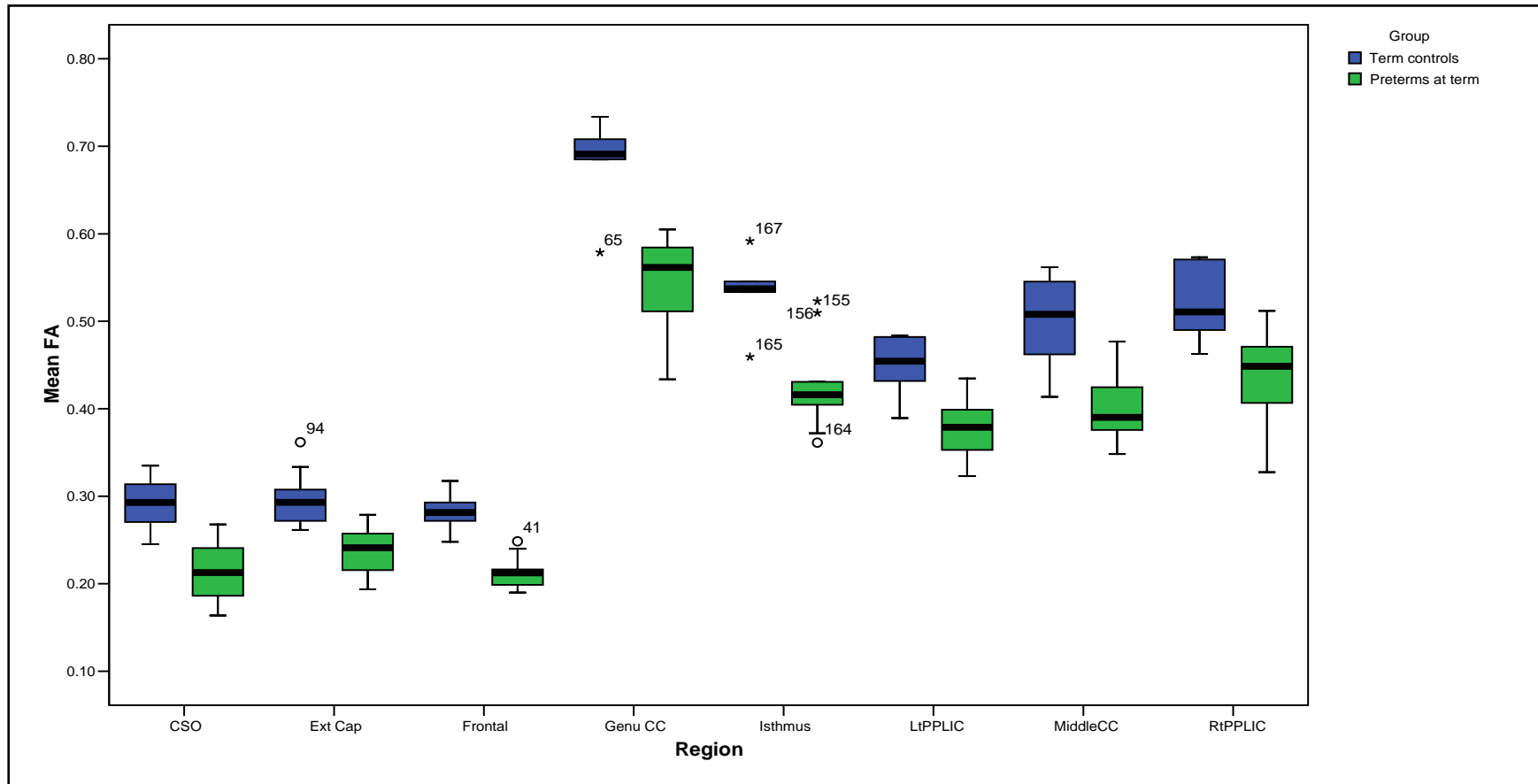


Figure 4.6: A box plot of FA values in regions of difference between term-born control infants and preterm infants born ≤ 28 weeks GA imaged at term

ROIs were defined in areas of the brain where voxelwise statistical analysis revealed significant reductions in FA at term in extremely preterm infants compared to gender-matched term-born controls. The bold lines represent the median value of the mean FA across subject in the regions studied, the boxes the inter-quartile range of mean FA values and the whiskers the range. Outliers, greater than twice the inter-quartile range from the median value, are represented by asterisks or open circles.

Key: CSO = centrum semiovale, ExtCap = external capsule, Frontal = frontal white matter, GenuCC = genu of the corpus callosum, Isthmus = isthmus of the corpus callosum, LtPPLIC = posterior portion of the left posterior limb of the internal capsule, RtPPLIC = posterior portion of the right posterior limb of the internal capsule, MiddleCC = middle body of the corpus callosum.

4.5 Discussion

In this study DTI and automated tract-based analysis were used to investigate brain microstructure in preterm infants imaged at term equivalent age. The centrum semiovale, frontal white matter and genu of the corpus callosum were found to have significantly lower FA compared to age- and sex-matched term-born controls. The most immature infants (i.e. those infants born ≤ 28 weeks gestational age) displayed additional and more extensive reductions in FA, suggesting more severe white matter microstructural abnormalities with increasing premature exposure to the ex-utero environment. These differences were significant after a Bonferroni correction in subsequent ROI analyses in areas of the brain where voxelwise cross-subject statistics revealed significant differences in FA between the term control infants and the preterm born groups.

Reductions in FA may be due to a reduction in axial diffusivity (i.e. decreased λ_1) or an increase in radial diffusivity (i.e. increased λ_2 and/or λ_3). Animal studies have demonstrated that these eigenvalues of the effective diffusion tensor are more sensitive markers of myelination than FA (Gulani et al., 2001; Song et al., 2002, Song et al., 2005; Moeller et al., 2007). To investigate the observed reduction in FA the three eigenvalues of the diffusion tensor were therefore separately considered and it was found that regions which exhibited decreased FA showed elevated intermediate (λ_2) and/or minor (λ_3) eigenvalues (Figures 3 and 4). These findings are consistent with previous ROI-based analysis of DTI data from preterm and term born control infants (Counsell et al., 2006). It is not completely clear what the biological significance of this is. However, animal studies suggest that demyelination (and, most likely, altered premyelination) processes increase radial diffusivity in the cerebral white matter with minimal effects on axial diffusivity (Gulani et al., 2001; Song et al., 2002, Song et al., 2005). On the other hand, axonal damage is thought to lead to decreased λ_1 with a relatively smaller effect on λ_2 and λ_3 (Song et al., 2002; Arfanakis et al., 2002; Moeller et al, 2007).

TBSS detected reduced FA in a number of white matter regions where microstructural changes have been shown in previous ROI-based studies. Huppi (Huppi et al., 1998) found that ADC values in the central white matter are higher and relative anisotropy (RA) values are lower in both the central white matter and posterior limb of the internal capsule in preterm infants at term compared to term-born infants, and suggested this was due to delayed maturation or oligodendrocyte and/or axonal damage. A significant elevation in radial diffusivity in the posterior body of the corpus callosum in preterm infants imaged at term compared to term-born controls has previously been reported (Anjari et al., 2006a; Anjari et al., 2006b), a finding which may have the same biological explanation.

Elevated ADC values (Counsell et al., 2003a) and diminished RA values in white matter (Huppi et al., 2001) have been associated with abnormal white matter at term equivalent age. Miller et al reported a significant increase in ADC values with increasing GA in the frontal white matter and visual association areas in infants with moderate white matter injury (Miller et al., 2002). In addition, the authors observed an absence of the normal maturational increase in RA in a number of white matter regions in infants with moderate white matter injury and in the frontal region in infants with only minimal white matter injury (Miller et al., 2002). The frontal white matter in the preterm brain was not typically considered a major site of predilection for white matter injury, however the suggestion that there may be a particular susceptibility to injury in the frontal white matter (Miller et al., 2002) is consistent with the marked changes in this region seen in the present study.

Reduced FA in the preterm brain was also found in the genu of the corpus callosum and increased λ_2 and λ_3 in the genu and isthmus of the corpus callosum in infants born at less than or equal to 28 weeks gestation. An ultrasound investigation has revealed reduced callosal growth rate in very preterm infants from birth to term age (Anderson et al., 2005) and a conventional MRI study has demonstrated smaller callosal size in children who were born preterm (Rademaker et al., 2004). Furthermore, thinning of the isthmus of the corpus callosum correlated with minor motor impairment in a cohort of seven-year-olds

who were born preterm (Abernethy et al., 2004) and with verbal impairment in 14-15 year olds who were born preterm (Nosarti et al., 2004).

An important limitation of many ROI-based analyses is the reliance on arbitrary *a priori* definitions to manually delineate different brain regions. In addition, ROI studies are time-consuming and often have significant inter-subject variability which does not easily allow for comparison of many brain regions or large subject groups (Kubicki et al., 2002; Giuliani et al., 2005). Therefore, fully automated whole-brain measurement techniques for analysing MRI data are being increasingly used, the most common of which has been voxel-based morphometry (Ashburner and Friston, 2000). VBM uses image registration to bring brain images from different subjects into a common coordinate system for analysis (Ashburner and Friston, 2000; Crum et al., 2004), and has been used in DTI studies of schizophrenia (Giuliani et al., 2005), white matter asymmetry (Buchel et al., 2004) and supranuclear palsy (Padovani et al., 2006). There remains, however, ambiguity as to whether apparent differences highlighted using VBM approaches are due to differences in brain regions or to local misalignment. Smith et al performed a comparison study of TBSS and VBM-style analysis on FA data from schizophrenics and control subjects and found that VBM analysis generated several spurious results due to imperfect registration, including the demonstration of FA differences within the ventricles (Smith et al., 2006). Giuliani et al have observed that VBM findings do not always replicate ROI analyses of DTI data (Giuliani et al., 2005), and given that the choice of spatial smoothing extent of the segmentation output data also remains unresolved, some investigators have concluded that VBM should not be used with imperfectly registered images (Bookstein, 2001; Davatzikos, 2004). Tract-based spatial statistics overcomes some of the limitations of both ROI and VBM approaches to analyse neonatal data. TBSS aligns diffusion tensor FA data from different subjects via a nonlinear registration algorithm followed by projection onto an alignment-invariant tract representation prior to applying voxelwise statistics. The method therefore represents an observer-independent method of analysing neonatal DTI data without requiring spatial smoothing and can offer new insights into the development of the preterm brain.

4.6 Summary

In this study the results of voxelwise cross-subject statistical analysis of neonatal DTI data has been used to perform non-subjective ROI-based analyses only in areas of FA difference. It has allowed the detection of microstructural changes on a voxel basis in a small sample group of preterm infants at term for the first time. The centrum semiovale, frontal white matter and genu of the corpus callosum had significantly lower FA in this group of preterm infants at term equivalent age compared to age- and sex-matched term-born controls, with the most immature infants displaying additional and more extensive reductions in FA. This was due to an increase in radial diffusivity and most likely a result of delayed myelination or oligodendrocyte damage.

4.7 Further questions

It is likely that prematurity in itself is not responsible for some of the later problems that preterm-born infants are more susceptible to. It is perhaps more probable that specific clinical factors contribute to altered cerebral development in different parts of the brain. A further study with larger numbers of infants will allow the assessment of the association of clinical variables such as gender, infection and acute and chronic lung disease on white matter microstructural properties in the developing preterm brain.

Chapter 5

Fractional Anisotropy Changes Associated with Lung Disease Amongst Preterm-Born Infants

5.1 Introduction

In the previous study, it was demonstrated using TBSS that preterm-born infants have microstructural white matter differences compared to age- and gender-matched term-control subjects as early as term-equivalent age. However, it is not clear what aspect(s) of premature delivery is/are responsible for some of the later problems in brain growth and development, or if specific diseases or interventions during the perinatal period contribute to abnormal cerebral structure and growth patterns.

Epidemiological evidence suggests that respiratory disease amongst the preterm-born population is associated with adverse neurological outcome. Preterm infants with supplemental oxygen needs at 28 days postnatal life show reductions in deep grey matter volume at term age (Boardman et al., 2007) and those requiring oxygen at 36 weeks corrected age have reduced growth throughout the brain (Thompson et al., 2007). These reductions may have cognitive consequences, with Short (Short et al., 2003) and Hughes

(Hughes et al., 1999) reporting that at school-age, these infants have deficits in reading and mathematical ability compared to term-born peers.

It is suggested that problems with respiration and gas exchange, as well as pulmonary inflammation and the effects of mechanical ventilation may directly cause cerebral white matter damage. However respiratory insufficiency is more common in more preterm infants and it has not previously been possible to disassociate the effects of lung disease and its treatments from increasing immaturity at birth. TBSS allows multivariate statistical analysis of large groups of images. This new technical advance, allied to a much bigger study, allows confounding variables to be accounted for, and for the first time provides the tool needed to address the hypothesis that respiratory disease is independently associated with cerebral white matter abnormalities in preterm infants. This may allow a more advanced and subtle understanding of the effects of respiratory disease on cerebral white matter, and influence the clinical treatment of preterm infants to potentially prevent certain adverse neurological outcomes in the long-term.

5.2 Aim

The aim of this study was to use TBSS to investigate the association between both acute respiratory distress at birth and chronic lung disease and cerebral white matter in preterm infants imaged at term, having accounted for confounders including the effects of increasing prematurity, age of the infants at imaging, gender and approximate evidence of serious infection.

5.3 Materials and methods

The MRI data used in this study were acquired by other researchers as part of a number of ongoing studies at Hammersmith Hospital. Ethical permission was granted by the Hammersmith Hospital Research Ethics Committee (2003/6564 and 04/Q0406/125). Written parental consent was obtained prior to imaging for each subject.

5.3.1 Subjects

Fifty-three infants (30 female) who were born at a median (range) gestational age (GA) of 28^{+2} ($24^{+2} - 32^{+4}$) weeks and median birth weight of 1030 (640 – 1940) g were studied. The median (range) age at the time of imaging, defined as the time from the first day of the mother's last menstrual period, was 42^{+0} ($38^{+1} - 44^{+2}$) weeks and the median (range) weight was 3400 (2000 – 5500) g.

Twelve (6 female) of the cohort had prolonged (>18 hours) rupture of membranes (PROM) with a median (range) of 1 (1 - 9) day, and seventeen were delivered vaginally. In total, forty-two infants were treated with surfactant and forty-three with antenatal steroids. None of the cohort was given steroids in the postnatal period. Three subjects required inotropes.

There were ten (4 female) infants with evidence of acute respiratory disease in the immediate perinatal period, defined as the need for mechanical ventilatory support for at least two days following delivery (median (range) of 3.5 (2 – 33) days).

Fifteen (9 female) neonates in the cohort were classed as having chronic lung disease, defined by the need for supplemental inspired oxygen at 36 weeks post-menstrual age.

Lacking a definitive test for septicaemia, available data suggesting serious infection was gathered. Fifteen (9 female) of these infants had clinical evidence of sepsis, including

culture-positive blood films for coagulase-negative staphylococcus aureus (n = 7) or enterococcus species (n = 1), varicella IgG (n = 1) or raised C-reactive protein (n = 6).

Table 5.1 shows the overlap between each of the confounding variables, study variables and exploratory variables amongst the study population.

Subject	Gender	Gestational age (weeks)	Age at scan (weeks)	PROM > 24 hours	Acute lung disease status	CLD status	Sepsis status
1	f	24.3	44.0	0	1	1	1
2	m	24.4	42.0	0	1	0	0
3	f	24.7	39.1	1	1	1	1
4	m	25.1	43.7	0	1	1	0
5	f	25.3	41.9	0	0	0	0
6	f	25.3	41.9	0	0	0	0
7	f	25.7	42.1	1	0	1	0
8	f	25.7	42.1	0	0	1	0
9	f	26.0	40.7	0	0	0	1
10	f	26.0	41.6	1	0	1	0
11	f	26.0	42.0	0	0	0	0
12	m	26.1	41.4	0	0	0	1
13	f	26.1	41.7	1	0	0	0
14	f	26.1	41.7	0	0	0	1
15	m	26.1	43.0	0	0	1	1
16	f	26.1	43.3	0	0	1	0
17	m	26.1	43.3	0	0	1	0
18	m	26.3	43.6	0	0	1	1
19	f	26.7	39.7	0	1	0	0
20	f	26.7	40.6	0	0	0	0
21	f	26.7	40.6	0	0	0	0
22	f	27.4	44.0	1	0	0	1
23	f	27.9	38.1	1	0	1	0
24	f	27.9	38.1	0	0	1	0
25	m	27.9	43.1	0	0	0	1
26	m	28.0	40.1	1	1	0	1
27	f	28.3	42.7	0	1	1	1
28	m	28.3	44.3	0	0	0	0
29	m	28.4	43.0	0	0	1	0
30	m	28.4	43.0	0	0	0	0
31	f	28.7	42.0	1	0	0	0
32	f	28.7	42.9	1	0	0	0
33	f	29.0	41.9	0	0	0	1
34	f	29.3	43.0	0	0	0	1
35	m	29.3	40.3	0	1	0	0
36	f	29.7	42.1	0	0	0	0
37	m	30.0	40.3	0	1	1	0
38	f	30.0	43.3	0	0	0	0
39	m	30.1	42.3	0	1	0	1
40	m	30.4	41.0	0	0	0	0
41	m	30.4	42.0	0	0	0	0
42	m	30.4	42.0	0	0	0	0
43	f	30.6	42.0	1	0	0	0
44	f	30.6	40.7	0	0	0	0
45	m	30.6	40.7	0	0	0	0
46	f	30.7	39.9	0	0	0	0
47	m	30.7	39.1	1	0	0	0
48	m	30.9	41.4	0	0	0	0
49	m	31.0	40.4	0	0	0	1
50	m	31.6	43.0	1	0	0	0
51	m	31.6	43.0	0	0	0	0
52	f	32.1	44.1	0	0	0	0
53	f	32.6	43.9	0	0	0	0

Table 5.1: A correlation table of the association between each of the confounding variables, study variables and exploratory variables in the study population

5.3.2 Magnetic resonance imaging

MRI was performed on a Philips Achieva 3 Tesla system (Philips Medical Systems, Netherlands) using an eight-channel phased array head coil. The infants were prepared for examination in the same way described in Section 4.3.2.

Sagittal 3D magnetization prepared rapid acquisition gradient echo (MPRAGE) images (TR 17 ms, TE 4.6 ms, flip angle 13° , voxel size $0.82 \times 0.82 \times 1.6 \text{ mm}^3$) and transverse T2-weighted fast spin echo (FSE) (TR 5200 ms, TE = 12.8 ms, flip angle 90° , voxel size $0.86 \times 0.86 \times 1 \text{ mm}^3$) were obtained prior to DTI.

5.3.2.1 *Diffusion Tensor Imaging*

Single shot EPI DTI was acquired in 15 noncollinear directions using the following parameters: TR 8000 ms, TE 49 ms, slice thickness 2 mm, field of view 224 mm, matrix 128×128 (voxel size = $1.75 \times 1.75 \times 2 \text{ mm}^3$), b value = 750 s/mm^2 . The data were acquired with a SENSE factor of 2 and the scanning time for this sequence was 5 minutes.

5.3.3 Data analysis

As in the previous study, data analysis was performed using tools included in FSL v3.3.7 (Smith et al., 2004). Data were transferred off-line and the fifteen diffusion weighted images were registered to the $b = 0 \text{ s/mm}^2$ image to correct for differences in spatial distortion due to eddy currents (Behrens et al., 2003). Images were brain extracted using BET (Smith, 2002), before FA maps were generated by fitting the diffusion tensor model to the data using 'dtifit' (Behrens et al., 2003).

Voxelwise statistical pre-processing of the FA data was carried out using TBSS v1.0 (Smith et al., 2006) as described previously. Multivariate voxelwise statistical analysis

was performed on the data using Randomise (Nichols and Holmes, 2002), as described in Section 4.3.4.

The correlation between FA and study variables was assessed using linear regression analysis of voxelwise cross-subject statistics corrected for multiple comparisons using cluster-based thresholding (cluster size = 3, p-value < 0.05). To assess the amount of variance in the FA data that could be explained by any of the study variables, regions which showed a significant correlation between FA and any of the study variables were then further explored with local region-of-interest (ROI) based analyses. In each region, SPSS 12.0 (<http://www.spss.com/SPSS>) was used to fit the FA data to a forced-entry multivariate linear regression model containing both the study variable as well as the confounder variables of GA and age at imaging as free parameters. Beta-coefficients were calculated for each parameter, and R-squared values and the standard error of the estimate were obtained for the model. The effect of outliers on the model was assessed by determining the standardised residuals and Cook's distance for each data point.

Prior to the primary analysis the effect of the two known confounders on FA were examined: gestational age at delivery and age at imaging. The association between acute or chronic respiratory disease and FA was then assessed, having regressed out the effects of GA and age at imaging. Finally some exploratory analyses were performed to determine if the observed effects might be further confounded by other variables: gender, serious infection and premature rupture of membranes (PROM).

5.4 Results

5.4.1 Confounding variables

5.4.1.1 *Increasing prematurity*

FA values in the splenium and posterior body of the corpus callosum, the left posterior limb of the internal capsule (PLIC), left frontal white matter and left inferior longitudinal white matter were significantly linearly correlated with GA after having regressed out the effects of age at scan on the data (Figure 5.1). A linear relationship between GA and FA was also suggested in the genu of the corpus callosum and left inferior longitudinal fasciculus, but this did not survive full multiple comparison correction with cluster-based thresholding (cluster-size = 3; $p < 0.05$)

5.4.1.2 *Age at imaging*

After regressing out the effects of GA, FA values throughout the whole of the cerebral white matter contained within the skeleton were found to be positively correlated with post-menstrual age at scan.

5.4.2 Study variables

5.4.2.1 *Acute lung disease*

Infants that were ventilated for ≥ 2 days ($n = 10$) had a localised area of reduced FA within the genu of the corpus callosum compared to infants that were not ventilated or who were ventilated for shorter periods (Figure 5.2). Defining this as a region of interest and fitting a linear model to the FA with GA, age at imaging and acute lung disease status as free parameters revealed that prolonged ventilation was associated with an FA change

of -0.074 (standard error 0.017 , 95% confidence interval -0.109 to -0.039) after accounting for GA and age at imaging (Figure 5.3). The Cook's distance was not more than 0.25 for any of the data points, suggesting that the model was not significantly affected by outliers. The model explained 46% of the variance in FA (Table 5.2). A correlation between acute lung disease status and FA at term was not found when the data were averaged over the whole of the mean FA skeleton (Student's t-test, $p = 0.39$).

5.4.2.2 *Chronic lung disease*

Preterm-born infants that required oxygen therapy at 36 weeks gestation ($n = 9$) were considered to have chronic lung disease and seen to have lower FA compared to chronic lung disease-negative subjects in the left inferior longitudinal fasciculus (Figure 5.4), but not in any other brain areas. A region of interest was placed here and a linear model of FA was constructed with GA, age at imaging and chronic lung disease status as free parameters, showing that chronic lung disease was associated with a -0.036 (standard error 0.007 , 95% confidence interval -0.051 to -0.022) change in FA at term-equivalent age (Figure 5.5). The maximal Cook's distance was 0.33 , and the model had an R-squared of 0.534 (Table 5.3). There was not a statistically significant correlation between chronic lung disease status and FA at term when the data were averaged over the whole of the mean FA skeleton (Student's t-test, $p = 0.21$).

5.4.3 Exploratory variables

5.4.3.1 *Gender*

No gender-related differences in cerebral white matter at term age were found, as assessed by FA in any region following preterm birth.

5.4.3.2 *Evidence of serious infection*

The effects of both culture-positive and clinically-diagnosed sepsis on white matter were analysed, but found no differences in FA compared to infants with no documented evidence of serious infection.

5.4.3.3 *Prolonged rupture of membranes*

Differences in FA were not observed in any region between infants whose mothers did and did not have membrane rupture ≥ 18 hours prior to delivery.

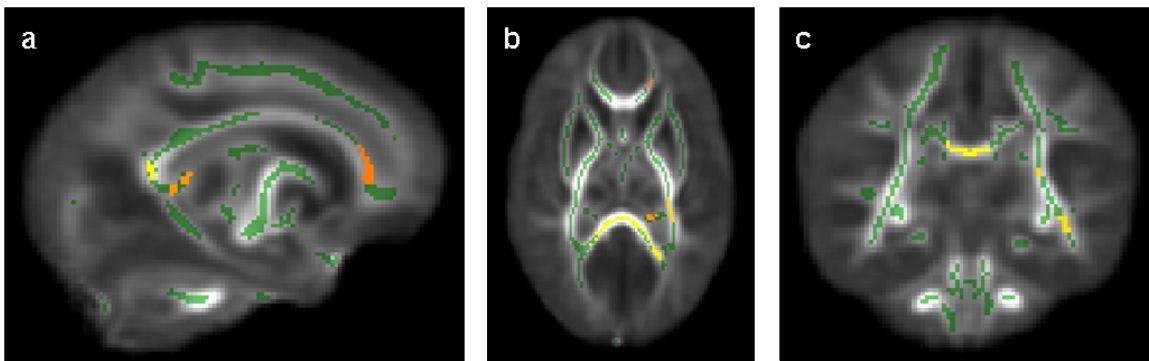


Figure 5.1: The effect of increasing prematurity at birth on cerebral white matter at term equivalent age

Mean FA skeleton (green) overlaid on mean FA map in the sagittal (a), axial (b) and coronal (c) and planes. Voxels showing a significant linear correlation ($c \geq 3$, $p < 0.05$) between FA and GA are shown in orange/yellow and include the splenium (b, c) and posterior body of the corpus callosum, the left posterior limb of the internal capsule (b), the left frontal white matter (a) and left inferior longitudinal white matter (c).

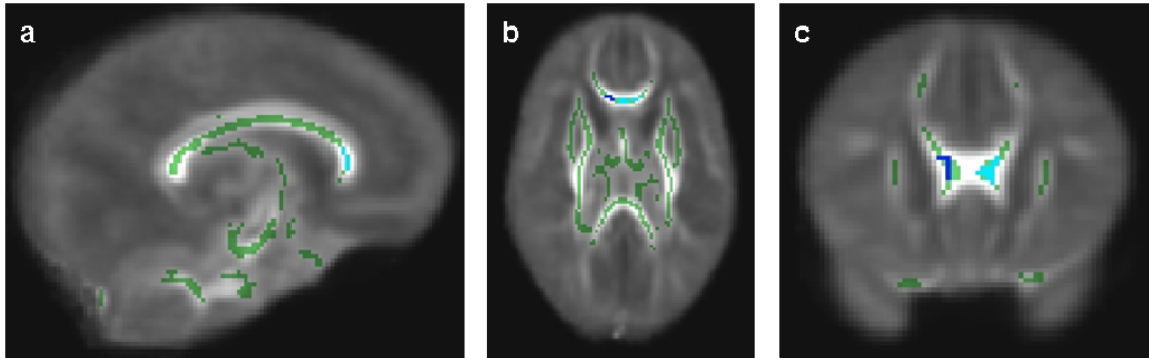


Figure 5.2: The association between acute lung disease and FA at term-equivalent age

Mean FA skeleton overlaid on the mean FA map. Regions in green represent areas where there was no significant difference in FA values between infants that developed acute lung disease compared to infants that did not require ventilation for ≥ 2 days. Voxels in blue represent regions where the FA was significantly lower in the acute lung disease group after having regressed out the effects of GA and age at scan, and delineate only the genu of the corpus callosum (a) (b) (c).

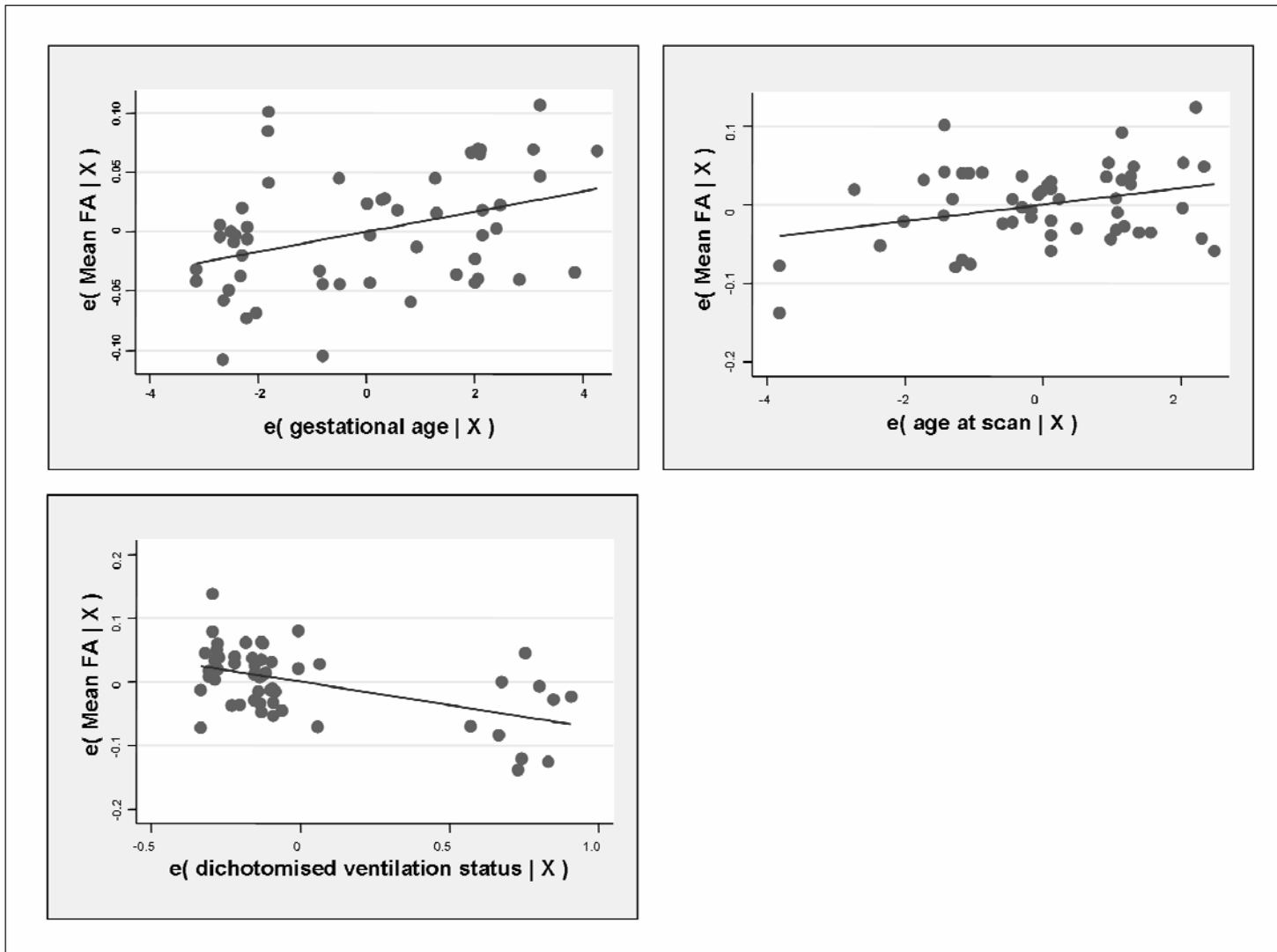


Figure 5.3: The association between acute lung disease and FA in the genu of the corpus callosum at term-equivalent age

A multivariate linear model comprising GA, age at imaging and acute lung disease status was fitted to the FA values in an ROI in the genu of the corpus callosum (for model parameters see Table 5.2). This figure shows the scatter plots of the residuals of FA and each of the predictors in this region (GA, top left; age at scan, right; acute lung disease status, bottom left) when all three variables are regressed separately on the remaining predictors.

Key: $e(\text{FA} | X)$ = FA residuals given the regression model; $e(\text{gestational age at birth} | X)$ = residuals of gestational age at birth given the model; $e(\text{age at scan} | X)$ = residuals of age at scan given the model; $e(\text{dichotomised ventilation status} | X)$ = residuals in acute lung disease status given the model.

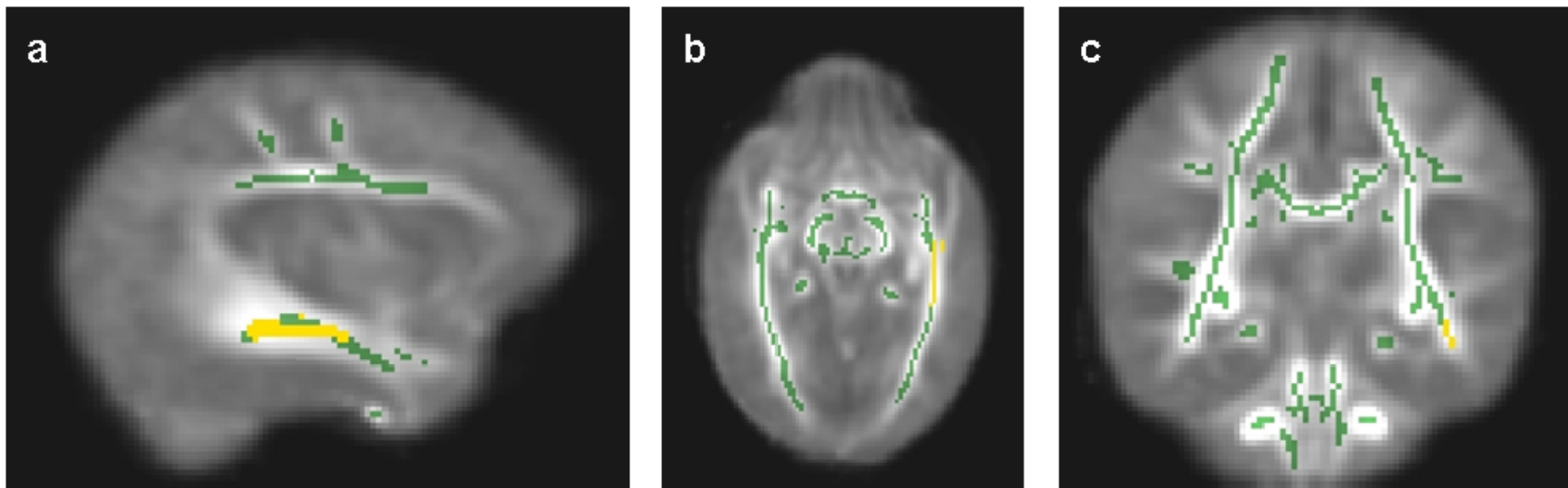


Figure 5.4: The association between chronic lung disease and FA at term-equivalent age

Mean FA skeleton overlaid on the mean FA map. Regions in green represent areas where there was no significant difference in FA values between the cohort of infants that had chronic lung disease, as defined by supplemental oxygen requirement at 36 weeks PMA, and those that were negative for chronic lung disease. Voxels in yellow highlight the left inferior longitudinal fasciculus, the only region found where FA was significantly lower in the group that had chronic lung disease after having regressed out the effects of GA and age at scan.

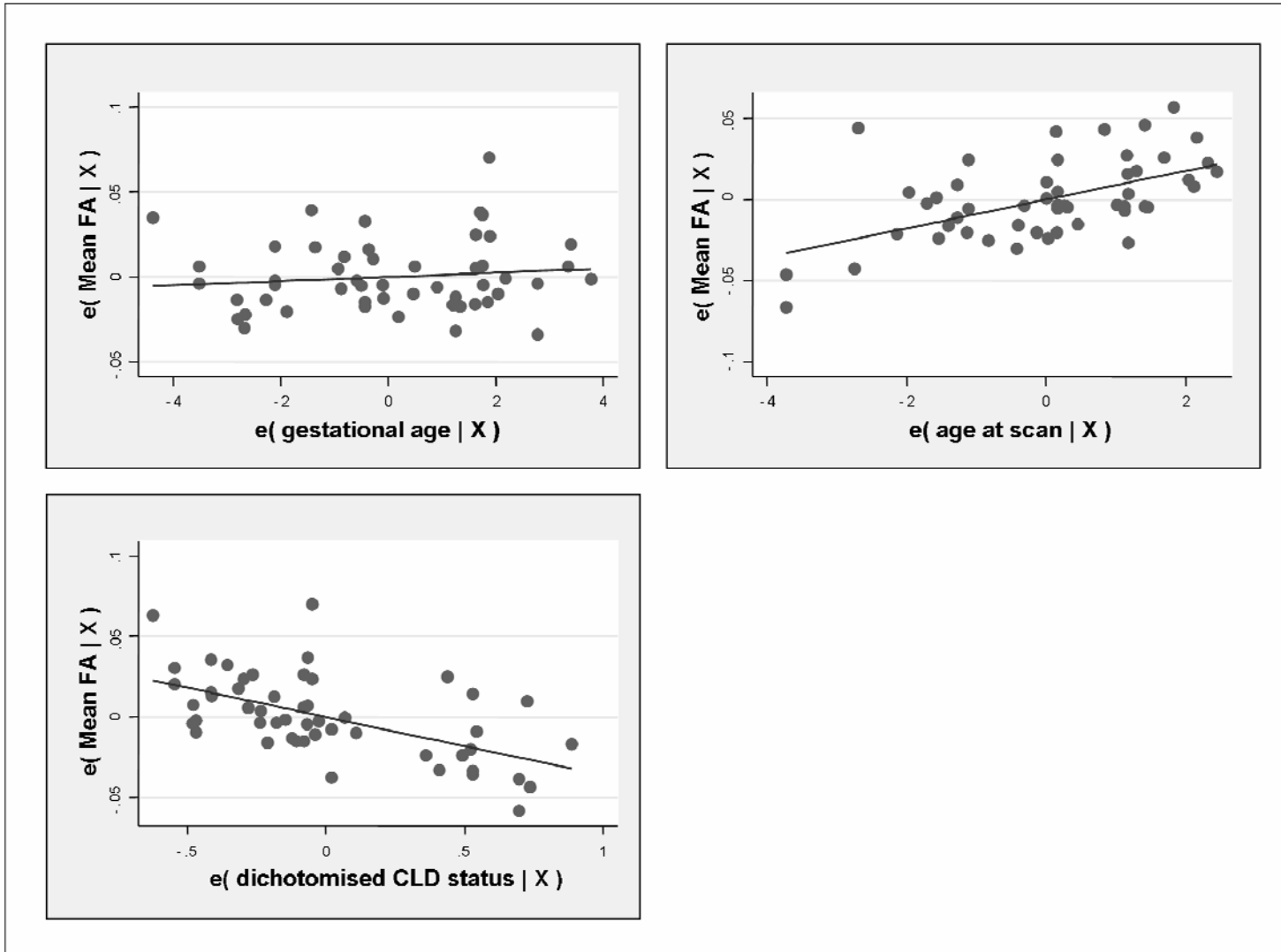


Figure 5.5: The association between chronic lung disease and FA in the left inferior longitudinal fasciculus at term-equivalent age

A multivariate linear model comprising GA, age at imaging and chronic lung disease status was fitted to the FA values in an ROI in the left inferior longitudinal fasciculus. This figure shows the scatter plots of the residuals of FA and each of the predictors in this region (GA, left; age at scan, middle; chronic lung disease status, right) when both variables are regressed separately on the remaining predictors.

Key: $e(\text{FA} | X)$ = FA residuals given the regression model; $e(\text{gestational age at birth} | X)$ = residuals of gestational age at birth given the model; $e(\text{age at scan} | X)$ = residuals of age at scan given the model; $e(\text{dichotomised CLD status} | X)$ = residuals in chronic lung disease status given the model.

<i>Model parameters</i>	<i>Unstandardised coefficients</i>			<i>FA correlations</i>				
	B	95% confidence interval for B		Standard error	Zero-order	Partial	t-stat	p-value
		Lower bound	Upper bound					
(Constant)	-0.110	-0.632	0.210	0.209	-	-	-1.008	0.319
GA	0.008	0.002	0.015	0.003	0.407	0.372	2.803	0.007
Age at imaging	0.011	0.002	0.019	0.004	0.310	0.320	2.363	0.022
Acute lung disease status	-0.074	-0.109	-0.039	0.017	-0.564	-0.516	-4.214	<0.001

Table 5.2: FA multivariate linear model summary in the genu of the corpus callosum

FA was found to be significantly correlated with acute lung disease status in the genu of the corpus callosum. A multivariate linear model containing GA, age at imaging and dichotomised acute lung disease status was fitted to the FA data in this region with the following summary statistics.

<i>Model parameters</i>	<i>Unstandardised coefficients</i>				<i>FA correlations</i>		<i>t-stat</i>	<i>p-value</i>
	B	95% confidence interval for B		Standard error	Zero-order	Partial		
		Lower bound	Upper bound					
(Constant)	-0.112	-0.299	0.075	0.093	-	-	-1.207	0.233
GA	0.001	-0.002	0.004	0.001	0.329	0.117	0.826	0.413
Age at imaging	0.009	0.005	0.013	0.002	0.431	0.540	4.495	<0.001
Chronic lung disease status	-0.036	-0.051	-0.022	0.007	-0.579	-0.580	-4.984	<0.001

Table 5.3: FA multivariate linear model summary in the left inferior longitudinal fasciculus

FA was found to be significantly correlated with chronic lung disease status in the left inferior longitudinal fasciculus. A multivariate linear model containing GA, age at imaging and chronic lung disease status was fitted to the FA data in this region with the following summary statistics.

5.5 Discussion

Preterm infants with neurodevelopmental impairment frequently have multiple risk factors, including early respiratory difficulties, evidence of antenatal or postnatal sepsis and chronic lung disease. The neuropathological substrate for this impairment is thought to involve cerebral white matter damage but the convergence of multiple risk factors has previously made it difficult to determine specific associations between white matter abnormality and clinical events. In this study DTI data was analysed with TBSS to objectively investigate the association between acute and chronic lung disease status and cerebral white matter in preterm infants imaged at term-equivalent age. Having regressed out the strong effects of GA and age at scan on FA, infants that developed acute lung disease (i.e. those who were ventilated for ≥ 2 days; $n = 10$), displayed a highly localised region of reduced FA within the genu of the corpus callosum relative to infants that were not ventilated or who were ventilated for shorter periods (Figure 2). Fitting a multivariate linear model to the mean FA values in this region, developing acute lung disease was found to be correlated with a change in FA of -0.074 (95% confidence interval -0.109 to -0.039) at term-equivalent age. Amongst infants diagnosed with chronic lung disease, described as supplemental oxygen requirement at 36 weeks, decreased FA in the left inferior longitudinal fasciculus compared to infants negative for chronic lung disease (Figure 4) was found. Again a multivariate linear model was fitted, suggesting that positive chronic lung disease status is associated with a -0.036 (95% confidence interval -0.109 to -0.039) change in FA in this region at term-equivalent age.

Infants with acute lung disease requiring prolonged ventilatory support frequently have a number of risk factors that are associated with preterm brain injury, including antenatal sepsis and patent ductus arteriosus, and prolonged mechanical ventilation has independently been linked with brain injury including intraventricular haemorrhage due to fluctuating cerebral blood flow patterns (Perlman et al., 1983; Perlman et al., 1985) mediated by arterial carbon dioxide levels (Collins et al., 2001). It is unclear why white matter within the genu of the corpus callosum would be more susceptible to this form of

injury and have reduced FA at term-equivalent age. To my knowledge there are no documented neuroanatomical or neurovascular features of the genu that suggest a plausible hypothesis for the specificity of this finding. However, it has been suggested that since the blood supply to the genu of the corpus callosum is from the terminal branches of the anterior cerebral artery, the region may be particularly susceptible to hypoxic-ischaemic injury as it is the equivalent of a watershed zone (Coley and Hogan, 1997). This result suggests that either risks associated with acute lung disease or injury associated with patterns of ventilation may render this area of the brain more vulnerable to later abnormality, and may over time lead to deficits in cognition and executive function. This is consistent with a study of preterm infants in later life that showed a reduction in volume in this region compared to term-born control infants, and suggested an association with neurodevelopmental impairment (Caldu et al., 2006).

The incidence of chronic lung disease is approximately one in three in preterm infants with a birth weight of <1000 g (Jobe and Bancalari, 2001). Antenatal infection may make the foetal respiratory system more vulnerable to potentially harmful postnatal stimuli such as mechanical ventilation, and this may result in an excessive inflammatory response in neonatal airways and lung tissue (Maxwell et al., 2006; Speer, 2004). However, though there are strong associations between perinatal infection, the foetal inflammatory response and both chronic lung disease and white matter disease, Dammann (Dammann et al., 2004) reported that newborns that develop chronic lung disease are not at increased risk of white matter disease, as detected using ultrasound. Diffusion tensor imaging can discriminate more subtle microstructural white matter deficits however, and in this study a highly localised focal reduction in FA within the left inferior longitudinal fasciculus was found. This is unprecedented and the functional effects are not known, although a recent study has proposed that the left inferior longitudinal fasciculus plays a key role in semantic language processing (Mandonnet et al., 2007). However it is important to recognize that the localizations found in this study represent brain regions where white matter is abnormal across the group of infants. It is possible that individuals will each have other regions of white matter damage. Further studies will be needed to explore the within group variation, but the present study detects

regions of predilection for white matter damage in the population. The prevention or treatment of CLD with corticosteroids is associated with neurodevelopmental impairment (Yeh et al., 1998; Yeh et al., 2004; Short et al., 2003; O'Shea et al., 1999; Shinwell et al., 2000), but no infants in this group received postnatal treatment with steroids.

The effect of increasing prematurity on white matter microstructure has been described previously; DTI has been used to characterize developmental changes in the preterm brain and to elucidate microstructural white matter developmental trajectories in preterm infants born at different gestational ages (Neil et al., 1998; Miller et al., 2002; Partridge et al., 2004). As outlined in Section 3.3.2, these ROI based studies have shown regionally dependent anisotropy increases in white matter with increasing gestational age (Counsell et al., 2003a).

Elevated ADC values (Huppi et al., 2001) and diminished RA values in white matter (Weinberger et al., 1982) have been reported to be associated with abnormal white matter at term equivalent age. Compared to those with normal-appearing white matter, preterm infants with evidence of white matter injury have been reported to fail to demonstrate the normal maturational decrease in ADC near-term age (Miller et al., 2002), and it has recently been shown that elevated mean ADC values in preterm infants imaged at term are associated with reduced developmental quotient scores at two years corrected age (Krishnan et al., 2007).

The current study demonstrates that the FA reductions noted in the splenium, the left PLIC and the left frontal white matter occurs in a linearly dose-dependent manner with decreasing GA. This was not found to be the case in any of the other regions with abnormal diffusion properties in my previous TBSS study of preterm infants at term compared to term-born infants, though defining manual ROIs on the mean FA skeleton based on those results did show a nonlinear trend of decreasing FA with increasing immaturity at birth. The bilateral asymmetry in the relationship between FA and GA in the PLIC, frontal white matter and inferior longitudinal white matter is interesting. Weinberger (Weinberger et al., 1982) found that the right and left frontal lobes have

different volumes as early as 20 weeks gestation in humans, but the correlation with microstructural changes remains unclear, and has not been previously highlighted in the literature.

Male preterm infants are known to be at increased risk of brain injury in the perinatal period, leading to an increased prevalence of motor abnormalities including cerebral palsy associated with focal lesions (Wood et al., 2005), as well as diffuse white matter injury, resulting in increased incidence of learning and behavioural disorders at school age (Wood et al., 2005). However, in this study a correlation between gender distribution and FA values in any of the major cerebral white matter pathways at term age was not found. The reasons for this are unclear but may be because the microstructural neuro-imaging correlates related to these long-term gender outcomes following preterm birth are not associated with FA in the centre of white matter tracts, but it is more likely that the study is underpowered to detect differences in this exploratory variable and that the effects of gender are more subtle than the effects of respiratory disease.

There has been much recent evidence that antenatal infection and the inflammatory response may at least partially explain the relationship between preterm birth and white matter disease (Dammann et al., 2002; Dammann and Leviton, 2004). Group B streptococcal infection has been implicated in this effect (Faix and Donn, 1985), and histology studies have shown that chorioamnionitis, an expression of maternal infection, is associated with increased risk of cPVL lesions (Wu, 2002). Recently, Krishnan (Krishnan et al., 2007) found elevated ADC values in the white matter at the level of the centrum semiovale in preterm infants with postnatal sepsis. However, in our exploratory analysis of the effect of sepsis we used a wide range of indicators to select affected preterm-born infants without any sign of focal lesions on conventional MRI, but did not find an association between clinical evidence of sepsis and white matter abnormality. As in the gender study, this may be due to effects on white matter away from the centre of major tracts or because the study is underpowered. However the most likely reason is that clinical measures of sepsis status such as raised C-reactive protein are neither sensitive nor specific markers and fail to capture the true inflammatory burden distributed within

this population. Half of the subjects in the sepsis group did not have culture-positive sepsis, and the assessment of sepsis can at best be regarded as approximate. This study does not rule out a significant role of infection and inflammation in cerebral white matter disease. More specific markers of infection may enable a more accurate elucidation of the relationship between these factors.

5.6 Summary

In summary, this study has demonstrated that acute and chronic lung disease in the neonatal period may be associated with regionally specific effects on white matter integrity, as assessed by FA values, over and above the effects of GA at birth. The group of infants who developed acute lung disease displayed reductions in FA restricted to the genu of the corpus callosum, whereas the infants requiring long-term oxygen therapy had a large region of lower FA in the left inferior longitudinal fasciculus. Region-specific effects on FA related to gender or clinical sepsis status were not observed in the centres of major white matter pathways, but increasing immaturity at birth was linearly correlated with FA at term-equivalent age in a number of different white matter regions.

Our findings suggest that specific insults and support requirements in the neonatal period may lead to regionally specific effects on white matter integrity, as assessed by FA values, and may be an important predictor of the types of neurocognitive vulnerabilities that infants born preterm may be at risk from. Additional studies will be needed to explore whether or not these are causative relationships, however, and if so why these areas may be more susceptible to changes than others in within the developing preterm brain.

Chapter 6

Optimisation of a B-Spline Based Registration Algorithm for Retrospective Correction of Geometric Distortions in Neonatal DTI Data

6.1 Introduction

Group-wise analysis of anatomical MRI data is increasingly being performed using automated voxel-based morphometry style techniques. However, as described in Section 2.6, most diffusion MRI data is acquired with an EPI readout, which makes achieving accurate image alignment prior to such analyses difficult. This is particularly true if the images are collected in the absence of higher order shimming, and if there is no additional field map data or images with opposing phase-encode directions which can be used to unwarp the diffusion data. Our previous studies used TBSS that works around the problems of EPI distortions and inaccurate registration by only including voxels in the centre of the major white matter pathways in the brain, away from distorted regions.

6.2 Aim

In this chapter, work is presented on the application and optimisation of a nonlinear registration algorithm based on B-splines for retrospective correction of distortions in neonatal DTI data in the absence of additional information regarding B0 field inhomogeneities across the image, eddy currents and small motion artefacts. The goal was to develop a method which will allow non-subjective cross-subject comparisons of whole brain DTI data, without the need to perform the data reduction processes entailed in both TBSS and ROI approaches. Achieving accurate registration of diffusion data to an anatomical image acquired during the same scanning session is an important first step in this approach, and improves the robustness of subsequent normalisation to a common template.

6.3 Materials and methods

The MRI data used in this study were acquired by other researchers as part of a number of ongoing studies at Hammersmith Hospital. Ethical permission was granted by the Hammersmith Hospital Research Ethics Committee (2003/6564 and 04/Q0406/125). Written, informed parental consent was obtained for all subjects included in this study.

6.3.1 Subjects

Ten (5 female) preterm infants were studied at term-equivalent age. The median (range) gestational age of the cohort was 30^{+2} ($28^{+5} - 32^{+1}$) weeks, and the median (range) age at the time of imaging, defined as the time from the first day of the mother's last menstrual period, was 43^{+0} ($39^{+6} - 44^{+1}$) weeks.

6.3.2 Magnetic resonance imaging

MRI was performed using a Philips 3T Intera system with a six-channel phased array head coil, with infants prepared for imaging according to Section 4.3.2.

High resolution T2-weighted fast spin echo (FSE) images were acquired in the transverse plane with a TR of 5200 ms, a TE of 12.8 ms, a flip angle of 90° , and a slice thickness of 2 mm, with a -1 mm slice gap. The field of view was set to $220 \times 220 \text{ mm}^2$ and the matrix size was 256×256 , corresponding to a voxel size of $0.86 \times 0.86 \times 1 \text{ mm}^3$.

6.3.2.1 *Diffusion tensor imaging*

Single shot echo planar DTI was acquired in 15 non-collinear gradient directions. The pulse sequence parameters used were as follows: TR 9000 ms, TE 49 ms, slice thickness 2 mm, field of view 224 mm, matrix 128×128 (resulting voxel size = $1.75 \times 1.75 \times 2 \text{ mm}^3$), $b = 750 \text{ s/mm}^2$. In order to reduce the echo train length and therefore minimise distortions related to dephasing effects, parallel imaging was used; the data were acquired with a SENSE factor of 2 and the scanning time for this sequence was between 4 – 5 minutes.

6.3.3 Image registration

The single-shot echo planar image in which no diffusion gradients were applied (the $b = 0 \text{ s/mm}^2$ image) was coregistered to the high resolution undistorted anatomical T2-weighted FSE data acquired during the same session. This was in order to correct for differences in subject motion between the acquisition of anatomical and DTI data as well as for geometric distortions associated with B0 field inhomogeneities. Prior to registration, both the source and target images were brain-extracted using BET (Smith, 2002), part of the FSL package (Smith et al., 2004).

6.3.3.1 *Image similarity measure*

Normalised mutual information (NMI) (Studholme, 1999), a variant of mutual information (MI) (Collignon et al., 1995) was chosen as the similarity metric (see section 2.7.3.3.2).

6.3.3.2 *Transformation models*

6.3.3.2.1 *Affine registration model*

Affine registration of source data to target data was performed using `areg` or its variants, part of the Image Registration Toolkit (<http://wwwhomes.doc.ic.ac.uk/~dr/software/>; Rueckert et al., 1999). When 3D volumes of the source and target data were registered, this was parameterised by 12 degrees of freedom, allowing for rotations, translations, scales and shears in all three orthogonal directions. Registrations using `areg_x` were limited to only allow transformations in the phase-encode (anterior → posterior) direction. In the 2D slice-to-slice approach, either a full affine registration was allowed, described by 6 DOFs (`areg2D`), or was restricted to only permit transformations along the phase encode direction (`areg2D_x`).

6.3.3.2.2 *Nonlinear registration model*

Nonlinear registration of the source data was performed using `nreg` or its variants (<http://wwwhomes.doc.ic.ac.uk/~dr/software/>; Rueckert et al., 1999). This models the local distortion in the data using a free-form deformation (FFD) model based on B-splines (Lee et al., 1996), which is a powerful tool for modelling 3D deformable objects and has been previously applied to neonatal brain data (Boardman et al., 2006). FFDs deform an object by manipulating an underlying mesh of control points to yield a smooth deformation of structures embedded in the image, where the control points act as parameters of the transformation (see Section 2.7.8.4 for more details). A slight

modification to the tool was developed that restricted nonlinear transformations of the data to the phase-encode direction (nreg_x).

6.3.3.2.3 *Affine and nonlinear registration parameters*

The parameters required for the affine and nonlinear registration models are listed in Table 6. Other than for the choice of the similarity measure, the parameters that seemed to allow maximum correspondence between the source (the $b = 0$ s/mm² image) and the target (the T2-weighted FSE image) data were empirically determined for both the affine and nonlinear models.

6.3.3.3 *Optimal transformation*

The optimal transformation was found by minimising a cost function associated with the global and local transformation parameters, and comprised two competing goals: the cost associated with the voxel-based similarity measure (in this case, NMI) and the deformation cost term (λ), which was based on the squared sum of the second derivatives of the deformation field and constrained the transformation to be smooth (Rueckert et al., 1999; Boardman et al., 2006).

In order to assess the effect of different affine and nonlinear registration parameters in correcting for subject motion between the acquisition of the two images and EPI-induced distortions in different parts of the brain, visual inspection was first used. The $b = 0$ s/mm² image following registration and transformation into T2 space with the given parameters was overlaid on the T2-weighted FSE image. Algorithms that seemed to produce the closest alignment between the images were then empirically optimised to robustly maximise correspondence in an acceptable time frame (deemed to be less than one hour processing time on a standard desktop workstation).

6.3.3.4 Comparison with other registration algorithms

The most successful and robust algorithm (that is, the one that closely aligned pairs of images from the same subject and could do so for all ten subjects in the study group), was compared to two widely used registration methods incorporated in MR image analysis packages:

1. FLIRT (see Section 2.7.8.1), a tool for aligning brain images using affine transformations and incorporated in FSL version 4.0; and
2. Align_warp (section 2.7.8.2.2), part of the AIR version 5.0 software suite that uses a higher order polynomial model and can allow up to 1365 independent degrees of freedom to register images.

6.3.3.4.1 FLIRT

The FLIRT parameters used to register pairs of images are given in Table 6. The parameters were selected based on recommendations suggested by developers of the algorithm for registering EPI data (acquired for functional MRI studies) to intrasubject anatomical data, and so are appropriate for this study. Two different FLIRT registrations were compared to the optimised B-spline based algorithm: a 7 DOF model (allowing translations and rotations in x, y and z along with a global scale) and a full 12 DOF model, with all other registration parameters kept fixed.

Option	Chosen Parameter
Transformation model	Global rescale (7 parameter model) / Affine (12 parameter model)
Cost function	Normalised mutual information
Interpolation mode	Trilinear
Search range	-90° to +90° across the x, y and z axes

Table 6.1: FLIRT registration parameters

On the left are the options available to the user in FLIRT to align the images and on the right are the parameters selected in this study.

6.3.3.4.2 *Align_warp*

The nonlinear registration tool incorporated in AIR was first initialised using the alignlinear tool. That is, the images were first registered to each other using an affine transformation model, which provided the starting estimates for the subsequent nonlinear registration. The registration/transformation parameters for both the affine (alignlinear) and nonlinear (align_warp) components of the registration algorithm are given in Table 6. A very brief description of each parameter is provided, but for a fuller explanation see <http://bishopw.loni.ucla.edu/AIR5/technicalnotes.html>.

Option	Chosen Parameter (alignlinear)	Chosen Parameter (align_warp)
Transformation model	Affine (12 parameter model)	Fourth order nonlinear (105 parameter model)
Cost function	Least squares with intensity rescaling	Sum of squared differences (fixed)
Interpolation mode	Trilinear	Trilinear
Number of iterations	25	50
Maximum number of iterations without improvement	5	2
Initial sampling (for cost function calculation)	81 (i.e. every 81 st voxel)	81
Final sampling	1 (every voxel)	9
Scaling decrement ratio	3	3
Convergence threshold	1.0×10^{-5}	5.0×10^{-1}

Table 6.2: Alignlinear and align_warp registration parameters

6.3.4 Validation of geometric and motion correction distortion algorithm

A landmark-based strategy was employed to assess the quality of geometric and motion correction distortion algorithms and quantify the improvement in correspondence between the target (T2-weighted) and the source ($b = 0$ s/mm²) images from the same subject. In each of the subjects' data, fifteen point landmarks were positioned throughout the brain in regions that were easily identifiable on both the anatomical T2-weighted

image (Figures 6.1-15, top row) and the unregistered $b = 0$ s/mm² image (Figures 6.1-15, bottom row). The distance between corresponding landmarks was then calculated as the Euclidian distance between the points:

$$R = \sqrt{(P_x - Q_x)^2 + (P_y - Q_y)^2 + (P_z - Q_z)^2}$$

where R is the distance between the landmark $P_{x,y,z}$ in the T2-weighted image and the corresponding landmark $Q_{x,y,z}$ in $b = 0$ s/mm² image.

Following registration with each of the models chosen, the new location of these landmarks in the registered $b = 0$ s/mm² image was found by transforming the data into T2 space with the same transformation parameters used to transform the unregistered $b = 0$ s/mm² image.

6.3.4.1 *Fiducial localisation error*

In order to measure the consistency of landmark positioning, five of the infants had all 15 landmarks independently placed on both the source and the unregistered target image on three separate occasions on consecutive days.

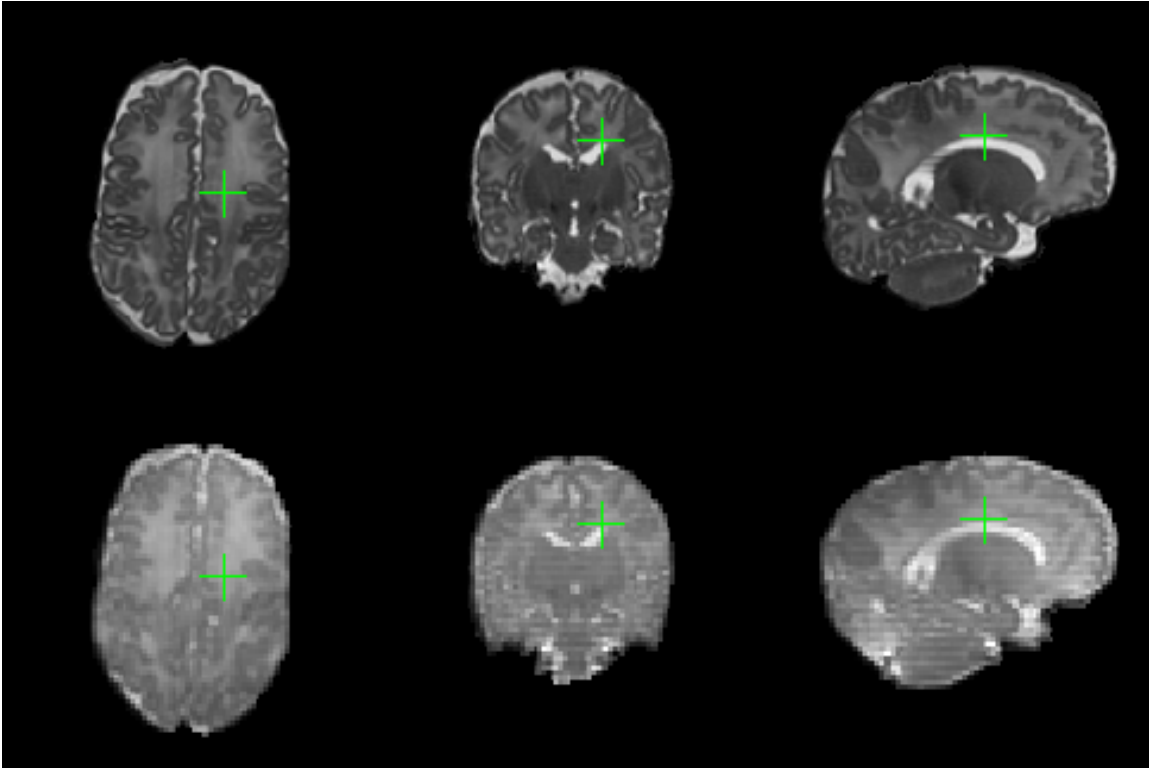


Figure 6.1: Landmark 1 - Most superior point of the left lateral ventricle (judged on a parasagittal sagittal slice)

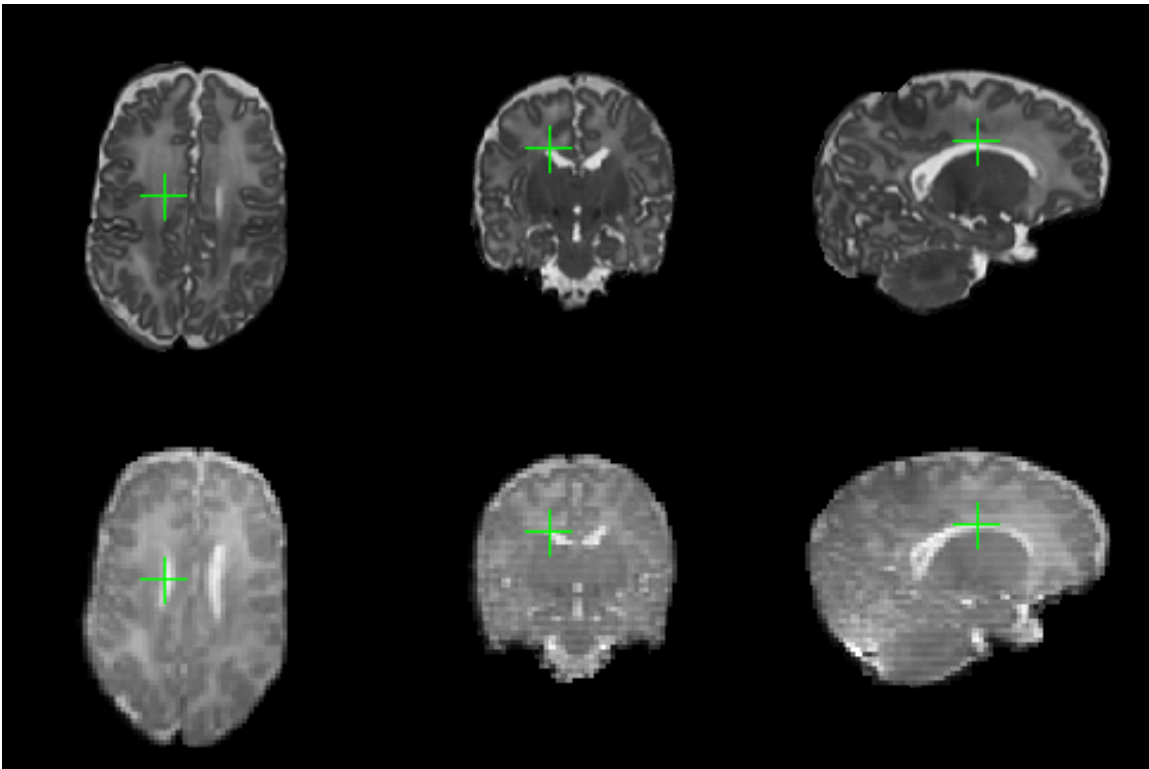


Figure 6.2: Landmark 2 - Most superior point of the right lateral ventricle (judged on a parasagittal slice)

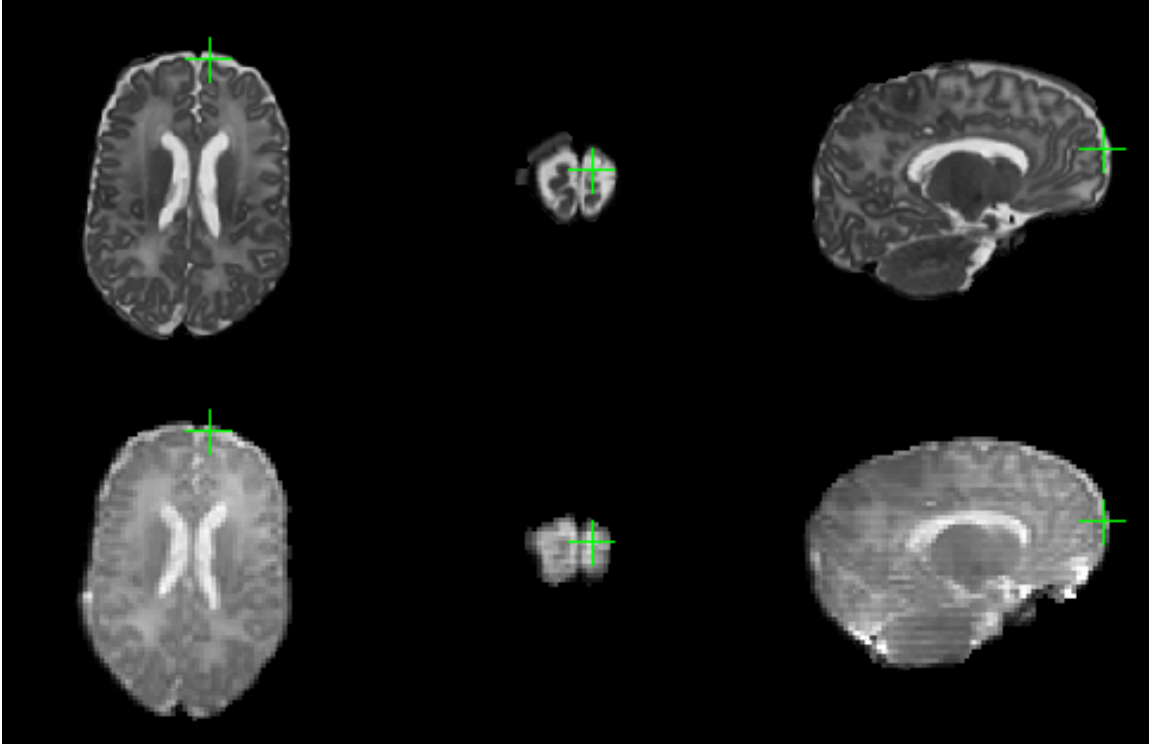


Figure 6.3: Landmark 3 - The most anterior point of the left hemisphere of the brain
This was not the true anterior-most part of the brain, but the most superior point on the coronal slice where grey matter could be seen in the left frontal lobe.

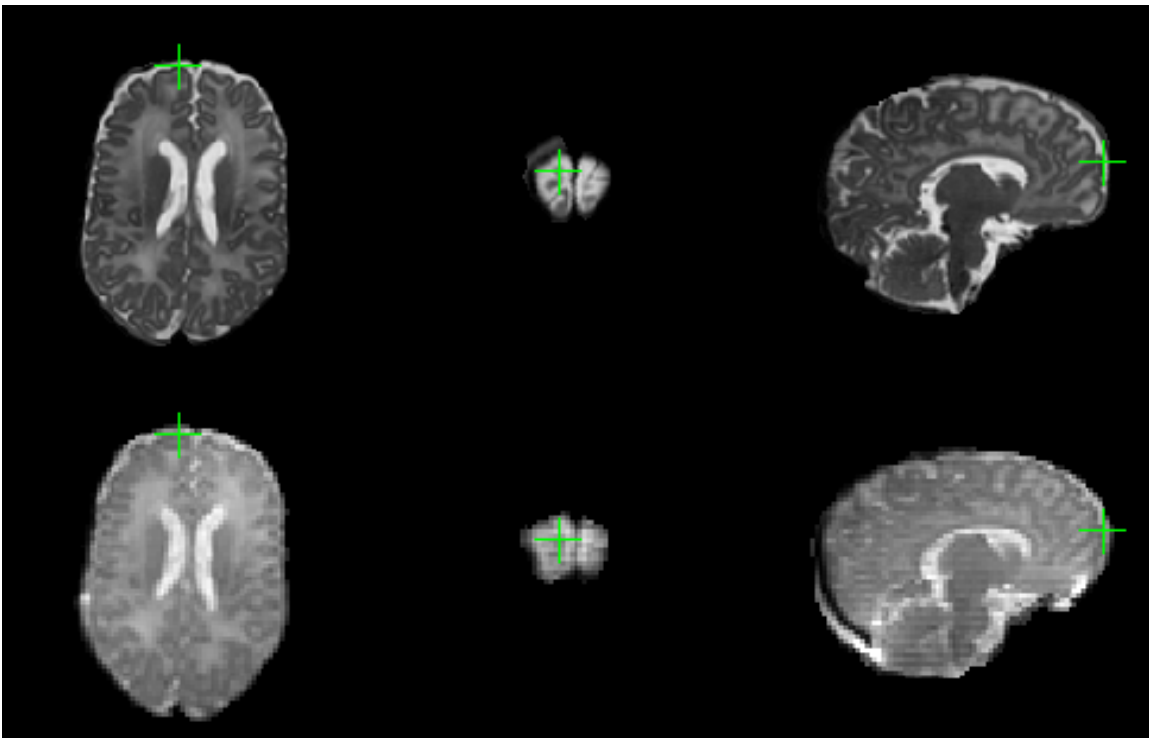


Figure 6.4: Landmark 4 - The most anterior point of the right hemisphere of the brain
Like landmark 3, this was not the true anterior-most part of the brain, but the most superior point on the coronal slice where grey matter could be seen in the right frontal lobe.

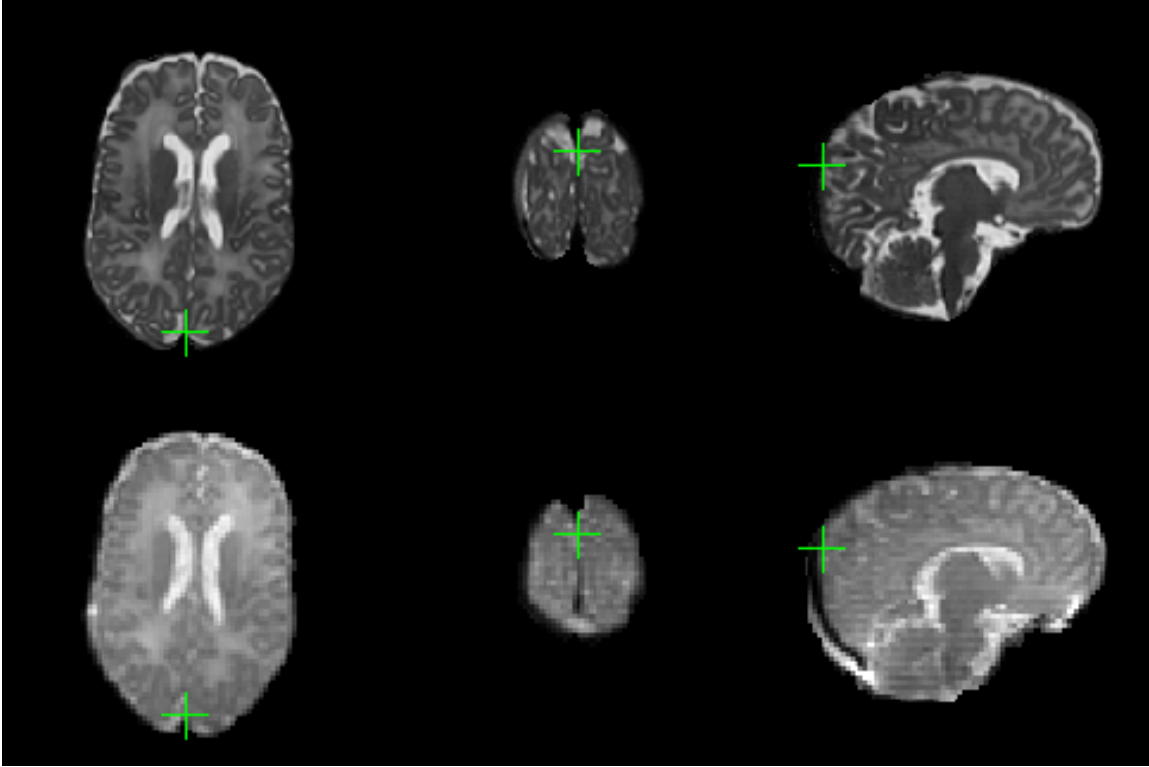


Figure 6.5: Landmark 5 - The most posterior part of the brain

This was not the true posterior-most part of the brain, but the most superior point on the most posterior coronal slice where the two cerebral hemispheres joined together.

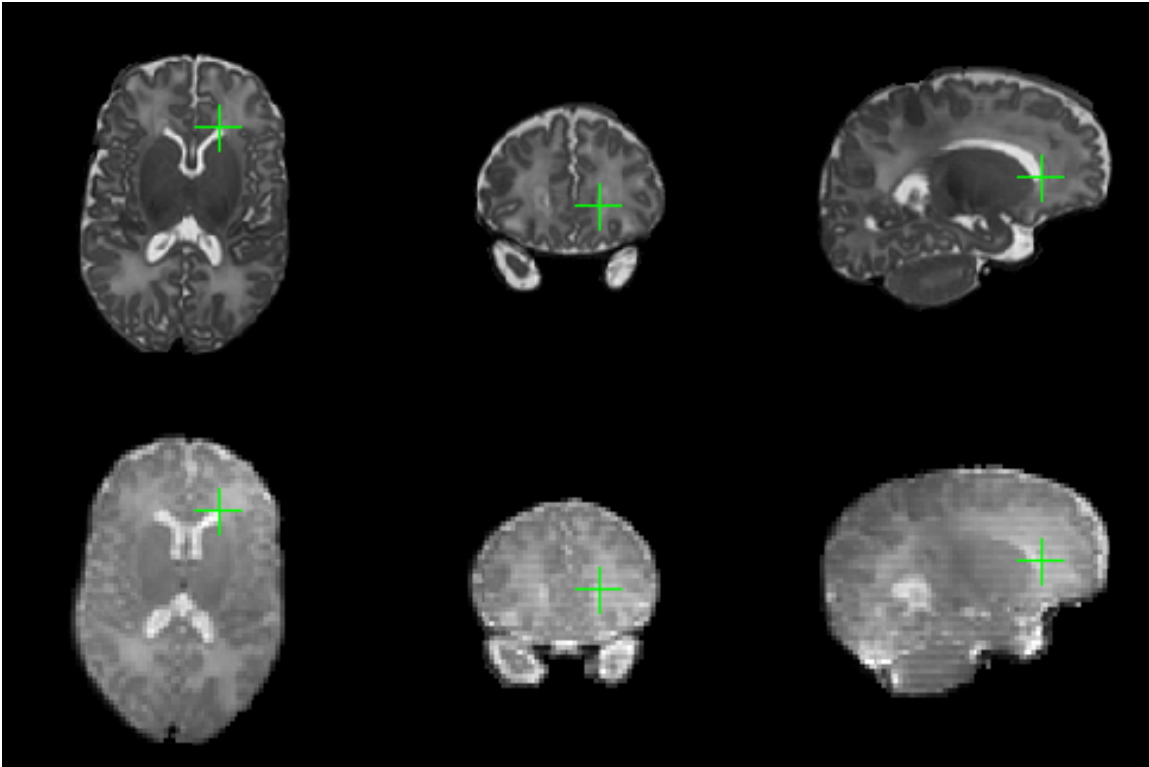


Figure 6.6: Landmark 6 - The most anterior point of the left anterior horn of the lateral ventricle

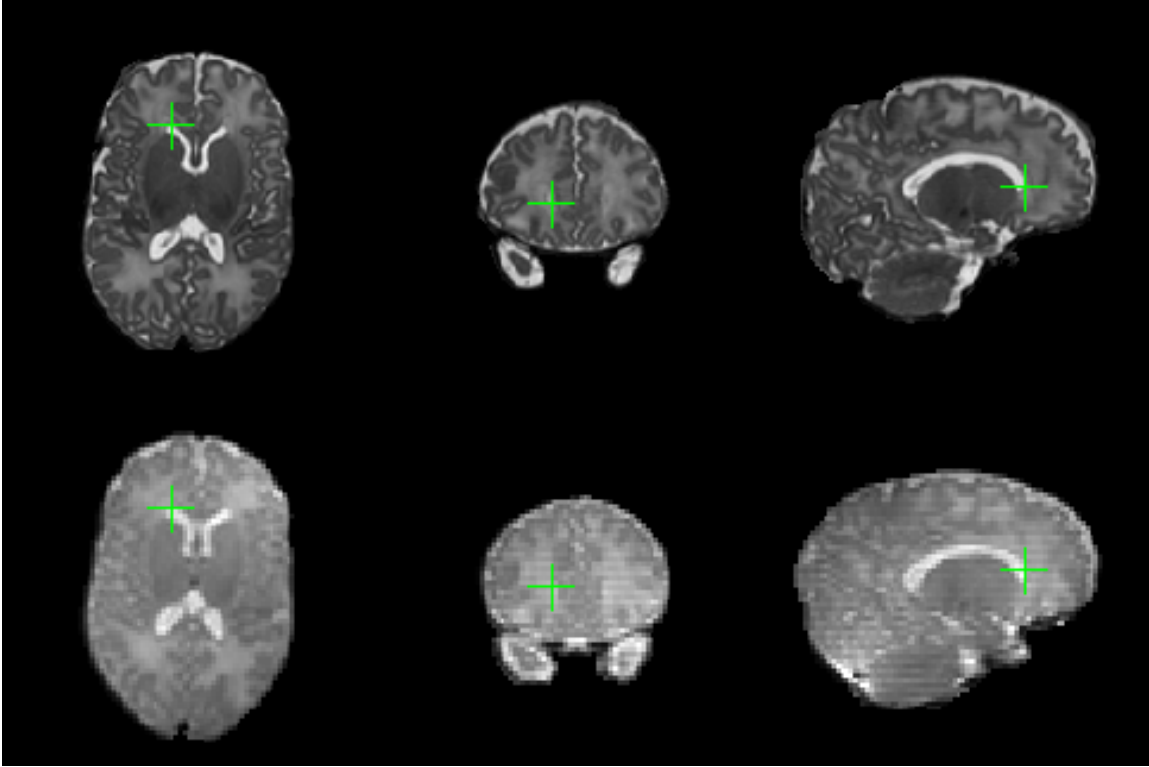


Figure 6.7: Landmark 7 - The most anterior point of the right anterior horn of the lateral ventricle

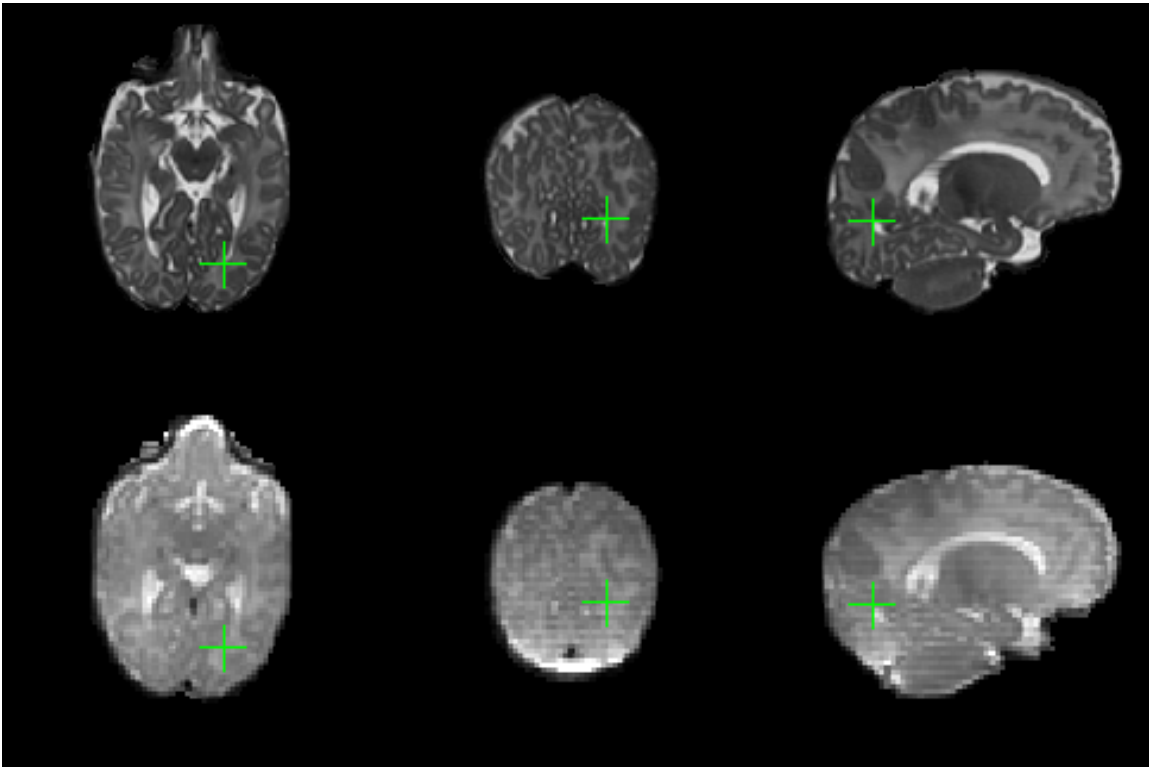


Figure 6.8: Landmark 8 - The most posterior point of the posterior horn of the left lateral ventricle

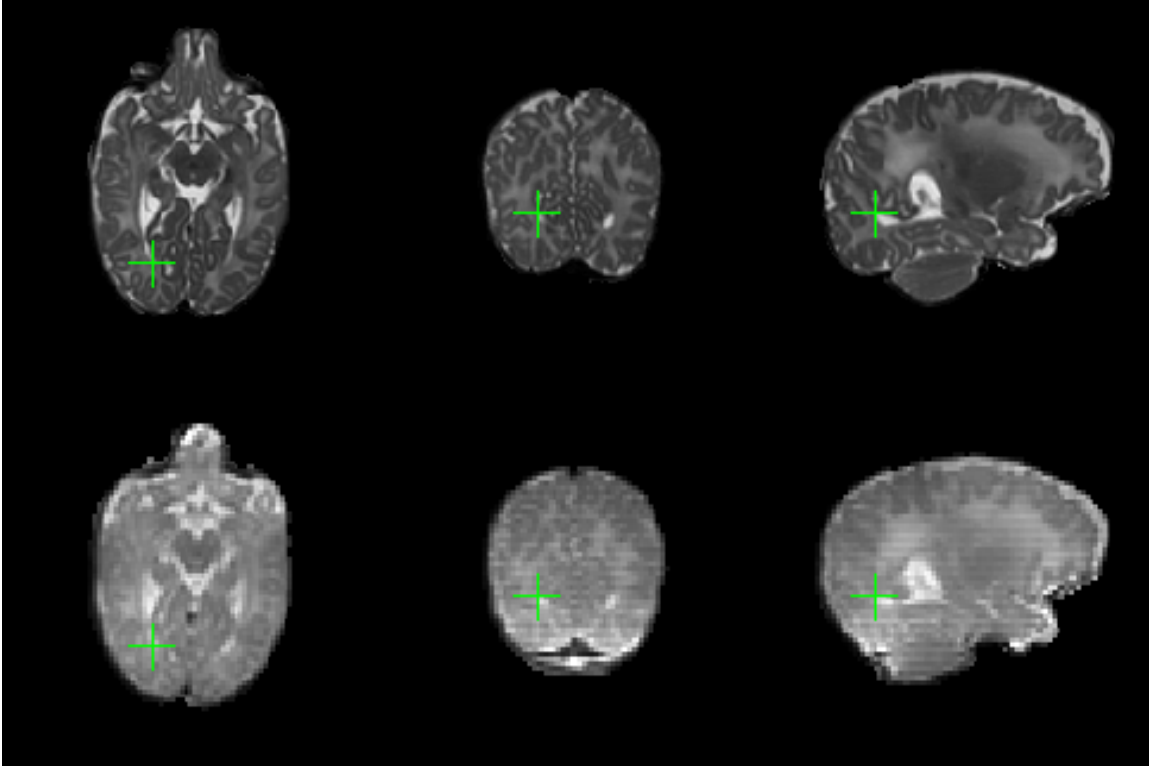


Figure 6.9: Landmark 9 - The most posterior point of the posterior horn of the right lateral ventricle

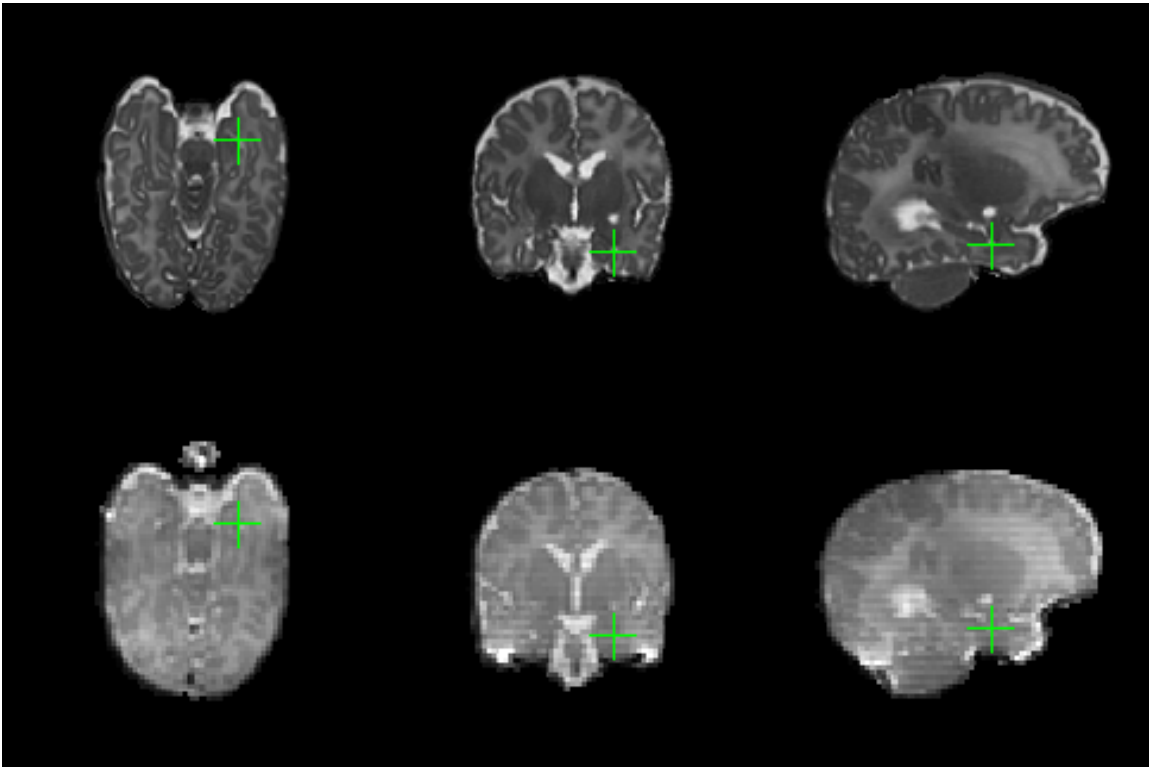


Figure 7.10: Landmark 10 - The most inferior point of the inferior horn of the left lateral ventricle

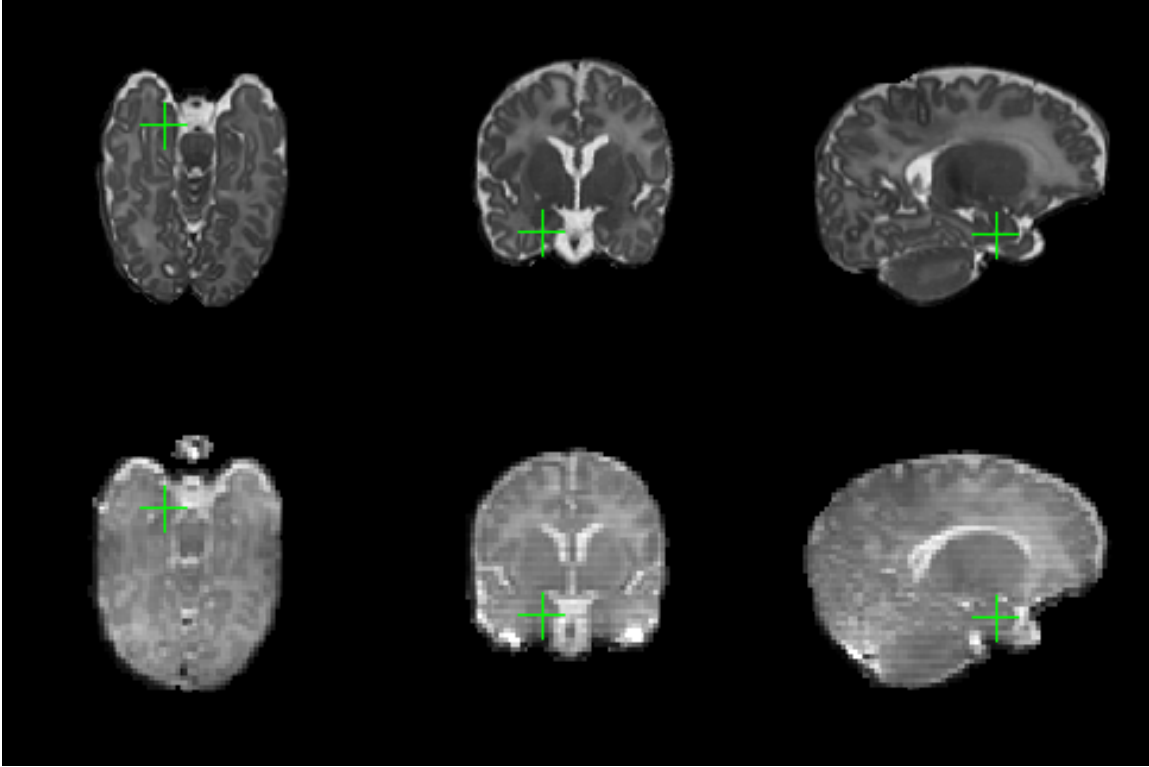


Figure 6.11: Landmark 11 - The most inferior point of the inferior horn of the right lateral ventricle

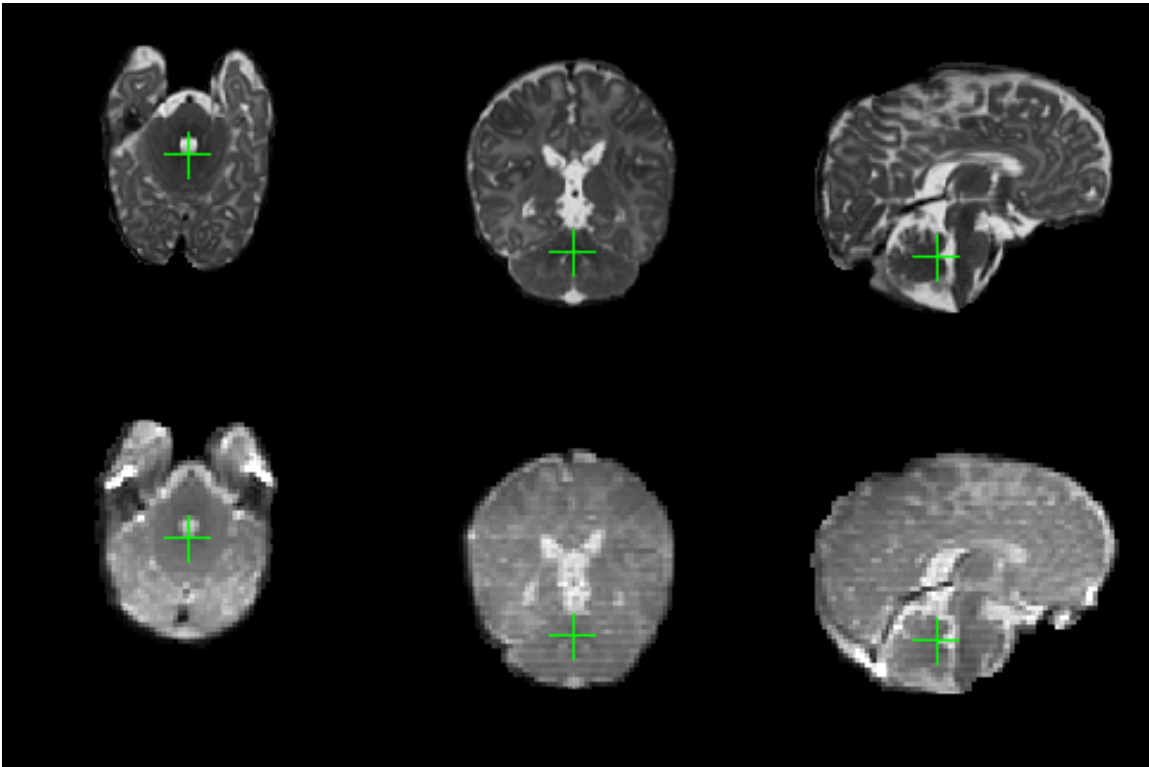


Figure 6.12: Landmark 12 - The tip of fourth ventricle
The most posterior point at the junction of the cerebellum and the fourth ventricle.

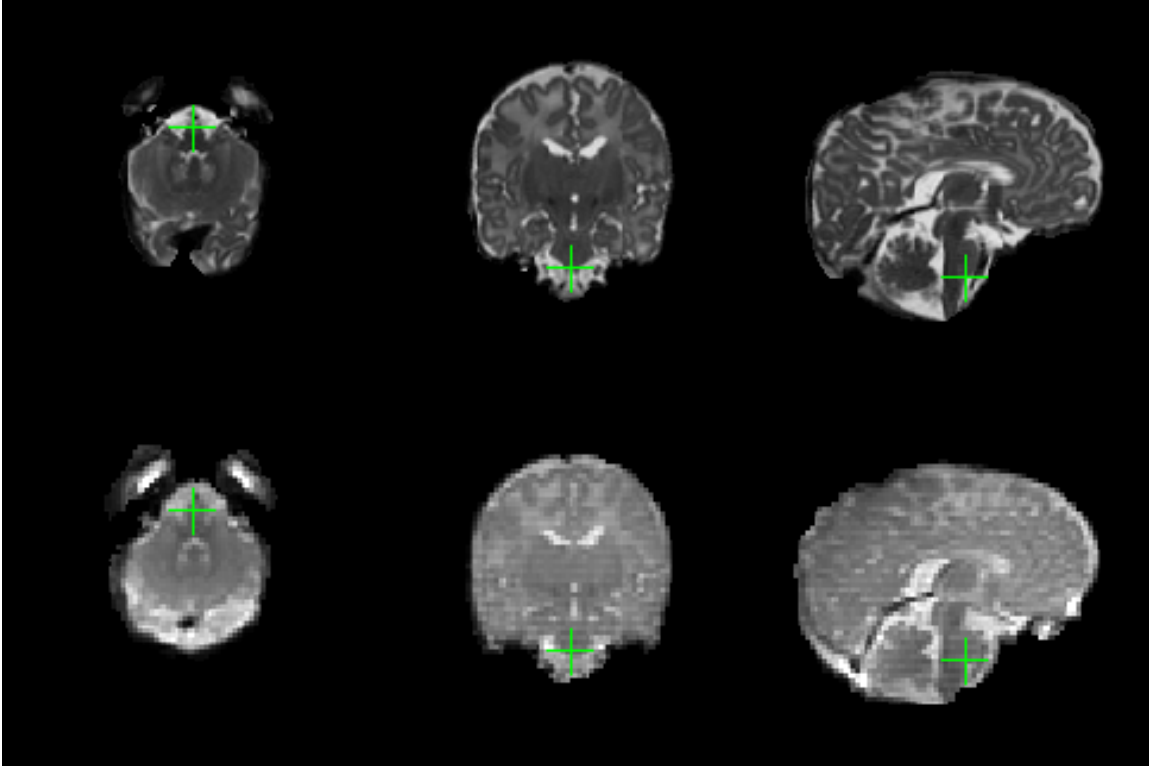


Figure 6.13: Landmark 13 - The most anterior point of the ponto-medullary junction

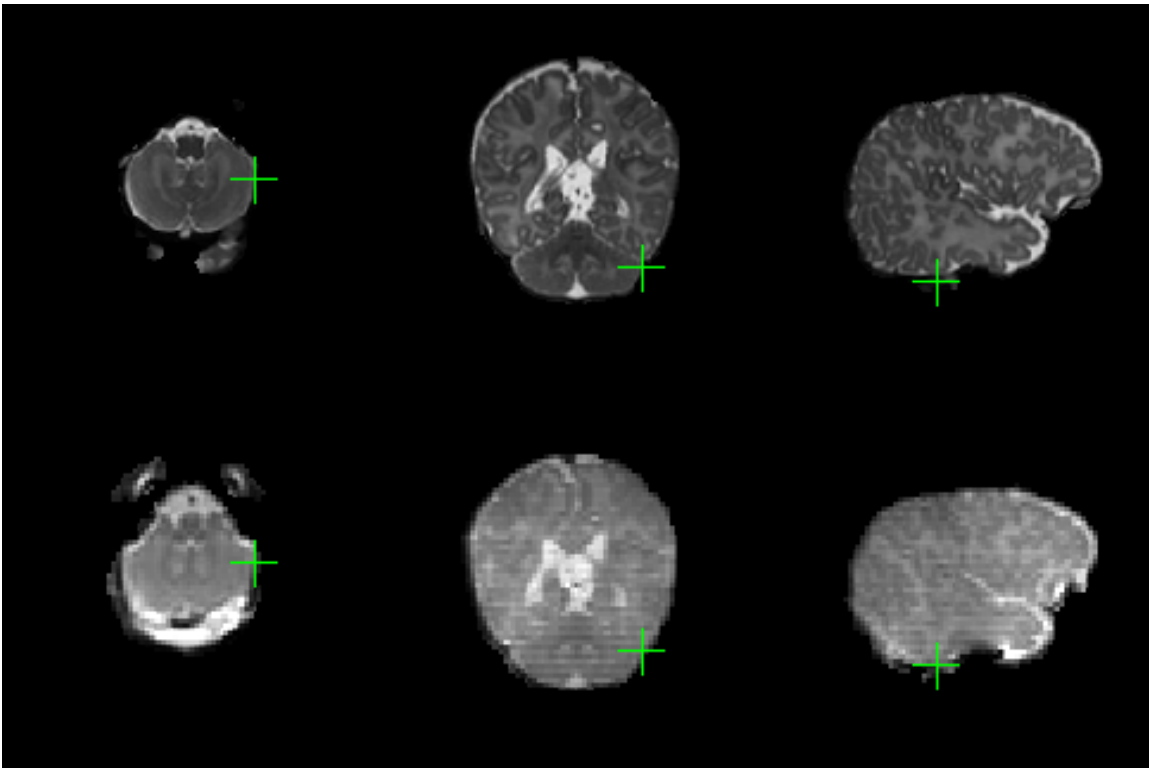


Figure 6.14: Landmark 14 - The most lateral point of the left cerebellar hemisphere

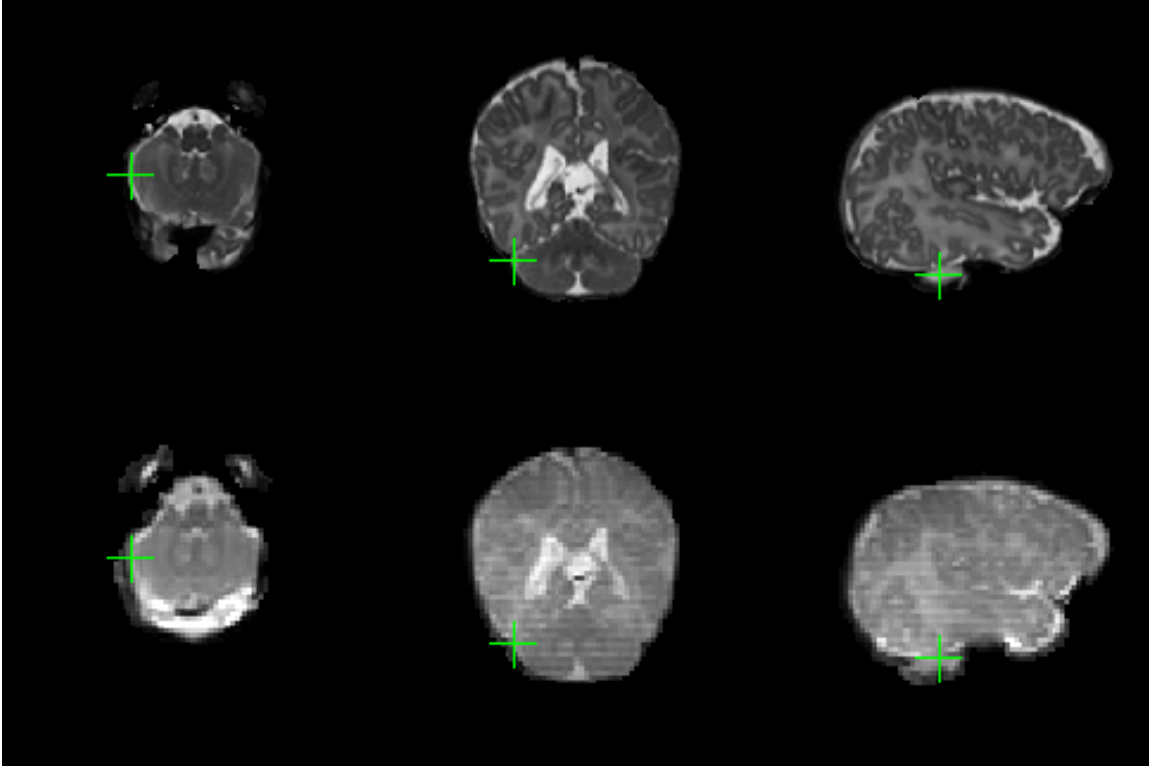


Figure 6.15: Landmark 15 - The most lateral point of the right cerebellar hemisphere

6.4 Results

6.4.1 Optimised B-spline based registration of EPI ($b = 0$ s/mm²) data to high resolution anatomical (T2-weighted FSE) data

Figure 6.16 shows just some of the B-spline based registration models that were attempted in order to align the images. A brief description of the rationale and the results from only the most promising of these are described in the following section.

Initially, only an affine transformation model was used to register the data. This was empirically optimised, and was found to improve correspondence between the $b = 0$ s/mm² image and the T2-weighted FSE image, since it allowed for the correction of subject motion between the acquisition of the two images. The alignment of the deep grey matter structures was particularly good, and subvoxel accuracy could be achieved. However, similar to the results presented below for the FLIRT 7 and FLIRT 12 parameter models, the cortex could not always be robustly aligned, particularly near regions of large geometric distortions in the EPI data.

Given that the magnitude of the distortions present in EPI data are different depending on axial slice position (Figure 6.17), a 2D slice-by-slice registration was attempted. Based on the output of the 3D affine registration model described above, the $b = 0$ s/mm² images were transformed into their corresponding target (T2) space before being resliced to produce equivalent source and target slices. Each $b = 0$ s/mm² slice was then registered to its corresponding target slice using a 2D affine or a 2D affine followed by a 2D nonlinear registration algorithm. Registered slices were then recombined to produce a distortion corrected $b = 0$ s/mm² brain volume. However, as can be seen the nonlinear (Figure 6.18b) transformations applied to neighbouring $b = 0$ s/mm² slices were not necessarily consistent, resulting in obvious discontinuities in the recombined 3D data which were not present in the target data (Figure 6.18c).

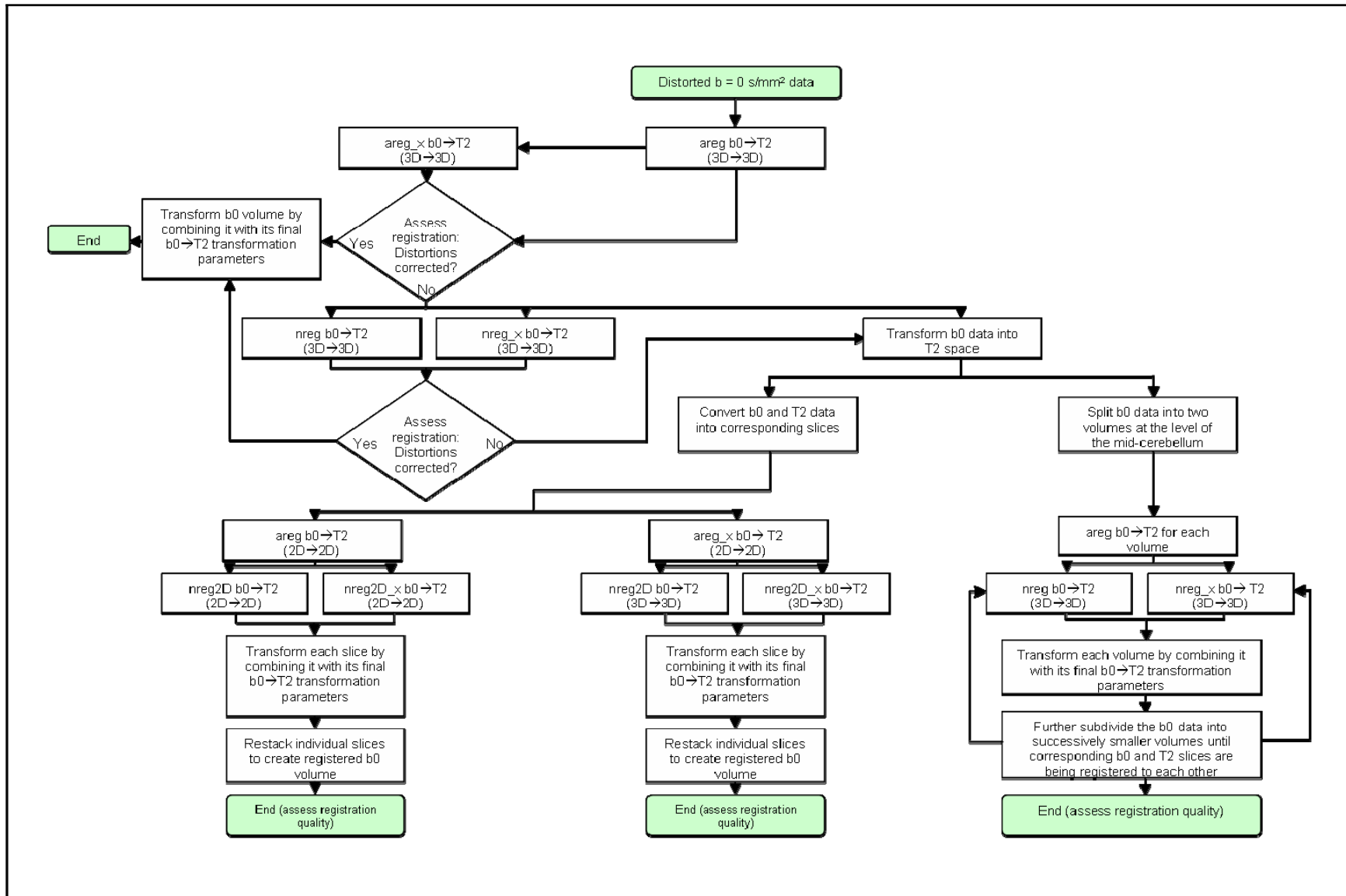


Figure 6.16: An overview of some of the B-spline based registration models used

Key: b0 = echo planar image with no diffusion weighting applied ($b = 0$ s/mm² image); T2 = T2-weighted FSE image; areg = affine registration model; areg_x = linear registration model with transformations limited to the phase encode direction; nreg = nonlinear registration model; nreg_x = nonlinear registration model with transformations limited to the phase encode direction.

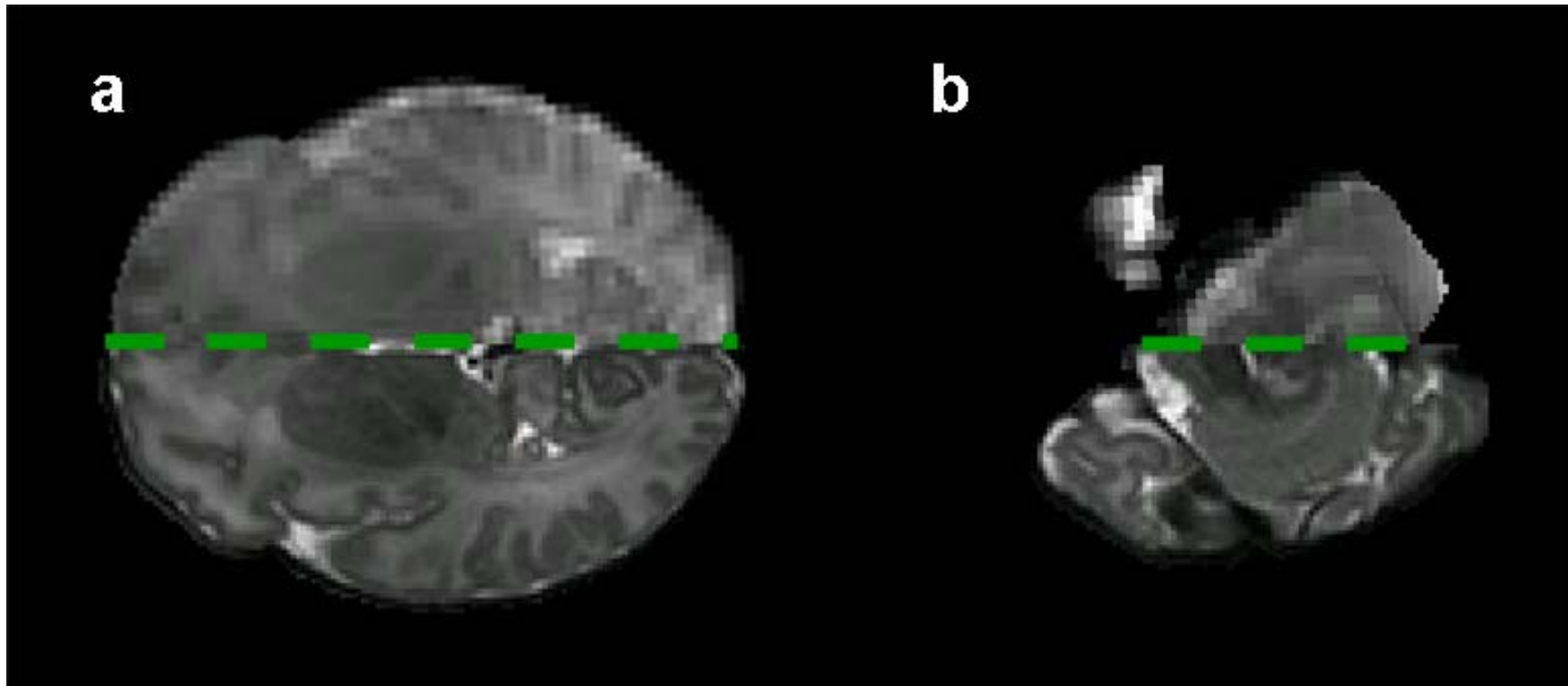


Figure 6.17: Distortions in EPI data in two different slices

Geometric distortion artefacts associated with inhomogeneities in the B0 field are very small at the level of the thalamus in neonatal data, so a transverse $b = 0 \text{ s/mm}^2$ image acquired at this level with an EPI readout (above the hatched line) aligns very well with a coregistered T2-weighted image (below the hatched line) following affine registration (a). The B0 field is very nonuniform at air/bone and bone/tissue interfaces, however, and a transverse $b = 0 \text{ s/mm}^2$ image at the level of the cerebellum (above the hatched line) is still very misaligned with a coregistered T2-weighted image (below the hatched line) following affine registration (b).

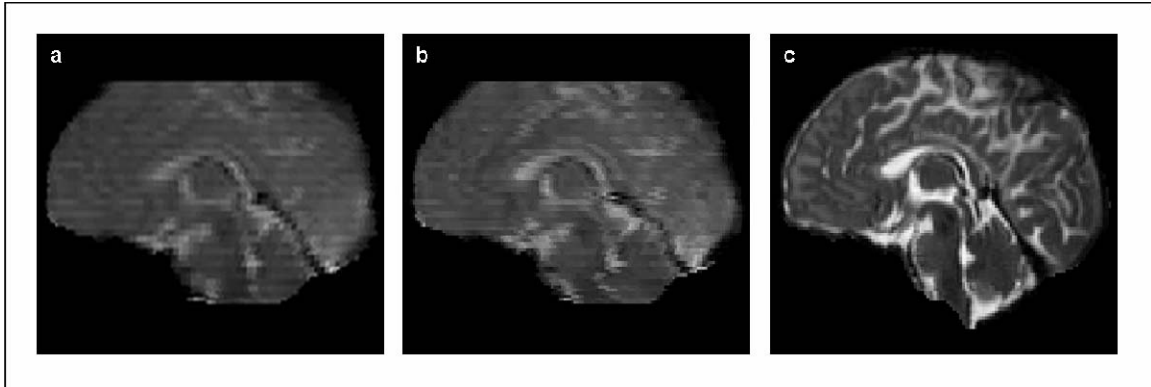


Figure 6.18: Slice-by-slice registration

Unregistered source ($b = 0 \text{ s/mm}^2$) image (a); distortion corrected $b = 0 \text{ s/mm}^2$ brain volume following nonlinear slice-by-slice registration (b); target (T2-weighted FSE) image (c).

In order to improve consistency in the transformations applied to neighbouring slices, subdividing the diffusion data into stacks of consecutive slices where the distortions are similar and registering these to the corresponding T2 data was attempted. This allowed for better initial affine correction of the scaling and shearing distortions in the data prior to further subdividing the two stacks of data in an iterative manner until individual slices were registered (Figure 6.19). However, though this allowed for improved correspondence between images, the repeated reslicing and transforming of the $b = 0 \text{ s/mm}^2$ data resulted in the accumulation of significant interpolation artefacts.

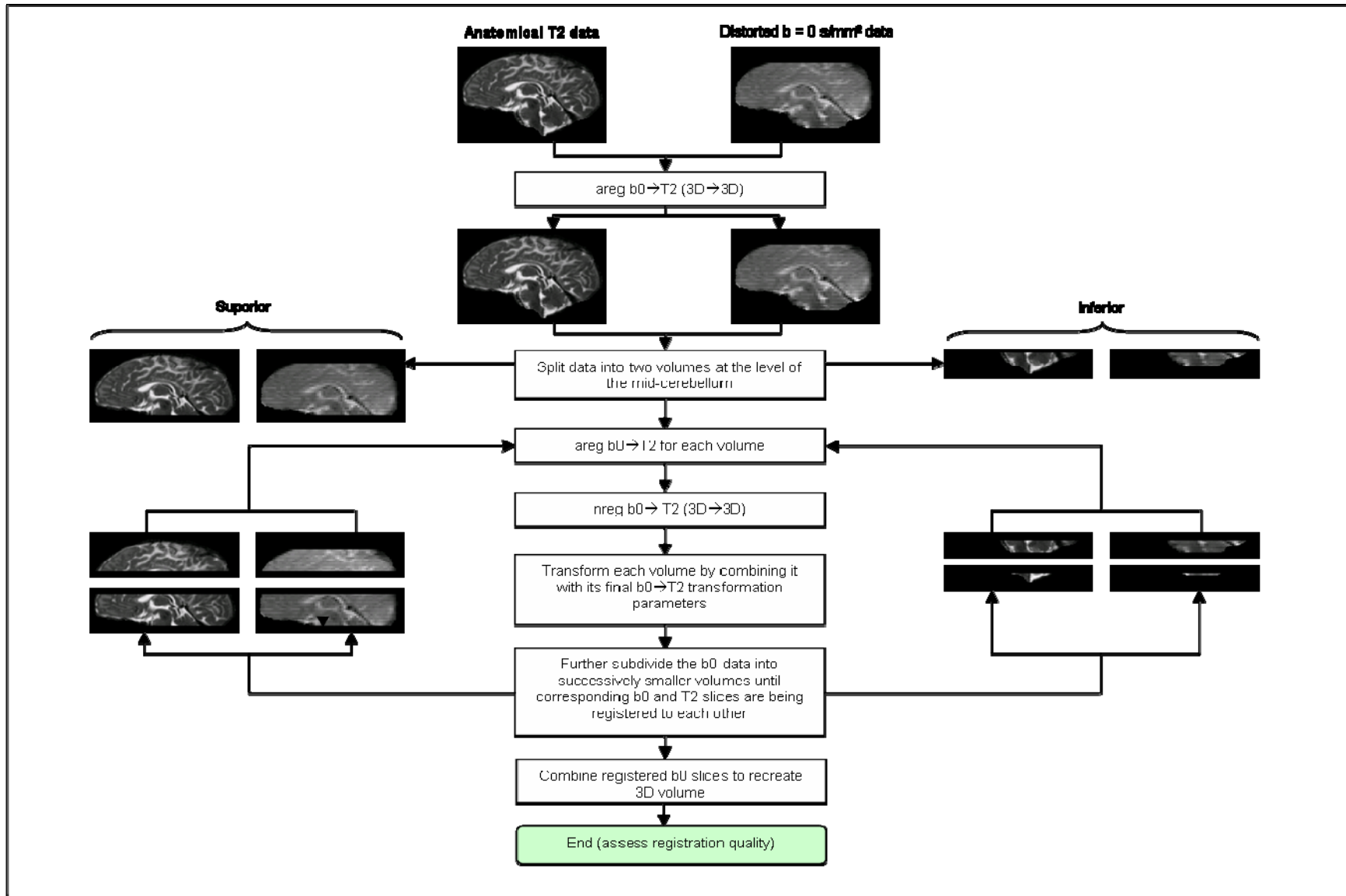


Figure 6.19: A hierarchical distortion correction registration algorithm using free-form deformations based on B-splines

First, the whole brain $b = 0 \text{ s/mm}^2$ image was registered to the T2-weighted image using affine transformations. Following this, the two images were divided into two corresponding axial blocks of slices. Each block of $b = 0 \text{ s/mm}^2$ slices were individually registered to the equivalent block of T2-weighted image slices, first with affine transformations and then with nonlinear transformations. Blocks were then divided again and re-registered, before being further subdivided and registered until individual corresponding $b = 0 \text{ s/mm}^2$ slices and T2-weighted slices were being registered. Registered $b = 0 \text{ s/mm}^2$ slices were then recombined into a 3D volume.

Moving away from slice-by-slice registration approaches, a registration model was then optimised which used the previous estimate from the optimised 3D affine registration model as a starting point for a subsequent 3D nonlinear registration between the two images. This was parameterised to either only permit transformations in the phase-encode direction, or to allow control point displacement that was only regularised by the additional term in the cost function which constrained the transformation to be smooth. It was this final optimised model that consistently produced better alignment between the $b = 0 \text{ s/mm}^2$ images and the anatomical images than all the other B-spline based approaches attempted. A description of the parameters required for the affine and nonlinear registration models can be found in Table 6. The empirically derived values for these parameters in the optimised algorithm are given in Table 6., and it was the results of this method that were compared to the outputs from FLIRT and align_warp.

Option	Description
Number of resolution levels	The number of different control point spacings for the target and source images during registration with a multilevel approach.
Number of bins	The number of bins when constructing the joint histogram for the target and source.
ϵ (Epsilon)	The stopping point for the iterations of the optimisation (the registration terminates when the change in the similarity metric calculated for successive iterations is less than ϵ).
Padding value	Allows exclusion of all image data outside the brain in the target image during registration and cost-function calculation. All voxels with the padding value intensity in the target image are ignored during registration.
Similarity	Image similarity measure used to compare the images.
Interpolation	The interpolation method to compute voxel intensities between control points.
Optimisation method	The optimisation method used when attempting to minimise the chosen cost function.
Source/Target blurring	Both the source and the target image can be blurred by different Gaussian kernels at different resolution levels (e.g. when control point spacing is coarse, the images can be heavily blurred to remove high frequency detail).
Source/Target resolution	Both the source and target image can be resampled at different resolution levels.
Number of iterations	The maximum number of iterations to use during optimisation at each resolution level (the registration will terminate earlier if the difference in the similarity metric calculated for successive iterations is less than ϵ).
Number of steps	The number of steps used when parameters are changed in the optimisation of the transformation parameters.
Length of steps	The amount by which the parameters are incremented when optimising the transformation parameters.
λ_{1-3}	The weighting values for different types of regularisation penalty terms in the cost function. Up to three different regularisation terms can be included in the cost function.
Control point spacing	The spacing between control points. These can be different in the x, y, and z axes and can vary by different amounts at successive resolution levels.

Table 6.3: The parameters required for affine and nonlinear registration of the source and target data using a FFD model based on B-splines

Option	Chosen Parameter (affine model, areg)	Chosen Parameter (nonlinear model, nreg)
Number of resolution levels	3	2
Number of bins	128	128
ϵ (Epsilon)	0.0001	0.0001
Padding value	-1	-1
Similarity	Normalised mutual information	Normalised mutual information
Interpolation	Linear	Sinc
Optimisation method	Gradient descent	Gradient descent
Source blurring (in mm)	Level 1: 1	Level 1: 0
	Level 2: 2	Level 2: 1
	Level 3: 4	
Target blurring (in mm)	Level 1: 0.5	Level 1: 0
	Level 2: 1.0	Level 2: 1
	Level 3: 2.0	
Source resolution (in mm)	Level 1: 2.0 x 2.0 x 2.0	Level 1: 1.75 x 1.75 x 2
	Level 2: 4.0 x 4.0 x 4.0	Level 2: 4.0 x 4.0 x 4.0
	Level 3: 8.0 x 8.0 x 8.0	
Target resolution (in mm)	Level 1: 1.0 x 1.0 x 1.0	Level 1: 0.86 x 0.86 x 1
	Level 2: 2.0 x 2.0 x 2.0	Level 2: 2.0 x 2.0 x 2.0
	Level 3: 4.0 x 4.0 x 4.0	
Number of iterations	Level 1: 20	Level 1: 20
	Level 2: 20	Level 2: 20
	Level 3: 20	
Number of steps	Level 1: 4	Level 1: 4
	Level 2: 4	Level 2: 4
	Level 3: 4	
Length of steps	Level 1: 2	Level 1: 1.5
	Level 2: 4	Level 2: 3.0
	Level 3: 8	
λ_{1-3}	-	$\lambda_1 = 0.1, \lambda_2 = 0, \lambda_3 = 0$
Control point spacing (in mm)	-	Level 1: 10 x 10 x 10
		Level 2: 5 x 5 x 5

Table 6.4: Optimised B-spline registration parameters

The parameters that achieved the best correspondence between the source and target image for both the affine (middle column) and nonlinear (right column) components of the registration algorithm are listed.

6.4.2 Consistency of landmark positioning (fiducial localisation error)

As described in Section 6.3.4.1, in order to assess the reproducibility of landmark positioning in both the unregistered $b = 0$ s/mm² image and the T2-weighted FSE image, in five of the infants' data all fifteen landmarks were placed on both images on three separate occasions. For each of these landmarks in each subject, the mean x, y and z coordinates were found and the Euclidian distance between the mean coordinates and the three independent attempts at landmark placement was calculated. Figure 6.20 shows the mean Euclidian distance from the mean coordinates to the independent attempts in both the $b = 0$ s/mm² image and the T2-weighted image at each of the fifteen landmarks.

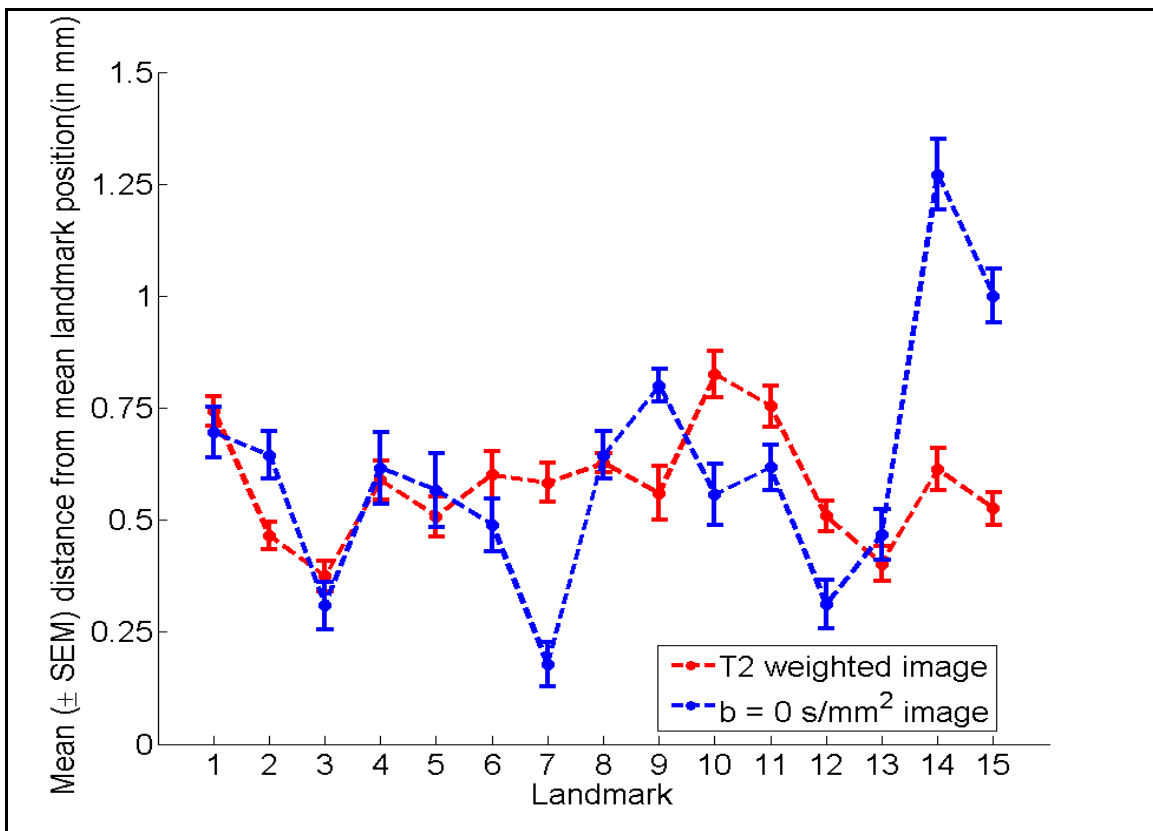


Figure 6.20: Reproducibility of landmark positioning at each landmark

In the histograms below, the data from all landmarks across all subjects is combined for the T2-weighted images (Figure 6.21) and the $b = 0 \text{ s/mm}^2$ images (Figure 6.22). A full statistical analysis of the fiducial localisation error is beyond the scope of this thesis (see for example Wiles (Wiles et al., 2008) or Fitzpatrick (Fitzpatrick et al., 1998) for more details). However, since over 95% of all landmarks were placed within 1 mm of the relevant ‘mean landmark’ in all the $b = 0 \text{ s/mm}^2$ and T2-weighted images, it can be assumed that landmarks can be accurately placed and that this is not a large source of variability when comparing different registration algorithms. The exception to this are those landmarks placed on each subject’s $b = 0 \text{ s/mm}^2$ image at landmarks 14 and 15. These landmarks were placed at the most lateral points of the left and right cerebellar hemispheres. The axial slices on which these were placed contain significant areas of signal loss and pile-up (as can be seen in Figure 6.14 and Figure 6.15), making accurate reproduction difficult, and should be taken into account when comparing registration performance at these two points.

Histograms showing the distance between mean landmark position and the individually placed landmarks for each of the fifteen landmarks are included in Appendix A.

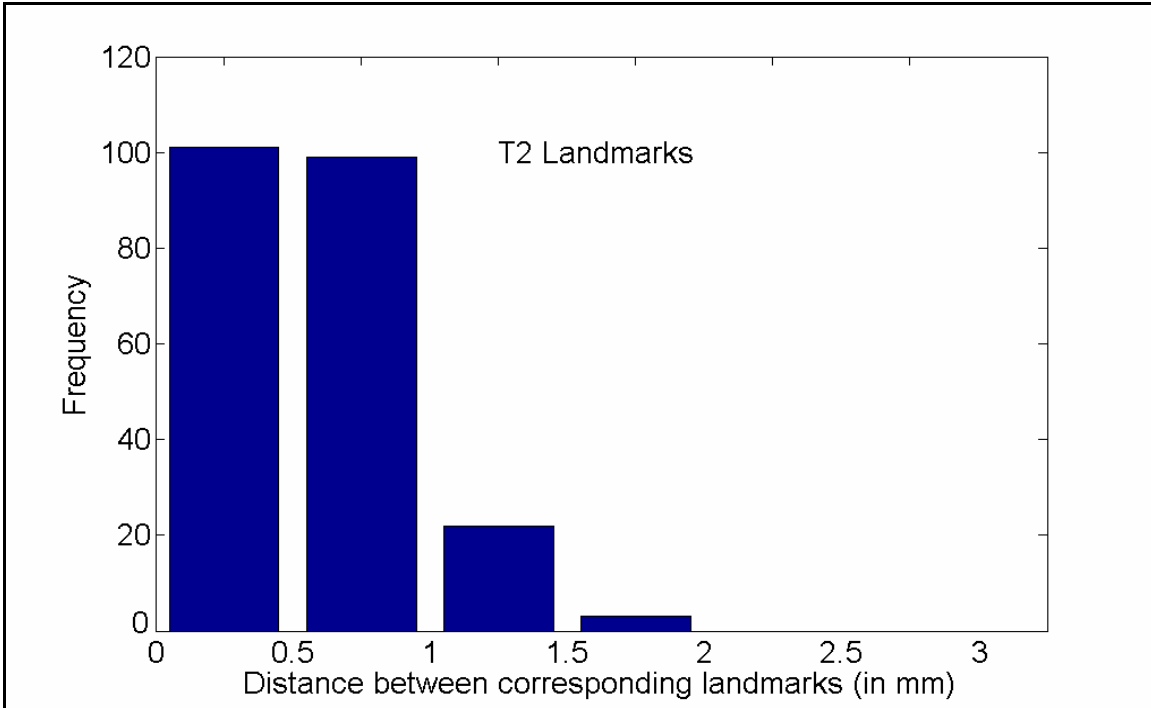


Figure 6.21: A histogram showing the distance between the mean landmark position and the individually placed landmarks for all fifteen landmarks placed on each subject's T2-weighted image

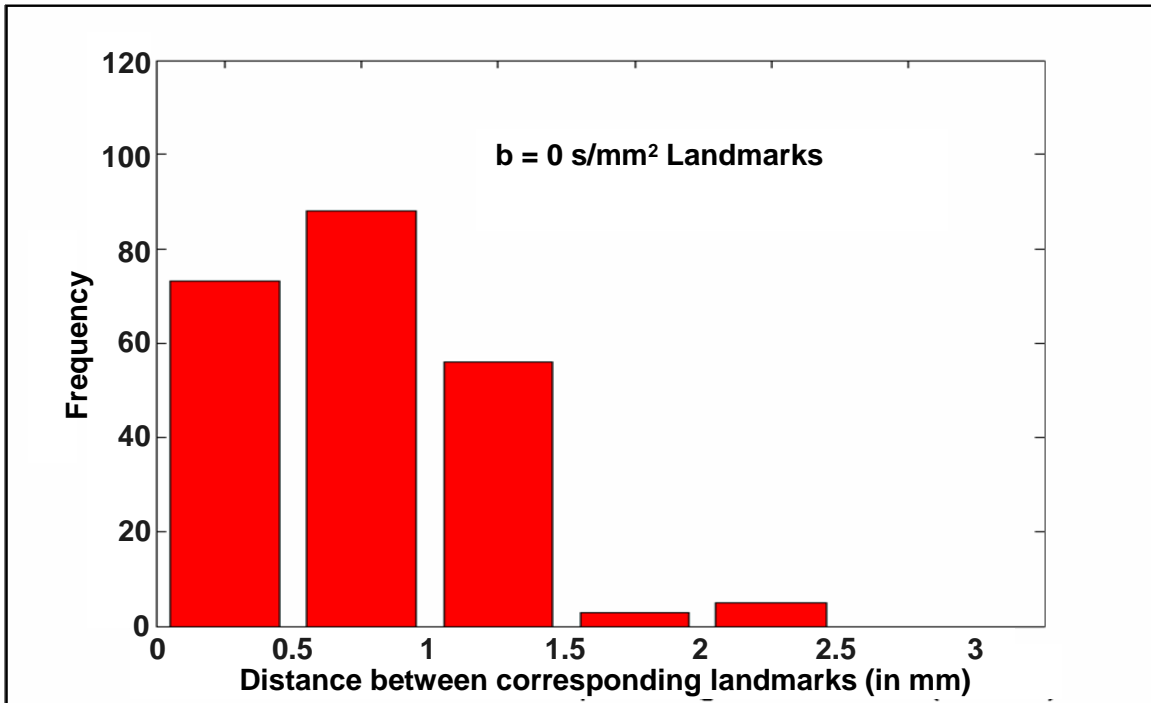


Figure 6.22: A histogram showing the distance between the mean landmark position and the individually placed landmarks for all fifteen landmarks placed on each subject's $b = 0 \text{ s/mm}^2$ image

6.4.3 Visual comparison of optimised B-spline registration algorithm, FLIRT and align_warp

Figure 6.23 shows the correspondence between the T2-weighted image (left of the hatched line) and the $b = 0$ s/mm² image (right of the hatched line) from a representative subject prior to registration (a) and following each of the registration methods used in this study (b-e). In this parasagittal slice it can be seen that the baby has moved between the acquisition of the two images, and before registration they are in obvious misalignment (a). Registering the images using FSL's FLIRT algorithm parameterised by 7 (Figure 6.23b) or 12 (Figure 6.23c) degrees of freedom has successfully matched the borders of the lateral ventricle and cerebral cortex at the level of the hatched line delineating the two images. Nonlinear registration with AIR's align_warp tool initialised by an affine registration (performed using alignlinear) (Figure 6.23d) and using the optimised B-Spline based method (Figure 6.23e) matches this correspondence. However, as can be seen by the deformation field representing the displacements of the initially regularly-spaced control points (Figure 6.23f), in order to match the images in other regions of the slice required significant amounts of nonlinear warping.

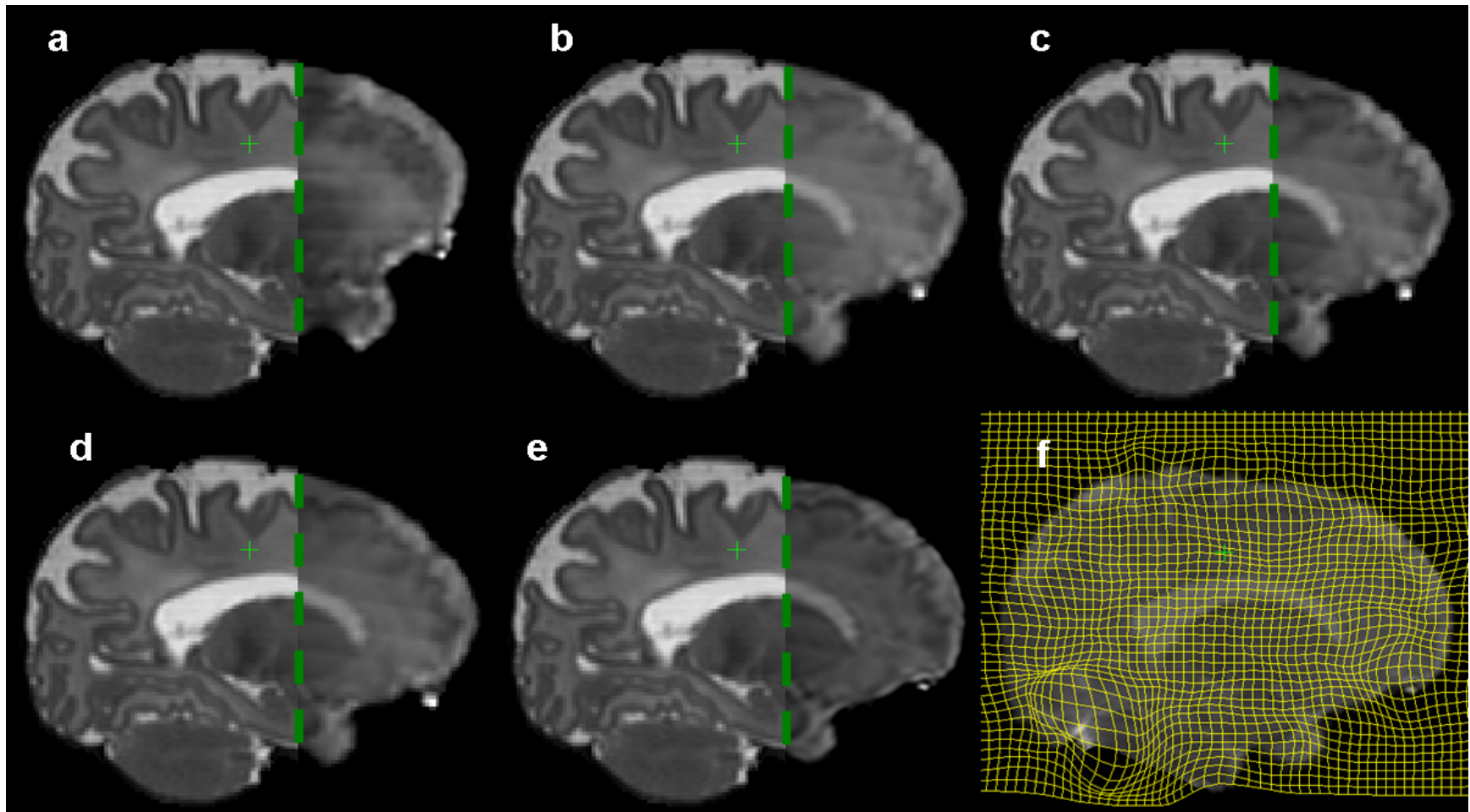


Figure 6.23: T2-weighted (left of hatched line) and $b = 0 \text{ s/mm}^2$ (right of hatched line) image correspondence before and after registration (sagittal slice)

Unregistered image (a); registration with FLIRT 7 DOF transformation model (b); registration with FLIRT 12 DOF transformation model (c); nonlinear registration using AIR's align_warp tool (d); nonlinear registration using the proposed optimised B-spline based registration algorithm (e); the B-spline based registration algorithm's deformation field (f).

Although both the 7 and 12 degree of freedom affine transformation models with the appropriate registration parameters in FLIRT could align anatomy at the level of the previous sagittal image, Figure 6.24b and 6.24c show that in the presence of local distortions in addition to movement between the acquisition of the images an affine model is insufficient to accurately register the anatomy. Although the deep grey matter is again well aligned, the cortex is misregistered (arrows). This cannot be corrected by a limited degree of freedom nonlinear registration using the align_warp tool in AIR, which was initialised using an affine transformation model (Figure 6.24d). Using the proposed optimised B-spline model, however, correspondence between both cortical as well as deep grey matter can be achieved.

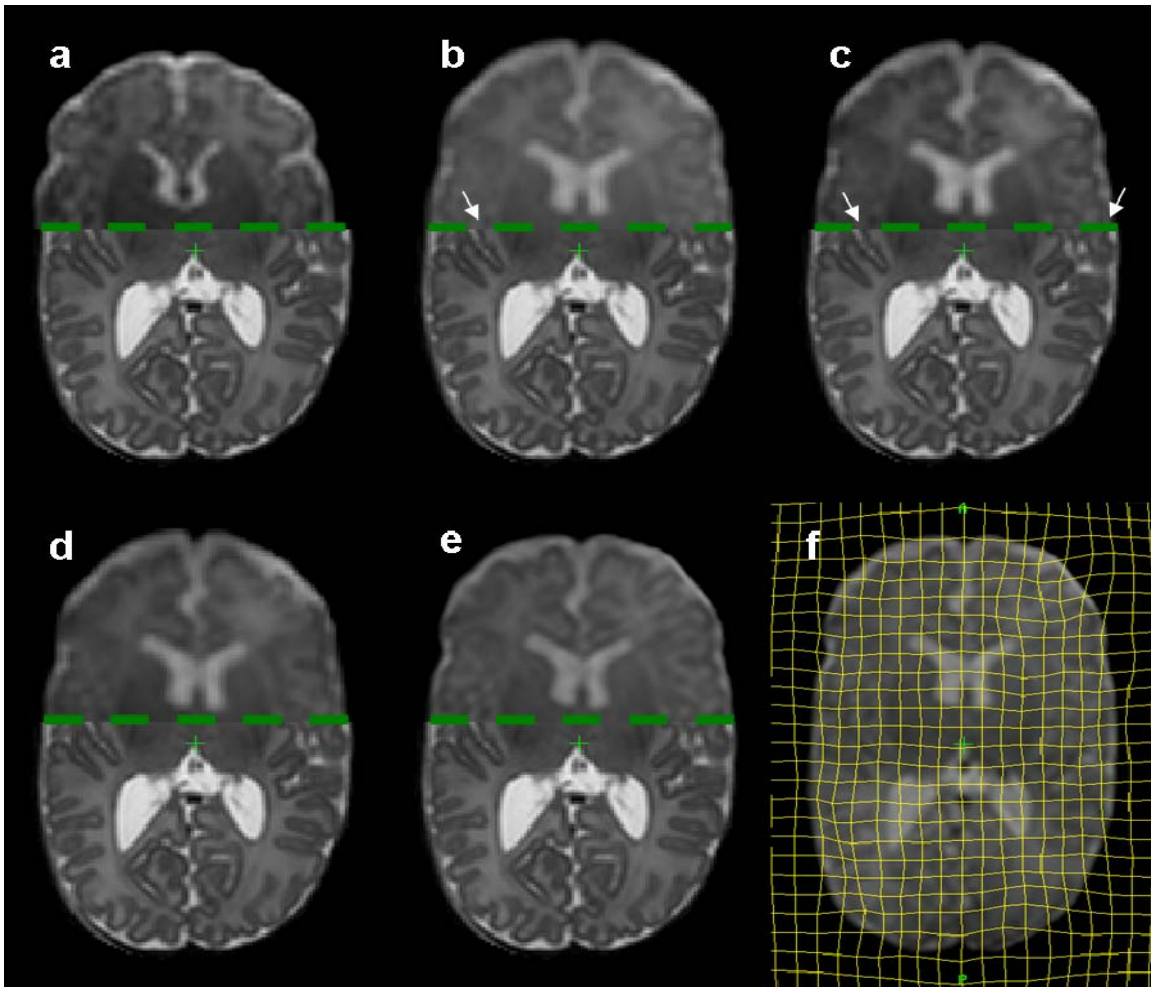


Figure 6.24: T2-weighted (below hatched line) and $b = 0$ s/mm² (above of hatched line) image correspondence before and after registration (axial slice)
 Unregistered image (a); registration with FLIRT 7 DOF transformation model (b); registration with FLIRT 12 DOF transformation model (c); nonlinear registration using AIR's align_warp tool (d); nonlinear registration using the proposed optimised B-spline based registration algorithm (e); the B-spline based registration algorithm's deformation field (f).

In this coronal slice from the same infant, the FLIRT linear transformation models have provided good alignment between the two images (Figure 6.25b and c). However, registration with the AIR nonlinear (align_warp) model has not been as successful, despite the increased degrees of freedom allowed (Figure 6.25d). Good correspondence between the ventricles or inferior portions of the parietal cortex between the images at this level has not been achieved (arrows).

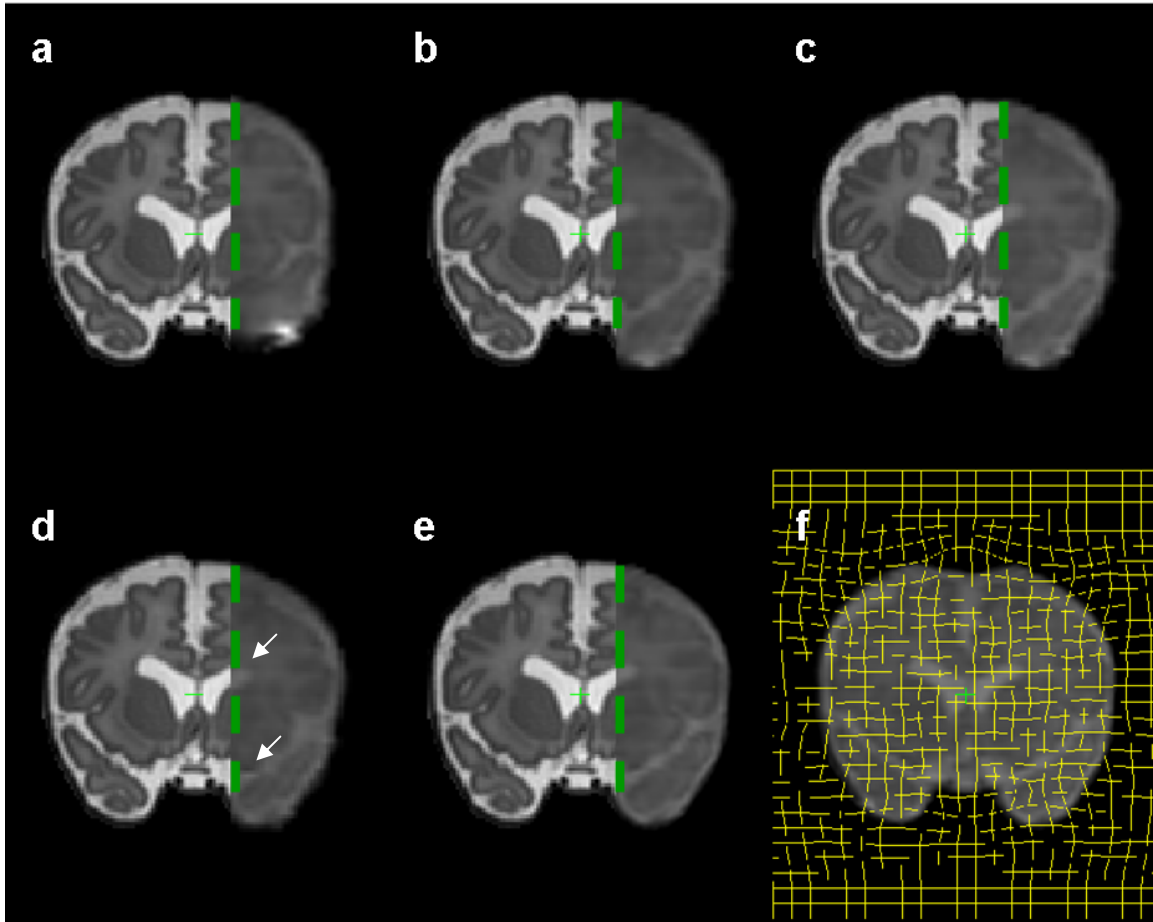


Figure 6.25: T2-weighted (left of hatched line) and $b = 0 \text{ s/mm}^2$ (right of hatched line) image correspondence before and after registration (coronal slice)

Unregistered image (a); registration with FLIRT 7 DOF transformation model (b); registration with FLIRT 12 DOF transformation model (c); nonlinear registration using AIR's align_warp tool (d); nonlinear registration using the proposed optimised B-spline based registration algorithm (e); the B-spline based registration algorithm's deformation field (f).

6.4.4 Landmark-based comparison of optimised B-spline registration algorithm, FLIRT and align_warp

6.4.4.1 *Overall comparison of registration performance (fiducial registration error)*

Figure 6.26 shows histograms of the difference between corresponding landmarks on the $b = 0$ s/mm² and T2-weighted images prior to registration (a) and following registration with the FLIRT 7 DOF (b), FLIRT 12 DOF (c), AIR nonlinear (d) and optimised B-spline (e) models. Registration with all models reduces the variance in the distribution of differences between corresponding landmarks.

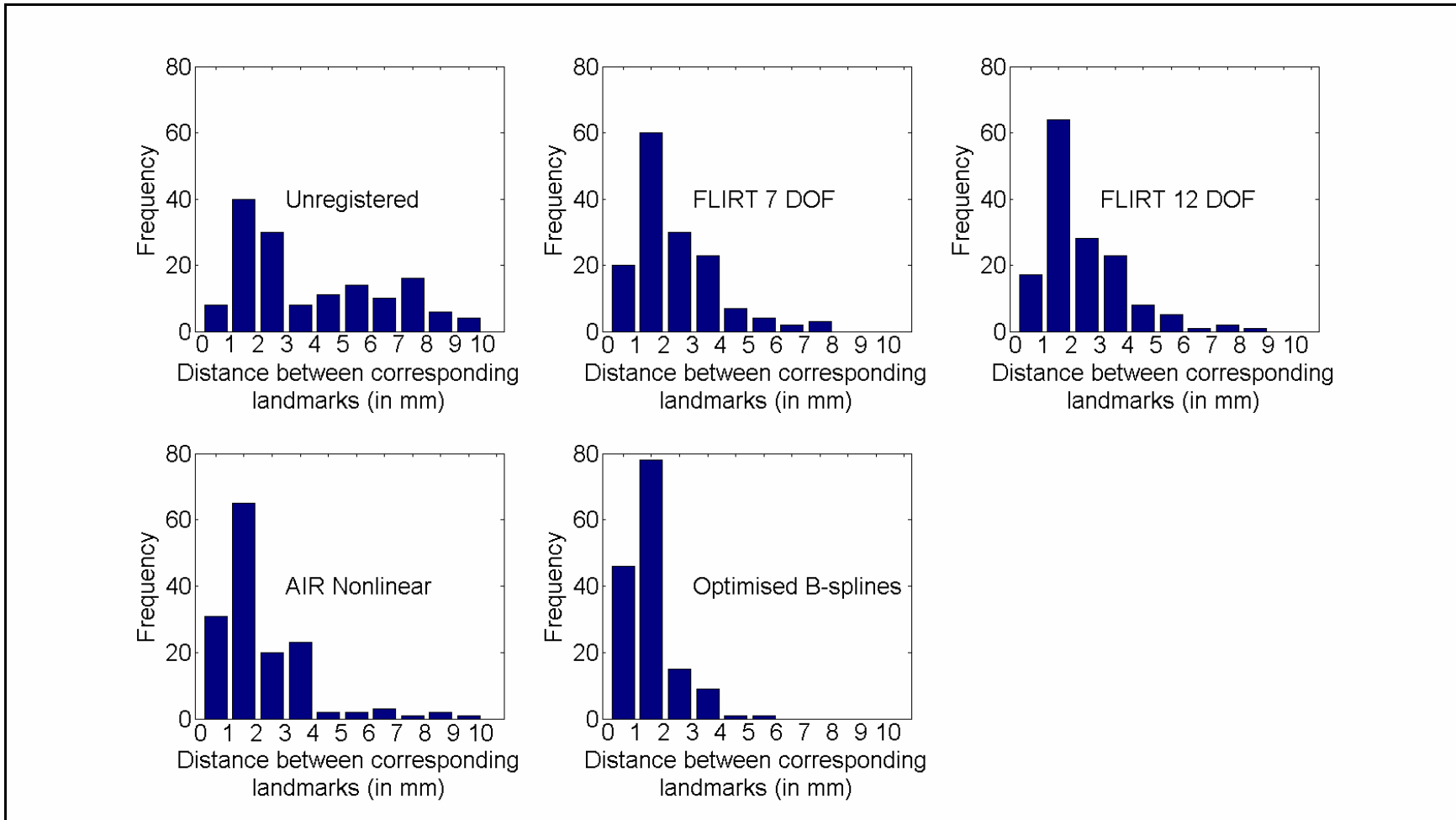


Figure 6.26: Histograms of the difference between corresponding landmarks on the $b = 0 \text{ s/mm}^2$ and T2-weighted images prior to and following registration with the different models used

6.4.4.2 Registration performance across subjects (fiducial registration error)

Table 6. shows the mean distance between corresponding landmarks in the $b = 0$ s/mm² and T2-weighted images before registration (second row) and following registration with the FLIRT 7 DOF (third row) and 12 DOF (fourth row) models, AIR's align_warp tool (fifth row) and after using the optimised B-spline registration (sixth row) on a subject-by-subject basis. Across all subjects, registration with FLIRT and with the optimised B-spline algorithm resulted in smaller mean distances between corresponding landmarks in the T2-weighted and transformed $b = 0$ s/mm² images than between the T2 images and the unregistered $b = 0$ s/mm² images. In general, registration using AIR's align_warp algorithm with the parameters listed in Table 6. also improved correspondence, but the performance was more variable. The mean distances between corresponding landmarks were larger following registration in subjects 3 ($p = 0.21$), 6 ($p < 0.005$) and 7 ($p < 0.05$). This was reflected in the registered $b = 0$ s/mm² images in these subjects, which were still in obvious misalignment with the target T2-weighted image following registration. Table 6. is presented as a line graph in Figure 6.27.

	Subject									
	1	2	3	4	5	6	7	8	9	10
Unregistered	2.41 ± 0.32	2.57 ± 0.41	3.07 ± 0.43	6.95 ± 0.46	7.15 ± 0.39	1.71 ± 0.20	1.61 ± 0.14	5.83 ± 0.55	1.68 ± 0.18	6.57 ± 0.45
FLIRT 7 DOF	2.18 ± 0.21	2.39 ± 0.40	2.74 ± 0.35	2.53 ± 0.39	2.24 ± 0.30	1.67 ± 0.19	1.55 ± 0.11	4.10 ± 0.81	1.35 ± 0.17	3.16 ± 0.40
FLIRT 12 DOF	2.25 ± 0.21	2.41 ± 0.40	2.76 ± 0.36	2.56 ± 0.40	2.10 ± 0.27	1.62 ± 0.18	1.29 ± 0.18	3.98 ± 0.81	1.36 ± 0.18	3.18 ± 0.41
AIR Nonlinear	1.43 ± 0.13	1.59 ± 0.12	3.51 ± 0.75	2.92 ± 0.55	2.32 ± 0.38	2.64 ± 0.41	2.14 ± 0.24	1.83 ± 0.35	1.67 ± 0.26	1.70 ± 0.25
Optimised B-Spline	1.37 ± 0.14	1.45 ± 0.19	1.69 ± 0.24	2.19 ± 0.26	1.44 ± 0.21	1.07 ± 0.18	1.48 ± 0.22	1.38 ± 0.23	1.06 ± 0.16	1.15 ± 0.17

Table 6.5: Mean differences (\pm SEM) in mm between corresponding landmarks in the T2-weighted and $b = 0$ s/mm² image on a subject-by-subject basis

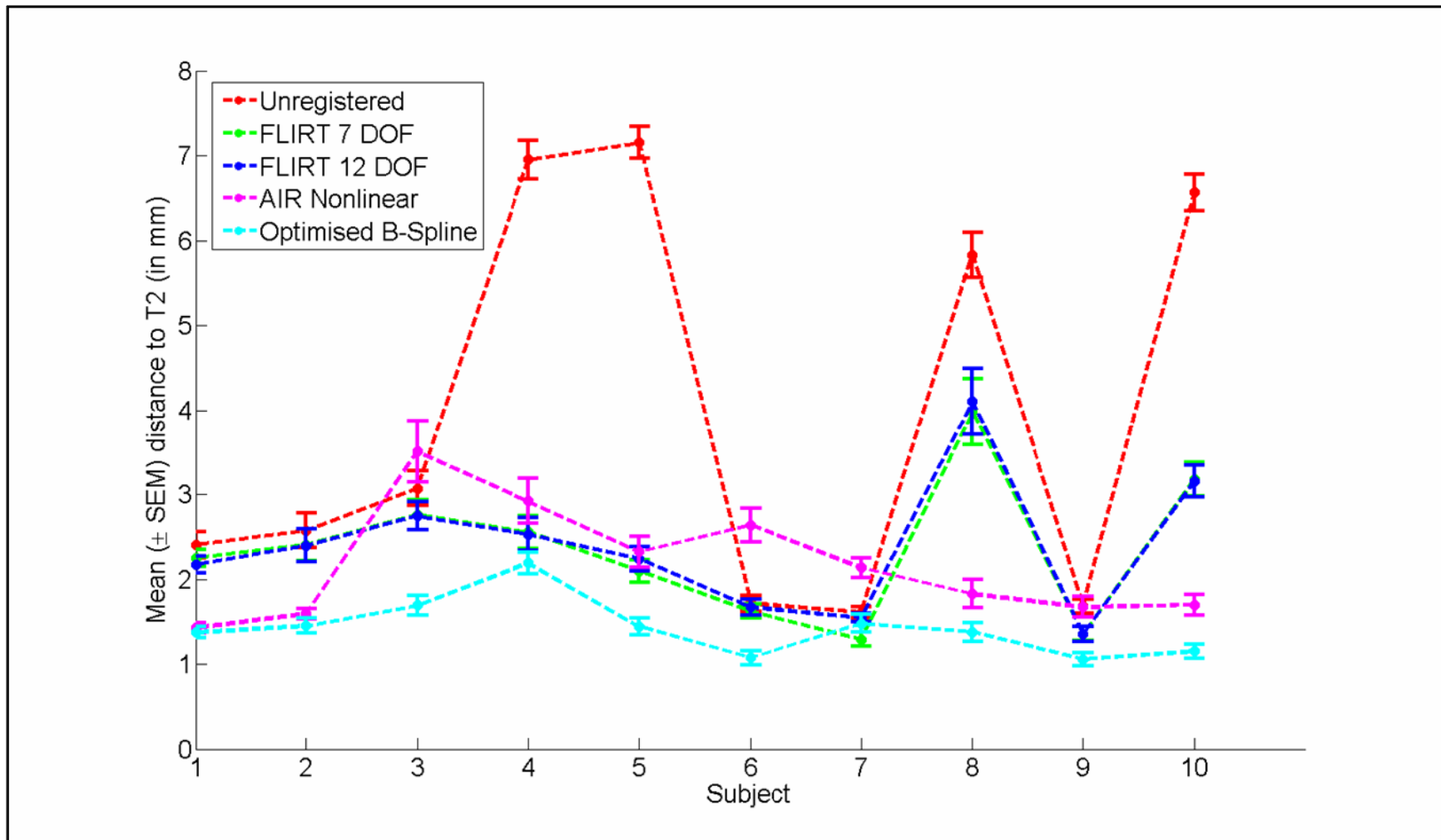


Figure 6.27: Registration performance across subjects

Each line represents the Mean differences (\pm SEM) in mm between corresponding landmarks in the T2-weighted and $b = 0$ s/mm² image on a subject-by-subject basis.

6.4.4.3 Registration performance across landmarks (fiducial registration error)

Table 6. shows the mean distance between corresponding landmarks in the $b = 0 \text{ s/mm}^2$ and T2-weighted images before registration (second row) and following registration with the FLIRT 7 DOF (third row) and 12 DOF (fourth row) models, following AIR's align_warp tool (fifth row) and after using the optimised B-spline registration (sixth row) on a landmark-by-landmark basis. This is represented as a line graph in Figure 6.28. Across all landmarks, compared to the unregistered data there was a general trend of registration with FLIRT parameterised by 7 DOF (third row) and 12 DOF (fourth row) improving correspondence with the T2-weighted data. This was generally true of registration with AIR's nonlinear tool (fifth row), except for correspondence of landmark 15 between the source and target image following registration. In all cases, registration with the optimised B-spline method decreased corresponding landmark distances relative to the unregistered image.

	Landmark														
	1	2	3	4	5	6	7	8	9	10	11	12	13	14	15
Unregistered	3.41 ± 0.78	3.44 ± 0.76	3.93 ± 0.89	3.57 ± 0.87	3.98 ± 1.03	3.71 ± 0.75	3.80 ± 0.77	5.91 ± 1.09	5.25 ± 0.79	3.67 ± 0.80	3.65 ± 0.62	3.09 ± 0.64	4.22 ± 0.94	4.49 ± 1.11	3.22 ± 0.70
FLIRT 7 DOF	1.93 ± 0.22	1.91 ± 0.39	2.46 ± 0.72	2.27 ± 0.70	3.23 ± 0.91	1.64 ± 0.26	2.35 ± 0.37	2.70 ± 0.57	3.05 ± 0.42	2.18 ± 0.58	1.73 ± 0.37	2.18 ± 0.31	1.75 ± 0.27	3.19 ± 0.64	2.68 ± 0.50
FLIRT 12 DOF	1.97 ± 0.21	1.93 ± 0.39	2.39 ± 0.75	2.22 ± 0.70	3.18 ± 0.92	1.70 ± 0.23	2.40 ± 0.37	2.73 ± 0.56	2.91 ± 0.42	2.20 ± 0.54	1.71 ± 0.39	2.32 ± 0.36	1.95 ± 0.24	3.27 ± 0.63	2.98 ± 0.43
AIR Nonlinear	1.31 ± 0.14	1.30 ± 0.11	2.23 ± 0.19	2.77 ± 0.34	2.88 ± 0.46	1.35 ± 0.15	1.14 ± 0.21	2.05 ± 0.24	1.92 ± 0.22	1.56 ± 0.26	1.43 ± 0.28	2.81 ± 0.73	1.50 ± 0.40	4.26 ± 0.54	4.09 ± 0.98
Optimised B-Spline	1.04 ± 0.14	0.92 ± 0.14	1.77 ± 0.25	2.21 ± 0.30	1.89 ± 0.28	1.07 ± 0.21	1.11 ± 0.18	1.46 ± 0.22	1.65 ± 0.18	1.34 ± 0.15	1.48 ± 0.15	0.77 ± 0.18	1.59 ± 0.37	1.50 ± 0.22	1.62 ± 0.46

Table 6.6: Mean differences (\pm SEM) in mm between corresponding landmarks in the T2-weighted and $b = 0$ s/mm² image on a landmark-by-landmark basis

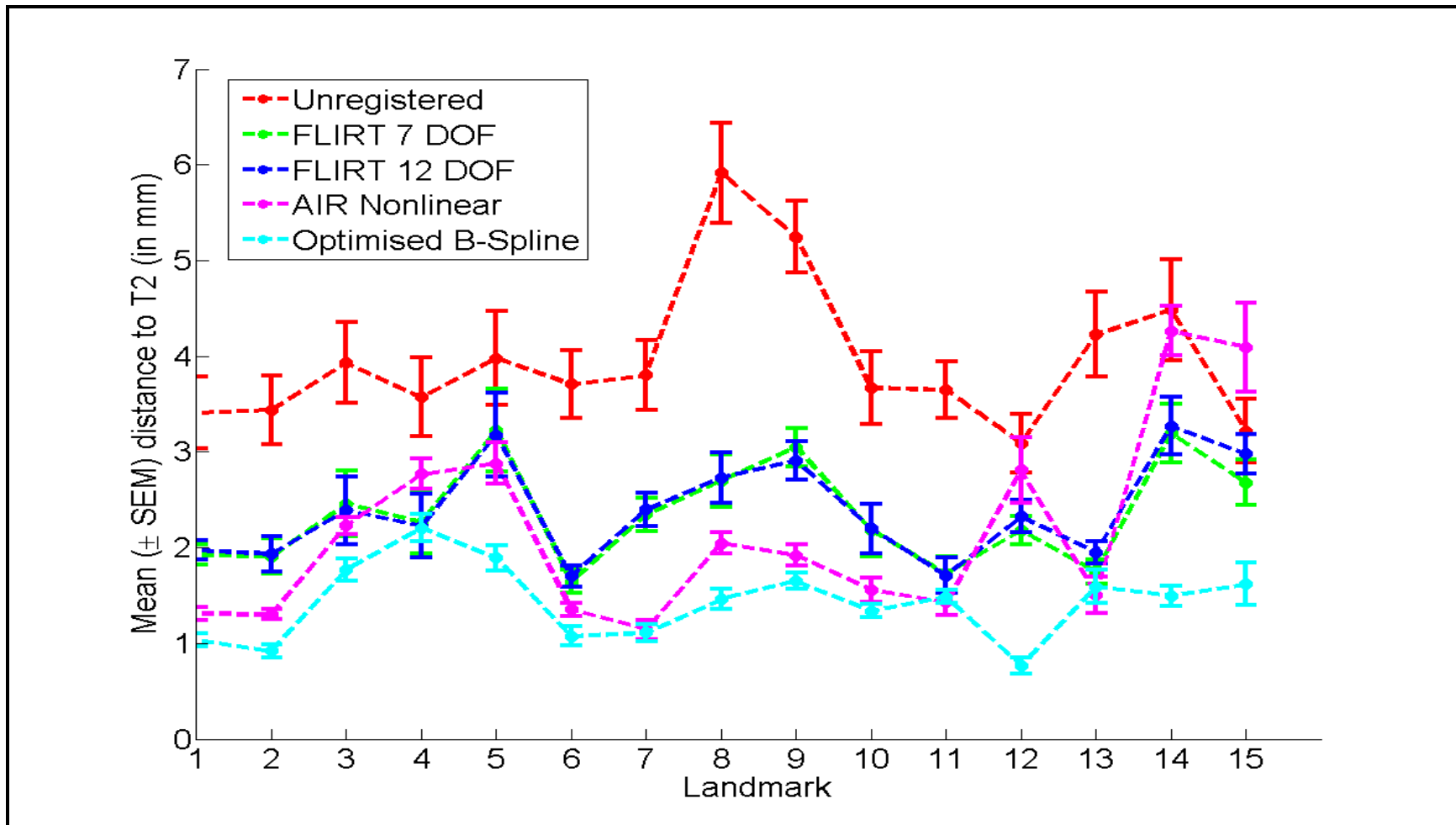


Figure 6.28: Registration performance across landmarks

Each line represents the mean distance between corresponding landmarks in the T2-weighted and $b = 0$ s/mm² image on a landmark-by-landmark basis prior to (red line) and following registration with the FLIRT 7 DOF (green line) and 12 DOF (blue line) models, the nonlinear registration tool in AIR (magenta line) and the optimised B-spline method (cyan line).

6.4.4.4 *Statistical comparison of registration performance*

Mann-Whitney U tests were performed to assess whether different registration methods improved landmark correspondence with the T2-weighted image compared to the unregistered $b = 0 \text{ s/mm}^2$ image and each of the other registration methodologies for each of the fifteen landmarks (Appendix B). To summarise the results, the two FLIRT models significantly improved correspondence between landmarks 6, 8, 9 (12 DOF model only) and 11 in the $b = 0 \text{ s/mm}^2$ image and the T2-weighted image ($p < 0.05$ in all cases). This was matched by the AIR's nonlinear model, which also significantly reduced the distance between Landmarks 1, 7 and 10 in the two images ($p < 0.05$). The optimised B-spline model proposed here further improved correspondence between the two images at the positions of Landmarks 2, 12, 13 and 14.

Table 6. and Figure 6.29 statistically summarise the data across all subjects and all landmarks. Table 6. is a significance matrix comparing registration performance between the different models used with a Mann-Whitney U test. All the algorithms significantly improved alignment between $b = 0 \text{ s/mm}^2$ and T2-weighted images from the same subject. No improvement was found using either the FLIRT 12 DOF model or the AIR nonlinear model relative to the FLIRT 7 DOF model. Registration using the optimised B-spline method was found to significantly improve correspondence compared to all the other methods (Figure 6.29).

	<i>Unregistered</i>	<i>FLIRT 7 DOF</i>	<i>FLIRT 12 DOF</i>	<i>AIR Nonlinear</i>	Optimised B-spline
Unregistered	-				
FLIRT 7 DOF	7.74×10^{-7}	-			
FLIRT 12 DOF	2.52×10^{-6}	1	-		
AIR Nonlinear	1.34×10^{-8}	1	1	-	
Optimised B-spline	4.07×10^{-21}	2.76×10^{-7}	7.03×10^{-9}	2.42×10^{-6}	-

Table 6.7: Significance matrix for all landmarks in all subjects (p-values corrected for multiple comparisons using a Bonferroni correction)

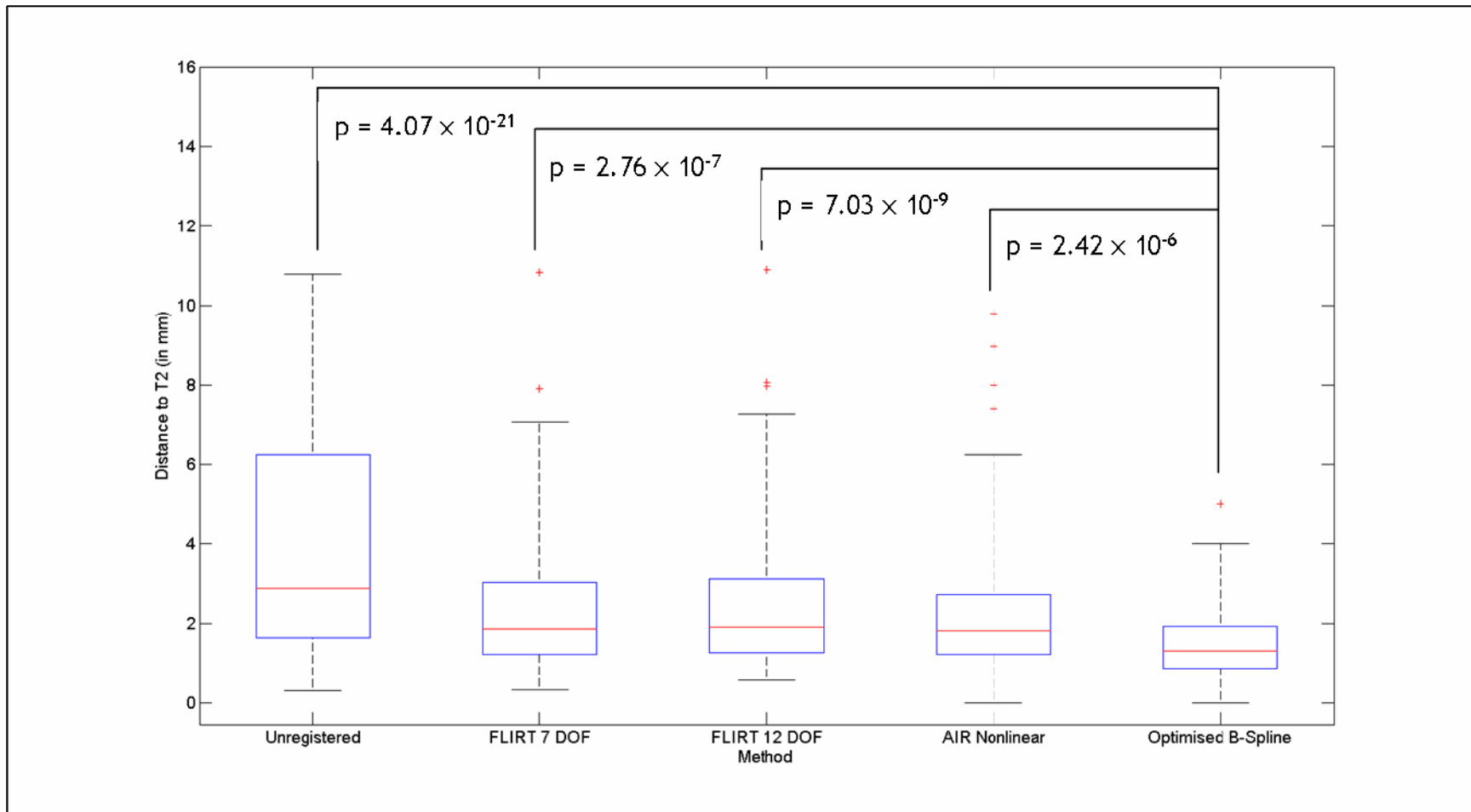


Figure 6.29: Box and whisker diagrams for final corresponding landmark distances using the different registration models
 The red lines represent the median values of the distances between corresponding landmarks in the $b = 0 \text{ s/mm}^2$ and T2-weighted images. The boxes represent the inter-quartile range and the whiskers the range. Outliers, greater than twice the inter-quartile range from the median value, are represented by asterisks. Registration using the optimised B-spline method significantly improved correspondence compared to all other methods used.

6.5 Discussion

In this study, the partial optimisation of a nonlinear registration algorithm based on B-splines was developed for the retrospective correction of distortions in neonatal DTI data. This is was achieved by coregistering $b = 0$ s/mm² data acquired with an EPI readout to high resolution anatomical T2-weighted data, with the eventual aim of facilitating subsequent group-wise analysis of DTI data from the whole of the brain. In the absence of a ground truth, the success of the optimised algorithms were assessed by manually placing corresponding landmarks throughout the brain (as in Woods et al., 1998b) on the T2-weighted and unregistered $b = 0$ s/mm² images, and measuring the Euclidian distances between the points before and after registration. The most accurate and robust of the optimised methods developed in this study was found to consist of two steps. First of all, an affine transformation model was estimated, using the parameters in column two of Table 6. The output from this affine registration was in turn used as the starting point for nonlinear registration using the B-spline-based multi-level free-form deformation model with the parameters listed in column three of Table 6. Under the model used, the global and the local components of the transformation were then combined by addition (Rueckert et al., 1999):

$$T(x', y', z') = T_{global}(x, y, z) + T_{local}(x, y, z)$$

The use of a dilated padding mask to exclude voxels outside the brain in the target image when calculating the cost function during each intermediate step in the registration process makes the algorithm highly computationally efficient, and for each subject the registration of the $b = 0$ s/mm² image to the T2-weighted image took less than one hour on a standard workstation.

The performance of the algorithm was compared to two widely used registration algorithms, FLIRT, a linear registration tool, and align_warp, a nonlinear transformation model defined by higher order polynomials, with parameters appropriate for this registration problem. It was found that using any of these methods significantly improved

the alignment between corresponding landmarks in the two images. Combining the data from all ten subjects included in the study, it was found that the difference between corresponding landmarks in the $b = 0 \text{ s/mm}^2$ and T2-weighted images was $\leq 4 \text{ mm}$ in 98% and $\leq 2 \text{ mm}$ in 83% of cases following registration with the optimised B-spline algorithm. This was compared to equivalent landmarks being $\leq 4 \text{ mm}$ in only 57% and $\leq 2 \text{ mm}$ in 32% of cases prior to registration, and $\leq 4 \text{ mm}$ in 86% and $\leq 2 \text{ mm}$ in 53% of cases following registration with FLIRT's 12 DOF model. In the majority of instances, registration with the B-spline model has therefore achieved subvoxel accuracy between the images, at least as measured at the points where the landmarks were placed. Registration was least successful in aligning the most anterior parts of the left and right cerebral hemispheres (Landmarks 3 and 4), placed on axial slices in the unregistered EPI image where distortions due to magnetic field inhomogeneities were pronounced. In comparison, registration was most successful in matching the most posterior point of the fourth ventricle (Landmark 12), where contrast between the CSF and cerebellum was high; across all subjects, the mean distance here between equivalent landmarks was $< 1 \text{ mm}$. In general, however, the registration algorithm proposed here improved correspondence fairly uniformly across all landmarks (Figure 6.28).

The algorithm has also proved to be relatively robust in coregistering $b = 0 \text{ s/mm}^2$ and T2-weighted image data across different subjects. This is in contrast to the `align_warp` algorithm incorporated in AIR, which proved to be as successful as the optimised B-spline method in coregistering some subjects' data, but worse than the FLIRT models in coregistering data from other subjects (Figure 6.27). The reasons for this are unclear, but are likely to be related to the similarity metric computed when assessing the performance of different transformation parameters. `Align_warp` does not allow specification of the cost function to be used; by default, the registration algorithm attempts to minimise the sum of squared differences (Section 2.7.3.1.1) between the two images to be aligned. This is appropriate for intramodality registration, and given that, like the FSE image, the $b = 0 \text{ s/mm}^2$ image is also predominantly T2-weighted, can be used to align these images with some success. However, regions of signal pile-up and related signal loss in the EPI data are not present in the undistorted T2-weighted image and may suggest why this

registration model is not as successful in matching landmarks placed in regions with large geometric distortions in the $b = 0$ s/mm² image. Defining the align_warp transformation model with lower (second and third) or higher (fifth or sixth) order polynomials did not appear to resolve this problem. Indeed, as described by Szeliski and Lavallée (Szeliski and Lavallée, 1996), the use of higher order polynomials resulted in artefacts that slightly degraded the quality of the registered image.

Such registration-induced artefacts are far less pronounced using spline-based methods, and group-wise studies of MR neuro-imaging data that used B-spline registration to align the images are increasingly common in the literature (see for example Rao et al., 2004; Bhatia et al., 2004; Boardman et al., 2006; Smith et al., 2006; Rueckert et al., 2006a; Rueckert et al., 2006b; Gousias et al., 2007; Aljabar et al., 2008).

6.6 Limitations

It is important to note, however, that registration methods cannot retrospectively correct for all the different types of distortion present in echo-planar diffusion MRI data. As discussed in Section 2.6.1.2, signal blurring may result due to different points in k-space experiencing different amounts of transverse decay during the long readout times required in single-shot EPI. This blurring, which occurs predominantly along the phase encode direction can only be minimised at source. In this study, this was attempted by the use of parallel imaging to reduce the echo train length (SENSE; Pruessmann et al., 1999). Nyquist ghosting and the incomplete suppression of signal from fat can induce additional artefacts in the data, though these were not seen in any of the images in the current study. As previously described, there were considerable distortions in the EPI data associated with inhomogeneities in the B₀ field. These were most pronounced in the transverse slices acquired at the level of the cerebellum, where the different magnetic susceptibilities of air, bone and brain led to inaccuracies in the localisation of the MR signal, and

therefore regions of signal loss and signal pile-up. When registering this data to the anatomical T2-weighted data, the optimised B-spline method attempted to ‘fill in’ regions of signal loss by ‘pulling back’ some of the data from regions of signal pile-up. This was purely based on an attempt to match intensities at corresponding locations in the source and target image, without any knowledge of what the true spatial location of the signal should be. In the absence of additional data acquired during the scan to measure the B0 field across the image (Jezzard and Balaban, 1995; Jenkinson, 2001; Cusack and Papadakis, 2002) or data acquired with the phase encode direction reversed (Andersson et al., 2003; Jones et al., 1999), for example, the true location of the signal cannot be retrospectively recovered using registration techniques. Even though the algorithm may achieve good correspondence, the intensities are not representative of a truly unwarped image, and so should not be included in any voxelwise statistical analysis.

Although registration methods based on B-splines are locally controlled and therefore displacing a control point only affects the transformation in the local neighbourhood of that point, Figure 6.23 shows that attempts to match intensities in regions of geometric distortions in the $b = 0 \text{ s/mm}^2$ data can significantly displace voxels at the level of other transverse slices where the B0 field is much more homogeneous. The spline based registration tool used here (Rueckert et al., 1999) allows for masking of the target image to exclude regions that should not be included in the cost function evaluation, but masking out regions susceptible to large B0 inhomogeneities resulted in sharp edges that degraded overall registration performance compared to only padding out regions outside the brain.

A final limitation of the results presented in this work concerns the validation strategy employed. In order to measure the initial and final alignment between coregistered images, anatomical landmarks were individually placed at fifteen different points throughout the brain. These were positioned at easily identifiable points where there was high contrast between the tissues, and the reproducibility of landmark positioning (that is, the fiducial localisation error) was found to be small. However, these tissue boundaries may have driven the registration algorithms, and so they many all have matched these

locations better than they did other points in the images. This, coupled with the fact that nonlinear algorithms do not allow the target registration error (i.e. the distance between corresponding points not used in calculating the registration transformation parameters; Fitzpatrick and West., 2001) to be calculated from the reported fiducial registration error (the error at the landmarks following registration) and fiducial localisation error, mean that the validation results need to be treated with care.

6.7 Suggestions for further work

6.7.1 Deweighting the cost function

One way in which the regions of signal loss and pile up may less strongly affect the evaluation of the cost function in the optimised B-spline method proposed in this work is to apply a second regularisation term that deweights these regions. Rather than exclude them totally from the cost function calculation and generate sharp edges that drive the registration and lead to inaccurate alignment, these regions may be deweighted in a manner similar to that employed in the FLIRT method.

6.7.2 Individually tailoring the coregistration parameters

The optimisation of the $b = 0$ s/mm² to T2-weighted anatomical coregistration algorithm presented here used the same parameters to coregister these images across different subjects. However, the subjects may have moved by different amounts between the acquisition of the two images, and the EPI data may have different degrees of distortion. Therefore, the robustness and accuracy of the coregistration may be improved by individually tailoring the registration parameters on a subject-by-subject basis. For example, if the $b = 0$ s/mm² and T2-weighted data are in large misalignment prior to

registration, then the coefficient of the regularisation term in the cost function that constrains the transformation to be smooth (λ) could be reduced and the initial step length made larger. In contrast, if the data are already in very close correspondence then the coefficient of the cost function regularisation term could be increased. In the absence of manual intervention it is not clear how much subject-dependent parameterisation could be achieved, but one possibility may be to use the magnitude of the evaluated similarity metric prior to registration and choose parameters based on this. This has not been attempted, however, and may not be suitable and introduce bias in the data.

6.7.3 Coregistering tensor-derived scalar maps

In the current study, finding the parameters to accurately transform diffusion-derived MRI data into anatomical space was attempted by coregistering the $b = 0$ s/mm² image to the high resolution anatomical T2-weighted image. The optimised B-spline algorithm presented here has been shown to perform well at matching regions throughout the brain, but alignment may be improved by instead registering tensor-derived scalar maps such as FA or ADC data to the T2-weighted image. This is a promising alternative, and in the TBSS method FA maps are directly registered to a template image with fairly good results even prior to the perpendicular search step to find the centres of white matter tracts. Coregistering the data prior to registration to a template image may result in even better alignment prior to group-wise analysis.

This approach has subsequently been attempted in a very preliminary extension of the work presented here. Given the similarity in tissue contrast between $b = 0$ s/mm² images and ADC maps, the optimised registration algorithm was first used to attempt intrasubject alignment between the latter maps and high resolution T2-weighted data. However, initial results were not as successful as had been hoped, and on visual inspection the algorithm performed less well than if the $b = 0$ s/mm² image had been kept as the source. This is perhaps unsurprising given that the algorithm was optimised to register the image with no

diffusion weighting, but since this work is at a very early stage the promise of this approach remains intact, and the method is still being developed.

6.7.4 Normalisation to a study-specific average space

Most current voxel-based group-wise analyses of MRI data are performed by registering the data to an atlas space or to a group-specific individual target space. However, as discussed in Section 2.7.7.2.2, the chosen atlas may be very different to that of the subjects involved in the study or the individual target space may not be representative of the study population. In these cases, some images may be significantly warped during the registration process, and even then accurate alignment may not be achieved and bias may be introduced. It may therefore be advantageous to instead register diffusion-derived scalar maps that have already been coregistered to anatomical images to a study-specific atlas space. This has tentatively been attempted using the algorithm proposed by Bhatia (Bhatia et al., 2004), but it is highly computationally intensive and is not currently suitable for registering large study groups. Nevertheless, this remains a promising future option.

6.8 Conclusion

The ultimate aim of this work was to facilitate objective cross-subject comparisons of whole brain neonatal DTI data. A robust method of coregistering EPI data to high resolution anatomical T2-weighted to correct for geometric distortions has been presented that may improve subsequent normalisation of images from different subjects into a common space. Achieving accurate inter-subject alignment of diffusion-derived scalar maps to this common space is the next step. The inherently low signal-to-noise ratio and

large voxel sizes relative to the size of the neonatal brain, coupled with the inherent variability in the size, shape and cortical morphology of the brains of different subjects make this more challenging than intra-subject registration. Work is ongoing to overcome these hurdles, however, and may be assisted by the optimisation method presented in this thesis.

Chapter 7

Summary and Final Remarks

7.1 Summary

The increasing incidence of preterm birth has focused much attention on finding the neuro-imaging correlates of the adverse neurological outcomes that some of these infants suffer from. These include motor and sensory impairments that are associated with focal lesions on conventional MRI, but more subtle cognitive and behavioural impairments are increasingly reported and are related to more diffuse abnormalities of the cerebral white matter. Diffusion tensor magnetic resonance imaging measures the diffusion characteristics of water in tissues and may allow the detection of microstructural abnormalities that are not evident on conventional MRI. The aim of this work was to explore the developing preterm brain with DTI, in the hope of shedding more light on some of the microstructural neuro-imaging abnormalities that may be associated with preterm birth. The limitations of manual region of interest approaches in allowing non-subjective group-wise comparison of DTI data led to the search for a more objective tool to achieve this. TBSS, a recently proposed method for aligning FA data from multiple subjects prior to voxel-wise cross-subject statistical analysis, was attempted on data from 26 preterm-born infants imaged at term-equivalent age and 6 term-born control infants who had no evidence of focal abnormality on conventional MRI. The two-step registration process was found to achieve very good alignment of the centres of major white matter pathways throughout the brain. Subsequent analysis revealed that FA was

lower in the preterm-born group than the control group in the centrum semiovale, frontal white matter and genu of the corpus callosum, with the most immature infants displaying additional and more extensive regions of FA reduction. Microstructural changes in a number of these regions have been shown to be associated with preterm birth in previous ROI-based studies, but this is the first time they have been confirmed with objective observer-independent methods of analysing DTI data. These reductions in FA could be explained by elevations in diffusion perpendicular to the local white matter tract direction, and thus were found to be consistent with oligodendrocyte and/or axonal abnormality.

Preterm birth is associated with a number of clinical variables including infection in the neonatal period and preterm PROM. Amongst the most important of these variables are acute and chronic lung disease, affecting 50% of preterm infants born at <30 weeks gestational age (Ramanathan, 2008) and 33% of preterm infants with a birth weight of <1000 g (Birenbaum et al., 1983) respectively. These are, however, significantly associated with increasing prematurity at birth, and it had not previously been possible to dissociate their effects on cerebral white matter microstructure. However, TBSS has allowed for multivariate statistical analysis to assess the independent correlations of these different clinical variables with FA. Studying 53 preterm infants born at various gestational ages and imaged at term-equivalent age, it was found that acute lung disease is independently associated with a significant decrease in FA in the genu of the corpus callosum. Chronic lung disease, on the other hand, was associated with a highly localised FA reduction in the left inferior longitudinal fasciculus. This is the first time that lung disease has been reported to be correlated to such highly localised regions of FA change and the reasons why these particular white matter tracts are more susceptible than others is not clear. However, this study has shown the potential of TBSS to act as a biomarker for such processes, and may prove to be very useful in assessing neuro-imaging changes associated with different forms of neonatal intervention.

At present, the majority of group-wise analyses of DTI data are performed using ROI techniques. This is due to the fact that distortions present in diffusion MRI data acquired

with an EPI readout are complex, and coupled with the relatively large voxel sizes and the inherently low signal-to-noise ratio of this technique make accurate alignment to a common template more difficult than the equivalent problem with high resolution anatomical MRI data. TBSS has successfully achieved this and in our first study produced results consistent with previously published ROI studies. However, given that both of these methods involve a lot of data reduction, objective cross-subject whole brain analysis remains an outstanding challenge. The partial optimisation of an affine followed by a nonlinear registration algorithm based on B-splines was proposed to coregister $b = 0$ s/mm^2 images acquired with an EPI readout to high resolution anatomical T2-weighted data. This was developed in an attempt to account for geometric distortions in EPI data and transform diffusion-derived scalar maps into anatomical space prior to spatial normalisation for group-wise analysis. The optimised algorithm has been shown to be relatively robust across subjects and in matching points placed throughout the brain. However, ongoing work remains and it is important to bear the limitations of the proposed method in mind, particularly in the matching and redistributing of signal from regions of the brain where EPI suffers from large distortions due to inhomogeneities in the B_0 field. Taking into account anatomical variability and the relatively large voxel size suggests that automated objective group-wise analysis of DTI data from the whole of the developing preterm brain, particularly of the cortical grey matter, is still some way away. However, this study represents a potentially important first step along this path.

7.2 Conclusion and final remarks

In conclusion, this work has provided objective quantitative evidence confirming that preterm-born infants have microstructural differences in cerebral white matter pathways compared to term-born controls. These differences in FA have subsequently been shown to be significantly linearly correlated with gestational age. Taking this as well as age at imaging into account when performing multivariate statistical analysis has revealed that

acute and chronic lung disease are independently associated with FA reductions at term age in the genu of the corpus callosum and in the left inferior longitudinal fasciculus respectively, Though the reasons for the selective vulnerability of these sites is unclear, this finding may be clinically relevant and suggests the use of TBSS as a neuro-imaging biomarker in assessing medical interventions in these diseases.

Finally, the partial optimisation of a nonlinear registration algorithm based on B-splines has been presented that is capable of coregistering EPI data to high resolution anatomical images better than two other commonly used registration tools. This represents the first step in the alignment of diffusion-derived scalar maps to a common template to allow cross-subject statistical analysis. Whole brain analysis is probably still some way away, however. It is likely that in addition to improved registration methods, enhanced acquisition protocols that are capable of minimising even more of the distortions seen in EPI data at source and allow for increased signal-to-noise ratio and/or reduced voxel size will be required before such studies can be performed. These are areas of active research however, and are already helping to further the potential of using diffusion tensor imaging to investigate the developing preterm brain.

Appendices

Appendix A: The reproducibility of landmark positioning at each landmark

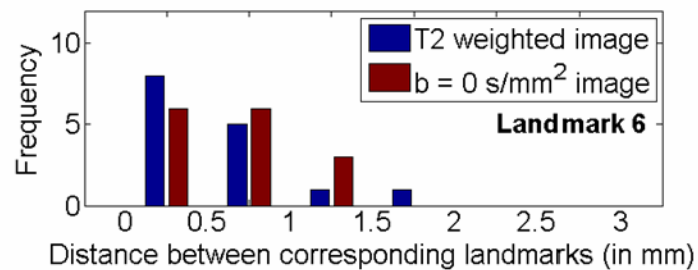
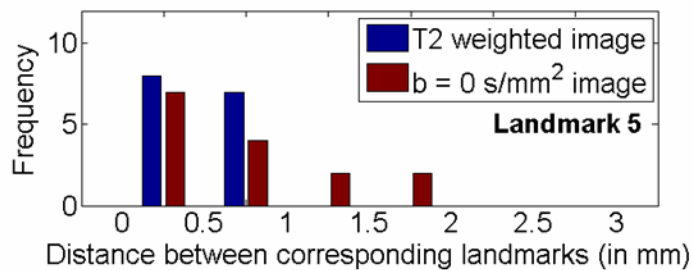
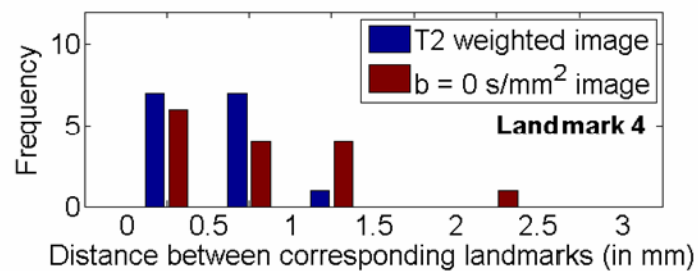
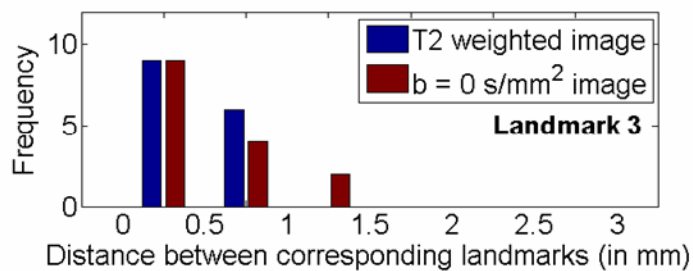
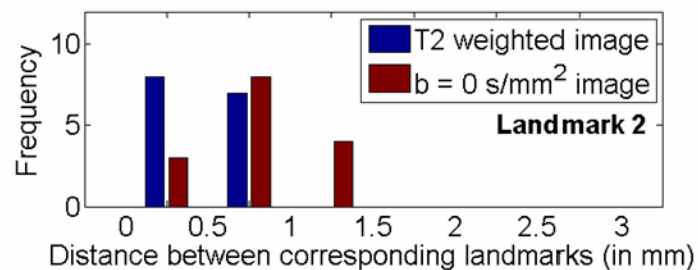
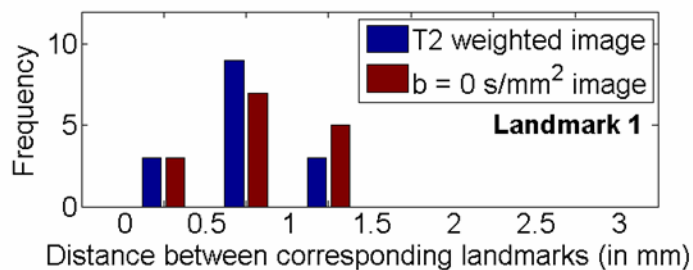


Figure A.1: Reproducibility of landmark positioning at Landmarks 1-6

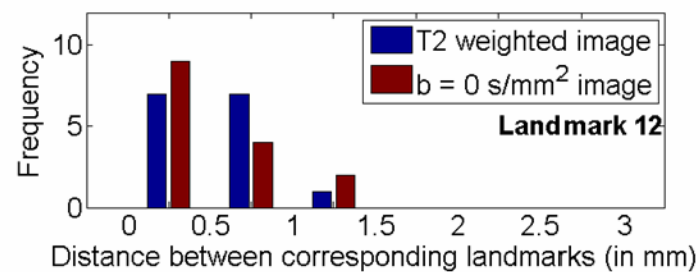
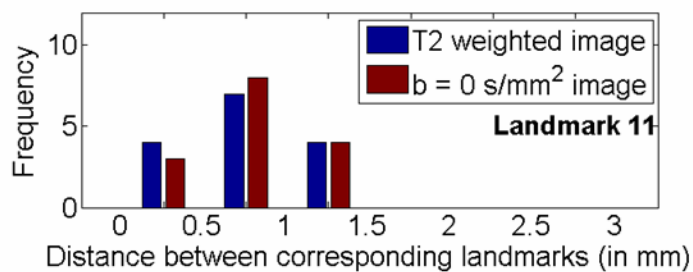
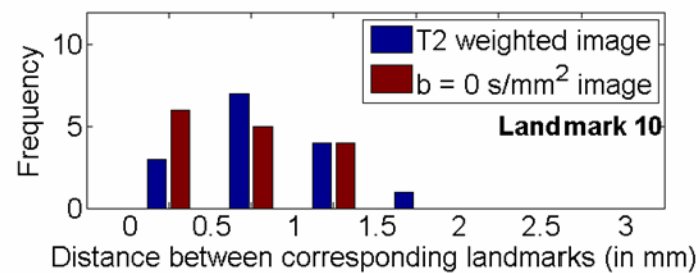
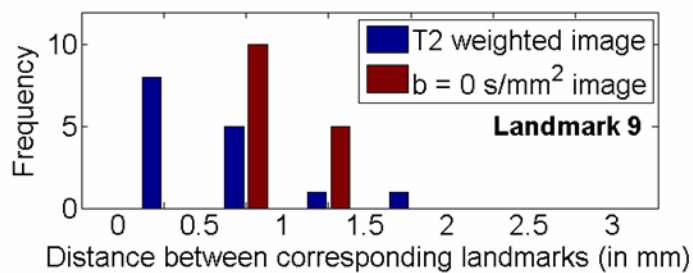
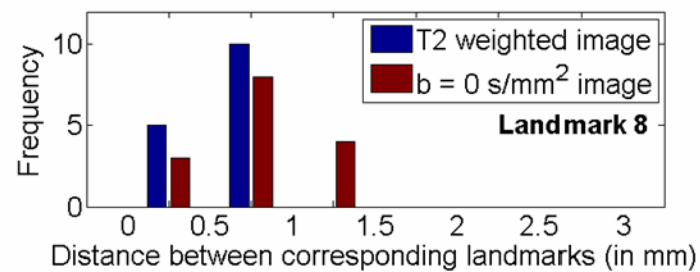
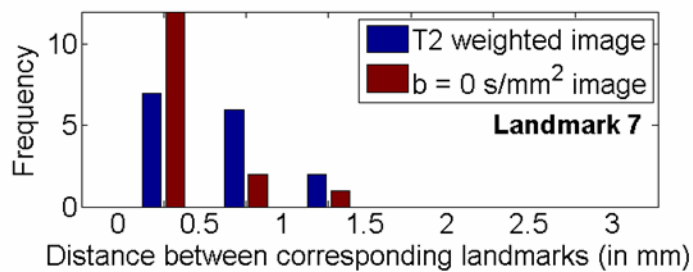


Figure A.2: Reproducibility of landmark positioning at Landmarks 7-12

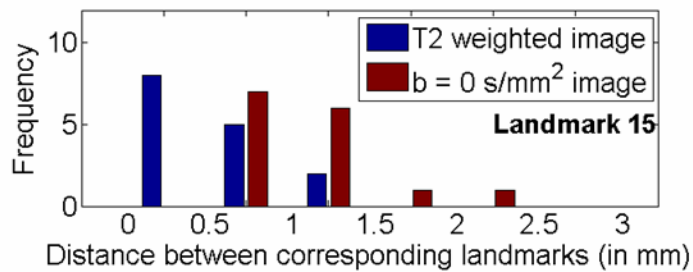
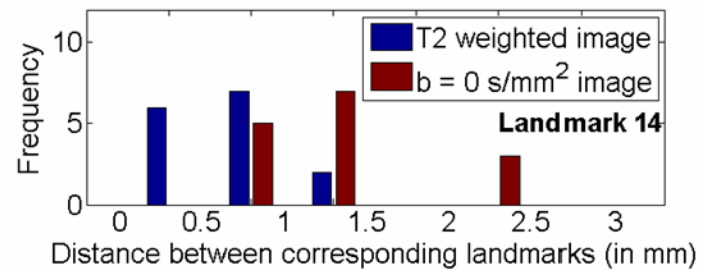
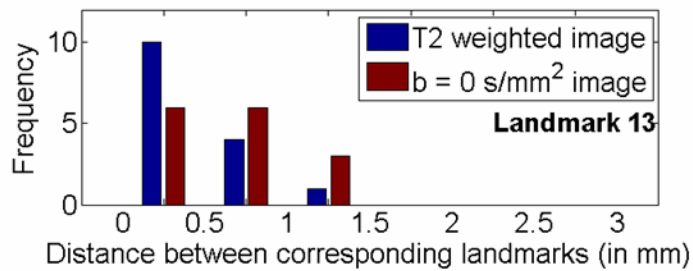


Figure A.3: Reproducibility of landmark positioning at Landmarks 13-15

Appendix B: The effect of different registration methodologies for achieving correspondence in different brain regions

	Unregistered	FLIRT 7 DOF	FLIRT 12 DOF	AIR Nonlinear	Optimised B-spline
Unregistered	-				
FLIRT 7 DOF	0.16	-			
FLIRT 12 DOF	0.21	0.85	-		
AIR Nonlinear	0.02	0.04	0.03	-	
Optimised B-splines	0.01	<0.005	<0.005	0.31	-

Table B.1: Landmark 1 - Most superior point of the left lateral ventricle (judged on a parasagittal sagittal slice)
Significance matrix for this landmark across all subjects (p-values corrected for multiple comparisons with a Bonferroni correction).

	Unregistered	FLIRT 7 DOF	FLIRT 12 DOF	AIR Nonlinear	Optimised B-spline
Unregistered	-				
FLIRT 7 DOF	0.14	-			
FLIRT 12 DOF	0.14	0.91	-		
AIR Nonlinear	0.05	0.52	0.34	-	
Optimised B-splines	0.01	0.02	0.01	0.08	-

Table B.2: Landmark 2 - Most superior point of the right lateral ventricle (judged on a parasagittal slice)

Significance matrix for this landmark across all subjects (p-values corrected for multiple comparisons with a Bonferroni correction).

	Unregistered	FLIRT 7 DOF	FLIRT 12 DOF	AIR Nonlinear	Optimised B-spline
Unregistered	-				
FLIRT 7 DOF	0.19	-			
FLIRT 12 DOF	0.06	0.73	-		
AIR Nonlinear	0.52	0.27	0.19	-	
Optimised B-splines	0.08	0.97	0.85	0.13	-

Table B.3: Landmark 3 - The most anterior point of the left hemisphere of the brain

Significance matrix for this landmark across all subjects (p-values corrected for multiple comparisons with a Bonferroni correction).

	Unregistered	FLIRT 7 DOF	FLIRT 12 DOF	AIR Nonlinear	Optimised B-spline
Unregistered	-				
FLIRT 7 DOF	0.31	-			
FLIRT 12 DOF	0.24	0.85	-		
AIR Nonlinear	0.85	0.10	0.08	-	
Optimised B-splines	0.68	0.52	0.47	0.33	-

Table B.4: Landmark 4 - The most anterior point of the right hemisphere of the brain

Significance matrix for this landmark across all subjects (p-values corrected for multiple comparisons with a Bonferroni correction).

	Unregistered	FLIRT 7 DOF	FLIRT 12 DOF	AIR Nonlinear	Optimised B-spline
Unregistered	-				
FLIRT 7 DOF	0.62	-			
FLIRT 12 DOF	0.57	0.85	-		
AIR Nonlinear	0.62	0.91	0.91	-	
Optimised B-splines	0.08	0.27	0.27	0.07	-

Table B.5: Landmark 5 - The most posterior part of the brain

Significance matrix for this landmark across all subjects (p-values corrected for multiple comparisons with a Bonferroni correction).

	Unregistered	FLIRT 7 DOF	FLIRT 12 DOF	AIR Nonlinear	Optimised B-spline
Unregistered	-				
FLIRT 7 DOF	0.03	-			
FLIRT 12 DOF	0.03	0.73	-		
AIR Nonlinear	<0.001	0.57	0.24	-	
Optimised B-splines	<0.001	0.24	0.16	0.47	-

Table B.6: Landmark 6 - The most anterior point of the left anterior horn of the lateral ventricle

Significance matrix for this landmark across all subjects (p-values corrected for multiple comparisons with a Bonferroni correction).

	Unregistered	FLIRT 7 DOF	FLIRT 12 DOF	AIR Nonlinear	Optimised B-spline
Unregistered	-				
FLIRT 7 DOF	0.43	-			
FLIRT 12 DOF	0.43	0.85	-		
AIR Nonlinear	0.01	0.03	0.02	-	
Optimised B-splines	0.01	0.03	0.03	0.88	-

Table B.7: Landmark 7 - The most anterior point of the right anterior horn of the lateral ventricle

Significance matrix for this landmark across all subjects (p-values corrected for multiple comparisons with a Bonferroni correction).

	Unregistered	FLIRT 7 DOF	FLIRT 12 DOF	AIR Nonlinear	Optimised B-spline
Unregistered	-				
FLIRT 7 DOF	0.03	-			
FLIRT 12 DOF	0.03	1	-		
AIR Nonlinear	0.01	1	0.97	-	
Optimised B-splines	<0.001	0.16	0.10	0.02	-

Table B.8: Landmark 8 - The most posterior point of the posterior horn of the left lateral ventricle

Significance matrix for this landmark across all subjects (p-values corrected for multiple comparisons with a Bonferroni correction).

	Unregistered	FLIRT 7 DOF	FLIRT 12 DOF	AIR Nonlinear	Optimised B-spline
Unregistered	-				
FLIRT 7 DOF	0.06	-			
FLIRT 12 DOF	0.02	0.68	-		
AIR Nonlinear	<0.001	0.05	0.05	-	
Optimised B-splines	<0.001	0.01	0.02	0.41	-

Table B.9: Landmark 9 - The most posterior point of the posterior horn of the right lateral ventricle

Significance matrix for this landmark across all subjects (p-values corrected for multiple comparisons with a Bonferroni correction).

	Unregistered	FLIRT 7 DOF	FLIRT 12 DOF	AIR Nonlinear	Optimised B-spline
Unregistered	-				
FLIRT 7 DOF	0.14	-			
FLIRT 12 DOF	0.14	0.91	-		
AIR Nonlinear	0.04	0.34	0.19	-	
Optimised B-splines	0.01	0.19	0.08	0.38	-

Table B.10: Landmark 10 - The most inferior point of the inferior horn of the left lateral ventricle

Significance matrix for this landmark across all subjects (p-values corrected for multiple comparisons with a Bonferroni correction).

	Unregistered	FLIRT 7 DOF	FLIRT 12 DOF	AIR Nonlinear	Optimised B-spline
Unregistered	-				
FLIRT 7 DOF	0.04	-			
FLIRT 12 DOF	0.02	0.97	-		
AIR Nonlinear	0.02	0.79	0.85	-	
Optimised B-splines	0.02	0.79	0.79	0.71	-

Table B.11: Landmark 11 - The most inferior point of the inferior horn of the right lateral ventricle

Significance matrix for this landmark across all subjects (p-values corrected for multiple comparisons with a Bonferroni correction).

	Unregistered	FLIRT 7 DOF	FLIRT 12 DOF	AIR Nonlinear	Optimised B-spline
Unregistered	-				
FLIRT 7 DOF	0.34	-			
FLIRT 12 DOF	0.43	0.79	-		
AIR Nonlinear	0.52	1	1	-	
Optimised B-splines	<0.001	<0.005	<0.005	0.02	-

Table B.12: Landmark 12 - The tip of fourth ventricle

Significance matrix for this landmark across all subjects (p-values corrected for multiple comparisons with a Bonferroni correction).

	Unregistered	FLIRT 7 DOF	FLIRT 12 DOF	AIR Nonlinear	Optimised B-spline
Unregistered	-				
FLIRT 7 DOF	0.05	-			
FLIRT 12 DOF	0.16	0.38	-		
AIR Nonlinear	0.05	0.68	0.47	-	
Optimised B-splines	0.02	0.57	0.24	0.82	-

Table B.13: Landmark 13 - The most anterior point of the ponto-medullary junction

Significance matrix for this landmark across all subjects (p-values corrected for multiple comparisons with a Bonferroni correction).

	Unregistered	FLIRT 7 DOF	FLIRT 12 DOF	AIR Nonlinear	Optimised B-spline
Unregistered	-				
FLIRT 7 DOF	0.62	-			
FLIRT 12 DOF	0.73	0.91	-		
AIR Nonlinear	0.68	0.19	0.16	-	
Optimised B-splines	0.01	0.06	0.04	5.55E-04	-

Table B.14: Landmark 14 - The most lateral point of the left cerebellar hemisphere

Significance matrix for this landmark across all subjects (p-values corrected for multiple comparisons with a Bonferroni correction).

	Unregistered	FLIRT 7 DOF	FLIRT 12 DOF	AIR Nonlinear	Optimised B-spline
Unregistered	-				
FLIRT 7 DOF	0.68	-			
FLIRT 12 DOF	1	0.68	-		
AIR Nonlinear	0.52	0.57	0.91	-	
Optimised B-splines	0.14	0.10	0.03	0.01	-

Table B.15: Landmark 15 - The most lateral point of the right cerebellar hemisphere

Significance matrix for this landmark across all subjects (p-values corrected for multiple comparisons with a Bonferroni correction).

Reference List

Abernethy,L.J., Cooke,R.W., and Foulder-Hughes,L. (2004). Caudate and hippocampal volumes, intelligence, and motor impairment in 7-year-old children who were born preterm. *Pediatric Research* 55, 884-893.

Abernethy,L.J., Palaniappan,M., and Cooke,R.W.I. (2002). Quantitative magnetic resonance imaging of the brain in survivors of very low birth weight. *Archives of Disease in Childhood* 87, 279.

Ajayi-Obe,M., Saeed,N., Cowan,F.M., Rutherford,M.A., and Edwards,A.D. (2000). Reduced development of cerebral cortex in extremely preterm infants. *Lancet* 356, 1162-1163.

Alexander,A.L., Tsuruda,J.S., and Parker,D.L. (1997). Elimination of eddy current artifacts in diffusion-weighted echo-planar images: the use of bipolar gradients. *Magnetic Resonance in Medicine* 38, 1016-1021.

Alexander,D.C., Barker,G.J., and Arridge,S.R. (2002). Detection and modeling of non-Gaussian apparent diffusion coefficient profiles in human brain data. *Magnetic Resonance in Medicine* 48, 331–340.

Aljabar,P., Bhatia,K.K., Murgasova,M., Hajnal,J.V., Boardman,J.P., Srinivasan,L., Rutherford,M.A., Dyet,L.E., Edwards,A.D., and Rueckert,D. (2008). Assessment of brain growth in early childhood using deformation-based morphometry. *NeuroImage* 39, 348-358.

Allin,M., Matsumoto,H., Santhouse,A.M., Nosarti,C., AlAsady,M.H., Stewart,A.L., Rifkin,L., and Murray,R.M. (2001). Cognitive and motor function and the size of the cerebellum in adolescents born very pre-term. *Brain* 124, 60-66.

Alpert,N.M., Berdichevsky,D., Levin,Z., Morris,E.D., and Fischman,A.J. (1996). Improved Methods for Image Registration. *NeuroImage* 3, 10-18.

Anderson,N.G., Laurent,I., Cook,N., Woodward,L., and Inder,T.E. (2005). Growth rate of corpus callosum in very premature infants. *American Journal of Neuroradiology* 26, 2685-2690.

Anderson,P. and Doyle,L.W. (2003). Neurobehavioral Outcomes of School-age Children Born Extremely Low Birth Weight or Very Preterm in the 1990s. *Journal of the American Medical Association* 289, 3264-3272.

Andersson,J.L. and Skare,S. (2002). A model-based method for retrospective correction of geometric distortions in diffusion-weighted EPI. *NeuroImage*. 16, 177-199.

Andersson,J.L., Skare,S., and Ashburner,J. (2003). How to correct susceptibility distortions in spin-echo echo-planar images: application to diffusion tensor imaging. *NeuroImage* 20, 870-888.

Anjari, M., Srinivasan, L., Larkman, D. J., Allsop, J. M., Fitzpatrick, J. M., Cowan, F. M., Hajnal, J. V., Rutherford, M. A., Edwards, A. D., and Counsell, S. J. (2006a). High resolution diffusion tensor imaging of the corpus callosum in the preterm brain at 3 Tesla. *Proceedings of the ISMRM 14th Scientific Meeting & Exhibition*.

Anjari,M., Srinivasan,L., Larkman,D.J., Allsop,J.M., Fitzpatrick,J.M., Cowan,F.M., Hajnal,J.V., Rutherford,M.A., Edwards,A.D., and Counsell,S.J. (2006b). High resolution diffusion tensor imaging of the corpus callosum in the preterm brain at 3 Tesla. *Proceedings of the Pediatric Academic Societies Annual Meeting*.

Argyropoulou,M.I., Xydis,V., Drougia,A., Argyropoulou,P.I., Tzoufi,M., Bassounas,A., Andronikou,S., and Efremidis,S.C. (2003). MRI measurements of the pons and cerebellum in children born preterm; associations with the severity of periventricular leukomalacia and perinatal risk factors. *Neuroradiology* 45, 730-734.

Arroyo,E.J. and Scherer,S.S. (2000). On the molecular architecture of myelinated fibers. *Histochemistry and Cell Biology* 113, 1-18.

Ashburner,J. and Friston,K.J. (2000). Voxel-based morphometry--the methods. *NeuroImage*. *11*, 805-821.

Assaf,Y. and Cohen,Y. (2000). Assignment of the water slow diffusing component in the central nervous system using q-space diffusion MRS: implications for fiber tract imaging. *Magnetic Resonance in Medicine* *43*, 191–199.

Assaf,Y. and Basser,P.J. (2005). Composite hindered and restricted model of diffusion (CHARMED) MR imaging of the human brain. *NeuroImage* *27*, 48–58.

Assaf,Y. and Pasternak,O. (2008). Diffusion tensor imaging (DTI)-based white matter mapping in brain research: a review. *Journal of Molecular Neuroscience* *34(1)*, 51-61.

Back,S.A., Gan,X., Li,Y., Rosenberg,P.A., and Volpe,J.J. (1998). Maturation-Dependent Vulnerability of Oligodendrocytes to Oxidative Stress-Induced Death Caused by Glutathione Depletion. *Journal of Neuroscience* *18*, 6241.

Back,S.A., Luo,N.L., Borenstein,N.S., Levine,J.M., Volpe,J.J., and Kinney,H.C. (2001). Late Oligodendrocyte Progenitors Coincide with the Developmental Window of Vulnerability for Human Perinatal White Matter Injury. *Journal of Neuroscience* *21*, 1302.

Back,S.A., Luo,N.L., Borenstein,N.S., Volpe,J.J., and Kinney,H.C. (2002). Arrested Oligodendrocyte Lineage Progression During Human Cerebral White Matter Development: Dissociation Between the Timing of Progenitor Differentiation and Myelinogenesis. *Journal of Neuropathology & Experimental Neurology* *61*, 197.

Back,S.A., Riddle,A., and McClure,M.M. (2007). Maturation-Dependent Vulnerability of Perinatal White Matter in Premature Birth. *Stroke* *38*, 724.

Bada,H.S., Korones,S.B., Perry,E.H., Arheart,K.L., Ray,J.D., Pourcyrous,M., Magill,H.L., rd,W., Somes,G.W., and Clark,F.C. (1990). Mean arterial blood pressure changes in premature infants and those at risk for intraventricular hemorrhage. *Journal of Pediatrics* *117*, 607-614.

- Bajcsy,R. and Kovacic,S. (1989). Multiresolution elastic matching. *Computer Vision, Graphics and Image Processing* 46, 1–21.
- Banker,B. and Larroche,J.C. (1962). Periventricular leukomalacia of infancy. A form of neonatal anoxic encephalopathy. *Archives of Neurology* 7, 386-410.
- Barkovich,A.J. (2005). Magnetic resonance techniques in the assessment of myelin and myelination. *Journal of Inherited Metabolic Disease* 28, 311-343.
- Barkovich,A.J. (2000). *Pediatric Neuroimaging*. Lippincott Williams & Wilkins Philadelphia).
- Barkovich,A.J., Kjos,B.O., Jackson,D.E., Jr., and Norman,D. (1988). Normal maturation of the neonatal and infant brain: MR imaging at 1.5 T. *Radiology* 166, 173-180.
- Bassan,H., Feldman,H.A., Limperopoulos,C., Benson,C.B., Ringer,S.A., Veracruz,E., Soul,J.S., Volpe,J.J., and Plessis,A.J. (2006). Periventricular Hemorrhagic Infarction: Risk Factors and Neonatal Outcome. *Pediatric Neurology* 35, 85-92.
- Bassan,H., Limperopoulos,C., Visconti,K., Mayer,D.L., Feldman,H.A., Avery,L., Benson,C.B., Stewart,J., Ringer,S.A., Soul,J.S., Volpe,J.J., and du Plessis,A.J. (2007). Neurodevelopmental Outcome in Survivors of Periventricular Hemorrhagic Infarction. *Pediatrics* 120, 785-792.
- Basser,P.J. (1995). Inferring microstructural features and the physiological state of tissues from diffusion-weighted images. *NMR in Biomedicine* 8, 333-344.
- Basser,P.J., Mattiello,J., and LeBihan,D. (1994). MR diffusion tensor spectroscopy and imaging. *Biophysical Journal* 66, 259-267.
- Bastin,M.E. (1999). Correction of eddy current-induced artefacts in diffusion tensor imaging using iterative cross-correlation. *Magnetic Resonance Imaging* 17, 1011-1024.
- Battin,M.R., Maalouf,E.F., Counsell,S.J., Herlihy,A.H., Rutherford,M.A., Azzopardi,D., and Edwards,A.D. (1998). Magnetic resonance imaging of the brain in very preterm

infants: visualization of the germinal matrix, early myelination, and cortical folding. *Pediatrics* *101*, 957-962.

Batton,D.G. and Nardis,E.E. (1987). The effect of intraventricular blood on cerebral blood flow in newborn dogs. *Pediatric Research* *21*, 511-515.

Beaulieu,C. (2002). The basis of anisotropic water diffusion in the nervous system - a technical review. *NMR in Biomedicine*. *15*, 435–455.

Behrens,T.E., Woolrich,M.W., Jenkinson,M., Johansen-Berg,H., Nunes,R.G., Clare,S., Matthews,P.M., Brady,J.M., and Smith,S.M. (2003). Characterization and propagation of uncertainty in diffusion-weighted MR imaging. *Magnetic Resonance in Medicine* *50*, 1077-1088.

Behrman,R.E. and Stith Butler,A. (2006). Institute of Medicine, Committee on Understanding Preterm Birth and Assuring Healthy Outcomes Board on Health Sciences Policy: Preterm Birth: Causes, Consequences, and Prevention. Washington, DC: National Academies Press.

Bendon,R.W., Faye-Petersen,O., Pavlova,Z., Qureshi,F., Mercer,B., Miodovnik,M., Das,A.F., Meis,P.J., Moawad,A.H., and Iams,J.D. (1999). Fetal membrane histology in preterm premature rupture of membranes: comparison to controls, and between antibiotic and placebo treatment. The National Institute of Child Health and Human Development Maternal Fetal Medicine Units Network, Bethesda, MD, USA. *Pediatric and Developmental Pathology* *2*, 552-558.

Bhatia,K.K., Hajnal,J.V., Puri,B.K., Edwards,A.D., and Rueckert,D. (2004). Consistent groupwise non-rigid registration for atlas construction. *IEEE International Symposium on Biomedical Imaging: Macro to Nano* 908-911.

Bhutta,A.T., Cleves,M.A., Casey,P.H., Craddock,M.M., and Anand,K.J. (2002). Cognitive and behavioral outcomes of school-aged children who were born preterm: a meta-analysis. *Journal of the American Medical Association* *288*, 728-737.

Birenbaum,E., Lison,M., and Brish,M. (1983). Evaluation of respiratory support therapy in 135 newborn infants: survival and respiratory complications. *Israel Journal of Medical Sciences* *19*, 651-652.

Bloch,F. (1946). Nuclear Induction. *Physical Review* *70*, 460-474.

Blondel,B. and Kaminski,M. (2002). Trends in the occurrence, determinants, and consequences of multiple births. *Seminars in Perinatology* *26*, 239-249.

Boardman,J.P., Counsell,S.J., Rueckert,D., Hajnal,J.V., Bhatia,K.K., Srinivasan,L., Kapellou,O., Aljabar,P., Dyet,L.E., Rutherford,M.A., Allsop,J.M., and Edwards,A.D. (2007). Early growth in brain volume is preserved in the majority of preterm infants. *Annals of Neurology* *62*, 185-192.

Boardman,J.P., Counsell,S.J., Rueckert,D., Kapellou,O., Bhatia,K.K., Aljabar,P., Hajnal,J., Allsop,J.M., Rutherford,M.A., and Edwards,A.D. (2006). Abnormal deep grey matter development following preterm birth detected using deformation-based morphometry. *NeuroImage*. *32*, 70-78.

Bookstein,F.L. (2001). "Voxel-based morphometry" should not be used with imperfectly registered images. *NeuroImage*. *14*, 1454-1462.

Bookstein,F.L. (1989). Principal warps: thin-plate splines and the decomposition of deformations. *IEEE Transactions on Pattern Analysis and Machine Intelligence* *11*, 567-585.

Borch,K., Pryds,O., Holm,S., Lou,H., and Greisen,G. (1998). Regional cerebral blood flow during seizures in neonates. *Journal of Pediatrics* *132*, 431-435.

Botting,N., Powlis,A., Cooke,R.W., and Marlow,N. (1998). Cognitive and educational outcome of very-low-birthweight children in early adolescence. *Developmental Medicine and Child Neurology* *40*, 652-660.

Botting,N., Powls,A., Cooke,R.W.I., and Marlow,N. (1997). Attention Deficit Hyperactivity Disorders and Other Psychiatric Outcomes in Very Low Birthweight Children at 12 Years. *Journal of Child Psychology and Psychiatry* 38, 931-941.

Bro-Nielsen,M. and Gramkow,C. (1996). Fast fluid registration of medical images. *Visualization in Biomedical Computing, Lecture Notes in Computer Science 1131*, 267–76.

Buchel,C., Raedler,T., Sommer,M., Sach,M., Weiller,C., and Koch,M.A. (2004). White matter asymmetry in the human brain: a diffusion tensor MRI study. *Cerebral Cortex* 14, 945-951.

Bunge,R.P. Glial cells and the central myelin sheath. (1968). *Physiological Reviews* 48[1], 197-251.

Bystron,I., Blakemore,C., and Rakic,P. (2008). Development of the human cerebral cortex: Boulder Committee revisited. *Nature Reviews Neuroscience* 9, 110.

Calamante,F., Porter,D.A., Gadian,D.G., and Connelly,A. (1999). Correction for eddy current induced Bo shifts in diffusion-weighted echo-planar imaging. *Magnetic Resonance in Medicine* 41, 95-102.

Caldu,X., Narberhaus,A., Junque,C., Gimenez,M., Vendrell,P., Bargallo,N., Segarra,D., and Botet,F. (2006). Corpus callosum size and neuropsychologic impairment in adolescents who were born preterm. *Journal of Child Neurology* 21, 406-410.

Calvert,S.A., Erskine,L., and Fong,K. (1988). Serial measurements of cerebral blood flow velocity in preterm infants during the first 72 hours of life. *Acta Paediatrica Scandinavica* 77, 625-631.

Carpenter, M. B. and Sutin, J. *Human Nemoanatomy*. (1983). Williams & Wilkins Co, Baltimore.

Caviness Jr,V.S. (1989). Normal development of cerebral neocortex. *Developmental Neurobiology, Nestlé Nutrition Workshop Series* 12, 1-10.

Childs,A.M., Cornette,L., Ramenghi,L.A., Tanner,S.F., Arthur,R.J., Martinez,D., and Levene,M.I. (2001). Magnetic Resonance and Cranial Ultrasound Characteristics of Periventricular White Matter Abnormalities in Newborn Infants. *Clinical Radiology* 56, 647-655.

Christensen,G.E., Miller,M.I. and Vannier,M. (1994). A 3D deformable magnetic resonance textbook based on elasticity. AAAI Spring Symposium Series: Applications of Computer Vision in Medical Image Processing 153-156

Christensen,G.E., Rabbitt,R.D. and Miller,M.I. (1996). Deformable templates using large deformation kinematics. *IEEE Transactions on Image Processing* 5, 1435-47.

Clarke,S., Kraftsik,R., van der Loos,H., and Innocenti,G.M. (1989). Forms and measures of adult and developing human corpus callosum: Is there sexual dimorphism? *The Journal of Comparative Neurology* 280, 213-230.

Coley,B.D. and Hogan,M.J. (1997). Cystic periventricular leukomalacia of the corpus callosum. *Pediatric Radiology*. 27, 583-585.

Collignon,A., Maes,F., Delaere,D., Vandermeulen,D., Suetens,P., and Marchal,G. (1995). Automated multi-modality image registration based on information theory. *Information Processing in Medical Imaging* 14, 263.

Collins,M.P., Lorenz,J.M., Jetton,J.R., and Paneth,N. (2001). Hypocapnia and other ventilation-related risk factors for cerebral palsy in low birth weight infants. *Pediatric Research* 50, 712-719.

Cooke,R.W.I. and Abernethy,L.J. (1999). Cranial magnetic resonance imaging and school performance in very low birth weight infants in adolescence. *Archives of Disease in Childhood Fetal & Neonatal Edition* 81, 116F.

Counsell,S.J., Allsop,J.M., Harrison,M.C., Larkman,D.J., Kennea,N.L., Kapellou,O., Cowan,F.M., Hajnal,J.V., Edwards,A.D., and Rutherford,M.A. (2003a). Diffusion-weighted imaging of the brain in preterm infants with focal and diffuse white matter abnormality. *Pediatrics* 112, 1-7.

Counsell,S.J., Maalouf,E.F., Fletcher,A.M., Duggan,P., Battin,M., Lewis,H.J., Herlihy,A.H., Edwards,A.D., Bydder,G.M., and Rutherford,M.A. (2002). MR imaging assessment of myelination in the very preterm brain. *American Journal of Neuroradiology* 23, 872-881.

Counsell,S.J., Rutherford,M.A., Cowan,F.M., and Edwards,A.D. (2003b). Magnetic resonance imaging of preterm brain injury. *Archives of Disease in Childhood Fetal & Neonatal Edition* 88, F269-F274.

Counsell,S.J., Shen,Y., Boardman,J.P., Larkman,D.J., Kapellou,O., Ward,P., Allsop,J.M., Cowan,F.M., Hajnal,J.V., Edwards,A.D., and Rutherford,M.A. (2006). Axial and radial diffusivity in preterm infants who have diffuse white matter changes on magnetic resonance imaging at term-equivalent age. *Pediatrics* 117, 376-386.

Crum,W.R., Hartkens,T., and Hill,D.L. (2004). Non-rigid image registration: theory and practice. *British Journal of Radiology* 77 *Spec No 2*, S140-S153.

Cusack,R. and Papadakis,N. (2002). New robust 3-D phase unwrapping algorithms: application to magnetic field mapping and undistorting echoplanar images. *NeuroImage*. 16, 754-764.

Dammann,O., Allred,E.N., Van Marter,L.J., Dammann,C.E., and Leviton,A. (2004). Bronchopulmonary dysplasia is not associated with ultrasound-defined cerebral white matter damage in preterm newborns. *Pediatric Research* 55, 319-325.

Dammann,O., Kuban,K.C., and Leviton,A. (2002). Perinatal infection, fetal inflammatory response, white matter damage, and cognitive limitations in children born preterm. *Mental Retardation and Developmental Disabilities Research Reviews* 8, 46-50.

Dammann,O. and Leviton,A. (1999). Brain Damage in Preterm Newborns: Might Enhancement of Developmentally Regulated Endogenous Protection Open a Door for Prevention? *Pediatrics* 104, 541-550.

Dammann,O. and Leviton,A. (2004). Inflammatory brain damage in preterm newborns--dry numbers, wet lab, and causal inferences. *Early Human Development* 79, 1-15.

Davatzikos,C. (2004). Why voxel-based morphometric analysis should be used with great caution when characterizing group differences. *NeuroImage*. 23, 17-20.

Davis,M.H., Khotanzad,A., Flamig,D.P., and Harms,S.E. (1997). A physics-based coordinate transformation for 3-D image matching. *IEEE Transactions on Medical Imaging* 16, 317-328.

de Vries,L.S., Rademaker,K.J., Groenendaal,F., Eken,P., van Haastert,I.C., Vandertop,W.P., Gooskens,R., and Meiners,L.C. (1998). Correlation between neonatal cranial ultrasound, MRI in infancy and neurodevelopmental outcome in infants with a large intraventricular haemorrhage with or without unilateral parenchymal involvement. *Neuropediatrics* 29, 180-188.

de Vries,L.S., Roelants-van Rijn,A.M., Rademaker,K.J., van Haastert,I.C., Beek,F.J.A., and Groenendaal,F. (2001). Unilateral parenchymal haemorrhagic infarction in the preterm infant. *European Journal of Paediatric Neurology* 5, 139-149.

Debillon,T., N'Guyen,S., Muet,A., Quere,M.P., Moussaly,F., and Roze,J.C. (2003). Limitations of ultrasonography for diagnosing white matter damage in preterm infants. *Archives of Disease in Childhood Fetal & Neonatal Edition* 88, F275-F279.

DeReuck,J., Chattha,A.S., and Richardson Jr,E.P. (1972). Pathogenesis and evolution of periventricular leukomalacia in infancy. *Archives of Neurology* 27, 229-236.

Drummond,P.M. and Colver,A.F. (2002). Analysis by gestational age of cerebral palsy in singleton births in north-east England 1970-94. *Paediatric and Perinatal Epidemiology* 16, 172-180.

Dyet,L.E., Kennea,N., Counsell,S.J., Maalouf,E.F., Ajayi-Obe,M., Duggan,P.J., Harrison,M., Allsop,J.M., Hajnal,J., Herlihy,A.H., Edwards,B., Laroche,S., Cowan,F.M., Rutherford,M.A., and Edwards,A.D. (2006). Natural history of brain lesions in extremely preterm infants studied with serial magnetic resonance imaging from birth and neurodevelopmental assessment. *Pediatrics* 118, 536-548.

Einstein,A. (1926). Investigations on the Theory of the Brownian Movement, edited by R. Fuerth, Methuen, London.

Evans,A.C., Collins,D.L., and Milner,B. (1992). An MRI-based stereotactic atlas from 250 young normal subjects. Society for Neuroscience Abstracts *18*.

Evrard,P., Gressens,P., and Volpe,J.J. (1992). New concepts to understand the neurological consequences of subcortical lesions in the premature brain. Biology of the Neonate *61*, 1-3.

Faix,R.G. and Donn,S.M. (1985). Association of septic shock caused by early-onset group B streptococcal sepsis and periventricular leukomalacia in the preterm infant. Pediatrics *76*, 415-419.

Fawer,C.L. and Levene,M.I. (1982). Elusive blood clots and fluctuating ventricular dilatation after neonatal intraventricular haemorrhage. Archives of Disease in Childhood *57*, 158.

Fern,R. and Moller,T. (2000). Rapid Ischemic Cell Death in Immature Oligodendrocytes: A Fatal Glutamate Release Feedback Loop. Journal of Neuroscience *20*, 34.

Ferrant,M., Warfield,S.K., Nabavi,A., Jolesz,F.A. and Kikinis,R. (2000). Registration of 3D intraoperative MR images of the brain using a finite element biomechanical model. Proc Medical Image Computing and Computer-Assisted Intervention *1935*, 19–28.

Fields,R.D. and Waxman,S.G. (1988). Regional membrane heterogeneity in premyelinated CNS axons: factors influencing the binding of sterol-specific probes. Brain Research *443*, 231-242.

Fitzpatrick,J.M. and West,J.B. (2001). The distribution of target registration error in rigid-bodypoint-based registration. IEEE Transactions on Medical Imaging *20*, 917-927.

Fitzpatrick,J.M., West,J.B., and Maurer,C.R., Jr. (1998). Predicting error in rigid-body point-based registration. IEEE Transactions on Medical Imaging *17*, 694-702.

Frahm,J., Merboldt,K.D., and Hanicke,W. (1988). Direct FLASH MR imaging of magnetic field inhomogeneities by gradient compensation. *Magnetic Resonance in Medicine* 6, 474-480.

Fukumizu,M., Takashima,S., and Becker,L.E. (1996). Glial reaction in periventricular areas of the brainstem in fetal and neonatal posthemorrhagic hydrocephalus and congenital hydrocephalus. *Brain and Development* 18, 35-39.

Fukumizu,M., Takashima,S., and Becker,L.E. (1995). Neonatal posthemorrhagic hydrocephalus: neuropathologic and immunohistochemical studies. *Pediatric Neurology* 13, 230-234.

Gilbert,C. (1997). Retinopathy of prematurity: epidemiology. *Journal of Community Eye Health* 10, 22-24.

Gilles,F.H., Shankle,W., and Dooling,E.C. (1983). Myelinated tracts: growth patterns. In: F.H. Gilles, A. Leviton and E.C. Dooling, eds. *The Developing Human Brain*, Boston, MA Wright & Co. 117.

Giuliani,N.R., Calhoun,V.D., Pearlson,G.D., Francis,A., and Buchanan,R.W. (2005). Voxel-based morphometry versus region of interest: a comparison of two methods for analyzing gray matter differences in schizophrenia. *Schizophrenia Research* 74, 135-147.

Glover,G.H. (1999). 3D z-Shim Method for Reduction of Susceptibility Effects in BOLD fMRI. *Magnetic Resonance in Medicine* 42, 290-299.

Goldenberg,R.L., Hauth,J.C., and Andrews,W.W. (2000). Intrauterine Infection and Preterm Delivery. *New England Journal of Medicine* 342, 1500.

Goldenberg,R.L., Culhane,J.F., Iams,J.D., and Romero,R. (2008). Epidemiology and causes of preterm birth. *The Lancet* 371, 75-84.

Goldman,J.E. (1992). Regulation of oligodendrocyte differentiation. *Trends in Neurosciences* 15, 359-362.

Good,C.D., Johnsrude,I.S., Ashburner,J., Henson,R.N.A., Friston,K.J., and Frackowiak,R.S.J. (2001). A Voxel-Based Morphometric Study of Ageing in 465 Normal Adult Human Brains. *NeuroImage 14*, 21-36.

Gould,S.J., Howard,S., Hope,P.L., and Reynolds,E.O. (1987). Periventricular intraparenchymal cerebral haemorrhage in preterm infants: the role of venous infarction. *Journal of Pathology 151*, 197-202.

Gousias,I.S., Rueckert,D., Heckemann,R.A., Dyet,L.E., Boardman,J.P., Edwards,A.D., and Hammers,A. (2007). Automatic segmentation of brain MRIs of 2-year-olds into 83 regions of interest. *NeuroImage*.

Gu,H., Feng,H., Zhan,W., Xu,S., Silbersweig,D.A., Stern,E., and Yang,Y. (2002). Single-shot interleaved z-shim EPI with optimized compensation for signal losses due to susceptibility-induced field inhomogeneity at 3 T. *NeuroImage 17*, 1358-1364.

Guimond,A., Meunier,J., and Thirion,J.P. (2000). Average Brain Models: A Convergence Study. *Computer Vision and Image Understanding 77*, 192-210.

Haacke,E.M., Brown,R.W., Thompson,M.R., and Venkatesan,R. *Magnetic Resonance Imaging: Physical Principles and Sequence Design*. 1999. New York: John Wiley & Sons, Inc.

Hajnal,J.V., Hawkes,D.J., and Hill,D.L.G. (2001). *Medical Image Registration*. CRC Press.

Hajnal,J.V., Oatridge,A., Bydder,G.M., and Young,I.R. (1994). A sinc based interpolation and coregistration method for precise image matching in functional imaging and other serial MRI studies. *Proceedings of the Second Meeting of the Society of Magnetic, San Francisco, CA*.

Hajnal,J.V., Saeed,N., Soar,E.J., Oatridge,A., Young,I.R., and Bydder,G.M. (1995). A Registration and Interpolation Procedure for Subvoxel Matching of Serially Acquired MR Images. *Journal of Computer Assisted Tomography 19*, 289.

Hambleton,G. and Wigglesworth,J.S. (1976). Origin of intraventricular haemorrhage in the preterm infant. *Archives of Disease in Childhood* 51, 651.

Hamilton,B.E., Martin,J.A. and Ventura,S.J. (2006). Births: preliminary data for 2005. *National Vital Statistics Reports* 55(11), 1-18.

Hamrick,S.E.G., Miller,S.P., Leonard,C., Glidden,D.V., Goldstein,R., Ramaswamy,V., Piecuch,R., and Ferriero,D.M. (2004). Trends in severe brain injury and neurodevelopmental outcome in premature newborn infants: The role of cystic periventricular leukomalacia. *The Journal of Pediatrics* 145, 593-599.

Haselgrove,J.C. and Moore,J.R. (1996). Correction for distortion of echo-planar images used to calculate the apparent diffusion coefficient. *Magnetic Resonance in Medicine* 36, 960-964.

Haydar,T.F., Wang,F., Schwartz,M.L., and Rakic,P. (2000). Differential Modulation of Proliferation in the Neocortical Ventricular and Subventricular Zones. *Journal of Neuroscience* 20, 5764.

Hildebrand,C. and Waxman,S.G. (1984). Postnatal differentiation of rat optic nerve fibers: Electron microscopic observations on the development of nodes of Ranvier and axoglial relations. *The Journal of Comparative Neurology* 224, 25-37.

Holling,E.E. and Leviton,A. (1999). Characteristics of cranial ultrasound white-matter echolucencies that predict disability: a review. *Developmental Medicine and Child Neurology* 41, 136-139.

Holmes,C.J., Hoge,R., Collins,L., Woods,R., Toga,A.W., and Evans,A.C. (1998). Enhancement of MR Images Using Registration for Signal Averaging. *Journal of Computer Assisted Tomography* 22, 324.

Horsfield,M.A. (1999). Mapping eddy current induced fields for the correction of diffusion-weighted echo planar images. *Magnetic Resonance Imaging* 17, 1335-1345.

Hughes,C.A., O'Gorman,L.A., Shyr,Y., Schork,M.A., Bozynski,M.E.A., and McCormick,M.C. (1999). Cognitive Performance at School Age of Very Low Birth Weight Infants with Bronchopulmonary Dysplasia. *Journal of Developmental and Behavioral Pediatrics* 20, 1.

Huppi,P.S., Maier,S.E., Peled,S., Zientara,G.P., Barnes,P.D., Jolesz,F.A., and Volpe,J.J. (1998). Microstructural development of human newborn cerebral white matter assessed in vivo by diffusion tensor magnetic resonance imaging. *Pediatric Research* 44, 584-590.

Huppi,P.S., Murphy,B., Maier,S.E., Zientara,G.P., Inder,T.E., Barnes,P.D., Kikinis,R., Jolesz,F.A., and Volpe,J.J. (2001). Microstructural brain development after perinatal cerebral white matter injury assessed by diffusion tensor magnetic resonance imaging. *Pediatrics* 107, 455-460.

Hussain, N., Clive, J., and Bhandari, V. (1999). Current Incidence of Retinopathy of Prematurity, 1989-1997. *American Academy of Pediatrics* 104[3].

Husted,C., Montez,B., Le,C., Moscarello,M.A., and Oldfield,E. (1993). Carbon-13 Magic-Angle Sample-Spinning Nuclear Magnetic Resonance Studies of Human Myelin, and Model Membrane Systems. *Urbana* 51, 801.

Hutton,C., Bork,A., Josephs,O., Deichmann,R., Ashburner,J., and Turner,R. (2002). Image Distortion Correction in fMRI: A Quantitative Evaluation. *NeuroImage* 16, 217-240.

Inder,T.E., Huppi,P.S., Warfield,S., Kikinis,R., Zientara,G.P., Barnes,P.D., Jolesz,F., and Volpe,J.J. (1999). Periventricular white matter injury in the premature infant is followed by reduced cerebral cortical gray matter volume at term. *Annals of Neurology* 46, 755-760.

Inder,T.E., Wells,S.J., Mogridge,N.B., Spencer,C., and Volpe,J.J. (2003). Defining the nature of the cerebral abnormalities in the premature infant: a qualitative magnetic resonance imaging study. *Journal of Pediatrics* 143, 171-179.

Indredavik,M.S., Vik,T., Heyerdahl,S., Kulseng,S., and Brubakk,A.M. (2005). Psychiatric symptoms in low birth weight adolescents, assessed by screening questionnaires. *European Child and Adolescent Psychiatry* 14, 226-236.

Jansons,K.M. and Alexander,D.C. (2003). Persistent angular structure: new insights from diffusion MRI data. Dummy version. *Information Processing in Medical Imaging* 18, 672–683.

Jenkinson,M. (2001). Improved unwarping of EPI images using regularised B0 maps. *NeuroImage* 13, S165.

Jenkinson,M., Bannister,P., Brady,M., and Smith,S. (2002). Improved Optimization for the Robust and Accurate Linear Registration and Motion Correction of Brain Images. *NeuroImage* 17, 825-841.

Jenkinson,M. and Smith,S. (2001). A global optimisation method for robust affine registration of brain images. *Medical Image Analysis* 5, 143-156.

Jensen,J.H., Helpert,J.A., Ramani,A., Lu,H. and Kaczynski,K. (2005). Diffusional kurtosis imaging: the quantification of non-Gaussian water diffusion by means of magnetic resonance imaging. *Magnetic Resonance in Medicine* 53, 1432–1440.

Jezzard,P. and Balaban,R.S. (1995). Correction for geometric distortion in echo planar images from B0 field variations. *Magnetic Resonance in Medicine* 34, 65-73.

Jezzard,P., Barnett,A.S., and Pierpaoli,C. (1998). Characterization of and correction for eddy current artifacts in echo planar diffusion imaging. *Magnetic Resonance in Medicine* 39, 801-812.

Jiang,H., van Zijl,P.C., Kim,J., Pearlson,G.D., and Mori,S. (2006). DtiStudio: resource program for diffusion tensor computation and fiber bundle tracking. *Computer Methods and Programs in Biomedicine* 81, 106-116.

Jobe,A.H. and Bancalari,E. (2001). Bronchopulmonary dysplasia. *American Journal of Respiratory and Critical Care Medicine* 163, 1723-1729.

Jones,D.K., Horsfield,M.A., and Simmons,A. (1999). Optimal strategies for measuring diffusion in anisotropic systems by magnetic resonance imaging. *Magnetic Resonance in Medicine* 42, 515-525.

Kapellou,O., Counsell,S.J., Kennea,N., Dyet,L., Saeed,N., Stark,J., Maalouf,E., Duggan,P., Jayi-Obe,M., Hajnal,J., Allsop,J.M., Boardman,J., Rutherford,M.A., Cowan,F., and Edwards,A.D. (2006). Abnormal cortical development after premature birth shown by altered allometric scaling of brain growth. *PLoS. Medicine* 3, e265.

Kim,D.J., Park,H.J., Kang,K.W., Shin,Y.W., Kim,J.J., Moon,W.J., Chung,E.C., Kim,I.Y., Kwon,J.S., and Kim,S.I. (2006). How does distortion correction correlate with anisotropic indices? A diffusion tensor imaging study. *Magnetic Resonance Imaging* 24, 1369-1376.

Kim,T.I., Sohn,J., Pi,S.Y., and Yoon,Y.H. (2004). Postnatal risk factors of retinopathy of prematurity. *Paediatric Perinatal Epidemiology* 18, 130-134.

Kinney,H.C. and Back,S.A. (1998). Human oligodendroglial development: Relationship to periventricular leukomalacia. *Seminars in Pediatric Neurology* 5, 180-189.

Kostovic,I. and Jovanov-Milosevic,N. (2008). Subplate zone of the human brain: historical perspective and new concepts. *Collegium Antropologicum* 32, 3-8.

Krishnan,M.L., Dyet,L.E., Boardman,J.P., Kapellou,O., Allsop,J.M., Cowan,F., Edwards,A.D., Rutherford,M.A., and Counsell,S.J. (2007). Relationship between white matter apparent diffusion coefficients in preterm infants at term-equivalent age and developmental outcome at 2 years. *Pediatrics* 120, e604-e609.

Kubicki,M., Shenton,M.E., Salisbury,D.F., Hirayasu,Y., Kasai,K., Kikinis,R., Jolesz,F.A., and McCarley,R.W. (2002). Voxel-based morphometric analysis of gray matter in first episode schizophrenia. *NeuroImage*. 17, 1711-1719.

Kybic,J., Thevenaz,P., Nirkko,A., and Unser,M. (2000). Unwarping of unidirectionally distorted EPI images. *IEEE Transactions on Medical Imaging* 19, 80-93.

Larroche,J.C. (1972). Post-haemorrhagic hydrocephalus in infancy. Anatomical study. *Biology of the Neonate* 20, 287-299.

Laszkiewicz,I., Mouzannar,R., Wiggins,R.C., and Konat,G.W. (1999). Delayed Oligodendrocyte Degeneration Induced by Brief Exposure to Hydrogen Peroxide. *Journal of Neuroscience Research* 55, 303-310.

Lauterbur,P.C. (1973). Image formation by induced local interactions: examples employing nuclear magnetic resonance. *Nature* 242, 190-191.

Le Bihan,D., Breton,E., Lallemand,D., Grenier,P., Cabanis,E., and Laval-Jeantet,M. (1986). MR imaging of intravoxel incoherent motions: application to diffusion and perfusion in neurologic disorders. *Radiology* 161, 401-407.

Le Bihan,D., Poupon,C., Amadon,A., and Lethimonnier,F. (2006). Artifacts and pitfalls in diffusion MRI. *Journal of Magnetic Resonance Imaging* 24, 478-488.

Lee,S., Wolberg,G., Chwa,K.Y., and Shin,S.Y. (1996). Image metamorphosis with scattered feature constraints. *IEEE Transactions on Visualization and Computer Graphics* 2, 337-354.

Lee,S., Wolberg,G., and Shin,S.Y. (1997). Scattered data interpolation with multilevel B-splines. *IEEE Transactions on Visualization and Computer Graphics* 3, 228-244.

Lehmann,T.M., Gonner,C., and Spitzer,K. (1999). Survey: interpolation methods in medical image processing. *IEEE Transactions on Medical Imaging* 18, 1049-1075.

Levene,M. (2004). Is intensive care for very immature babies justified? *Acta Paediatrica* 93, 149-152.

Levene,M.I., Fawer,C.L., and Lamont,R.F. (1982). Risk factors in the development of intraventricular haemorrhage in the preterm neonate. *Archives of Disease in Childhood* 57, 410.

Leviton,A. and Gilles,F.H. (1984). Acquired perinatal leukoencephalopathy. *Annals of Neurology* 16, 1-8.

Levy,M.L., Masri,L.S., and McComb,J.G. (1997). Outcome For Preterm Infants with Germinal Matrix Hemorrhage and Progressive Hydrocephalus. *Neurosurgery* 41, 1111.

Lin,Y., Okumura,A., Hayakawa,F., Kato,T., Kuno,K., and Watanabe,K. (2001). Quantitative evaluation of thalami and basal ganglia in infants with periventricular leukomalacia. *Developmental Medicine and Child Neurology* 43, 481-485.

Maalouf,E.F., Duggan,P.J., Counsell,S.J., Rutherford,M.A., Cowan,F., Azzopardi,D., and Edwards,A.D. (2001). Comparison of findings on cranial ultrasound and magnetic resonance imaging in preterm infants. *Pediatrics* 107, 719-727.

Maalouf,E.F., Duggan,P.J., Rutherford,M.A., Counsell,S.J., Fletcher,A.M., Battin,M., Cowan,F., and Edwards,A.D. (1999). Magnetic resonance imaging of the brain in a cohort of extremely preterm infants. *Journal of Pediatrics* 135, 351-357.

Mandonnet,E., Nouet,A., Gatignol,P., Capelle,L., and Duffau,H. (2007). Does the left inferior longitudinal fasciculus play a role in language? A brain stimulation study. *Brain* 130, 623-629.

Mansfield,P. (1977). Multi-planar image formation using NMR spin echoes. *Journal of Physics. Atomic and Molecular Physics* 10, L55.

Marlow,N., Wolke,D., Bracewell,M.A., and Samara,M. (2005). Neurologic and developmental disability at six years of age after extremely preterm birth. *New England Journal of Medicine* 352, 9-19.

Maxwell,N.C., Davies,P.L., and Kotecha,S. (2006). Antenatal infection and inflammation: what's new? *Current Opinion in Infectious Diseases* 19, 253-258.

McColm,J.R. and Fleck,B.W. (2001). Retinopathy of prematurity: causation. *Seminars in Neonatology* 6, 453-460.

McDonald,J.W., Levine,J.M., and Qu,Y. (1998). Multiple classes of the oligodendrocyte lineage are highly vulnerable to excitotoxicity. *NeuroReport* 9, 2757.

McKerracher,L., Chamoux,M., and Arregui,C.O. (1996). Role of laminin and integrin interactions in growth cone guidance. *Molecular Neurobiology* 12, 95-116.

McKinstry,R.C., Mathur,A., Miller,J.H., Ozcan,A., Snyder,A.Z., Schefft,G.L., Almli,C.R., Shiran,S.I., Conturo,T.E., and Neil,J.J. (2002). Radial Organization of Developing Preterm Human Cerebral Cortex Revealed by Non-invasive Water Diffusion Anisotropy MRI. *Cerebral Cortex* 12, 1237-1243.

Ment,L.R., Duncan,C.C., Ehrenkranz,R.A., Lange,R.C., Taylor,K.J., Kleinman,C.S., Scott,D.T., Sivo,J., and Gettner,P. (1984). Intraventricular hemorrhage in the preterm neonate: timing and cerebral blood flow changes. *Journal of Pediatrics* 104, 419-425.

Ment,L.R., Ehrenkranz,R.A., Lange,R.C., Rothstein,P.T., and Duncan,C.C. (1981). Alterations in Cerebral Blood Flow in Preterm Infants with Intraventricular Hemorrhage. *Pediatrics* 68, 763-769.

Mercer,B.M. (2003). Preterm Premature Rupture of the Membranes. *American Journal of Obstetrics & Gynecology* 101, 178-193.

Miga,M.I., Paulsen,K.D., Lemery,J.M., Eisner,S.D., Hartov,A.H., Kennedy,F.E. and Roberts,D.W. (1999). Model-updated image guidance: Initial clinical experiences with gravity-induced brain deformation. *IEEE Transactions on Medical Imaging* 18, 866-874.

Miller,S.P., Cozzio,C.C., Goldstein,R.B., Ferriero,D.M., Partridge,J.C., Vigneron,D.B., and Barkovich,A.J. (2003). Comparing the Diagnosis of White Matter Injury in Premature Newborns with Serial MR Imaging and Transfontanel Ultrasonography Findings. *American Journal of Neuroradiology* 24, 1661-1669.

Miller,S.P., Vigneron,D.B., Henry,R.G., Bohland,M.A., Ceppi-Cozzio,C., Hoffman,C., Newton,N., Partridge,J.C., Ferriero,D.M., and Barkovich,A.J. (2002). Serial quantitative diffusion tensor MRI of the premature brain: development in newborns with and without injury. *Journal of Magnetic Resonance Imaging* 16, 621-632.

Mistry,N.N. and Hsu,E.W. (2006). Retrospective distortion correction for 3D MR diffusion tensor microscopy using mutual information and Fourier deformations. *Magnetic Resonance in Medicine* 56, 310-316.

Miyawaki,T., Matsui,K., and Takashima,S. (1998). Developmental characteristics of vessel density in the human fetal and infant brains. *Early Hum Development* 53, 65-72.

Mori,S. (2007). *Introduction to Diffusion Tensor Imaging*. Elsevier Science.

Morrison,J.J., Rennie,J.M. (1997). Clinical, scientific and ethical aspects of fetal and neonatal care at extremely preterm periods of gestation. *British Journal of Obstetrics and Gynaecology* 104, 1341-50.

Morriss,M.C., Zimmerman,R.A., Bilaniuk,L.T., Hunter,J.V., and Haselgrove,J.C. (1999). Changes in brain water diffusion during childhood. *Neuroradiology* 41, 929-934.

Moser,K., MacFarlane,A., Chow,Y.H., Hilder,L., and Dattani,N. (2007). Introducing new data on gestation-specific infant mortality among babies born in 2005 in England and Wales. *Health Statistics Quarterly* 35, 13-27.

Mukherjee,P., Miller,J.H., Shimony,J.S., Conturo,T.E., Lee,B.C.P., Almlı,C.R., and McKinstry,R.C. (2001). Normal Brain Maturation during Childhood: Developmental Trends Characterized with Diffusion-Tensor MR Imaging. *Radiology* 221, 349-358.

Mukherjee,P., Miller,J.H., Shimony,J.S., Philip,J.V., Nehra,D., Snyder,A.Z., Conturo,T.E., Neil,J.J., and McKinstry,R.C. (2002). Diffusion-tensor MR imaging of gray and white matter development during normal human brain maturation. *American Journal of Neuroradiology* 23, 1445-1456.

Neil,J.J., Shiran,S.I., McKinstry,R.C., Schefft,G.L., Snyder,A.Z., Almlı,C.R., Akbudak,E., Aronovitz,J.A., Miller,J.P., Lee,B.C., and Conturo,T.E. (1998). Normal brain in human newborns: apparent diffusion coefficient and diffusion anisotropy measured by using diffusion tensor MR imaging. *Radiology* 209, 57-66.

Netsch,T. and van Muiswinkel,A. (2004). Quantitative evaluation of image-based distortion correction in diffusion tensor imaging. *IEEE Transactions on Medical Imaging* 23, 789-798.

Nichols,T.E. and Holmes,A.P. (2002). Nonparametric permutation tests for functional neuroimaging: a primer with examples. *Human Brain Mapping* 15, 1-25.

Niehaus,A., Stegmuller,J., Diers-Fenger,M., and Trotter,J. (1999). Cell-Surface Glycoprotein of Oligodendrocyte Progenitors Involved in Migration. *Journal of Neuroscience* 19, 4948.

Nishimura,D.G. (1996). Principles of Magnetic Resonance Imaging. Department of Electrical Engineering: Stanford University.

Nosarti,C., Al-Asady,M.H.S., Frangou,S., Stewart,A.L., Rifkin,L., and Murray,R.M. (2002). Adolescents who were born very preterm have decreased brain volumes. *Brain* 125, 1616.

Nosarti,C., Allin,M.P., Frangou,S., Rifkin,L., and Murray,R.M. (2005). Hyperactivity in adolescents born very preterm is associated with decreased caudate volume. *Biological Psychiatry* 57, 661-666.

Nosarti,C., Rushe,T.M., Woodruff,P.W., Stewart,A.L., Rifkin,L., and Murray,R.M. (2004). Corpus callosum size and very preterm birth: relationship to neuropsychological outcome. *Brain* 127, 2080-2089.

Nunes,R.G., Jezzard,P., and Clare,S. (2005). Investigations on the efficiency of cardiac-gated methods for the acquisition of diffusion-weighted images. *Journal of Magnetic Resonance* 177, 102-110.

O'Shea,T.M., Counsell,S.J., Bartels,D.B., and Dammann,O. (2005). Magnetic resonance and ultrasound brain imaging in preterm infants. *Early Human Development* 81, 263-271.

O'Shea,T.M., Kothadia,J.M., Klinepeter,K.L., Goldstein,D.J., Jackson,B.G., Weaver,R.G., III, and Dillard,R.G. (1999). Randomized placebo-controlled trial of a 42-

day tapering course of dexamethasone to reduce the duration of ventilator dependency in very low birth weight infants: outcome of study participants at 1-year adjusted age. *Pediatrics* 104, 15-21.

Office of National Statistics. Live births by multiplicity and gestational age: England and Wales, 2005 (http://www.statistics.gov.uk/downloads/theme_population/pretermbirths_2005.xls). 2005.

Padovani,A., Borroni,B., Brambati,S.M., Agosti,C., Broli,M., Alonso,R., Scifo,P., Bellelli,G., Alberici,A., Gasparotti,R., and Perani,D. (2006). Diffusion tensor imaging and voxel based morphometry study in early progressive supranuclear palsy. *Journal of Neurology, Neurosurgery and Psychiatry* 77, 457-463.

Papadakis,N.G., Martin,K.M., Pickard,J.D., Hall,L.D., Carpenter,T.A., and Huang,C.L.H. (2000). Gradient preemphasis calibration in diffusion-weighted echo-planar imaging. *Magnetic Resonance in Medicine* 44, 616-624.

Papile,L.A., Burstein,J., Burstein,R., and Koffler,H. (1978). Incidence and evolution of subependymal and intraventricular hemorrhage: a study of infants with birth weights less than 1,500 gm. *Journal of Pediatrics* 92, 529-534.

Papile,L.A., Munsick-Bruno,G., and Schaefer,A. (1983). Relationship of cerebral intraventricular hemorrhage and early childhood neurologic handicaps. *Journal of Pediatrics* 103, 273-277.

Partridge,S.C., Mukherjee,P., Henry,R.G., Miller,S.P., Berman,J.I., Jin,H., Lu,Y., Glenn,O.A., Ferriero,D.M., Barkovich,A.J., and Vigneron,D.B. (2004). Diffusion tensor imaging: serial quantitation of white matter tract maturity in premature newborns. *NeuroImage*. 22, 1302-1314.

Pasternak,O., Sochen,N. and Assaf,Y. (2004). Separation of white matter fascicles from diffusion MRI using ϕ -functional regularization. *Proceedings of the International Society for Magnetic Resonance in Medicine* 12, 1227.

Pasternak, O., Sochen, N. and Assaf, Y. (2006). PDE based estimation and regularization of multiple diffusion tensor fields. In J. Weickert & H. Hagen (eds.), Visualization and image processing of tensor fields. Berlin: Springer.

Perlman, J.M. (1998). White matter injury in the preterm infant: an important determination of abnormal neurodevelopment outcome. *Early Human Development* 53, 99-120.

Perlman, J.M., Goodman, S., Kreusser, K.L., and Volpe, J.J. (1985). Reduction in intraventricular hemorrhage by elimination of fluctuating cerebral blood-flow velocity in preterm infants with respiratory distress syndrome. *New England Journal of Medicine* 312, 1353-1357.

Perlman, J.M., McMennamin, J.B., and Volpe, J.J. (1983). Fluctuating cerebral blood-flow velocity in respiratory-distress syndrome. Relation to the development of intraventricular hemorrhage. *New England Journal of Medicine* 309, 204-209.

Peterson, B.S., Anderson, A.W., Ehrenkranz, R., Staib, L.H., Tageldin, M., Colson, E., Gore, J.C., Duncan, C.C., Makuch, R., and Ment, L.R. (2003). Regional Brain Volumes and Their Later Neurodevelopmental Correlates in Term and Preterm Infants. *Pediatrics* 111, 939-948.

Pierpaoli, C., Marenco, S., Rohde, G., Jones, D.K., and Barnett, A.S. (2003). Analyzing the contribution of cardiac pulsation to the variability of quantities derived from the diffusion tensor. *Proceedings of the 11th Annual Meeting of ISMRM, Toronto, Canada* 70.

Pluim, J.P.W., Maintz, J.B.A., and Viergever, M.A. (2003). Mutual-information-based registration of medical images: a survey. *IEEE Transactions on Medical Imaging* 22, 986-1004.

Press, W.H., Teukolsky, S.A., Vetterling, W.T., and Flannery, B.P. (2002). *Numerical recipes in C: the art of scientific computing*. Cambridge University Press.

Pruessmann, K.P., Weiger, M., Scheidegger, M.B., and Boesiger, P. (1999). SENSE: Sensitivity Encoding for Fast MRI. *Magnetic Resonance in Medicine* 42, 952-962.

Purcell,E.M., Torrey,H.C., and Pound,R.V. (1946). Resonance Absorption by Nuclear Magnetic Moments in a Solid. *Physical Review* 69, 37-38.

Rademaker,K.J., Lam,J.N., van,H., I, Uiterwaal,C.S., Liefink,A.F., Groenendaal,F., Grobbee,D.E., and de Vries,L.S. (2004). Larger corpus callosum size with better motor performance in prematurely born children. *Seminars in Perinatology* 28, 279-287.

Ramanathan,R. (2008). Optimal ventilatory strategies and surfactant to protect the preterm lungs. *Neonatology*. 93, 302-308.

Rao,A., Chandrashekara,R., Sanchez-Ortiz,G.I., Mohiaddin,R., Aljabar,P., Hajnal,J.V., Puri,B.K., and Rueckert,D. (2004). Spatial transformation of motion and deformation fields using nonrigid registration. *IEEE Transactions on Medical Imaging* 23, 1065-1076.

Reese,T.G., Heid,O., Weisskoff,R.M., and Wedeen,V.J. (2003). Reduction of eddy-current-induced distortion in diffusion MRI using a twice-refocused spin echo. *Magnetic Resonance in Medicine* 49, 177-182.

Reimer,P., Parizel,P.M., and Stichnoth,F.A. (1999). *Clinical MR imaging: a practical approach*. Berlin; New York: Springer.

Remahl,S. and Hildebrand,C. (1990). Relation between axons and oligodendroglial cells during initial myelination I. The glial unit. *Journal of Neurocytology* 19, 313-328.

Resch,B., Gerdermann,A., Maurer,U., Ritschl,E., and M³ller,W. (1996). Neurodevelopmental outcome of hydrocephalus following intra-/periventricular hemorrhage in preterm infants: short-and long-term results. *Child's Nervous System* 12, 27-33.

Rivkin,M.J. (2000). Developmental neuroimaging of children using magnetic resonance techniques. *Mental Retardation and Developmental Disabilities Research Reviews* 6, 68-80.

- Rohde,G.K., Barnett,A.S., Basser,P.J., Marengo,S., and Pierpaoli,C. (2004). Comprehensive approach for correction of motion and distortion in diffusion-weighted MRI. *Magnetic Resonance in Medicine* 51, 103-114.
- Rueckert,D., Aljabar,P., Heckemann,R.A., Hajnal,J.V., and Hammers,A. (2006a). Diffeomorphic registration using B-splines. *Medical Image Computing and Computer Assisted Intervention* 9, 702-709.
- Rueckert,D., Chandrashekar,R., Aljabar,P., Bhatia,K.K., Boardman,J.P., Srinivasan,L., Rutherford,M.A., Dyet,L.E., Edwards,A.D., and Hajnal,J.V. (2006b). Quantification of Growth and Motion Using Non-rigid Registration. *Lecture Notes in Computer Science* 4241, 49.
- Rueckert,D., Sonoda,L.I., Hayes,C., Hill,D.L., Leach,M.O., and Hawkes,D.J. (1999). Nonrigid registration using free-form deformations: application to breast MR images. *IEEE Transactions on Medical Imaging* 18, 712-721.
- Saigal,S., Szatmari,P., Rosenbaum,P., Campbell,D., and King,S. (1991). Cognitive abilities and school performance of extremely low birth weight children and matched term control children at age 8 years: a regional study. *Journal of Pediatrics* 118, 751-760.
- Schmithorst,V.J. and Dardzinski,B.J. (2002). Automatic Gradient Preemphasis Adjustment: A 15-Minute Journey to Improved Diffusion-Weighted Echo-Planar Imaging. *Magnetic Resonance in Medicine* 47, 208-212.
- Schnabel,J.A., Rueckert,D., Quist,M., Blackall,J.M., Castellano-Smith,A.D., Hartkens,T., Penney,G.P., Hall,W.A., Liu,H., Truwit,C.L., Gerritsen,F.A., Hill,D.L.G., and Hawkes,D.J. (2001). A Generic Framework for Non-rigid Registration Based on Non-uniform Multi-level Free-Form Deformations. *Proceedings of the 4th International Conference on Medical Image Computing and Computer-Assisted Intervention*. 573-581.
- Schneider,J.F.L., Il'yasov,K.A., Hennig,J., and Martin,E. (2004). Fast quantitative diffusion-tensor imaging of cerebral white matter from the neonatal period to adolescence. *Neuroradiology* 46, 258-266.

Shen,D. and Davatzikos,C. (2002). HAMMER: hierarchical attribute matching mechanism for elastic registration. *IEEE Transactions on Medical Imaging* 21, 1421-1439.

Shen,Y., Larkman,D.J., Counsell,S., Pu,I.M., Edwards,D., and Hajnal,J.V. (2004). Correction of high-order eddy current induced geometric distortion in diffusion-weighted echo-planar images. *Magnetic Resonance in Medicine* 52, 1184-1189.

Shinwell,E.S., Karplus,M., Reich,D., Weintraub,Z., Blazer,S., Bader,D., Yurman,S., Dolfen,T., Kogan,A., Dollberg,S., Arbel,E., Goldberg,M., Gur,I., Naor,N., Sirotta,L., Mogilner,S., Zaritsky,A., Barak,M., and Gottfried,E. (2000). Early postnatal dexamethasone treatment and increased incidence of cerebral palsy. *Archives of Disease in Childhood, Fetal & Neonatal Edition* 83, F177-F181.

Short,E.J., Klein,N.K., Lewis,B.A., Fulton,S., Eisengart,S., Kercsmar,C., Baley,J., and Singer,L.T. (2003). Cognitive and academic consequences of bronchopulmonary dysplasia and very low birth weight: 8-year-old outcomes. *Pediatrics* 112, e359.

Shuman,R.M. and Selednik,L.J. (1980). Periventricular leukomalacia. A one-year autopsy study. *Archives of Neurology* 37, 231-235.

Sinha,S.K., Gupta,S., and Donn,S.M. (2008). Immediate respiratory management of the preterm infant. *Seminars in Fetal and Neonatal Medicine* 13, 24-29.

Skare,S. and Andersson,J.L. (2001). On the effects of gating in diffusion imaging of the brain using single shot EPI. *Magnetic Resonance Imaging* 19, 1125-1128.

Skidmore,M.D., Rivers,A., and Hack,M. (1990). Increased risk of cerebral palsy among very low-birthweight infants with chronic lung disease. *Developmental Medicine and Child Neurology* 32, 325-332.

Skinner,S.J., Campos,G.A., and Liggins,G.C. (1981). Collagen content of human amniotic membranes: effect of gestation length and premature rupture. *American Journal of Obstetrics & Gynecology* 57, 487-489.

Smith,S.M. (2002). Fast robust automated brain extraction. *Human Brain Mapping* 17, 143-155.

Smith,S.M., Jenkinson,M., Johansen-Berg,H., Rueckert,D., Nichols,T.E., Mackay,C.E., Watkins,K.E., Ciccarelli,O., Cader,M.Z., Matthews,P.M., and Behrens,T.E. (2006). Tract-based spatial statistics: voxelwise analysis of multi-subject diffusion data. *NeuroImage*. 31, 1487-1505.

Smith,S.M., Jenkinson,M., Woolrich,M.W., Beckmann,C.F., Behrens,T.E., Johansen-Berg,H., Bannister,P.R., De,L.M., Drobnyak,I., Flitney,D.E., Niazy,R.K., Saunders,J., Vickers,J., Zhang,Y., De,S.N., Brady,J.M., and Matthews,P.M. (2004). Advances in functional and structural MR image analysis and implementation as FSL. *NeuroImage*. 23 *Suppl 1*, S208-S219.

Song,A.W. (2001). Single-shot EPI with signal recovery from the susceptibility-induced losses. *Magnetic Resonance in Medicine* 46, 407-411.

Speer,C.P. (2004). Pre- and postnatal inflammatory mechanisms in chronic lung disease of preterm infants. *Paediatric Respiratory Reviews* 5 *Suppl A*, S241-S244.

Stejskal,E. and Tanner,J.E. (1965). Spin diffusion measurements: spin echoes in the presence of a time-dependent field gradient. *Journal of Chemical Physics* 42, 288-292.

Stewart,A.L., Rifkin,L., Amess,P.N., Kirkbride,V., Townsend,J.P., Miller,D.H., Lewis,S.W., Kingsley,D.P., Moseley,I.F., Foster,O., and Murray,R.M. (1999). Brain structure and neurocognitive and behavioural function in adolescents who were born very preterm. *Lancet* 353, 1653-1657.

Studholme,C. (1999). An overlap invariant entropy measure of 3D medical image alignment. *Pattern Recognition* 32, 71.

Studholme,C., Cardenas,V., Maudsley,A., and Weiner,M. (2003). An intensity consistent filtering approach to the analysis of deformation tensor derived maps of brain shape. *NeuroImage* 19, 1638-1649.

Studholme,C., Constable,R.T., and Duncan,J.S. (2000). Accurate alignment of functional EPI data to anatomical MRI using a physics-based distortion model. *IEEE Transactions on Medical Imaging* 19, 1115-1127.

Suzuki,Y., Matsuzawa,H., Kwee,I.L., and Nakada,T. (2003). Absolute eigenvalue diffusion tensor analysis for human brain maturation. *NMR in Biomedicine* 16, 257-260.

Szatmari,P., Saigal,S., Rosenbaum,P., Campbell,D., and King,S. (1990). Psychiatric disorders at five years among children with birthweights less than 1000g: a regional perspective. *Developmental Medicine and Child Neurology* 32, 954-962.

Szeliski,R. and Lavallée,S. (1996). Matching 3-D anatomical surfaces with non-rigid deformations using octree-splines. *International Journal of Computer Vision* 18, 171-186.

Takashima,S., Mito,T., and Ando,Y. (1986). Pathogenesis of periventricular white matter hemorrhages in preterm infants. *Brain Development* 8, 25-30.

Takashima,S. and Tanaka,K. (1978). Development of cerebrovascular architecture and its relationship to periventricular leukomalacia. *Archives of Neurology* 35, 11-16.

Takeichi, M. (1988). The cadherins: cell-cell adhesion molecules controlling animal morphogenesis. *Development* 102[4], 639-655.

Talairach,J. and Tournoux,P. (1988). *Co-Planar Stereotaxic Atlas of the Human Brain: 3-Dimensional Proportional System: An Approach to Cerebral Imaging*. Thieme.

Tanner,S.F., Ramenghi,L.A., Ridgway,J.P., Berry,E., Saysell,M.A., Martinez,D., Arthur,R.J., Smith,M.A., and Levene,M.I. (2000). Quantitative comparison of intrabrain diffusion in adults and preterm and term neonates and infants. *American Journal of Roentgenology* 174, 1643-1649.

Thevenaz,P., Blu,T., and Unser,M. (2000). Image interpolation and resampling. *Handbook of Medical Imaging, Processing and Analysis* 393-420.

Thevenaz,P. and Unser,M. (2000). Optimization of mutual information for multiresolution image registration. *IEEE Transactions on Image Processing* 9, 2083-2099.

Thompson,D.K., Warfield,S.K., Carlin,J.B., Pavlovic,M., Wang,H.X., Bear,M., Kean,M.J., Doyle,L.W., Egan,G.F., and Inder,T.E. (2007). Perinatal risk factors altering regional brain structure in the preterm infant. *Brain* 130, 667-677.

Toft,P.B., Leth,H., Peitersen,B., Lou,H.C., and Thomsen,C. (1996). The apparent diffusion coefficient of water in gray and white matter of the infant brain. *Journal Computer Assisted Tomography* 20, 1006-1011.

Tuch,D.S., Reese,T.G., Wiegell,M.R., Makris,N., Belliveau,J.W. and Wedeen,V.J. (2002). High angular resolution diffusion imaging reveals intravoxel white matter fiber heterogeneity. *Magnetic Resonance in Medicine* 48, 577–582.

Unser,M. (1999). Splines: a perfect fit for signal and image processing. *IEEE Signal Processing Magazine* 16, 22.

Vadillo-Ortega,F., Sadowsky,D.W., Haluska,G.J., Hernandez-Guerrero,C., Guevara-Silva,R., Gravett,M.G., and Novy,M.J. (2002). Identification of matrix metalloproteinase-9 in amniotic fluid and amniochorion in spontaneous labor and after experimental intrauterine infection or interleukin-1 [beta] infusion in pregnant rhesus monkeys. *American Journal of Obstetrics & Gynecology* 186, 128.

van de Bor,M., Ens-Dokkum,M., Schreuder,A.M., Veen,S., Brand,R., and Verloove-Vanhorick,S.P. (1993). Outcome of periventricular-intraventricular haemorrhage at five years of age. *Developmental Medicine and Child Neurology* 35, 33-41.

Volpe,J.J. (2001). Neurobiology of Periventricular Leukomalacia in the Premature Infant. *Pediatric Research* 50, 553.

Volpe,J.J. (1989). Intraventricular hemorrhage and brain injury in the premature infant. Diagnosis, prognosis, and prevention. *Clinical Perinatology* 16, 387-411.

Volpe,J.J. (2003). Cerebral white matter injury of the premature infant-more common than you think. *Pediatrics 112*, 176-180.

Volpe,J.J. (1998). Neurologic Outcome of Prematurity. *Archives of Neurology 55*, 297-300.

Watson,D. (1991). Regional variation in the abundance of axonal cytoskeletal proteins. *Journal of Neuroscience Research 30*, 226-231.

Weinberger,D.R., Luchins,D.J., Morihisa,J., and Wyatt,R.J. (1982). Asymmetrical volumes of the right and left frontal and occipital regions of the human brain. *Annals of Neurology 11*, 97-100.

West,J., Fitzpatrick,J.M., Wang,M.Y., Dawant,B.M., Maurer Jr,C.R., Kessler,R.M., Maciunas,R.J., Barillot,C., Lemoine,D., and Collignon,A. (1997). Comparison and Evaluation of Retrospective Intermodality Brain Image Registration Techniques. *Journal of Computer Assisted Tomography 21*, 554.

Whitaker,A.H., Feldman,J.F., Van Rossem,R., Schonfeld,I.S., Pinto-Martin,J.A., Torre,C., Blumenthal,S.R., and Paneth,N.S. (1996). Neonatal cranial ultrasound abnormalities in low birth weight infants: relation to cognitive outcomes at six years of age. *Pediatrics 98*, 719-729.

Whitelaw,A., Mowinckel,M.C., and Abildgaard,U. (1995). Low levels of plasminogen in cerebrospinal fluid after intraventricular haemorrhage: a limiting factor for clot lysis? *Acta Paediatrica 84*, 933-936.

Wiles,A.D., Likholyot,A., Frantz,D.D., and Peters,T.M. (2008). A Statistical Model for Point-Based Target Registration Error With Anisotropic Fiducial Localizer Error. *IEEE Transactions on Medical Imaging 27*, 378-390.

Wimberger,D.M., Roberts,T.P., Barkovich,A.J., Prayer,L.M., Moseley,M.E., and Kucharczyk,J. (1995). Identification of "premyelination" by diffusion-weighted MRI. *Journal of Computer Assisted Tomography 19*, 28-33.

Wood,N.S., Costeloe,K., Gibson,A.T., Hennessy,E.M., Marlow,N., and Wilkinson,A.R. (2005). The EPICure study: associations and antecedents of neurological and developmental disability at 30 months of age following extremely preterm birth. *Archives of Disease in Childhood, Fetal and Neonatal Edition* 90, F134-F140.

Woods,R.P., Cherry,S.R., and Mazziotta,J.C. (1992). Rapid Automated Algorithm for Aligning and Reslicing PET Images. *Journal of Computer Assisted Tomography* 16, 620.

Woods,R.P., Grafton,S.T., Holmes,C.J., Cherry,S.R., and Mazziotta,J.C. (1998a). Automated Image Registration: I. General Methods and Intrasubject, Intramodality Validation. *Journal of Computer Assisted Tomography* 22, 139.

Woods,R.P., Grafton,S.T., Watson,J.D.G., Sicotte,N.L., and Mazziotta,J.C. (1998b). Automated Image Registration: II. Intersubject Validation of Linear and Nonlinear Models. *Journal of Computer Assisted Tomography* 22, 153.

Wu,Y.W. (2002). Systematic review of chorioamnionitis and cerebral palsy. *Mental Retardation and Developmental Disabilities Research Reviews* 8, 25-29.

Yeh,T.F., Lin,Y.J., Huang,C.C., Chen,Y.J., Lin,C.H., Lin,H.C., Hsieh,W.S., and Lien,Y.J. (1998). Early dexamethasone therapy in preterm infants: a follow-up study. *Pediatrics* 101, E7.

Yeh,T.F., Lin,Y.J., Lin,H.C., Huang,C.C., Hsieh,W.S., Lin,C.H., and Tsai,C.H. (2004). Outcomes at school age after postnatal dexamethasone therapy for lung disease of prematurity. *New England Journal of Medicine* 350, 1304-1313.

York,J.R., Landers,S., Kirby,R.S., Arbogast,P.G., and Penn,J.S. (2004). Arterial Oxygen Fluctuation and Retinopathy of Prematurity in Very-Low-Birth-Weight Infants. *Journal of Perinatology* 24, 82-87.

Zin,A. (2001). The Increasing Problem of Retinopathy of Prematurity. *Community Eye Health* 14, 58.